



**EFFECT OF DIMPLE PATTERN ON THE  
SUPPRESSION OF BOUNDARY LAYER  
SEPARATION ON A LOW PRESSURE  
TURBINE BLADE**

THESIS

John P. Casey, Second Lieutenant, USAF  
AFIT/GAE/ENY/04-M05

**DEPARTMENT OF THE AIR FORCE  
AIR UNIVERSITY**

**AIR FORCE INSTITUTE OF TECHNOLOGY**

---

**Wright-Patterson Air Force Base, Ohio**

The views expressed in this thesis are those of the author and do not reflect the official policy or position of the United States Air Force, Department of Defense, or the United States Government.

AFIT/GAE/ENY/04-M05

EFFECT OF DIMPLE PATTERN ON THE SUPPRESSION OF BOUNDARY LAYER  
SEPARATION ON A LOW PRESSURE TURBINE BLADE

THESIS

Presented to the Faculty

Department of Aeronautics and Astronautics

Graduate School of Engineering and Management

Air Force Institute of Technology

Air University

Air Education and Training Command

In Partial Fulfillment of the Requirements for the  
Degree of Master of Science in Aeronautical Engineering

John P. Casey, BS

Second Lieutenant, USAF

March 2004

APPROVED FOR PUBLIC RELEASE; DISTRIBUTION UNLIMITED.

AFIT/GAE/ENY/04-M05

EFFECT OF DIMPLE PATTERN ON THE SUPPRESSION OF BOUNDARY LAYER  
SEPARATION ON A LOW PRESSURE TURBINE BLADE

John P. Casey, BS  
Second Lieutenant, USAF

Approved:

---

Dr. Paul I. King (Chairman)

---

date

---

Lt Col Raymond C. Maple (Member)

---

date

---

Maj Richard J. McMullan (Member)

---

date

## **Abstract**

Three dimple patterns were investigated to ascertain their relative effectiveness on controlling boundary layer separation from a low-pressure turbine blade. The three cases included a single row of dimples at 65% of the axial chord with 2.22 cm spacing, a single row of dimples at 65% of the axial chord with 4.44 cm spacing, and a two-row staggered pattern with rows at 65% and 76% of the axial chord with 4.44 cm spacing. The multiple row case was such that the center of the upstream dimple set at the midpoint between two downstream dimples. The dimple spacing was measured center-on-center. Each of the dimple patterns was studied and compared to an unmodified blade at axial chord Reynolds numbers based on inlet velocity of 25k, 45k, and 100k. Experimental data was collected in a low-speed, draw down wind tunnel containing a linear turbine cascade of 8 Pak-B blades. Measurements of surface pressure, boundary layer parameters, wake velocity, and total pressure losses were made to examine the flow. No dimple pattern dramatically outperformed the others. Each of the dimple patterns studied improved the average total pressure loss coefficient by 34% for Re 25k and 1% Tu. Complementing the experimental effort was a three-dimensional computational fluid dynamics study. Four models were built and analyzed. The models included an unmodified blade, blades with dimples at 65% of the axial chord with 2 cm or 4 cm spacing, respectively, and a multiple row case consisting of dimples at 65% and 76% of the axial chord with 2 cm spacing. Again the upstream dimple set at the midpoint between two downstream dimples. The computational fluid dynamics study provided detailed flow visualization in and around the dimples as well as a comparison to experimental data for solver verification. It was shown that the computational and experimental results showed similar trends in wake loss and boundary layer traverses.

## **Acknowledgments**

There are a few key people I would like to recognize whose help was invaluable in the completion of this research. First, I would like to extend my appreciation to my advisor Dr. Paul King. His support and guidance over the past year have help direct the course of this research. Further, I would like to thank my sponsor, Dr. Rolf Sondergaard, from the Air Force Research Laboratory. Dr. Sondergaard's expertise in experimental research proved priceless throughout this project. His knowledge of both experimental methodology and turbine dynamics made the collection and reduction of data very efficient.

This work was also supported in part by a grant of computer time from the DOD High Performance Computing Modernization Program at ASC/MSRC. There are two people, in particular, at ASC/MSRC who gave tirelessly of their time to support me in my research efforts. Dr. Hugh Thornburg dedicated an enormous amount of time and energy to this project. He was instrumental in the development of computational models, the processing of the flow solution, and the post-processing. Also Dr. Rhonda Vickery aided in the flow field visualization. Special thanks are also paid to the MSRC personnel who helped create my account and obtain building access.

I would like to recognize the members of my committee who supported me through my entire time at AFIT. Lt Col Maple and Maj McMullan were significant contributors to my entire academic career at AFIT. In particular, they helped guide the direction of my computational efforts.

Lastly, and most important, I want to thank my family and friends who supported me through the entire process. Their immeasurable contribution made the pursuit of this degree possible. I thank you all.

John Philip Casey

# TABLE OF CONTENTS

	Page
Abstract .....	iv
Acknowledgments.....	v
List of Figures .....	ix
List of symbols .....	xviii
CHAPTER 1. INTRODUCTION .....	1
1.1 LOW PRESSURE TURBINE OPERATION AT LOW REYNOLDS NUMBERS .....	3
1.2 PREVIOUS EXPERIMENTS IN FLOW SEPARATION ON LPT BLADES .....	4
1.3 CURRENT RESEARCH OBJECTIVES .....	6
1.4 CHAPTER SUMMARY .....	9
CHAPTER 2. BACKGROUND AND THEORY .....	10
2.1 DETERMINATION OF LPT PERFORMANCE IMPROVEMENTS .....	11
2.2 LOW PRESSURE TURBINE BOUNDARY LAYER AERODYNAMICS.....	17
2.2.1 <i>Experimental Laminar-to-Turbulent Boundary Layer Transition</i> .....	18
2.2.2 <i>Numerical Models for Low Pressure Turbine Performance</i> .....	19
2.3 SEPARATION CONTROL ON LOW PRESSURE TURBINES .....	21
2.3.1 <i>Active and Passive Controls</i> .....	22
2.3.2 <i>Previous Research in Dimples for Boundary Layer Control</i> .....	27
CHAPTER 3. EXPERIMENTAL STUDY.....	30
3.1 WIND TUNNEL AND CASCADE CHARACTERISTICS .....	30
3.1.1 <i>Wind Tunnel Geometry and Features</i> .....	31
3.1.2 <i>Cascade Features</i> .....	33
3.1.3 <i>Test Section Characteristics</i> .....	35
3.2 INSTRUMENTATION .....	37
3.2.1 <i>Temperature Instrumentation</i> .....	39
3.2.2 <i>Velocity Instrumentation</i> .....	39
3.2.3 <i>Pressure Instrumentation</i> .....	41
3.3 DATA COLLECTION METHODOLOGY.....	44
3.3.1 <i>Wake Velocity and Loss Coefficient Profiles</i> .....	45
3.3.2 <i>Local Surface Pressure Profiles</i> .....	46
3.3.3 <i>Boundary Layer Profiles</i> .....	46

	Page
3.4	LOCAL SURFACE PRESSURE COEFFICIENT PROFILES .....48
3.5	BOUNDARY LAYER VELOCITY AND UNSTEADINESS PROFILES .....52
3.5.1	<i>Boundary Layer Profiles for an Unmodified Pak-B Blade at Tu 1%.....</i> 54
3.5.2	<i>Boundary Layer Profiles for Pak-B with Dimples at 65% of the axial chord and 1% Tu.....</i> 58
3.6	WAKE VELOCITY PROFILES .....60
3.6.1	<i>Wake Velocity Profiles for an Unmodified Pak-B Blade.....</i> 61
3.6.2	<i>Wake Velocity Profiles for Pak-B with Dimples at 65% of the axial chord with 2.22 cm Spacing at Tu 1%.....</i> 63
3.6.3	<i>Wake Velocity Profiles for Pak-B with Dimples at 65% of the axial chord with 4.44 cm Spacing at Tu 1%.....</i> 65
3.7	TOTAL PRESSURE LOSS COEFFICIENT .....66
3.7.1	<i>Total Pressure Loss Coefficient Profiles for an Unmodified Pak-B Blade .</i> 67
3.7.2	<i>Total Pressure Loss Coefficient Profiles for a Pak-B with Several Dimple Patterns at Tu 1%.....</i> 68
3.7.3	<i>Comparison of Average Total Pressure Loss Coefficients.....</i> 70
3.8	SUMMARY AND CONCLUSIONS OF EXPERIMENTAL RESEARCH .....73
CHAPTER 4.	COMPUTATIONAL FLUID DYNAMICS STUDY..... 75
4.1	COMPUTATIONAL SOFTWARE AND FLOW SOLVER CHARACTERISTICS.....77
4.2	GRID MODEL CHARACTERISTICS .....81
4.2.1	<i>Grid Topology for an Unmodified Pak-B Blade.....</i> 81
4.2.2	<i>Grid Topology for Pak-B Blade with 2 cm Dimple Spacing.....</i> 83
4.2.3	<i>Grid Topology for Pak-B Blade with 4 cm Dimple Spacing.....</i> 85
4.2.4	<i>Grid Topology for Pak-B Blade with Multiple Rows.....</i> 86
4.3	COMPUTATIONAL RESULTS .....88
4.3.1	<i>Separation Location.....</i> 88
4.3.2	<i>Velocity Field Comparisons.....</i> 92
4.3.3	<i>Streak Line Comparisons.....</i> 101
4.3.4	<i>Computational Boundary Layer Measurements.....</i> 107
4.3.5	<i>Computational Wake Loss Measurements.....</i> 108
4.4	SUMMARY AND CONCLUSIONS OF COMPUTATIONAL RESEARCH .....111
CHAPTER 5.	COMPARISONS BETWEEN EXPERIMENTAL & COMPUTATIONAL RESULTS..... 113
5.1	BOUNDARY LAYER MEASUREMENT COMPARISONS .....113
5.2	WAKE LOSS COMPARISONS .....116
CHAPTER 6.	SUMMARY AND RECOMMENDATIONS..... 118



	Page
APPENDIX A. Instrumentation Interface .....	123
APPENDIX B. Calibration Procedures.....	126
B.1    PRESSURE TRANSDUCER CALIBRATION .....	126
B.2    IFA-100 SETUP PROCEDURE.....	127
B.3    SINGLE-ELEMENT HOTWIRE/HOTFILM CALIBRATION .....	129
B.4    DUAL-ELEMENT HOTWIRE/HOTFILM CALIBRATION.....	131
APPENDIX C. Boundary Layer Traverses .....	135
APPENDIX D. Wake Velocity Profiles .....	159
APPENDIX E. Local Total Pressure Loss Coefficient Profiles .....	163
APPENDIX F. Computational Boundary Layer Measurements .....	167
APPENDIX G. CFD Time History Investigation .....	169
APPENDIX H. Tunnel Periodicity Study.....	172
References .....	173
Vita .....	177

## List of Figures

	Page
Figure 1. RQ-4 Global Hawk UAV (illustration by Virginia Reyes - Rouser, 2) .....	2
Figure 2. Pak-B blade with dimples at 50%, 55%, 65% and 76% of the axial chord.....	8
Figure 3. Various CFD grids developed for the current research .....	9
Figure 4. Brayton cycle and ideal gas turbine engine [Mattingly, 11: 233] .....	13
Figure 5. T-S diagram for a non-ideal turbine stage [Lake, 1] .....	14
Figure 6. T-S diagram illustrating possible improvement with higher turbine exit total pressure [Lake, 1].....	16
Figure 7. Illustration of the three cell types used in the 3-D Pak-B CFD model.....	20
Figure 8. Three surface vortex generator devices - Profile and surface views are shown with airflow depicted as an arrow [Lake, 1].....	24
Figure 9. Various other vortex generator devices - Profile and surface views are shown with airflow depicted as an arrow [Lake, 1] .....	25
Figure 10. Porous surface separation control device - Profile and surface views are shown with airflow depicted as an arrow [Lake, 1] .....	26
Figure 11. Various vortex generator devices with difficult application - Profile and surface views are shown with air flow depicted as an arrow [Lake, 1] .....	26
Figure 12. Aerolab Corporation modified drawdown wind tunnel (illustration courtesy of AFRL) .....	31
Figure 13. Cross-sectional area of wind tunnel [Lake, 1].....	32
Figure 14. Passive Turbulence grid - Generates approximately 4% $Tu$ (illustration courtesy of AFRL) .....	32
Figure 15. Plan view of test section [Bons et al., 39] .....	33
Figure 16. Removable cascade of eight Pak-B blades and endblade [Bons et al., 39].....	34
Figure 17. Test section geometry.....	35

	Page
Figure 18. Preliminary single pitch traverses with dimples at 65% of the axial chord with 2.22 cm spacing and 1% Tu .....	37
Figure 19. Wind tunnel instrumentation locations [Bons et al., 39] .....	38
Figure 20. Pressure instrumentation schematic [Rouser, 2] .....	44
Figure 21. $C_p$ curves for an unmodified Pak-B blade at various Reynolds numbers and 1% freestream turbulence .....	49
Figure 22. $C_p$ curves for an unmodified Pak-B blade at various Reynolds numbers and 4% freestream turbulence .....	49
Figure 23. Turbulence intensity comparison for Re 25k and 100k .....	51
Figure 24. $C_p$ curve on blade #6 for an unmodified and dimpled blade #5 at Re 45K and 1% Tu .....	52
Figure 25. Wall Location Calculation at 73.0% of the axial chord, Re 45k and 1% Tu .	54
Figure 26. Reynolds number effects on boundary layer profiles of an unmodified Pak-B at Tu 1% .....	55
Figure 27. Boundary Layer Comparison with prior research, Re 25k and 1% Tu .....	57
Figure 28. Boundary Layer Comparisons for different dimple patterns at Re 25k and 1% Tu .....	59
Figure 29. Boundary Layer Comparisons for different dimple patterns for Re 45K and 1% Tu .....	60
Figure 30. Reynolds number effect on exit velocity angles .....	61
Figure 31. Wake velocity profiles for varying Reynolds numbers behind an unmodified Pak-B blade at 1% Tu .....	62
Figure 32. Wake velocity profile comparisons with previous research for an unmodified Pak-B blade at 1% Tu .....	63
Figure 33. Wake velocity profiles for varying Reynolds numbers behind a Pak-B blade with dimples at 65% of the axial chord with 2.22 cm spacing at 1% Tu .....	64

	Page
Figure 34. Wake velocity profile comparisons with previous research for a Pak-B blade with dimples at 65% of the axial chord with 2.22 cm spacing and 1% Tu.....	65
Figure 35. Wake velocity traverses for dimples at 65% of the axial chord with 4.44 cm and 1% Tu at 3 spanwise locations .....	66
Figure 36. Wake loss profile comparisons with previous research for varying Reynolds numbers behind an unmodified Pak-B blade and 1% Tu .....	67
Figure 37. Wake loss profiles for various dimple patterns at Re 25k and 1% Tu .....	69
Figure 38. Wake loss profiles for various dimple patterns at Re 45k and 1% Tu .....	69
Figure 39. Wake loss profiles for various dimple patterns at Re 100k and 1% Tu .....	70
Figure 40. Average Total Pressure Loss Coefficients for various Reynolds numbers and dimple patterns at 1% Tu.....	71
Figure 41. Average Total Pressure Loss Coefficients for various Reynolds numbers and dimple patterns at 4% Tu.....	71
Figure 42. Average Total Pressure Loss Coefficients for unmodified blade at various Reynolds numbers and freestream turbulence levels .....	72
Figure 43. Pak-B blade unmodified surface topology [Rouser, 2] .....	82
Figure 44. Pak-B blade mid-passage grid topology [Rouser, 2].....	83
Figure 45. Pak-B blade with dimples at 65% of the axial chord and 2 cm spacing grid topology .....	84
Figure 46. Pak-B blade with 2 cm center-on-center dimple close-up.....	85
Figure 47. Pak-B blade with dimples at 65% of the axial chord and 4 cm spacing grid topology .....	86
Figure 48. Pak-B blade with multiple rows grid topology.....	87
Figure 49. Pak-B blade with multiple rows of dimples close-up.....	87
Figure 50. Separation and reattachment lines on an unmodified Pak-B computational model at Re 25k and 0% Tu.....	89

	Page
Figure 51. Separation and reattachment lines on a computational Pak-B blade with dimples at 65% of the axial chord with 2 cm spacing at Re 25k and 0% Tu.....	90
Figure 52. Separation and reattachment lines on a computational Pak-B blade with dimples at 65% of the axial chord with 4 cm spacing at Re 25k and 0% Tu.....	91
Figure 53. Separation and reattachment lines on a computational Pak-B blade with dimples at 65% and 76% of the axial chord with 2 cm spacing at Re 25k and 0% Tu .....	92
Figure 54. Velocity magnitude contours for an unmodified Pak-B computational model at Re 25k and 0% Tu .....	93
Figure 55. Velocity magnitude vectors for an unmodified Pak-B computational model at Re 25k and 0% Tu .....	94
Figure 56. Velocity magnitude contours and vectors for a computational Pak-B model with dimples at 65% of the axial chord and 2 cm spacing at Re 25k and 0% Tu.....	95
Figure 57. Velocity vectors pointing upstream entering the dimple at 65% of the axial chord with 4 cm spacing .....	97
Figure 58. Velocity magnitude contours and vectors for a computational Pak-B model with dimples at 65% of the axial chord and 4 cm spacing at Re 25k and 0% Tu.....	98
Figure 59. Velocity contours for each of the computational grids examined at 0.6 sec..	99
Figure 60. Velocity vectors near the upstream dimple on a computational Pak-B blade with dimples at 65% and 76% of the axial chord at Re 25k and 0% Tu .....	100
Figure 61. Streak lines through a dimple at 65% of the axial chord with 2 cm spacing at Re 25k and 0% Tu.....	101
Figure 62. Vortex within dimple at 65% of the axial chord with 2 cm spacing at Re 25k and 0% Tu .....	102
Figure 63. Surface streak lines on a computational Pak-B blade with dimples at 65% of the axial chord and 4 cm spacing at Re 25k and 0% Tu at 0.27525 sec.....	103

	Page
Figure 64. Streak lines on a computational Pak-B blade with dimples at 65% of the axial chord and 4 cm spacing at Re 25k and 0% Tu at 0.6 sec.....	103
Figure 65. Streak lines above and within a dimple at 65% of the axial chord with 4 cm spacing .....	104
Figure 66. Streak lines at the 65% axial chord dimple on multiple row Pak-B computational blade at Re 25k and 0% Tu .....	105
Figure 67. Streak lines on a computational Pak-B blade with dimples at 65% and 76% of the axial chord at Re 25k and 0% Tu at 0.6 sec .....	105
Figure 68. Streak lines showing exit angles over each of the CFD models examined at 0.6 seconds .....	106
Figure 69. Time averaged boundary layer profiles for computational Pak-B blades at Re 25k and 0% Tu .....	108
Figure 70. Time averaged wake loss profile for computational Pak-B blades at Re 25k and 0% Tu .....	108
Figure 71. Computational average total pressure loss coefficients at Re 25k and 0% Tu.....	110
Figure 72. Wake loss calculations over two different averaging intervals .....	110
Figure 73. Boundary layer comparisons between CFD and Experiment for an unmodified Pak-B blade at Re 25k and 0% Tu .....	114
Figure 74. Boundary layer comparisons between CFD and Experiment for a Pak-B blade with a single row of dimples at 65% of the axial chord with 2 cm spacing at Re 25k.....	115
Figure 75. Boundary layer comparisons between CFD and Experiment for a Pak-B blade with a single row of dimples at 65% of the axial chord with 4 cm spacing at Re 25k.....	115
Figure 76. Average total pressure loss coefficients for each of the cases studied.....	116
Figure 77. Total pressure loss profile comparisons between CFD and experimental results.....	117
Figure 78. Instrumentation Schematic [Rouser, 2] .....	123

	Page
Figure 79. Boundary layer profiles for an unmodified Pak-B blade at Re 100k and 1% Tu .....	135
Figure 80. Boundary layer profiles for an unmodified Pak-B blade at Re 45k and 1% Tu .....	136
Figure 81. Boundary layer profiles for an unmodified Pak-B blade at Re 25k and 1% Tu .....	137
Figure 82. Boundary layer profiles for an unmodified Pak-B blade at Re 100k and 4% Tu .....	138
Figure 83. Boundary layer profiles for an unmodified Pak-B blade at Re 45k and 4% Tu .....	139
Figure 84. Boundary layer profiles for an unmodified Pak-B blade at Re 25k and 4% Tu .....	140
Figure 85. Boundary layer profiles for a Pak-B blade with dimples at 65% of the axial chord with 2.22 cm spacing at Re 100k and 1% Tu .....	141
Figure 86. Boundary layer profiles for a Pak-B blade with dimples at 65% of the axial chord with 2.22 cm spacing at Re 45k and 1% Tu .....	142
Figure 87. Boundary layer profiles for a Pak-B blade with dimples at 65% of the axial chord with 2.22 cm spacing at Re 25k and 1% Tu .....	143
Figure 88. Boundary layer profiles for a Pak-B blade with dimples at 65% of the axial chord with 2.22 cm spacing at Re 100k and 4% Tu .....	144
Figure 89. Boundary layer profiles for a Pak-B blade with dimples at 65% of the axial chord with 2.22 cm spacing at Re 45k and 4% Tu .....	145
Figure 90. Boundary layer profiles for a Pak-B blade with dimples at 65% of the axial chord with 2.22 cm spacing at Re 25k and 4% Tu .....	146
Figure 91. Boundary layer profiles for a Pak-B blade with dimples at 65% of the axial chord with 4.44 cm spacing with probe behind a covered dimple at Re 100k and 1% Tu .....	147
Figure 92. Boundary layer profiles for a Pak-B blade with dimples at 65% of the axial chord with 4.44 cm spacing with probe behind a covered dimple at Re 45k and 1% Tu .....	148

	Page
Figure 93. Boundary layer profiles for a Pak-B blade with dimples at 65% of the axial chord with 4.44 cm spacing with probe behind a covered dimple at Re 25k and 1% Tu .....	149
Figure 94. Boundary layer profiles for a Pak-B blade with dimples at 65% of the axial chord with 4.44 cm spacing with probe behind a covered dimple at Re 100k and 4% Tu .....	150
Figure 95. Boundary layer profiles for a Pak-B blade with dimples at 65% of the axial chord with 4.44 cm spacing with probe behind a covered dimple at Re 45k and 4% Tu .....	151
Figure 96. Boundary layer profiles for a Pak-B blade with dimples at 65% of the axial chord with 4.44 cm spacing with probe behind a covered dimple at Re 25k and 4% Tu .....	152
Figure 97. Boundary layer profiles for a Pak-B blade with dimples at 65% of the axial chord with 4.44 cm spacing with probe behind an open dimple at Re 100k and 1% Tu .....	153
Figure 98. Boundary layer profiles for a Pak-B blade with dimples at 65% of the axial chord with 4.44 cm spacing with probe behind an open dimple at Re 45k and 1% Tu .....	154
Figure 99. Boundary layer profiles for a Pak-B blade with dimples at 65% of the axial chord with 4.44 cm spacing with probe behind an open dimple at Re 25k and 1% Tu .....	155
Figure 100. Boundary layer profiles for a Pak-B blade with dimples at 65% of the axial chord with 4.44 cm spacing with probe behind an open dimple at Re 100k and 4% Tu .....	156
Figure 101. Boundary layer profiles for a Pak-B blade with dimples at 65% of the axial chord with 4.44 cm spacing with probe behind an open dimple at Re 45k and 4% Tu .....	157
Figure 102. Boundary layer profiles for a Pak-B blade with dimples at 65% of the axial chord with 4.44 cm spacing with probe behind an open dimple at Re 25k and 4% Tu .....	158
Figure 103. Wake velocity profiles behind an unmodified Pak-B blade and 1% Tu ....	159
Figure 104. Wake velocity profiles behind an unmodified Pak-B blade and 4% Tu ....	159



	Page
Figure 105. Wake velocity profiles behind a Pak-B blade with dimples at 65% of the axial chord with 2.22 cm spacing and 1% Tu.....	160
Figure 106. Wake velocity profiles behind a Pak-B blade with dimples at 65% of the axial chord with 2.22 cm spacing and 4% Tu.....	160
Figure 107. Wake velocity profiles behind a Pak-B blade with dimples at 65% of the axial chord with 4.44 cm spacing and 1% Tu.....	161
Figure 108. Wake velocity profiles behind a Pak-B blade with dimples at 65% of the axial chord with 4.44 cm spacing and 4% Tu.....	161
Figure 109. Wake velocity profiles behind a Pak-B blade with dimples at 65% and 76% of the axial chord with 4.44 cm spacing and 1% Tu.....	162
Figure 110. Wake velocity profiles behind a Pak-B blade with dimples at 65% and 76% of the axial chord with 4.44 cm spacing and 4% Tu.....	162
Figure 111. Wake loss profiles behind an unmodified Pak-B blade and 1% Tu.....	163
Figure 112. Wake loss profiles behind an unmodified Pak-B blade and 4% Tu.....	163
Figure 113. Wake loss profiles behind a Pak-B blade with dimples at 65% of the axial chord with 2.22 cm spacing and 1% Tu.....	164
Figure 114. Wake loss profiles behind a Pak-B blade with dimples at 65% of the axial chord with 2.22 cm spacing and 1% Tu.....	164
Figure 115. Wake loss profiles behind a Pak-B blade with dimples at 65% of the axial chord with 4.44 cm spacing and 1% Tu.....	165
Figure 116. Wake loss profiles behind a Pak-B blade with dimples at 65% of the axial chord with 4.44 cm spacing and 1% Tu.....	165
Figure 117. Wake velocity profiles behind a Pak-B blade with dimples at 65% and 76% of the axial chord with 4.44 cm spacing and 1% Tu.....	166
Figure 118. Wake velocity profiles behind a Pak-B blade with dimples at 65% and 76% of the axial chord with 4.44 cm spacing and 4% Tu.....	166
Figure 119. Boundary layer profiles for an unmodified, computational Pak-B blade at Re 25k and 0% Tu .....	167

	Page
Figure 120. Boundary layer profiles for a computational Pak-B blade with dimples at 65% of the axial chord with 2 cm spacing at Re 25k and 0% Tu.....	167
Figure 121. Boundary layer profiles for a computational Pak-B blade with dimples at 65% of the axial chord with 4 cm spacing at Re 25k and 0% Tu.....	168
Figure 122. Boundary layer profiles for a computational Pak-B blade with dimples at 65% and 76% of the axial chord with 2 cm spacing at Re 25k and 0% Tu .....	168
Figure 123. Time History plot of at Re 25k and different dimple patterns .....	170
Figure 124. The time averaged velocity magnitude throughout each solution.....	171
Figure 125. Surface Static Pressure Coefficient Comparison between Blade 4 and Blade 6 at various Reynolds numbers and 4% Tu .....	172

## List of symbols

<b><u>Symbol</u></b>	<b><u>Definition</u></b>
$C$	Calibration curve fit constant, y – intercept
$c$	Axial chord length (m)
$C_D$	Aircraft drag coefficient
$C_L$	Aircraft lift coefficient
$C_P$	Pressure coefficient
$c_P$	Specific heat at constant pressure (J/kg K)
$D$	Calibration curve fit constant, curve slope
$D$	Diameter (m)
$dP$	Differential change in pressure (Pa)
$ds$	Differential change in entropy (J/kg K)
$dT$	Differential change in temperature (K)
$E$	Energy (J)
$exp$	Exponential
$g$	Acceleration due to gravity (m/s <sup>2</sup> )
$h_{pr}$	Low heating value of the fuel
$Hz$	Hertz
$k$	Depth (m)
$k$	Thousand
$K-\varepsilon$	Turbulent model
$K-\omega$	Turbulent model
$L$	One pitch length
$\ln$	Natural log
$\dot{m}$	Mass flow rate (kg/s)
$Nu$	Nusselt number

$P$	Pressure (Pa)
$q$	Dynamic pressure (Pa)
$Q$	Heat transfer (J)
$R$	Gas constant (J/kg K)
$R$	Range (m)
$Re$	Reynolds number
$s$	Entropy (J/kg K)
$T$	Temperature (K)
$T-S$	Temperature – Entropy
$T-S$	Tollmien - Schlichting
$Tu$	Freestream turbulence level (%)
$U$	Velocity (m/s)
$W$	Work (J)
$W$	Weight (N)
$y$	pitch direction

## **Greek**

<b><u>Symbol</u></b>	<b><u>Definition</u></b>
$\Delta$	Change
$\partial$	Partial derivative
$\gamma$	Ratio of specific heats
$\gamma$	Average total pressure loss coefficient
$\eta$	Efficiency
$\mu$	Viscosity (kg/m s)
$\pi$	Turbine stage total pressure ratio
$\rho$	Density (kg/m <sup>3</sup> )

$\tau$	Turbine stage total temperature ratio
$\omega$	Local total pressure loss coefficient

## Subscripts

<u>Symbol</u>	<u>Definition</u>
0-9	Engine station numbering
0	Total, stagnation, overall
c	Compressor
D	Drag
L	Lift
R	Relative to the rotor
s	Static
t	Total
t	Turbine

## Superscripts

<u>Symbol</u>	<u>Definition</u>
–	Time-Average, mean value
<sup>2</sup>	Squared
<sup>o</sup>	Degree

## Units

<u>Symbol</u>	<u>Definition</u>
cm	Centimeter
in H <sub>2</sub> O	Inches of Water
J	Joule
K	Kelvin

kg	Kilogram
m	Meter
mm	Millimeter
N	Newton
Pa	Pascal
sec	Second
W	Watt

## **Abbreviations**

<b><u>Symbol</u></b>	<b><u>Definition</u></b>
2-D	Two-dimensional
3-D	Three-dimensional
A/D	Analog to Digital
AFB	Air Force Base
AIAA	American Institute of Aeronautics and Astronautics
ASC	Aeronautical Systems Center
ASME	American Society of Mechanical Engineers
CFD	Computational fluid dynamics
DES	Detached eddy simulation
Eqn.	Equation
Fig.	Figure
LEBU	Large-eddy break-up
LES	Large eddy simulation
LPT	Low pressure turbine
MEMS	Micro-electromechanical systems
MS	Masters of Science

MSRC	Major Shared Resource Center
NASA	National Aerospace Administration
PC	Personal computer
RANS	Reynolds Averaged Navier Stokes
RPM	Revolutions per minute
TSFC	Thrust Specific Fuel Consumption
UAV	Unmanned aerial vehicles
USAF	United States Air Force
VBI	Vane blade interaction
VGD	Vortex generator device
VGJ	Vortex generator jet

# EFFECT OF DIMPLE PATTERN ON THE SUPPRESSION OF BOUNDARY LAYER SEPARATION ON A LOW PRESSURE TURBINE BLADE

## CHAPTER 1. INTRODUCTION

Recently, the United States Air Force has employed Unmanned Aerial Vehicles (UAVs) for high altitude reconnaissance. The range and endurance of UAVs such as the RQ-4 Global Hawk (Fig. 1) is limited by the low-pressure turbine (LPT) efficiency. Low Reynolds numbers experienced by LPT blades cause losses in efficiency and loading. This problem is seen in the Global Hawk program where the on design flight conditions are a standard cruise velocity of Mach 0.6 at an altitude of 65,000 ft [Lake, 1]. These flight conditions can result in LPT blade operating at inlet axial chord Reynolds number below 25k. The immediate impact of this extremely low Reynolds number is the development of laminar boundary layers over the turbine blades. The combined effect of the laminar flow and large turning angles associated with LPT blades results in flow separation over a substantial section of the blade's suction surface [Rouser, 2]. The loss in efficiency due to the boundary layer separation places restrictions on the aircraft range, altitude and electrical power extracted from the engine. A solution must be reached that will help delay separation at low Reynolds numbers, but not adversely affect blade



efficiency at higher Reynolds numbers. Comprehensive research is ongoing in the area of boundary layer separation control as a feasible solution to this problem.



Figure 1. RQ-4 Global Hawk UAV (illustration by Virginia Reyes - Rouser, 2)

In an attempt to study and improve LPT efficiency at low Reynolds number conditions, Pratt and Whitney developed the Pak-B profile. The commercially used Pratt and Whitney Pak airfoil was the foundation for the two-dimensional (2-D) Pak-B shape. Extruding the Pak-B shape in the spanwise direction yields a blade that can be used for local three-dimensional (3-D) analysis. Unfortunately, this blade does not truly represent a 3-D blade since it neglects taper and twist [Rouser, 2].

The investigation performed by Lake [1] involved testing various passive control techniques on a Pak-B blade. Ultimately, Lake [1] concluded that recessed dimples prevent separation if positioned just forward of the natural chordwise separation location. He reported for an operating Reynolds number of 45,000 and freestream turbulence of 4% that losses were reduced as much as 51.7% [Lake, 1]. Lake [1] inferred that the dimples energized the flow and forced the laminar boundary layer to transition to turbulence prior to separation thereby acting similar to vortex generators.

Recessed dimples possess great potential for reducing low Reynolds number losses without dramatically affecting higher Reynolds number efficiencies [Rouser, 2]. Moreover, these passive controls do not require a dramatic engine redesign. They do not carry with them any additional weight penalty nor require additional power from the engine. Most important, they can be easily retrofitted into existing engine hardware. It is important, however, that flow mechanisms produced by these passive controls be very well understood to assist in the exact size and placement of the dimples for an optimal engine design.

The current research investigated several dimple patterns for suppression of boundary layer separation on a low pressure turbine blade. Dimples placed at 65% of the axial chord with 2.22 cm and 4.44 cm center-on-center spacing and a multiple row case featuring dimples at 65% and 76% of the axial chord spaced 4.44 cm center-on-center were the cases investigated. The dimples in the multiple row case were arranged in a chevron pattern such that the center of an upstream dimple aligned with the midpoint between two downstream dimples. The study involved both wind tunnel experiments as well as computational simulations of the Pak-B profile. The unmodified blade was also tested for comparison. The computational study helped visualize the flow structure and helped shape the direction of further experimental studies for the evaluation of performance improvements.

## **1.1 Low Pressure Turbine Operation at Low Reynolds Numbers**

Historically, turbomachinery design has been focused on developing compressors for maximum pressure ratio and high-pressure turbines to sustain maximum temperatures. The LPT is not subject to extreme environmental conditions that would

require active cooling or other material or mechanical considerations. Therefore, research on the LPT is intended to optimize aerodynamic characteristics and maximize loading and efficiency. This research is required to further the capabilities of high altitude reconnaissance UAVs by enabling efficient operation of LPTs at low Reynolds numbers.

The environment in the vicinity of the LPT is intrinsically unsteady. It is common for the blades to shed wakes periodically. These wakes, in turn, travel downstream and pass over the blades in the next row. Inside the wake is a region of high local freestream turbulence. Halstead et al. [3; 4] conclude the turbulence intensity can reach as high as 20%. The momentary high turbulence levels suppress boundary layer separation although this effect is only temporary. The laminar flow existing between shedding cycles is vulnerable to flow separation due to the low turbulence intensity [Lake, 1].

## **1.2 Previous Experiments in Flow Separation on LPT Blades**

Turbine aerodynamics are often studied with linear cascade tunnels. Two-dimensional effects can be studied using linear cascades, as the blades are not rotating, and the flow is nearly uniform in the spanwise direction as it enters the test section [Rouser, 2]. A linear cascade consists of several blades lined-up in a row simulating the turning angle experienced in the low-pressure turbine. Chapter 3 presents a detailed discussion of the linear cascade tunnel used in the current research.

Previous experiments involving Reynolds numbers less than 200k have increased the understanding of the transitional boundary layers around LPT blades at low Reynolds numbers. Many of these experimentalists utilized linear cascades to help with their

research. Rivir [5] used a Langston airfoil to examine turbulent length scale effects on transition locations. Sharma et al. [6] discovered the loss coefficient nearly tripled as the Reynolds number was brought below 95k as compared to higher Reynolds numbers. Murawski et al. [7] and Qiu and Simon [8] have shown that flow separation from a Pak-B blade at low Reynolds numbers deteriorates the LPT performance, and have documented velocities, surface pressures, separation locations and boundary layer thicknesses. Murawski et al. [7] reported separation from 75% to 90% of the axial chord at inlet axial chord Reynolds numbers as low as 53k. Further, Qui and Simon [8] confirmed turbulent reattachment occurs aft the 90% axial chord location. Simon and Volino [9] have reported the efficiency losses of the Pak-B profile operating at conditions similar to those seen by high altitude UAVs. Hourmouziadis [10] also experimented with low Reynolds numbers and documented a reduction in efficiency and a dramatic increase in profile losses.

Much of the above research laid a firm foundation for Lake [1] to quantify the losses associated with flow separation at low Reynolds numbers for the Pak-B profile. Lake [1] confirmed an increase in the total pressure loss coefficient and wake momentum deficit related to the separated flow. He resolved that a natural chordwise separation location exists at about 70% of the axial chord on a Pak-B blade at an inlet axial chord Reynolds number of 45k and sought to control the separated-flow transition and laminar separation on a Pak-B blade [Lake, 1]. Lake [1] experimented with trip wires, spanwise V-grooves and recessed dimples. He documented a reduction of the losses associated with separated flow due to the successful integration of surface modifications [Lake, 1]. Lake [1] concluded that, of the techniques he explored, dimples had the greatest potential

in effectively eliminating losses associated with low Reynolds numbers. Lake's work provided a detailed understanding of LPT performance at low Reynolds operating conditions.

Rouser [2] furthered Lake's work by investigating full dimples as well as streamwise half-dimples at 50%, 55%, and 65% axial chord locations and extended the research to an operating Reynolds number of 25k. Rouser [2] concluded that for an inlet axial chord Reynolds number of 25k full dimples placed at 65% of the axial chord reduced separation losses by as much as 28%. He also developed computational models of the Pak-B blade with full and half-dimples at 60% of the axial chord, in addition to a grid representing a Pak-B blade without any surface modifications. The CFD investigation gave insight to the flow structure in and downstream of the dimples. The CFD was pursued with both a laminar solver as well as solvers that utilized Spalart-Allamara,  $K-\omega$ , and  $K-\epsilon$  turbulence modeling. The CFD indicated that the flow was transitional, and the turbulence models applied tended to enhance any inherent instability in the flow. With the turbulence models turned on, the solver failed to resolve a separation location [Rouser, 2]. Therefore, the computer simulations were run with a laminar flow solver and the expected separation location was resolved at about 66% of the axial chord [Rouser, 2].

### **1.3 Current Research Objectives**

The objective of the current research is to parameterize dimple placement to optimally control laminar boundary layer separation. Leading from Rouser's research, focus was placed on dimples at 65% of the axial chord. Three different dimple configurations were studied. First, dimples spaced 2.22 cm center-on-center were

analyzed. This duplicated Rouser's work for comparison. Second, a row of dimples was studied with 4.44 cm center-on-center spacing to analyze the spanwise affect of the dimples. Lastly, a second downstream row of dimples was added at 76% of the axial chord identical to the row at 65% of the axial chord. The dimples were staggered, however, so that a dimple in the second row was at the midpoint between two dimples in the first row. Both rows utilized the 4.44 cm center-on-center spacing.

The dimple modified Pak-B blade was mounted in a linear cascade of eight blades. Several experiments were performed on each dimple configuration to assess loss reduction. Boundary layer measurements were used to quantify the effect dimples had on the velocity and velocity unsteadiness inside the boundary layer. Further, the total pressure loss coefficient was measured by wake traverses. These wake traverses also provided wake velocity magnitude and total pressure loss profiles to be used as performance indicators. Finally, surface pressure measurements were made on blades adjacent to the modified blade to determine if the dimples cause any blade-to-blade interactions. Reynolds numbers of 25k, 45k, and 100k were used in each experiment. Figure 2 contains a picture of the blade that both Lake and Rouser used, and again was used in the current research for consistency. For the multiple row case, a second row of dimples was milled into the same blade at 76% of the axial chord (Fig. 2). A detailed description of the experimental methodology and results is contained in Chapter 3.

A CFD study was used to help visualize the flow structure inside the dimples. The computational efforts compliment the experimental work, aid data analysis and reduction, and help direct further experimental endeavors.

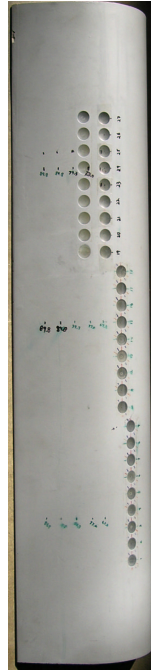


Figure 2. Pak-B blade with dimples at 50%, 55%, 65% and 76% of the axial chord

Four CFD grids were created to best represent the experimental work. The grids were based on the Pak-B blade profile. First a unmodified blade was built and analyzed for comparison. The next grid placed a dimple identical to that in the experimental work at 65% of the axial chord in the center of a blade section 2 cm wide (Fig. 3a). The third grid, Fig. 3b, utilized the same dimple centered on a blade 4 cm wide. The last grid contained a dimple centered in a 2 cm wide blade at 65% of the axial chord with a second row of dimples at 76% of the axial chord offset by 1 cm (Fig. 3c). All grids employed periodic boundary conditions in the spanwise direction to simulate a 2-D blade infinitely long with a full span of dimples with their respective center-on-center spacing. Also, all four blades used periodic boundary conditions in the pitchwise direction to simulate an infinite linear cascade. An inlet Reynolds number based on axial chord of 25k was used for each grid. Each of the grids was built in Gridgen, and run laminar and time-accurate

in Fluent<sup>®</sup>. Fieldview was used in the post processing to visualize separation and reattachment locations, velocity contours, and streak line development. Boundary layer and wake loss measurements were also made computationally to quantify the dimple pattern effectiveness, and to compare to experimental data. A detailed description of the computational methodology and results is contained in Chapter 4.

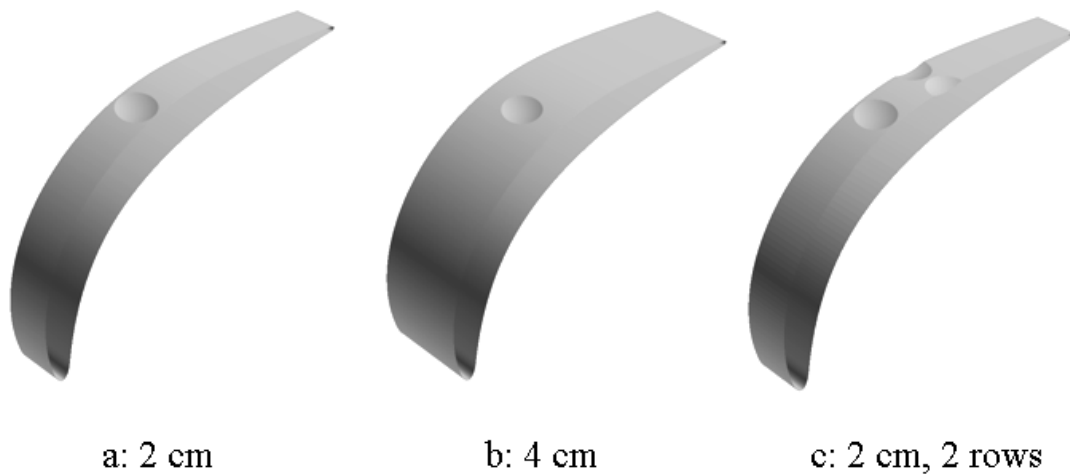


Figure 3. Various CFD grids developed for the current research

## 1.4 Chapter Summary

Chapter 1 contained a brief description of the investigation at hand and presented some background work that led to the current state of the research. Chapter 2 proceeds by discussing techniques used to evaluate turbine performance and boundary layer aerodynamics. Chapter 3 provides a detailed description of the experimental efforts to include methods and results. The computational results and methodology are presented in Chapter 4. Chapter 5 provides a comparison between the experimental and computational results. Finally, Chapter 6 provides final conclusions and recommendations for future work in this field.



## **CHAPTER 2. BACKGROUND AND THEORY**

The current research afforded numerous challenges in data collection and analysis. The problem posed involved determining improvements in overall turbine efficiency due to surface modifications in unsteady, transitional flow. With all turbine efficiency explorations, the affect of even the most modest improvement in engine efficiency could result in radical improvements in range, service ceiling, endurance, and extracted engine power to operate onboard systems. As a result, the experimental efforts focused on obtaining any data that may correlate to turbine efficiency. Within the confines of the linear cascade, velocity and pressure measurements were the most readily available parameters. These elements were used to develop loss coefficients that were helpful in comparing efficiencies.

This investigation was specifically geared to improving the turbine efficiency of high altitude reconnaissance aircraft. The operating Reynolds number experienced by the LPT for these missions falls as low as 25k. The suction surface boundary layer is known to separate under these conditions. It is believed that reducing the separated region may dramatically improve turbine efficiency. For this reason, a good picture of the boundary layer shape and development was required. Velocity and velocity unsteadiness measurements were made within the boundary layer, and compared at several chordwise locations to determine the separation location. Pressure and velocity measurements made in the downstream wake of the blades provided a macroscopic view of the separation effect.

The computational investigation provided a detailed picture of the surface flows on the blades and the flow between blades. The CFD study predicted the location of separation and reattachment lines. Once again the streamwise expanse of the separated region offered insight to the blade efficiency. Streak lines also illustrated intricate flow structures inside and downstream of the dimples. This aided in general understanding of the unsteady and transitional nature of the flow.

## 2.1 Determination of LPT Performance Improvements

A reasonable measure of aircraft engine performance is range capability. As seen in the Breguet range formula, aircraft cruise range is directly proportional to Thrust Specific Fuel Consumption (TSFC):

$$\frac{W_{final}}{W_{initial}} = \exp\left(-\frac{C_D}{C_L} \frac{TSFC * R}{U} g\right) \quad (1)$$

where  $U$  is the flight velocity,  $g$  is the acceleration due to gravity,  $C_D$  is the aircraft drag coefficient,  $C_L$  is the aircraft lift coefficient,  $R$  is the range,  $W_{final}$  is aircraft final weight, and  $W_{initial}$  is initial aircraft weight [Mattingly, 11: 46]. Rearranging Eqn. 1 to solve for the range, it is clear that for a given aircraft, at similar flight conditions, minimizing TSFC results in maximizing the range:

$$R = -\frac{C_L}{C_D} \ln\left(\frac{W_{final}}{W_{initial}}\right) \frac{U}{TSFC} \frac{1}{g} \quad (2)$$

The TSFC is given by:

$$TSFC = \frac{U}{\eta_o h_{pr}} \quad (3)$$

where  $\eta_o$  represents the overall engine efficiency and  $h_{pr}$  is low heating value of the fuel [Mattingly, 11: 30]. Therefore, increasing the overall engine efficiency decreases the TSFC. Over time, these improvements could save enormous amounts of money as well as improve the aircraft mission effectiveness.

A T-S diagram illustrates overall engine efficiency, where T is temperature and S is entropy. A relation for the Brayton cycle representing the ideal jet engine and a T-S diagram is shown in Fig. 4 [Mattingly, 11: 233]. The temperature increases across the compressor isentropically as illustrated from stations 2 to 3:

$$p = \text{const} * T^{c_p/R} \quad (4)$$

where p is pressure, T is temperature,  $c_p$  is the average ratio of specific heats at constant pressure, and R is the gas constant [Moran, 12]. The ideal Brayton cycle does not account for losses or entropy production across the compressor. From station 3 to 4, fuel is injected into the combustor causing an increase in temperature. Convention for an ideal engine assumes that this process occurs at constant pressure. The hot air expands through the ideal turbine and nozzle isentropically (stations 4 to 9). This results in a drop in both pressure and temperature.

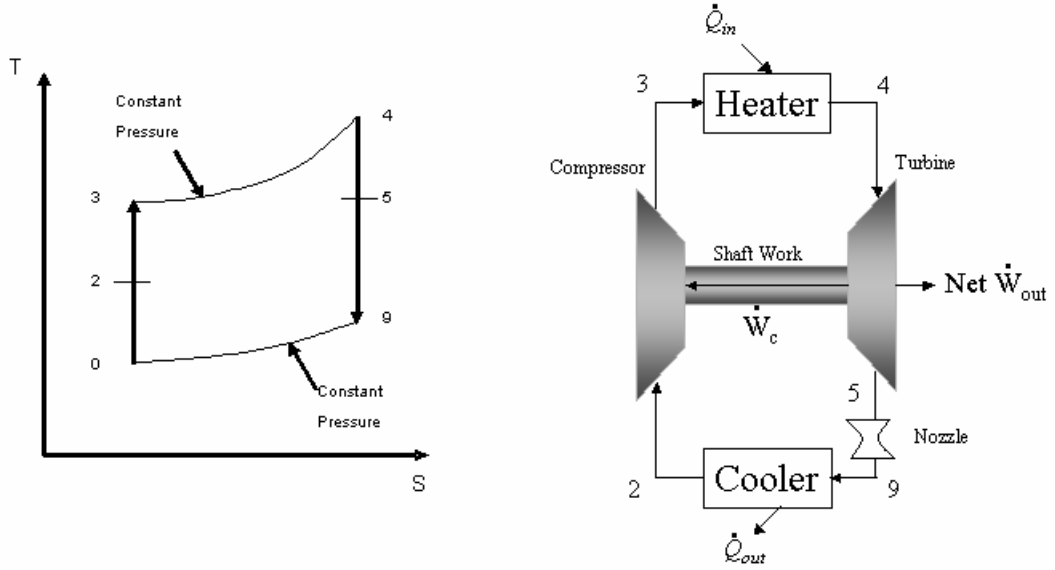


Figure 4. Brayton cycle and ideal gas turbine engine [Mattingly, 11: 233]

The first law of thermodynamics for a closed system is:

$$\Delta E = Q - W \quad (5)$$

where  $\Delta E$  is the net energy,  $Q$  represents the net heat and  $W$  is the net work transferred through the system [Moran and Shapiro, 12: 58]. Given a calorically perfect gas, the analysis of the ideal Brayton cycle yields the following equations for the compressor and turbine, respectively:

$$\dot{W}_c = \dot{m} c_p (T_{t3} - T_{t2}) \quad (6)$$

$$\dot{W}_t = \dot{m} c_p (T_{t4} - T_{t5}) \quad (7)$$

where  $\dot{m}$  is mass flow rate,  $c_p$  is the average specific heat at constant pressure and  $T_t$  is total temperature at the relevant position [Mattingly, 11: 234]. The work required by the compressor is supplied by the turbine such that  $\dot{W}_c = \dot{W}_t$  for the ideal engine. Naturally, a real turbine engine cycle is less than ideal and also experiences some off design

conditions. The losses associated with the turbine engine occur in many ways. One is flow separation. Flow separation is a major factor driving the overall turbine efficiency.

A T-S diagram can illustrate the non-ideal behavior of the turbine engine. Figure 5 depicts a T-S diagram for a single, non-ideal turbine stage. Entropy is generated and total pressure decreases over the stator at constant total temperature. Further, the entropy increases over the rotor. This is accompanied by a decrease in total pressure and total temperature.

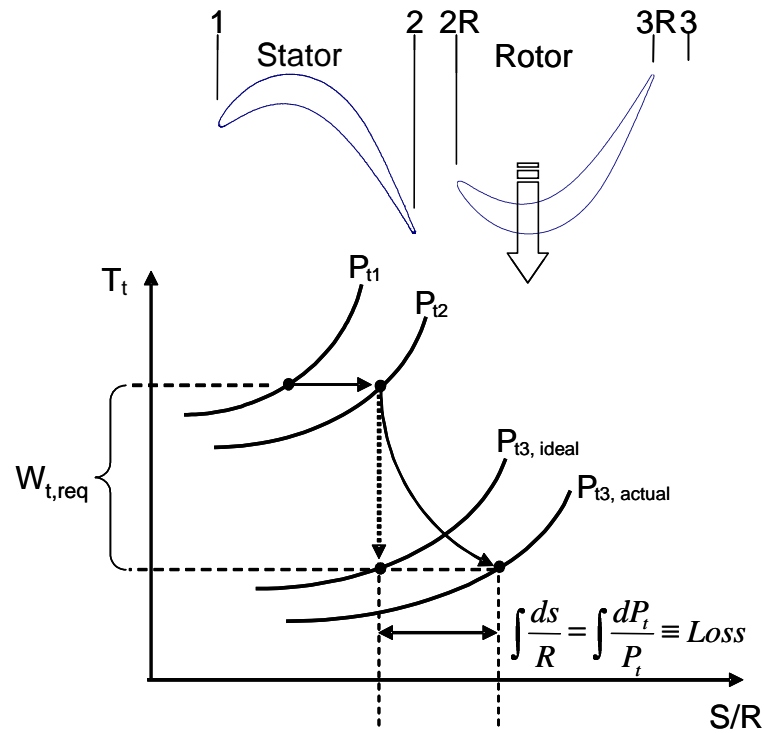


Figure 5. T-S diagram for a non-ideal turbine stage [Lake, 1]

Gibbs equation relates the change in entropy to the change in temperature and pressure:

$$ds = c_p \frac{dT_t}{T_t} - R \frac{dP_t}{P_t} \quad (8)$$

where  $ds$  is the change in entropy,  $R$  is the gas constant,  $T_t$  is total temperature,  $dT_t$  is the change in total temperature,  $P_t$  is total pressure and  $dP_t$  is the change in total pressure [Moran, 12]. As shown in Fig. 5, total temperature is constant across the stator, and Eqn. 8 reduces to the following:

$$ds = -R \frac{dP_t}{P_t} \quad (9)$$

Equation 9 shows the relationship between pressure drop and entropy production. Therefore, there must also be a relationship between pressure loss through a stage and stage efficiency. Mattingly [11: 358] correlates turbine stage efficiency and pressure drop in the following expression:

$$\eta_t = \frac{1 - \tau_t}{1 - \pi_t^{\chi_t - 1/\chi_t}} \quad (10)$$

where  $\chi$  is the ratio of specific heats in the turbine,  $\tau_t = T_{t3}/T_{t1}$  and  $\pi_t = P_{t3}/P_{t1}$ . The consequence of a decrease in exit total pressure for a fixed total temperature ratio is a reduction in efficiency. Therefore, there is a direct relationship between turbine performance and exit total pressure. Exit total pressure is a measurable quantity within the linear cascade and can lead to conclusions on turbine efficiency. The equation below shows the total pressure loss coefficient:

$$\omega = \frac{P_{t,inlet} - P_{t,exit}}{q_{inlet}} \quad (11)$$

where  $\omega$  is defined as the loss coefficient based on inlet dynamic pressure ( $q_{inlet}$ ).

Equation 11 shows that as the exit total pressure decreases the loss coefficients increase.

Eliminating the separated flow would result in higher exit total pressures and

correspondingly lower losses. Lake [1] theorized the effect of an improved exit total pressure in Fig. 6. The baseline plot represents a turbine without any surface modifications. Notice that a small improvement in exit total pressure (possibly by implementing boundary layer control) results in a significant decrease in entropy generation.

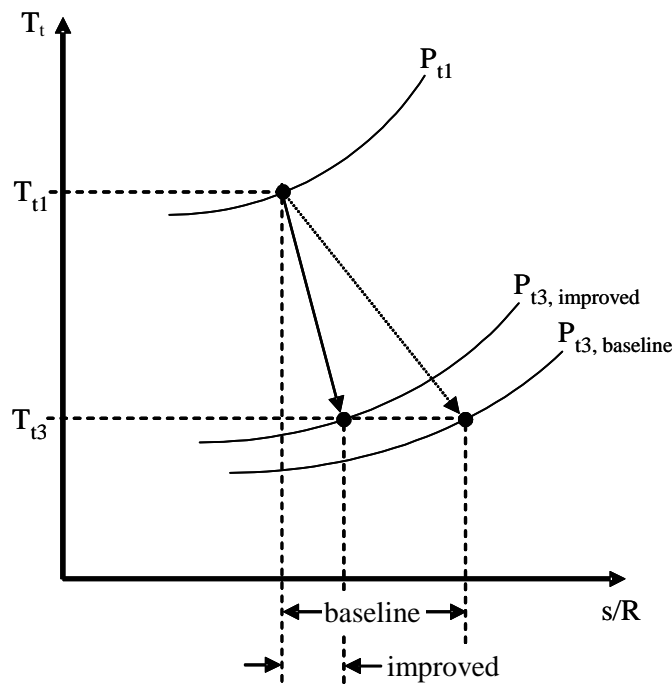


Figure 6. T-S diagram illustrating possible improvement with higher turbine exit total pressure [Lake, 1]

Lake [1] assumed  $\gamma_t = 1.3$ ,  $\tau_t = 0.84$ ,  $P_{t1} = 1731.6$  kPa,  $P_{t2R} = 1043.0$  kPa,  $T_3 = 1505.5$  K,  $T_{t3R} = 1664.4$  K,  $T_{t3} = 1560.0$  K, and the stage loss coefficient,  $\omega_{loss} = 0.15$ . Applying these values to Eqn. 12 returns a value of  $P_{t3} = 748.1$  kPa:

$$P_{t3} = \frac{P_{t2R}}{1 + \omega_{loss} \left[ 1 - \left( \frac{T_3}{T_{t3R}} \right)^{\gamma_t / \gamma_t - 1} \right]} \left( \frac{T_{t3}}{T_{t3R}} \right)^{\gamma_t / \gamma_t - 1} \quad (12)$$

where  $\gamma_t$  is the ratio of specific heats at the turbine. Entering these values into Eqn. 10 returns a stage efficiency of 0.9087. Lake [1] then showed that a 10% reduction in stage loss coefficient returns a 0.5% increase in stage efficiency.

Through his investigation, Lake [1] determined that dimples on the surface of a Pak-B blade reduced the loss coefficient. Rouser [2] showed in his research that a dimple at 65% of the axial chord had the greatest affect on reducing the loss coefficient. The current research further investigates the use of dimples at 65% of the axial chord varying the spanwise dimple spacing and incorporating an additional row at 76% of the axial chord for the reduction of losses. This is one more step towards optimizing the use of dimples as passive flow controllers on a low-pressure turbine blade.

## **2.2 Low Pressure Turbine Boundary Layer Aerodynamics**

The flowfields about LPT blades are unsteady and transitional. Freestream turbulence levels exist between 1% and 20% [Halstead et al., 3; 4]. Halstead et al. [3; 4] documented the presence of passing wakes, centrifugal effects and vortices. The boundary layers on LPT blades operating at low Reynolds numbers gradually transition from laminar to turbulent over the suction surface of the blade as shown experimentally by Werle [13], Mayle [14], and Addison and Hodson [15]. The process of boundary layer transition is nearly steady, yet, intermittently affected by time-dependent wakes traveling downstream due to the relative motion of rotor and stator. As the wake travels downstream, the region on the blade affected by the wake quickly shifts from transitional flow to turbulent flow and then returns to transitional flow after the wake has passed [Halstead et al., 4]. The current research does not consider the periodic passing wake as



the focus is placed on modifying the blade to reduce flow separation during low turbulence periods.

### **2.2.1 Experimental Laminar-to-Turbulent Boundary Layer Transition**

There is a desire to determine the location of transition and the length of blade surface under transition to correlate transition duration to performance losses. This is a difficult task considering the many factors that influence the transitional modes. The primary factors that affect transition are Reynolds number, freestream turbulence, and pressure gradients as shown in experiments by Mayle [14] and Walker [16]. Walker [16] also showed the three fundamental transition modes are: natural transition, bypass transition, and separation bubble transition.

The three primary transition modes exist under varying conditions. Natural transition is characterized by low freestream turbulence and no adverse pressure gradients. 2-D Tollmien-Schlichting (T-S) waves begin the process. As these T-S waves become unstable, they create 3-D loop vortices and large fluctuations [Mayle, 14]. The 3-D structures coalesce into turbulent spots. The turbulent spots grow as they move downstream. Eventually, the turbulent spots grow large enough to consume the entire boundary layer. Walker [16] dictated the end of the natural transition process occurs once the boundary layer becomes fully turbulent.

Flows consisting of higher levels of freestream turbulence can experience bypass transition. Freestream turbulence levels must be on the order of 20% in this case. The high turbulence environment allows for the manifestation of turbulent spots in the absence of 2-D Tollmien-Schlichting waves. Walker [16] found that linear stability

theory could still be used to predict disturbances in this transition mode, helping predict the length of the transitional flow.

Laminar flow in the presence of adverse pressure gradients may produce a separation bubble. In this case, transition occurs in the shear layer between the separation bubble and the freestream. The investigations by Mayle [14], in addition to Qiu and Simon [8], verified re-attachment to the blade surface is catalyzed by the separated flow becoming fully turbulent. The Pak-B blade operating at low Reynolds numbers experiences laminar to turbulent transition due to the formation of a separation bubble. The goal of this research is to parameterize upstream dimples to suppress or eliminate the separation bubble.

### **2.2.2 Numerical Models for Low Pressure Turbine Performance**

In the past, the resolution of the flow field about a LPT for a low Reynolds number flow has been unsatisfactory. Werle [13] reasoned this is in large part due to the lack of experimental data to compare to CFD codes. Halstead et al. [4, 17] tested four numerical models: STANX, KEP, a Navier-Stokes solver, and the Fan-Lakshminarayana code. All four produced unacceptable results. Lake [1] attempted to model the flow field using the 2-D Allison Vane-Blade Interaction (VBI) code. In general, the VBI code returned satisfactory results, but was shown to have problems in the low Reynolds number regime [Lake, 1]. The VBI code had trouble resolving the separated region [Lake, 1]. Further, Lake [1] commented the code was unable to handle the 3-D flow features that the dimples produce, and so was only able to run the code for the unmodified blade.

Lake [1] achieved moderate success with the VBI code by using an O-grid around the blade and an H-grid in the passage. Rouser furthered the CFD work by constructing a 3-D grid in Gridgen. He extruded a structured O-grid from the surface of the blade producing hexahedral cells in the near wall region. In the blade passage, however, an unstructured grid was used, filling the region with tetrahedral cells [Rouser, 2]. The region around the dimples was also an unstructured grid with prism cells down to the blade surface [Rouser, 2]. The three cell types are illustrated in Fig. 7.

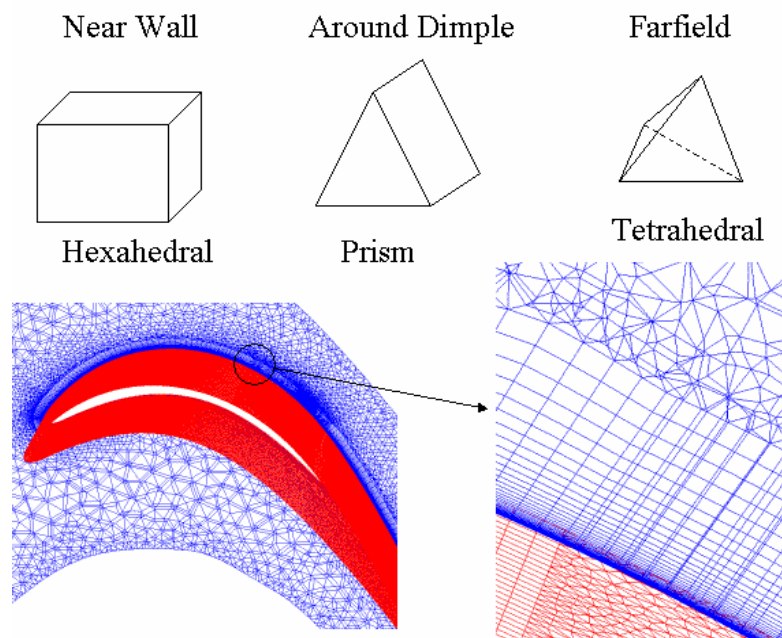


Figure 7. Illustration of the three cell types used in the 3-D Pak-B CFD model

Rouser [2] used Fluent to resolve the flowfield. He began the investigation by assuming a turbulent flow field and applied Reynolds Averaged Navier-Stokes (RANS) turbulence models throughout the entire domain. The solver predicted that the flow remain attached even with an inlet turbulence intensity of 1%. Continuing the computations from the mature attached solution, Rouser [2] turned off the turbulence models and proceeded with a laminar, viscous solver. In this case, he reported that the flowfield separation and

reattachment regions were accurately resolved, however, results for the turbulent region aft of the reattachment location were suspect [Rouser, 2]. A turbulence model that accurately predicts transition is required for this downstream region.

The current research also used a 3-D structured grid extruded from the blade surface and an unstructured tetrahedral grid for the blade passage. The region in and around the dimple(s) was filled with prism cells. The solution was solved time-accurately with only the laminar viscous solver. Turbulence models were not used. It is believed that this is more physically accurate than Rouser's [2] approach which employed a laminar solver beginning with an already steady turbulent solution. Contrary to Rouser's work, large vortical structures were resolved even with a dimpled blade. A multiple row dimple case was also studied to investigate any dimple-to-dimple interactions.

### **2.3 Separation Control on Low Pressure Turbines**

Murawski et al. [7] along with Qui and Simon [8] demonstrated that separation occurs more readily as axial chord Reynolds number drops below 300k or the freestream turbulence is less than 10% at low Reynolds numbers. Both of these conditions are met by the low-pressure turbine during the high altitude, low-speed cruise as with Global Hawk missions. As the Reynolds number drops, the transition location on the suction surface moves towards the trailing edge. If transition does not occur close enough to the leading edge, the flow will not be able to follow the high surface curvature and will create a separation bubble. Over the years focus has been given to modifying the LPT blades to reduce or eliminate the extent of separation by some flow control means.

### **2.3.1 Active and Passive Controls**

There are two main classes of flow control techniques: passive and active. As the name implies, active control requires some additional energy input so the controller can perform its function, while passive controls are generally geometric fixtures that are always “on”. Active controls have the advantage that they can be turned off during operating conditions that do not require flow control. Further, active techniques often allow for adjustments to control varying degrees of separation. Clearly, active control techniques are well suited to handle the control requirements at a wide range of operating conditions. The work by Johnston and Nishi [18] and Compton and Johnston [19] demonstrated that vortex generator jets (VGJs) effectively control separation on flat plates under adverse pressure gradients. Bons et al. [20] investigated the application of VGJs to a Pak-B blade. They showed that pulsating VGJs have the same effectiveness as steady flow jets with an order of magnitude less mass flow [Bons et al. 20]. The negative aspect of VGJs is that they require high-pressure air piped from the compressor to the turbine. Other active control techniques do not require addition airflow.

Lin et al. [21] experimented with Helmholtz resonators as a means of separation control with little success. Attempts have also been made to use micro-electromechanical systems (MEMS) to trip the flow and delay separation over a cylinder [Borgeson, 22]. Unfortunately, these active control techniques are difficult to apply in a turbine engine. MEMS currently cannot withstand the harsh environment experienced in the LPT. Also, MEMS are difficult to manufacture and install in a LPT blade. VGJs are not as difficult to manufacture but require additional hardware that adds weight to the engine. In

addition, they can become clogged with combustor exhaust particles. Further, each of these techniques requires additional power.

Passive controls are in general more robust. Passive controls are commonly geometric features that are easily built directly into existing components. For this reason, passive controls are well suited to endure the operating conditions. There are several different types of passive control techniques. Boundary layer separation from a LPT blade can be dealt with by an overall redesign of a turbine blade. This may be extremely costly and decrease engine performance at other flight conditions may be unacceptable. Another method is to maintain a given blade shape, but make some modification to the suction surface. Several researchers have investigated the use of surface treatments for flow control. Lin et al. [21] studied large-eddy breakup (LEBU) devices and submerged vortex-generators. They concluded that LEBU devices with small positive angle of attack effectively suppressed separation. Further, it was shown that submerged vortex-generators could control separation but effectiveness was highly dependent on location relative to the natural separation point and device height.

Chang [23], Austin [24], and Gamerding and Shreeve [25] investigated the effectiveness of a triangular plow vortex generator device (VGD). Gamerding and Shreeve [25] concluded that this device can help reduce shock-induced boundary layer separation, but also had the negative effect of decreasing the fully mixed out total pressure downstream. Rao and Kariya [26] implemented submerged semi-circular and simple vane VGDs. They concluded that the fully submerged VGDs might perform better than the simple vane; however, optimization is sensitive to height, sweep angle, spacing and length of the element [Rao and Kariya, 26]. Figure 8 shows these three

passive controls. Rao and Kariya [26] also considered the use of parallel concave slats on the surface of a flat plate (Fig. 9c). Their conclusions were the same as for the semi-circular VGDs, but they maintain that dependence on optimization parameters is less severe [Rao and Kariya, 26].

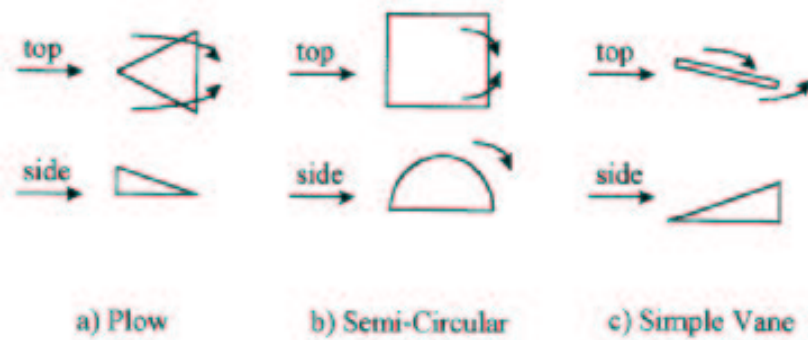


Figure 8. Three surface vortex generator devices - Profile and surface views are shown with airflow depicted as an arrow [Lake, 1].

Each of the passive controls discussed have been protruding devices no more than half the boundary layer thickness. Extending a device into the flow increases the overall drag associated with the blade. This drag penalty may offset any performance enhancement the device may induce. This is especially true at higher Reynolds numbers where the surface treatment may not be needed at all. Lin et al. [27] proposed several alternatives to the protruding surface treatments seen in Fig. 9. They investigated the use of a  $\pm 45^\circ$  small-scale riblet pattern and transverse grooves [Lin et al., 27]. The transverse grooves reduced the reattachment distance by nearly 50%, but the  $45^\circ$  configuration actually enhanced separation [Lin et al., 27].

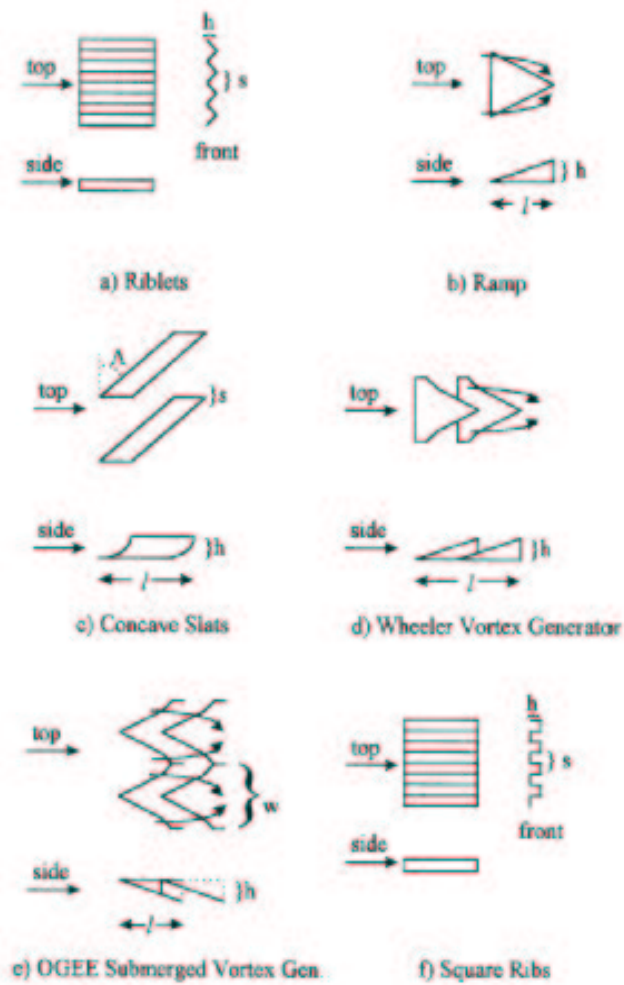


Figure 9. Various other vortex generator devices - Profile and surface views are shown with airflow depicted as an arrow [Lake, 1]

McCormick [28] attempted to avoid the drag penalty associated with protruding surfaces by using a passive cavity method (Fig. 10). The theory tries to take advantage of the adverse pressure gradient behind the separation location [McCormick, 28]. He concluded that passive cavity control dramatically reduces the total pressure loss through a shock system; however, boundary layer characteristics downstream were aggravated [McCormick, 28].



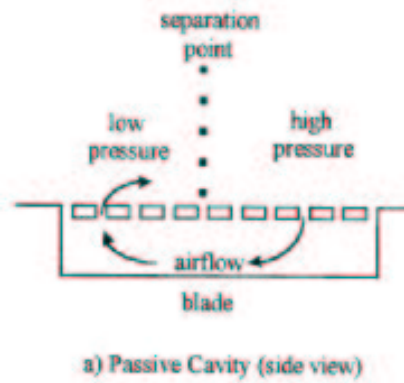


Figure 10. Porous surface separation control device - Profile and surface views are shown with airflow depicted as an arrow [Lake, 1]

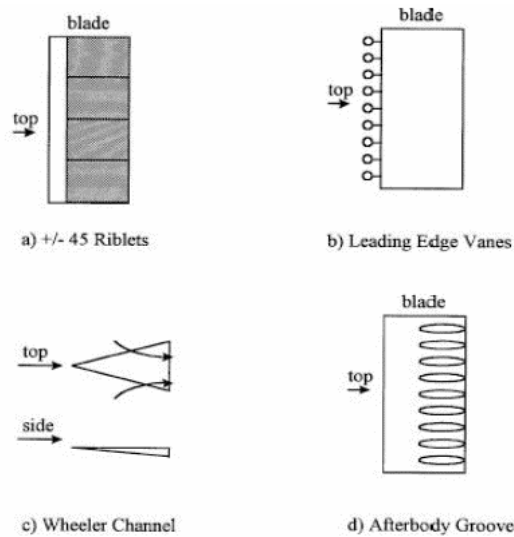


Figure 11. Various vortex generator devices with difficult application - Profile and surface views are shown with air flow depicted as an arrow [Lake, 1]

Chang [23] explored the use of leading edge vane VGDs (Fig. 11), Walsh [30, 31] and Bacher and Smith [33] looked into small-scale V-groove riblets (Fig. 9), Maciejewski and Rivir [34] investigated the use of small-scale square ribs, and Taylor [35] tested a large-scale vortex generator in the shape of a NACA 64-812 airfoil. Walsh found as much as an 8% drag reduction with the V-groove riblets installed on a surface [Walsh, 31]. All of these methods are somewhat difficult to implement. Therefore, Bloch and

Mueller [36] experimented with roughness strips near the leading edge of a Wortmann FX 63-137 airfoil. The roughness strips were much easier to install than the previously discussed methods.

Lake [1] also attempted to ascertain the effectiveness of three different passive controls: a V-groove channel, a boundary layer trip wire and dimples. Lake [1] concluded that these passive controls were sensitive to location relative to the natural separation point, and that the dimples delayed separation to the greatest extent. Rouser [2] went slightly further and maintained that dimples at 65% of the axial chord had the greatest affect on increasing turbine efficiency of the locations he studied.

### **2.3.2 Previous Research in Dimples for Boundary Layer Control**

Surface modifications are either protruding or recessed as previously discussed. Protruding modifications help entrain fast moving freestream air into the boundary layer. This energizes the boundary layer making it less prone to separation [Taylor, 35]. In addition, vortices shed off the trailing edge. The shedding helps mix the freestream and the boundary layer downstream. Recessed vortex generators of depth less than the boundary layer thickness have less drag than protruding structures of a similar height as shown by Lin et al. [27]. They also showed, however, recessed generators do not affect flow conditions as far downstream as protruding structures. Therefore, to be effective, recessed vortex generators must be placed closer to the natural separation location than protruding surfaces [Lin et al., 27]. Recessed structures have advantages over protruding structures when applied to engine design. They are easier to install and clean, and they are more apt to handle the harsh environment. It is clear from Lake's [1] and Rouser's

[2] work that recessed dimples have a great potential in the area of LPT flow separation control.

Much of the background research discussed has emphasized the fact that the effectiveness of the flow control technique is highly dependent on size, shape, and placement of the vortex generator. The current research took steps closer to an optimal dimple configuration. In particular, this work focused on the effect of spanwise spacing and multiple rows.

Lake derived his dimple structure from previous experimentation by Bearman and Harvey [37; 38]. Bearman and Harvey experimented with spherical and hexagonal dimples on a sphere. Their conclusions were that both effectively generated downstream vortices, and the hexagonal dimples were more efficient due to their shape edges [Bearman and Harvey, 37; 38]. Bearman and Harvey constructed their dimples to satisfy a non-dimensional roughness ratio of  $k/D = 9 \times 10^{-3}$  where  $k$  is the maximum dimple depth and  $D$  is the diameter of the sphere/cylinder.

Lake measured the boundary layer thickness on a Pak-B blade without dimples. He then applied the same non-dimensional roughness ratio as Bearman and Harvey and milled dimples into the blade. Lake [1] installed the dimples to a depth of 1.588 mm using a 5.08 cm diameter ball end mill. Due to the blade curvature the dimples were elliptical in shape having a streamwise length of 15.13 mm and a spanwise length of 17.53 mm. The dimples were spaced 2.22 cm center-on-center [Lake, 1].

Lake [1] installed dimples at three axial chord locations and investigated their effectiveness using a linear cascade of eight Pak-B blades at Reynolds numbers of 50k, 100k, and 200k. Only blade #5 had the surface modification. He tested the sensitivity of

loss reduction on dimple location by placing dimples at 50%, 55%, and 65% of the axial chord. Each of these locations was believed upstream of the natural separation point. Lake showed a dramatic reduction in loss but did not experiment with dimple size, shape, spacing or pattern.

Rouser [2] continued Lake's work by further investigating the use of dimples for boundary layer flow control. Rouser used the same experimental blade as Lake, and extended the Reynolds number test range down to 25k. Rouser repeated the unmodified and dimple cases for comparison. He then half filled each dimple with Playdoh® in the spanwise direction to test an asymmetric dimple. Rouser [2] concluded that of the configurations he tried, dimples at 65% of the axial chord had the greatest potential for flow control. The current research attempted to advance the science farther by investigating flow control dependence on spanwise dimple spacing and multiple rows. A second row of dimples identical to the row at 65% was milled into the blade at 76% of the axial chord to test multiple rows. As in Rouser's research, boundary layer traverses, surface pressure scans, and wake loss traverses were used to ascertain dimple pattern effectiveness.

## **CHAPTER 3. EXPERIMENTAL STUDY**

Three dimple configurations were tested in a large-scale, low-speed, drawdown wind tunnel and compared to an unmodified blade. An 8-blade linear turbine cascade was used to simulate flow through a low-pressure turbine. Blade 5 in the linear cascade was modified with different dimple patterns. The study was conducted using three measurement techniques; surface pressure scans, boundary layer traverses, and wake traverses. Surface pressure scans were performed on the blades adjacent to the modified blade to determine whether or not the modified blade affects the adjacent blades. Boundary layer traverses were taken to map the development of the boundary layer on the suction side of a turbine blade. Finally, wake traverses were performed to ascertain the effectiveness of surface modification to decrease separation losses. Each test was performed at axial chord Reynolds numbers based on inlet velocity of 25k, 45k and 100k.

### **3.1 Wind Tunnel and Cascade Characteristics**

A modified open loop Aerolab Corporation drawdown tunnel was used during the wind tunnel tests (Fig. 12). The tunnel modifications allow for variable turning angles in the test section. The tunnel and test section are identical to that used by Lake [1] and Rouser [2]. Some modifications were made to instrumentation set-up in the interim period between Lake and Rouser's [2] work. Instrumentation control and data collection were performed via National Instruments LabVIEW<sup>TM</sup> 6.1 software. Microsoft® Excel 2002 was used for most of the data reduction. Rouser [2] describes in detail the wind tunnel characteristics. A summary is provided here for convenience.

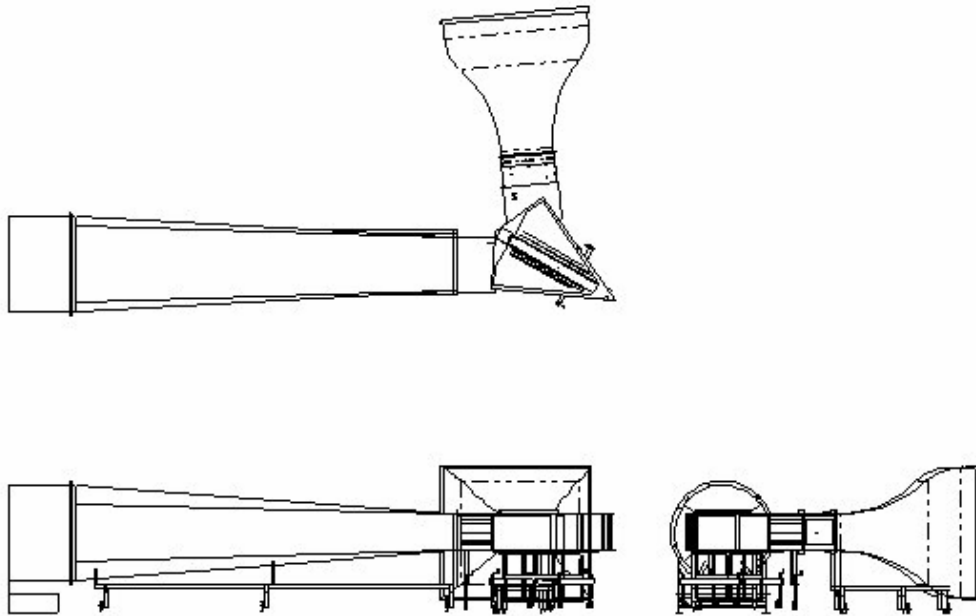


Figure 12. Aerolab Corporation modified drawdown wind tunnel  
(illustration courtesy of AFRL)

### 3.1.1 Wind Tunnel Geometry and Features

A Joy Technologies Axivane axial flow fan draws air through the wind tunnel. A Harmon/Commonwealth Corporation variable frequency motor controller fixes the motor RPM and adjusts the power input to maintain the motor speed. The motor speed determines the flow speed in the tunnel.

The inlet bell-mouth is 305 cm wide and 267 cm tall. A honeycomb flow straightener leads in to a convergent nozzle 229 cm long with exit dimensions 122 cm wide by 85.1 cm tall. This is an area reduction of 87%. Styrofoam inserts help minimize corner vortices (Fig. 13). The flow straightener and corner vortex suppression help obtain freestream turbulence levels less than 1% in the test section.

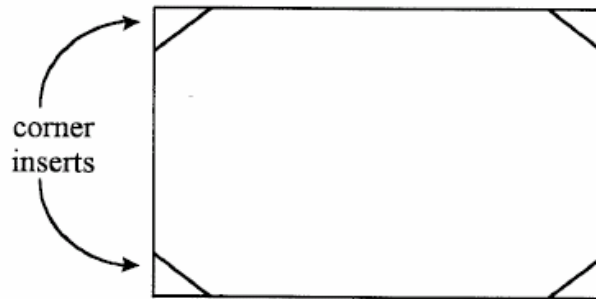


Figure 13. Cross-sectional area of wind tunnel [Lake, 1]

Just downstream of the nozzle and 190.7 cm upstream of blade #1 is a turbulence generation section. The tunnel can be run with the turbulence grid out yielding a clean configuration and less than 1% turbulence. A passive turbulence grid can also be installed in this section yielding freestream turbulence levels of approximately 4% from 127 cm to 254 cm downstream of the turbulence grid (Fig. 14). Isotropy and length scales were characterized by Lake [1].

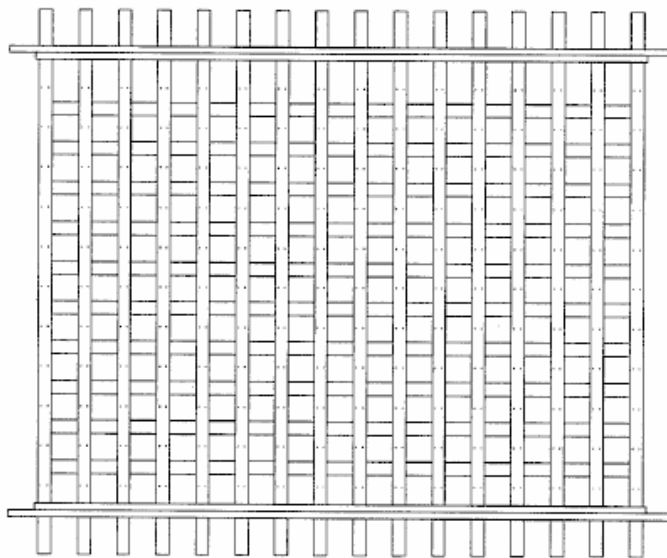


Figure 14. Passive Turbulence grid - Generates approximately 4% Tu (illustration courtesy of AFRL)

The wind tunnel is capable of flow turning angles up to  $130^\circ$  with the adjustable test section. The central hinge pivot joint allows for inlet and outlet flow angles to be altered independently. The current tunnel configuration is representative of the design specifications for the Pak-B blade. That is a  $35^\circ$  inlet angle relative to the axial direction (normal to the cascade inlet plane) and a  $60^\circ$  exit angle (Fig. 15). Lake [1] confirmed both the inlet and exit angles at  $Re\ 45k$ .

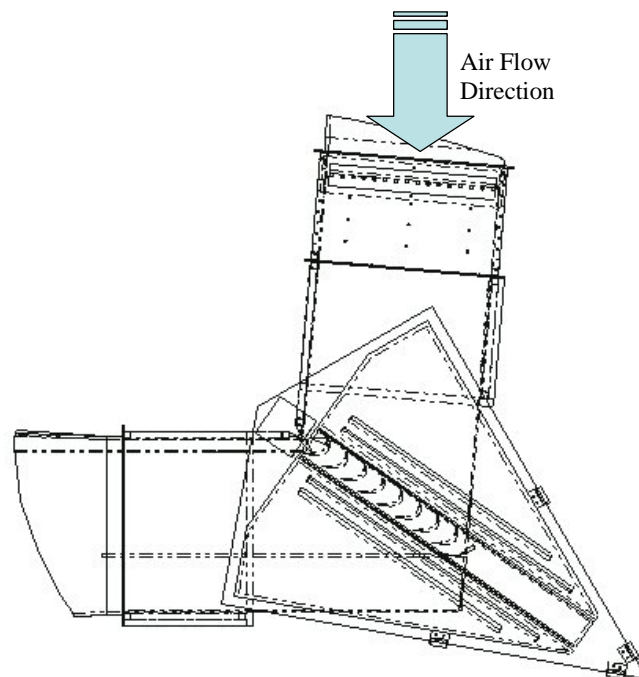


Figure 15. Plan view of test section [Bons et al., 39]

### 3.1.2 Cascade Features

The 8 Pak-B blades in the linear cascade have an axial chord of 17.78 cm. Each blade has a true chord of 25.99 cm. The blades in the test section were molded from Ultralloy 108 white resin with a span of 78.63 cm. The aspect ratio of 4.92 approximates a 2-D flowfield about the mid-span, with negligible effects from endwalls.



The cascade has an axial chord-to-spacing ratio, or solidity, of 1.129 (Fig. 16). The camber and stagger angle for the Pak-B profile cascade is  $36^\circ$  and  $25^\circ$ , respectively. The innermost wall of the cascade is shaped to approximate the suction surface of a Pak-B blade inboard of Blade #1, while the outermost wall approximates the Pak-B pressure surface outboard of Blade #8. Blade #1 is farthest inboard at 198 cm downstream of the turbulence grid. Blade #8 is farthest outboard at 300 cm downstream of the turbulence grid. The modified blade is in the fifth position 218 cm downstream of the turbulence grid within the 4% turbulence intensity region.

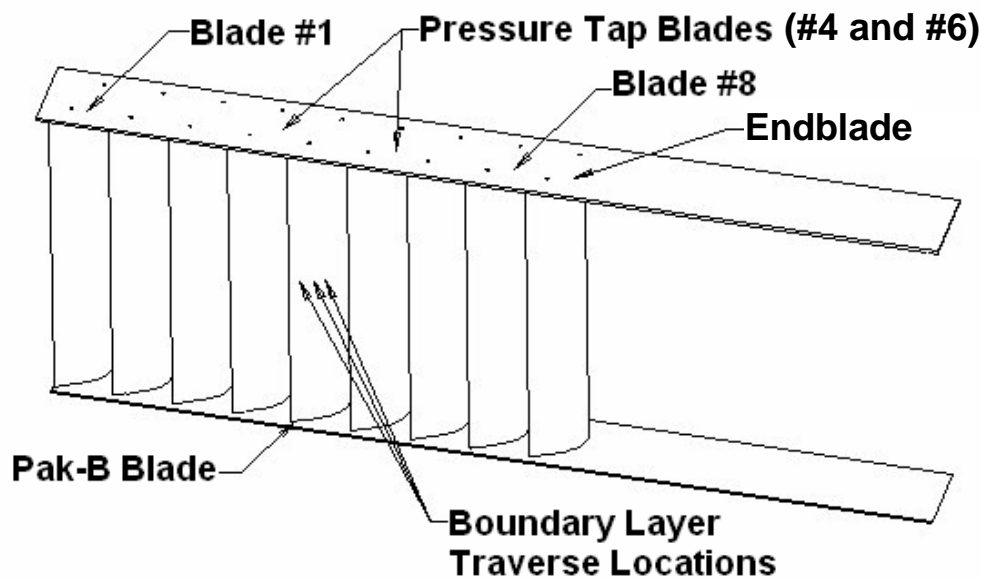


Figure 16. Removable cascade of eight Pak-B blades and endblade  
[Bons et al., 39]

The modified blade used in the current research is the same blade initially modified by Lake and used again by Rouser. The unmodified tests were performed by simply taping over the open dimples. The tape is 19mm wide and about 0.1 mm thick. The other dimple configurations were set-up by covering unwanted dimples in the same manner. It was determined that this is a better way to eliminate dimples than filling them

with Playdoh® and then taping over the filled dimples. This is because the Playdoh® dries out and causes wrinkles in the tape. The tape lends itself well to smoothly matching the existing blade surface.

### 3.1.3 Test Section Characteristics

The test section is constructed out of Plexiglas for optimal visibility and supported by steel struts. Inner and outer tailboards guide the exhaust region to ensure a proper exit angle (Fig. 17).

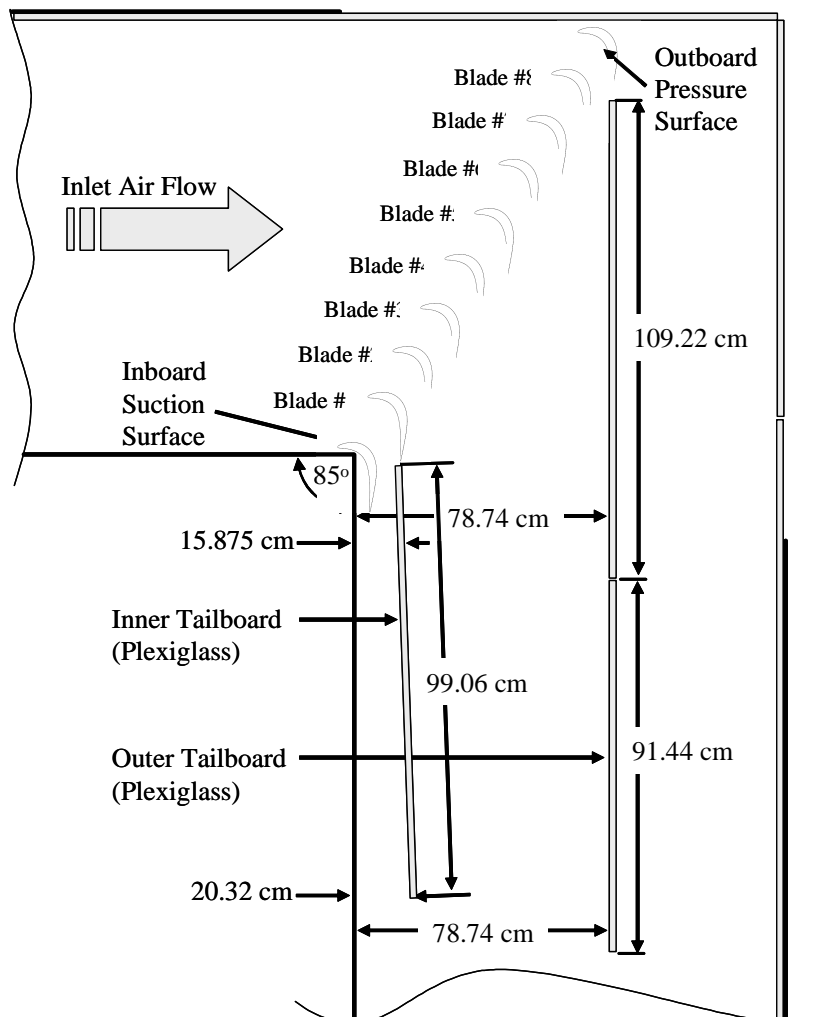


Figure 17. Test section geometry

The wind tunnel exhibits good uniformity and periodicity as demonstrated by Lake [1]. For the current research, single pitch wake loss traverses were conducted to further demonstrate the consistency of the wind tunnel performance. Wake loss traverses spanning 20 cm, in the wake of Blade #5 with dimples at 65% of the axial chord with 2.22 cm spacing were performed at varying Reynolds number. The runs were performed over the course of several days. Figure 18 is a plot of the spatially averaged total pressure loss coefficient,  $\gamma$ . To obtain  $\gamma$ , the local total pressure loss coefficient,  $\omega$  (Eqn. 11), was integrated over one pitch and normalized by the pitch (15.75 cm).

$$\gamma = \frac{1}{L} \sum_i^n \frac{1}{2} \Delta y_i (\omega_{i-1} + \omega_{i+1}) \quad (13)$$

where  $L$  is the pitch length,  $\Delta y$  is the pitchwise step size,  $i$  is the current step, and  $n$  is the total number of steps. Figure 18 illustrates the fact that over the course of several runs the average total pressure loss coefficient is repeatable. Further, the figure shows that for Reynolds numbers from 50k to 100k the loss coefficient varies inversely with Reynolds number. However, for Reynolds numbers from about 30k to 50k the loss coefficient is fairly constant. Reynolds numbers less than 30k experience a sharp rise in loss coefficient. This trend is expected during the full wake traverses.

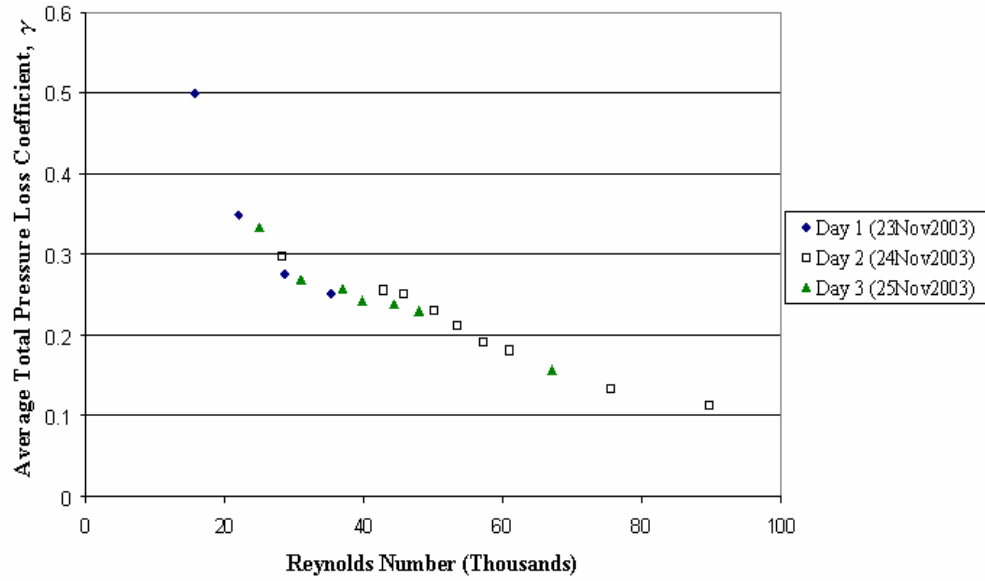


Figure 18. Preliminary single pitch traverses with dimples at 65% of the axial chord with 2.22 cm spacing and 1% Tu

## 3.2 Instrumentation

A series of thermocouples, pressure sensors and hot-films comprise the measurement devices used in the current research. Rouser [2] gives a detailed description of the instrumentation used in this research. A summary is provided here. Figure 19 illustrates the location of each of the measurement devices.

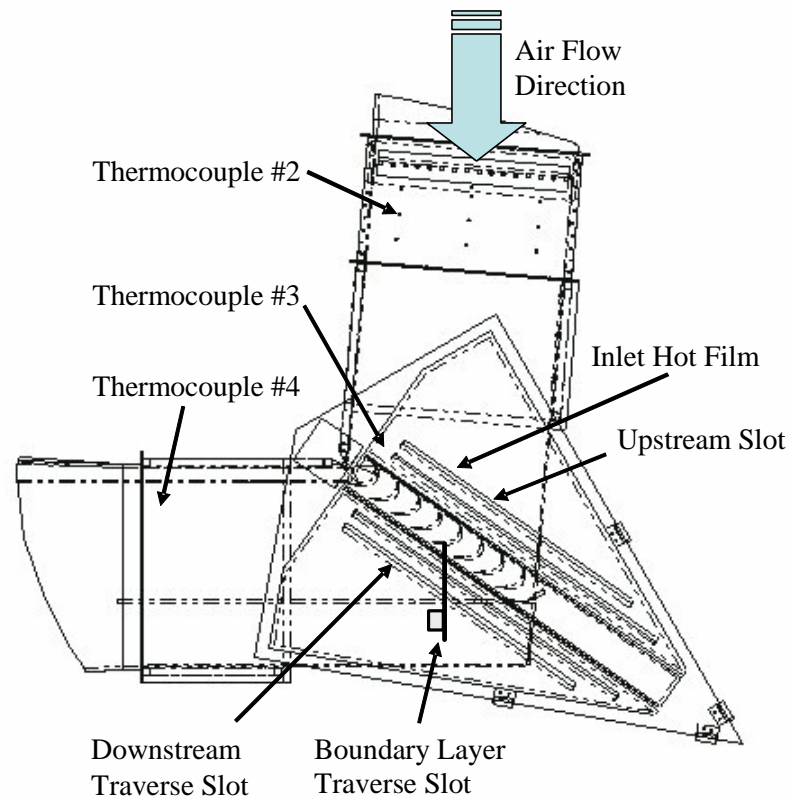


Figure 19. Wind tunnel instrumentation locations [Bons et al., 39]

There are three physical quantities measured in this research; temperature, velocity and pressure. A series of thermocouples provide continuous accurate measurements of the flow temperature throughout the tunnel. Several hot-film probes are used to determine flow speeds at different points in the tunnel. An inlet hot-film is used to set the tunnel inlet flow speed and acts as a Reynolds number reference. An X-film inserted through a downstream traverse slot measures wake velocities. A single element hot-film inserted through a slot in the outer tailboard is used to map velocity boundary layer development. A pitot-static tube extends through an upstream slot to gather the inlet total and static pressures. A Kiel probe is supported through a downstream traverse slot to measure the

downstream total pressure. Finally, 40 static pressure ports are placed around both blades #4 and #6 to measure the local static pressure on the blade surfaces.

The interface between the instrumentation and the data system is described in Appendix A.

### 3.2.1 Temperature Instrumentation

Four J-type thermocouples are suspended from the top of the tunnel to measure static temperatures (Fig. 19). The inlet temperature is measured by thermocouple #1. It is located upstream of the flow straightener honeycomb. The second thermocouple is suspended 45.7 cm downstream of the turbulence grid. Thermocouple #3 is suspended at the 40% axial chord line of blade #1. Thermocouple #4 is suspended 76.2 cm downstream of blade #1. Thermocouples #2, #3 and #4 are spanwise aligned with inlet and exit flow for blade #1. The thermocouples are accurate to  $\pm 0.2^\circ\text{F}$ .

Static temperature measurements are used in the software to calculate density. The experimental conditions were such that incompressibility was assumed ( $M$  on the order of 0.006 to 0.026), and the ideal gas law was used:

$$\rho = \frac{P}{RT} \quad (14)$$

where  $\rho$  is density,  $P$  is ambient static pressure,  $T$  is tunnel temperature and  $R$  is the gas constant for air [Moran, 12]. The ambient static pressure is a user input.

### 3.2.2 Velocity Instrumentation

Hot films were used for all velocity measurements. Boundary layer and inlet velocities are measured using a single element hot film (TSI 1210-20), and exit velocity is measured with an X-film (TSI 1240-20). The inlet velocity measurements set the

tunnel speed for Reynolds number matching. The measured exit velocities are used to obtain wake velocity profiles. The boundary layer velocities help map boundary layer profiles and give insight to boundary layer development.

The inlet hot film is inserted into the tunnel through the test section floor (Fig. 19). It is positioned one axial chord length upstream of the passage between blade #4 and blade #5. The purpose of this hot film is to measure the inlet velocity used in Reynolds number calculations and acts as a reference for setting inlet flow speed. The Reynolds number in the tunnel is determined using Eqn. 15:

$$\text{Re}_c = \frac{\rho U c}{\mu} = \frac{\left( \frac{P}{RT} \right) U c}{\mu} \quad (15)$$

where  $c$  is axial chord,  $U$  is inlet velocity from the hot film,  $T$  is the tunnel adiabatic wall temperature,  $P$  is the ambient pressure, and  $\mu$  is the viscosity of air as function of temperature.

The X-film is supported by a Velmex 3-axis traverse. Although the traverse can move 182.88 cm from inboard to outboard, only a 50 cm traverse from inboard of Blade #4 to outboard of Blade #6 was routinely used. The X-film is positioned downstream of the blade cascade extending through the downstream traverse slot (Fig. 19). The purpose of this element is to measure the wake velocities to determine the flow structure in the exit plane of the linear cascade.

Another hot-film is used to measure boundary layer velocity and velocity unsteadiness. This probe is inserted through a slot in the outer tailboard (Fig. 17) through the boundary layer traverse slot (Fig. 19). This probe is traversed orthogonally to the

suction surface of Blade #5. Boundary layer traverses were taken at 5 chordwise locations 67.2%, 73.0%, 79.3%, 84.8% and 89.8%. These are same locations used by both Lake [1] and Rouser [2].

### **3.2.3 Pressure Instrumentation**

A pitot-static tube extends from the bottom of the tunnel one axial chord length upstream of blade #5 through the upstream slot (Fig. 19). The difference between total and static pressure at this location yields the inlet dynamic pressure. The pitot-static tube is used as the upstream total pressure reference. Rouser [2] tested both a fixed reference point and a traversing reference point noting little difference between the two. He decided to use a traversing upstream reference. It was decided in the current research that for the tunnel configuration a fixed-upstream reference was necessary. The reason for this was a traversing pitot-static tube was causing wakes affecting downstream instrumentation. An attempt was made to position the instruments so that the upstream elements did not affect the downstream elements. As a result, another problem was discovered. Low Reynolds number flows created a thick boundary layer on the tunnel walls that began to interfere with the pitot-static tube suspended one axial chord length upstream of the turbine cascade. Positioning the instruments so they did not encounter wall effects, nor affected one another made it impossible to use a traversing pitot-static tube. In the current research, the pitot-static tube was inserted one axial chord length upstream of blade #5 about 30 cm from the tunnel floor.

Data from the pitot-static probe was used in the calculation of surface pressure coefficients. Surface pressure coefficients,  $C_p$ , were determined using the differential



between the inlet total pressure from the upstream pitot-static probe and surface static pressure divided by the differential between inlet total and static pressures:

$$C_p = \frac{\left( \overline{P_{t,inlet} - P_{s,local}} \right)}{\left( \overline{P_{t,inlet} - P_{s,inlet}} \right)} \quad (16)$$

where  $\left( \overline{P_{t,inlet} - P_{s,local}} \right)$  is a time average over 30 sec of direct differential samples of inlet total and local surface static pressures. The surface static pressures are measured on Blades #4 and #6. Each blade is equipped with 40 surface pressure taps, although only 37 are usable on blade #4 due to clogging resulting from the manufacturing processes. The taps run from leading to trailing edge staggered  $30^\circ$  from each other thus covering 22.86 cm of the span. Staggering the taps limits the possibility of taps interfering with one another. The main purpose of this measurement is to determine if the modified blade affects the pressure on adjacent blades. These measurements also provide an idea of where separation occurs on the unmodified blade. The axial chord location of each of the taps is represented in the  $C_p$  plots.

A Kiel Probe is located one axial chord length downstream of the cascade. The Kiel probe is suspended into the tunnel by the same Velmex traverse system as the X-film and positioned approximately 4 cm away from the X-film. It extends into the tunnel through the downstream traverse slot (Fig. 19). During wake loss traverses, the Kiel traverses along the exit plane from the turbine cascade in unison with the X-film. The upstream and downstream total pressures are measure periodically by the pitot-static tube and Kiel probe, respectively. The difference in total pressure is used to calculate a loss coefficient. Local total pressure loss coefficient is the differential between inlet and exit total pressure divided by the differential between inlet total and static pressure:

$$\omega = \frac{\overline{(P_{t,inlet} - P_{t,exit})}}{\overline{(P_{t,inlet} - P_{s,inlet})}} \quad (17)$$

where  $\overline{(P_{t,inlet} - P_{t,exit})}$  is a time average of direct differential samples of inlet and exit total pressures, and  $\overline{(P_{t,inlet} - P_{s,inlet})}$  is a time average of direct differential samples of inlet total and static pressures.

All of the pressure measurements are fed through a pressure manifold and into a Druck LPM 5481 pressure transducer. This transducer converts the pressure readings to voltages understood by the data acquisition cards. Figure 20 illustrates the pressure instrumentation system. A Scanivalve selector determines from what source the pressure transducer receives an input. The selected pressure is sent through the pressure manifold into the transducer. The upstream total pressure is always sent through the manifold. The manifold can be set to vent either side of the transducer during calibration.

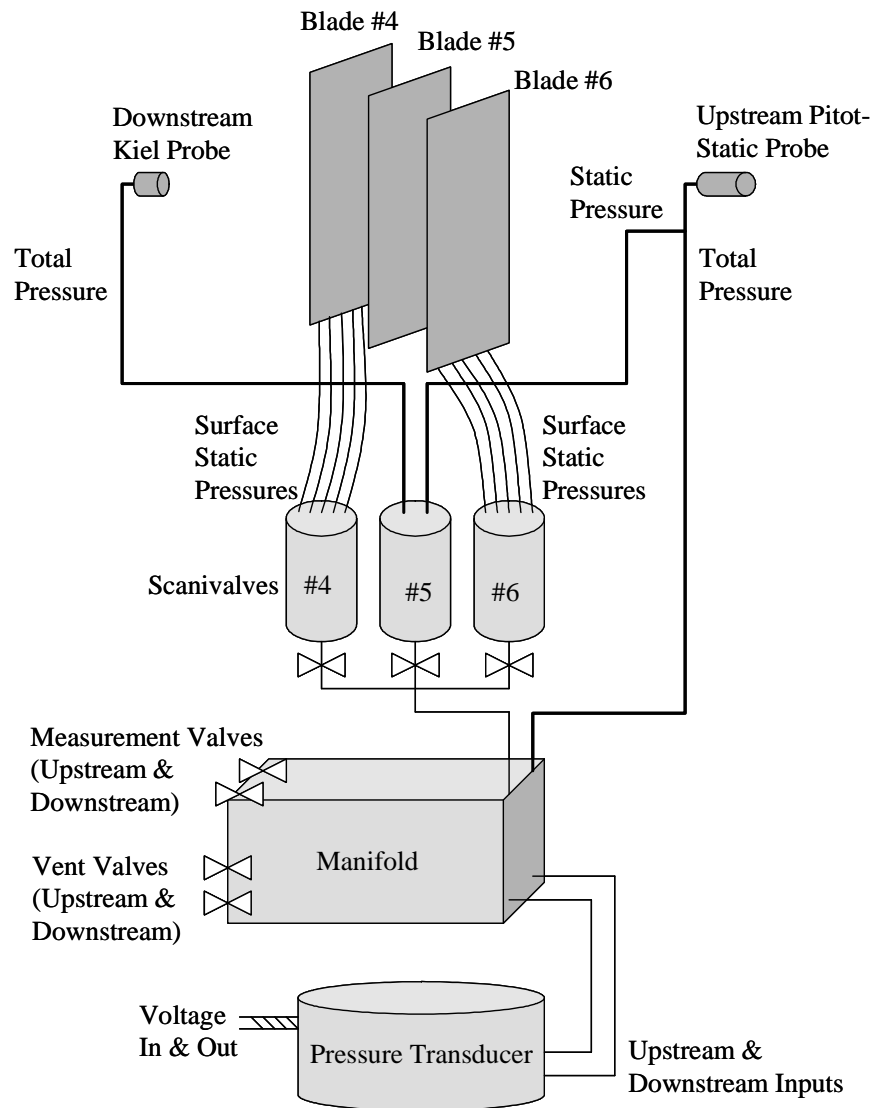


Figure 20. Pressure instrumentation schematic [Rouser, 2]

### 3.3 Data Collection Methodology

A LabVIEW<sup>TM</sup> program is run to set the wind tunnel operating conditions. User inputs include the current dew point temperature, ambient pressure, and hot-film calibration data. The program converts voltages returned by the hot-film into velocities and Reynolds numbers. Once the wind tunnel flow speed is set, one of the three data collection programs are started depending on which data set is desired. Each

LabVIEW™ program requires hot-film calibration data, pressure transducer calibration data, current dew point temperature, and current ambient pressure. The pressure transducer is calibrated off line using a high precision reference. The slope of the calibration curve is very stable, but the intercept can shift day to day with temperature. To account for this a zero intercept is taken at the beginning and end of each data run.

### **3.3.1 Wake Velocity and Loss Coefficient Profiles**

One LabVIEW™ program is dedicated to returning information about wake velocity profiles and pressure loss coefficients. This program drives the Velmex V-9000 traverse supporting the X-film and Kiel probe. For this experiment, the traverse was taken across blades #4, #5, and #6 in a 50 cm pitchwise sweep in 0.5 cm steps. Measurements were recorded for all dimple patterns: unmodified blade, dimples at 65% of the axial chord with 2.22 cm and 4.44 cm spacing, and dimples at 65% and 76% of the axial chord with 4.44 cm spacing staggered between the rows.

As the traverse moves from inboard to outboard in 0.5 cm steps, the exit velocity, exit angle and total pressure differential between the upstream and downstream locations are recorded. At the farthest outboard position, the Scanivalve selector switches to the upstream static pressure input. As the traverse returns to the inboard position in 6 equal steps, the upstream total to static pressure differential (dynamic pressure) is recorded. At the beginning and end of a traverse, the Scanivalve selector switches to an ambient pressure port to record a zero pressure differential, ensuring minimal thermal drift in the pressure transducer.

### **3.3.2 Local Surface Pressure Profiles**

Local surface static pressure measurements are made on these blades 4 and 6. The tap locations are discussed in Section 3.2.3. The pressure taps are connected to two Scanivalve Corporation 48-channel 48J9-1 multiplexers. The tap selection is incremented along the blade and relayed through the manifold to the pressure transducer. The differential pressure between the upstream total pressure and the local surface pressure are used to calculate local surface pressure coefficients.

Once the tunnel speed was set, a LabVIEW™ program dedicated to taking surface pressure measurements is started. The program increments through each of the pressure taps and records local surface static pressures. The surface pressure scans were done at Reynolds numbers of 25k, 45k and 100k at 1% and 4% turbulence intensity for the unmodified and single row cases.

### **3.3.3 Boundary Layer Profiles**

A TSI 1210-20 hot film measures the velocity within the boundary layer and the root mean square of the deviation from the mean velocity (velocity unsteadiness) at five axial chord locations on Blade #5. The unsteadiness is composed of both traditional random turbulence and large scale coherent motions associated with separation dynamics. The hot film is mounted to a National Aperture, Inc. motorized 5.08 cm MM-3M micro-traverse as discussed in Section 3.2.

The boundary layer traverses are the most difficult of each of the experiments and take the most time. Initially, the wind tunnel is set to a Reynolds number of 100k at 1% turbulence as discussed in Section 3.3. The probe is positioned approximately 30 mm above the blade surface. It is important that the probe be aligned orthogonal to the blade

surface at the desired axial chord location. The LabVIEW™ program dedicated to recorded boundary layer traverses is started. User inputs drive the probe towards the blade slowly. At each step the hot-film returns velocity and velocity unsteadiness information. This information is displayed in the user interface to the LabVIEW™ program. Once the velocity measurements read half of the freestream (about 7 m/s), the user records the distance to the blade surface (or nominal wall location). The traverse direction is reversed and the small steps are taken away from the blade to finely resolve the boundary layer. At the end of the traverse, the tunnel is set to a Reynolds number of 45k (to match Lake [1] and Rouser [2]), and the process was repeated. This time, however, the probe is driven to the previously recorded nominal wall location. This is repeated at a Reynolds number of 25k. At this point, the tunnel is shutdown for the turbulence grid installation. The three Reynolds number traverses are made again each time driving the probe to the recorded nominal wall location. At the end of these 6 runs, the tunnel is shut down again and the probe repositioned at the next axial chord location. The process is started again determining a new nominal wall location.

Boundary layer traverses were made at 67.2%, 73.0%, 79.3%, 84.8%, and 89.9% of the axial chord for the unmodified blade, and blade with dimples at 65% of the axial chord with 2.22 cm and 4.44 cm spacing. Lake [1] measured profiles downstream of dimples and downstream of spaces between dimples, noting no significant spanwise variation. For this reason, only one boundary layer traverse was made downstream of dimples with 2.22 cm spacing. Spanwise variations were suspected, however, for the 4.44 cm spacing case, and so boundary layer traverses were made downstream of dimples and in the spaces between dimples.

### 3.4 Local Surface Pressure Coefficient Profiles

Figures 21 and 22 show comparisons of surface pressure coefficient profiles for the unmodified Pak-B blade at Reynolds numbers ranging from 25k to 100k with freestream turbulence levels of 1% and 4%, respectively. Rouser's data is included along with the current research [Rouser, 2]. Both Rouser's work and the current research used a direct differential reading to determine the dynamic pressure. The measurements were time averaged. The curves were produced using the following definitions:

$$C_p = \frac{P_{t_{inlet}} - P_{s_{local}}}{q} = \left( \frac{(P_{t_{inlet}} - P_{s_{local}})}{\frac{1}{2} \frac{P_{amb}}{RT_{amb}} (\bar{U})^2} \right)_{Lake} = \left( \frac{(P_{t_{inlet}} - P_{s_{local}})}{(P_{t_{inlet}} - P_{s_{inlet}})} \right)_{Rouser} \quad (18)$$

where  $P_{t_{inlet}}$  is the total pressure measured upstream of the cascade using a fixed pitot-static probe located inboard of blade #4, and  $\bar{U}$  is the time averaged mean velocity measured upstream of the cascade using a fixed single element hot film located one axial chord length ahead of blade #4. The local static pressure of each tap is denoted by  $P_{s_{local}}$ . The operating Mach numbers were very low (on the order of 0.01) and therefore, compressibility corrections were not applied.

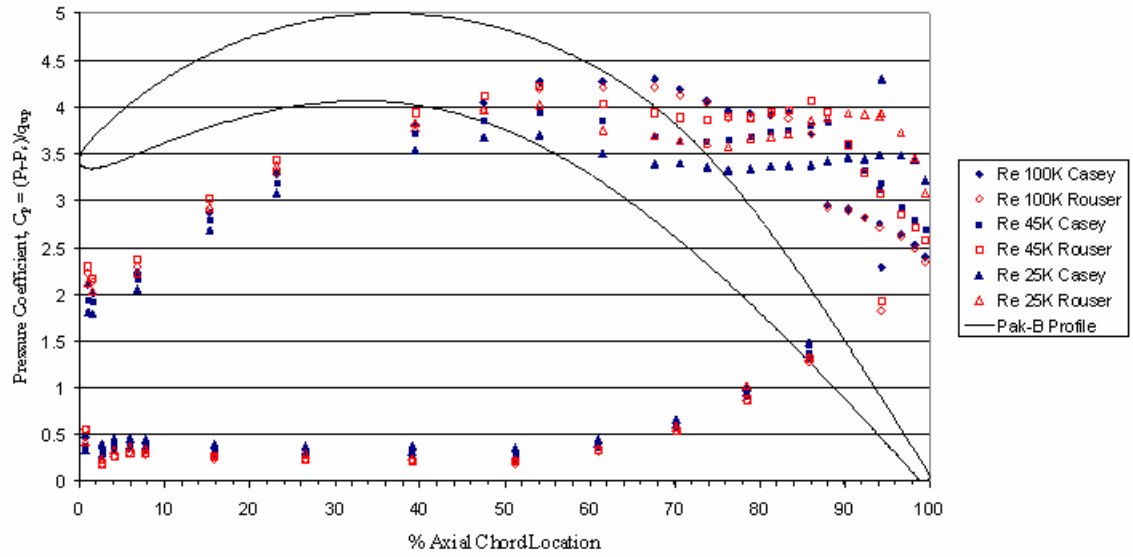


Figure 21.  $C_p$  curves for an unmodified Pak-B blade at various Reynolds numbers and 1% freestream turbulence

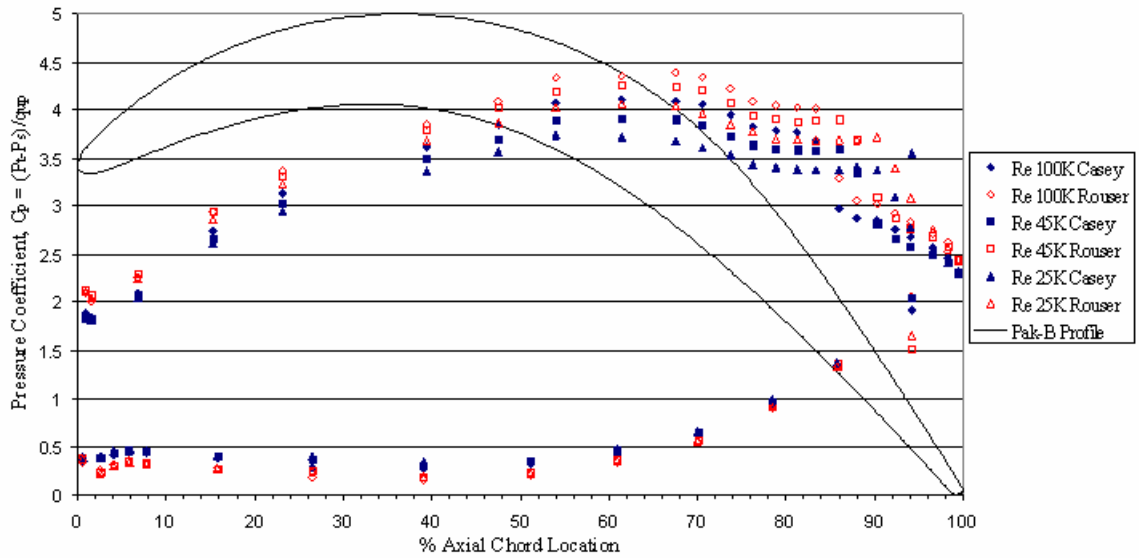


Figure 22.  $C_p$  curves for an unmodified Pak-B blade at various Reynolds numbers and 4% freestream turbulence

The onset of boundary layer separation can be inferred from  $C_p$  curves. The uncertainty of these measurements are  $\pm 0.015$ ,  $\pm 0.004$  and  $\pm 0.001$  for Reynolds numbers of 25k, 45k and 100k, respectively [Rouser, 2]. The extent of the separated region is an



indication of the blade efficiency. The insight  $C_p$  curves give towards the magnitude of the separated region leads to predictions of blade efficiency.

Boundary layer separation can be inferred to be near the point at which the suction side  $C_p$  curves first become flat. Reattachment is related to the point where the plateau ends. Figures 21 and 22 show the extent of the separation. Although the absolute numbers vary between the two researchers, there is agreement over the size of the separated region. The difference in the numbers may be attributed to variations in the inlet dynamic pressure. Rouser [2] reported that for Reynolds number of 45k and 1% turbulence intensity, separation occurs between 62% and 67% of the axial chord. The current research confirms this result. Rouser further reports that for Re 25k separation occurs slightly earlier, but still within the aforementioned range. The shape of the  $C_p$  curve in the current research closely follows that of Rouser's, and it is believed that separation may occur as early as 57% of the axial chord for Re 25k. It is noted that as the Reynolds number decreases so does the peak magnitude of  $C_p$ . This results in a fairly flat curve making determination of the separation point more difficult.

Agreement between the experiments is also shown in Fig. 22. The separation magnitude is less than that of the 1% turbulence case. This is expected since higher levels of turbulence tend to make the boundary layers more turbulent leading to a more attached flow field. The same trend is seen as the Reynolds number is increased. Again the more energized boundary layer flow is able to turn around the turbine blade further before separating. Figure 23 replots information from Fig. 21 and Fig. 22. Figure 23 illustrates that for Re 100k and 1% turbulence intensity, the separation bubble extends

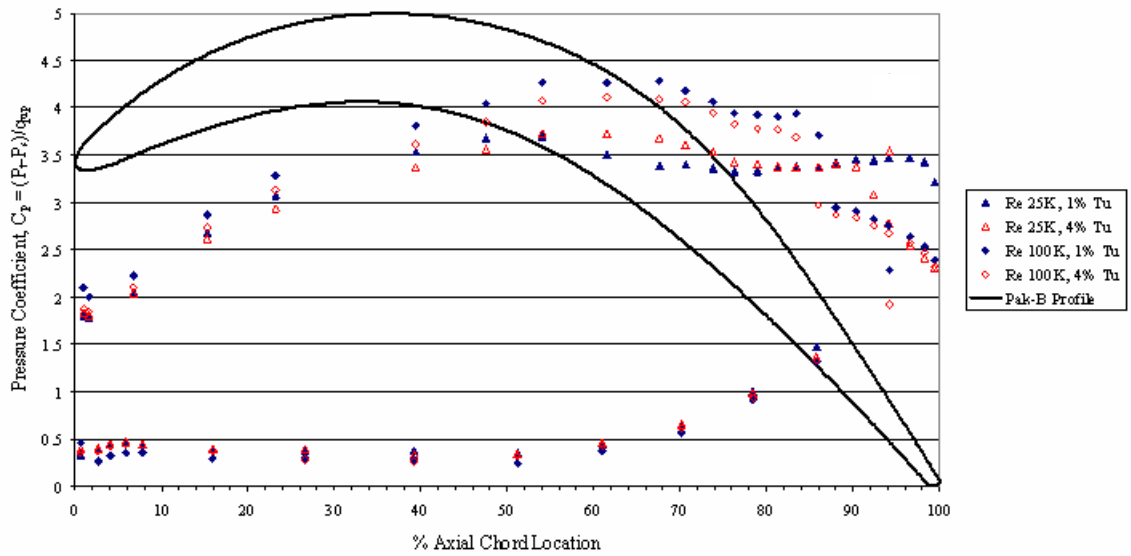


Figure 23. Turbulence intensity comparison for Re 25k and 100k

from  $69 \pm 2\%$  to  $86 \pm 2\%$  of the axial chord. At 4% turbulence and Re 100k, the separation bubble is reduced to the range of  $69 \pm 2\%$  to  $82 \pm 2\%$  of the axial chord. For the Re 25k and 1% turbulence case, separation extends from 60%-65% of the axial chord all the way to the trailing edge. The 4% turbulence case shows that separation begins at about the same point but reattachment occurs much earlier between 90% and 95% of the axial chord. These results lead to the conclusion that separation location is relatively independent of turbulence intensity. The reattachment location, however, can be dramatically affected by turbulent changes. Rouser [2] reported the same result.

Figure 24 shows the effect of dimple pattern on the  $C_p$  curve on an adjacent blade. It is clear that dimples on the suction side of blade #5 do not affect blade #6. Therefore, dimples do not significantly influence adjacent blades.

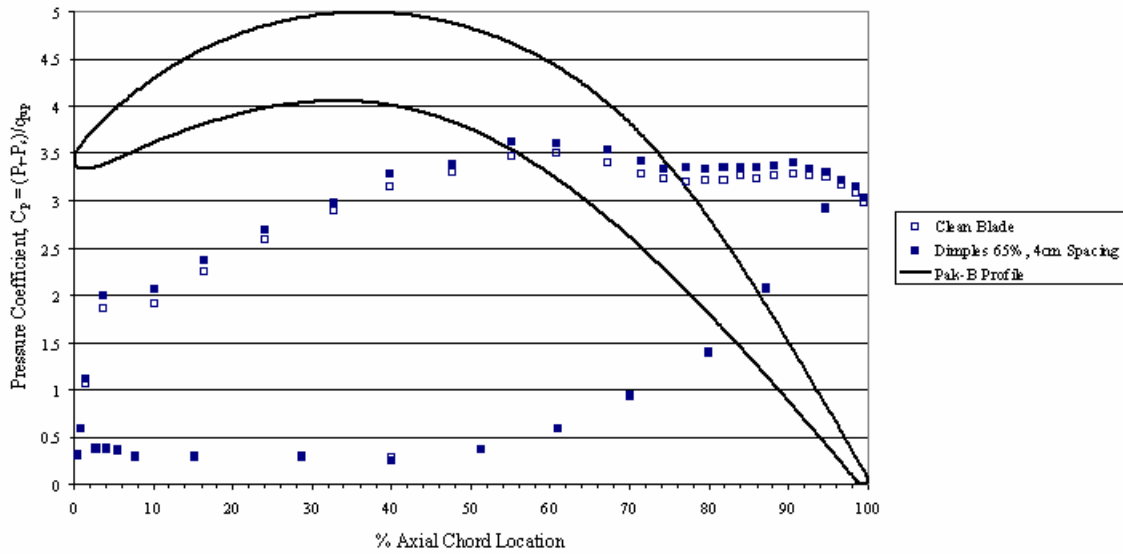


Figure 24.  $C_p$  curve on blade #6 for an unmodified and dimpled blade #5 at Re 45K and 1% Tu

### 3.5 Boundary Layer Velocity and Unsteadiness Profiles

Boundary layer profiles offer direct measurements of the onset of separated flow. An attached laminar boundary layer has a generally parabolic shape from zero velocity at the wall to the freestream velocity. Attached turbulent boundary layers have more unsteadiness and generally have a much steeper slope towards the freestream. Detached flow has a very distinct boundary layer. There is a double inflection point indicating a detached shear layer over the boundary layer. Unsteadiness profiles also help formulate a picture of the boundary layer. Attached laminar flow will have very low unsteadiness levels in the boundary layer. As the flow field becomes detached the unsteadiness levels increase dramatically.

Rouser recorded boundary layer profiles for the Pak-B blade with and without dimples for Reynolds numbers as low as 25k [Rouser, 2]. The current research presents

profiles for the unmodified blade and the Pak-B blade with dimples at 65% of the axial chord with 2.22 cm and 4.44 cm spacing measured center on center.

Recall that the boundary layer velocity is measured by driving a hot-film probe towards the blade. If the probe were to contact the blade the probe would break, and so the distance the probe is from the blade surface, and hence the measured thickness of the boundary layer, is somewhat ill-defined. Rouser [2] called the closest point the probe came to the wall the zero point, or blade surface. The current research linearly extrapolates a portion of the raw data to get an estimate of the wall location. Figure 25 demonstrates the process. Notice the measured velocity is plotted versus the distance the traverse moved. The linear extrapolation determines that the wall is located at 2.5736 cm from the hot-film probe's starting position. This extrapolation procedure is performed for all 6 runs at a given location (3 Reynolds numbers, 2 turbulence intensities). The average value of all 6 extrapolated wall locations determined the actual wall location. This value is then subtracted from distance the traverse has moved to give a distance relative to the wall. This process was used in each of the boundary layer plots. A complete set of velocity and unsteadiness profiles from the current research is included in Appendix C. For comparison plots contained in this section, the local measured velocity is normalized by the average inlet velocity: 2.28 m/s, 4.11 m/s, and 9.09 m/s for Re 25k, 45k, and 100k, respectively.

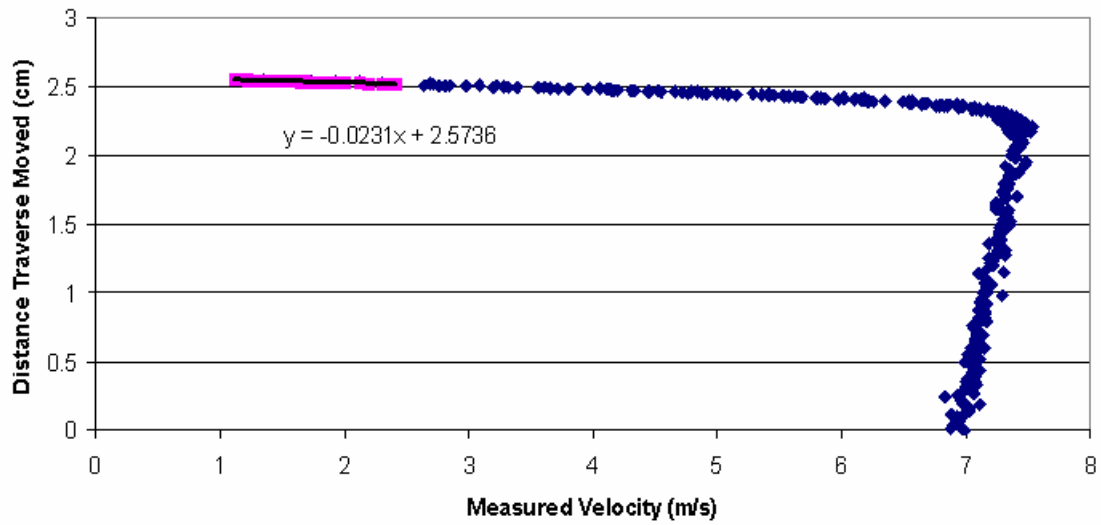


Figure 25. Wall Location Calculation at 73.0% of the axial chord, Re 45k and 1% Tu

### 3.5.1 Boundary Layer Profiles for an Unmodified Pak-B Blade at Tu 1%

Figure 26 depicts Reynolds number effects on boundary layer profiles for the unmodified Pak-B blade at 1% Tu. The average inlet velocity was used to normalize the measured velocity. At 67.2% of the axial chord each of the profiles appear attached. Note that for the Re 25k case the boundary layer is representative of a more laminar profile, while at 100k it appears more turbulent with a steeper slope. At 73.0% of the axial chord, both the 25k and 45k cases show signs that separation is beginning. This is evidenced by the slight change in shape of the boundary layer profile. The boundary layer is thicker and the slope of the curve has changed slightly. By 79.3% of the axial chord a clear separation bubble has formed at Re 25k and 45k. Also, the boundary layer for the Re 100k case has nearly doubled in thickness and shows signs of separation evidenced by the near wall velocity profile curvature. The boundary layer for Re 100k possibly reattaches quickly as seen in at 84.8% of the axial chord.

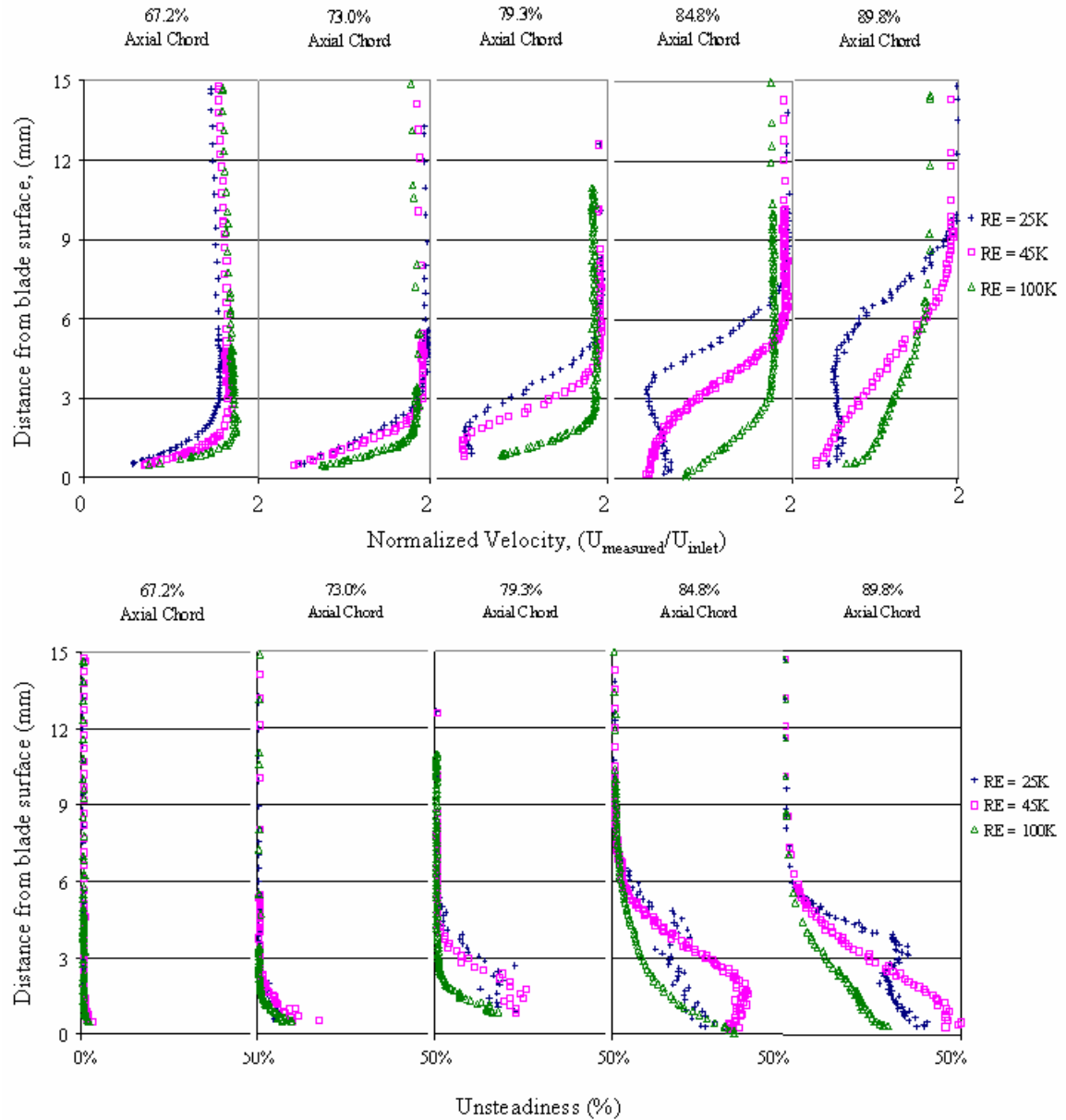


Figure 26. Reynolds number effects on boundary layer profiles of an unmodified Pak-B at Tu 1%

Also at this location the Re 45k case shows signs that reattachment is beginning. The boundary layer for the Re 45k case is almost completely reattached by 89.8% of the axial chord. For the Re 100k case at 89.8% the boundary layer is attached; however, it does not exhibit the natural near parabolic boundary layer shape due to the acceleration of the

freestream. The flow field is still fully separated at 89.8% of the axial chord for Re 25k. For this case, the separation bubble is nearly 6 mm thick and the whole boundary layer is over 9 mm thick.

Similar conclusions can be drawn from the unsteadiness profiles. The possibility of a small separation bubble beginning at 79.3% of the axial chord at Re 100k is a little more evident in the unsteadiness profiles. The unsteadiness levels for this case have grown significantly. The magnitude of the separation bubbles at Re 25k and 45k are also evident.

Figure 27 displays boundary layer profiles for Re 25k and 1% Tu for the current research and Rousser's work. Although some differences are apparent, the overall trends are the same. The boundary layer grows from 67.2% to 73.0%. The initial signs of separation are seen at 73.0% of the axial chord, and a separation bubble is evident at 79.3% of the axial chord. The separation bubble continues to grow through the rest of the measurement locations. The agreement between the two experiments evidences the true nature of the flow physics by accurately displaying the boundary layer development. The agreement yields credibility for the boundary layer measurements. Slight differences in the results between the two researchers may be attributed to minor fluctuations in the inlet dynamic pressure and the method by which the wall location was determined.

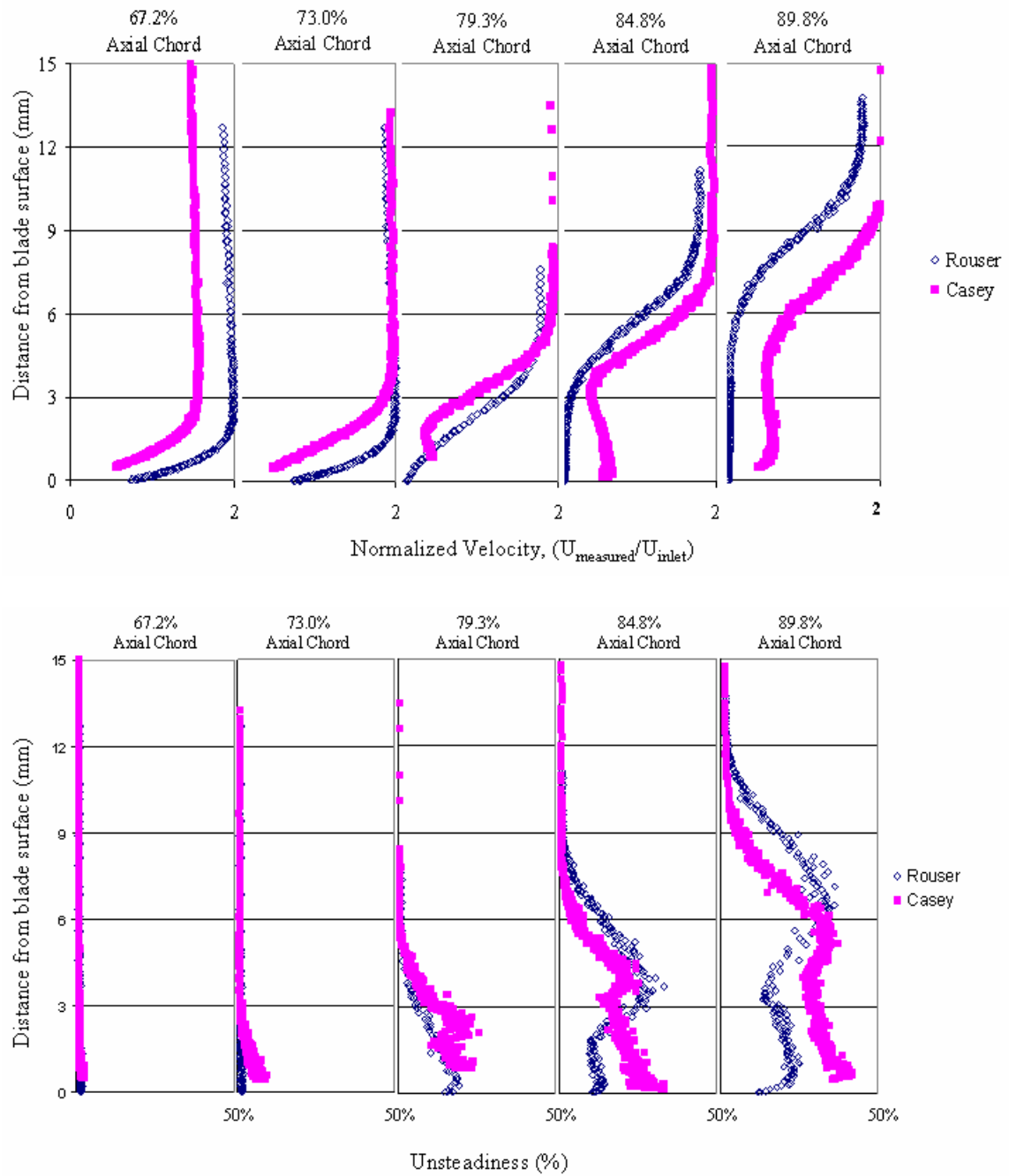


Figure 27. Boundary Layer Comparison with prior research, Re 25k and 1% Tu



### **3.5.2 Boundary Layer Profiles for Pak-B with Dimples at 65% of the axial chord and 1% Tu**

Figures 28 and 29 compare the boundary layer development for four different traverses: the unmodified case, the case with 2.22 cm dimple spacing, and the case with 4.44 cm dimple spacing in the wake of a dimple and the space between dimples. The plots display the normalized velocity measured for Re 25k and 45k. These conditions emphasize the flow dynamics.

Figure 28 displays the traverses made at Re 25k. The boundary layers look similar at 67.2%. By 73.0% of the axial chord the unmodified case deviates slightly from the three dimpled cases. All the boundary layers show signs of the beginning of separation, but the unmodified case seems to be more advanced. The indication of separation is the slight change in slope of the velocity gradient within the boundary layer. By 79.3% each case displays a significant separation bubble. The truly interesting view is at 89.8% of the axial chord. At this location, the unmodified blade still contains a large separation bubble; while the other three cases show signs that reattachment has begun. In fact, both the 2.22 cm spacing and the 4.44 cm spacing between dimples appear to be almost completely reattached. It is unclear as to why the region behind the dimple with 4.44 cm seems to reattach more slowly than the other two dimpled cases. Figure 28 agrees with the conclusions drawn from the surface pressure investigation. As the passive vortex generators develop turbulence in the flow field, the reattachment location is greatly affected; while the separation point seems unaffected. Certainly, however, the extent of the separated region has been reduced indicating an increase in efficiency.

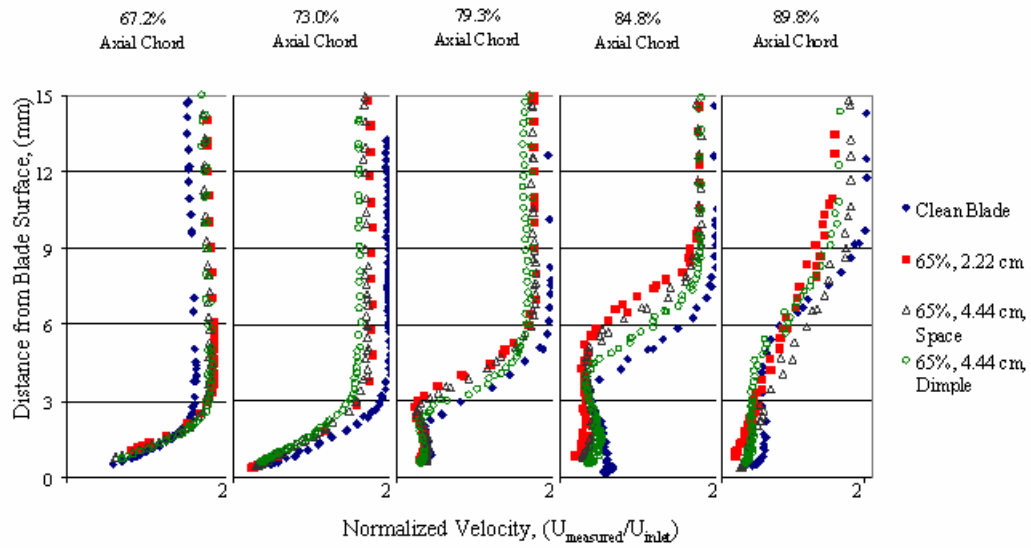


Figure 28. Boundary Layer Comparisons for different dimple patterns at Re 25k and 1% Tu

Figure 29 illustrates the affects of different dimple configurations on the boundary layer development at Re 45k and 1% Tu. Again the boundary layer appears to separate at about the same point between 73.0% and 79.3% of the axial chord; however, the three dimpled cases show significant signs of reattachment by 84.8% of the axial chord. At 84.8% of the axial chord the unmodified case contains a large separation bubble.

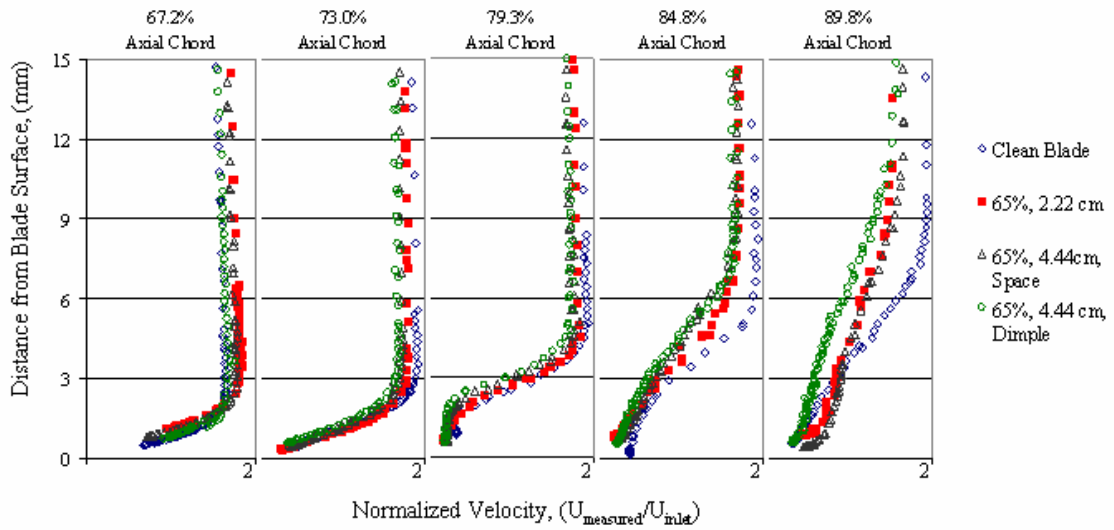


Figure 29. Boundary Layer Comparisons for different dimple patterns for Re 45K and 1% Tu

Further, the boundary layer influenced by the dimples at Re 45k displays similar characteristics to the boundary layer on the unmodified blade at Re 100k at 89.8% of the axial chord. This observation leads to the inference that the dimpled blade may perform similarly to the unmodified blade at less than half the Reynolds number.

### 3.6 Wake Velocity Profiles

Wake velocity profiles provide meaningful information about the flow structure leaving the turbine blades. The velocity profiles aid in the visualization of the momentum deficit. A smooth, stable flow field is evidence of the blade operating efficiently. A choppy wake could indicate large vortical structures shedding off the blades. Ideally, the wake profile is a series of peaks and valleys. The maximum velocity should occur at the centerline of a blade passage with a minimum just behind the trailing edge of a blade. As the Reynolds number decreases the flow does not turn all the way around the blades and the peak velocity shifts outboard as does the minimum velocity.

At very low Reynolds numbers, the flow separates effectively changing the blade shape and thus further reducing the turning angle (Fig. 30). A larger turning angle yields more extractable work from the flow. All profiles generated in this study are non-dimensionalized by the maximum velocity recorded for a given traverse. All of the traverses were run from the pressure side of blade #4 to the suction side of blade #6, and the plots represent the wake region behind blade #5. A complete set of profiles is included in Appendix D.

### 3.6.1 Wake Velocity Profiles for an Unmodified Pak-B Blade

Figure 31 shows the effect of Reynolds number on wake velocity profiles. The measured velocities have been normalized by the maximum measured velocity to obtain a percent of the maximum velocity.

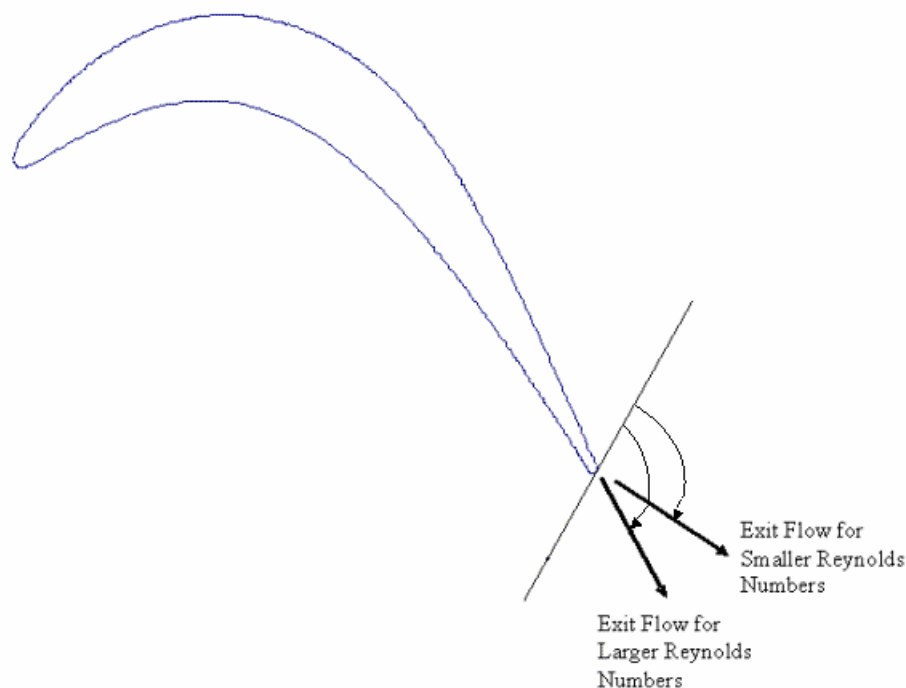


Figure 30. Reynolds number effect on exit velocity angles

As expected the higher Reynolds numbers have a narrower deficit region. At Re 25k, the minimum value is 80% of the freestream and is centered at about 28 cm. The valley spans about 15 cm. Increasing the Reynolds number to 45k, yields a minimum velocity of 86% of the freestream centered about 26 cm. Further, at a Reynolds number of 100k the minimum velocity is about 86%. There is no improvement in the minimum velocity when compared to the Re 45k case; however, the expanse of the valley for the Re 100k case is about half as wide decreasing from 13 cm to 7 cm and centered about 24 cm. The pitchwise shift and decrease in valley expanse indicates the flow is more attached and is exiting the cascade on a more on-design angle. These effects suggest a higher blade loading due to a greater wetted surface and more efficient blade operation due to the reduce wake region.

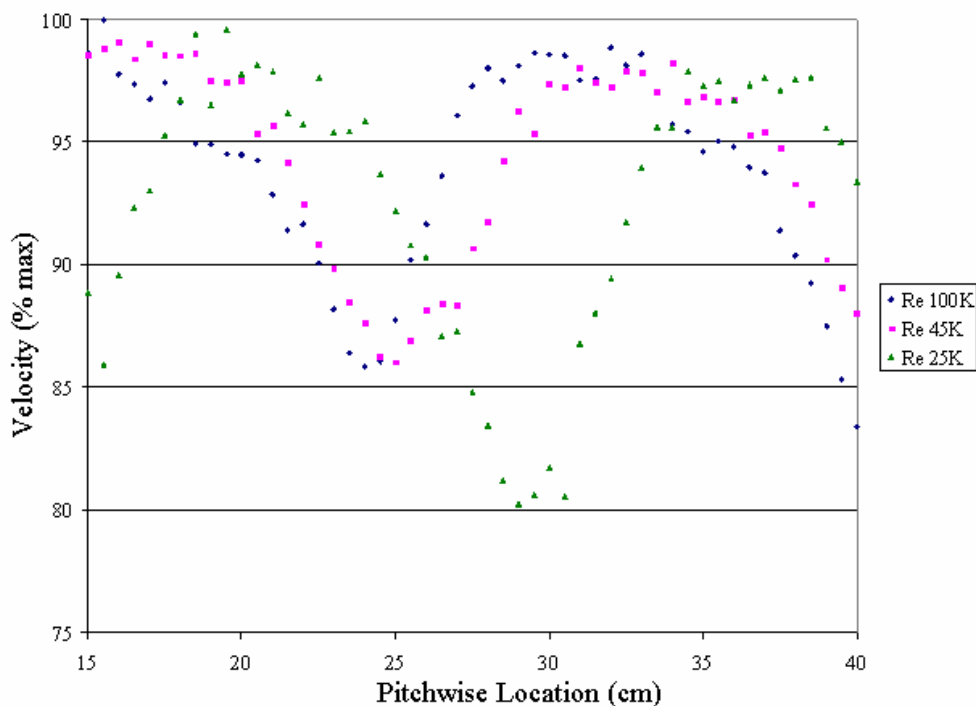


Figure 31. Wake velocity profiles for varying Reynolds numbers behind an unmodified Pak-B blade at 1% Tu

The profiles generated in the current research are compared to Rouser's [2] work in Fig. 32. The two experiments correlated extremely well. This further demonstrated the consistency in the experimental set-up and helped build confidence in the measured data.

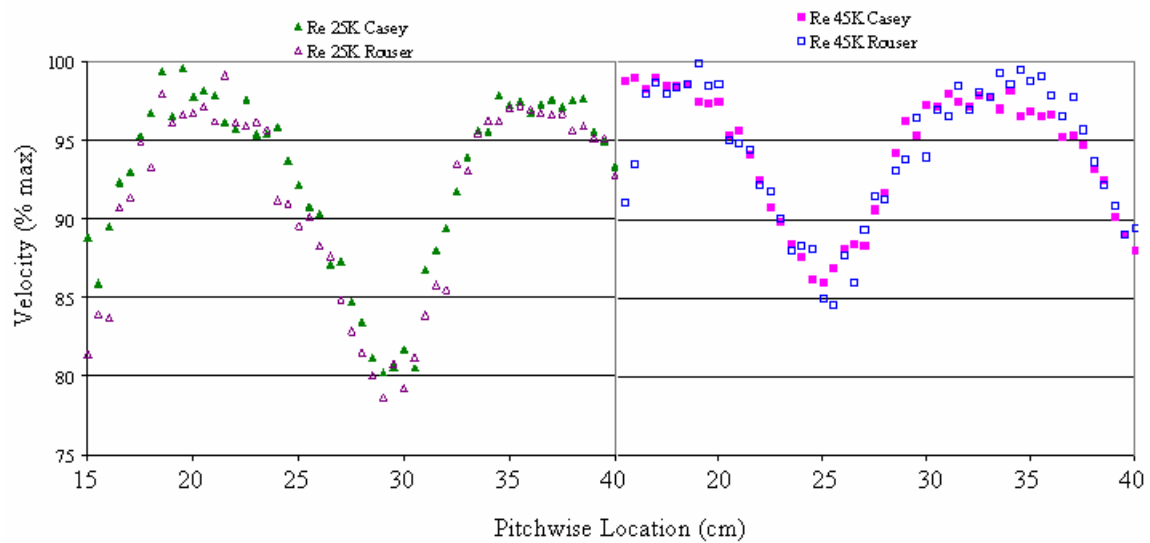


Figure 32. Wake velocity profile comparisons with previous research for an unmodified Pak-B blade at 1% Tu

### 3.6.2 Wake Velocity Profiles for Pak-B with Dimples at 65% of the axial chord with 2.22 cm Spacing at Tu 1%

Wake velocity profiles generated for a Pak-B blade with dimples at 65% of the axial chord with 2.22 cm spacing are shown in Figure 33. For convenience the unmodified profile for the Re 25k case is shown in Fig. 33 as well. Each Reynolds number case shows improvements over their respective unmodified cases. The most dramatic improvement occurs at Re 25k. The minimum velocity increases from 80% to about 85% of the freestream for Re 25k. Also the profile moves inboard by about 3 cm to 25.5 cm. For the Re 45k case the profile moved slightly inboard and is centered about

25 cm. The Re 25k and Re 45k cases return very similar profiles. At Re 100k the minimum velocity increased to about 88% of the freestream.

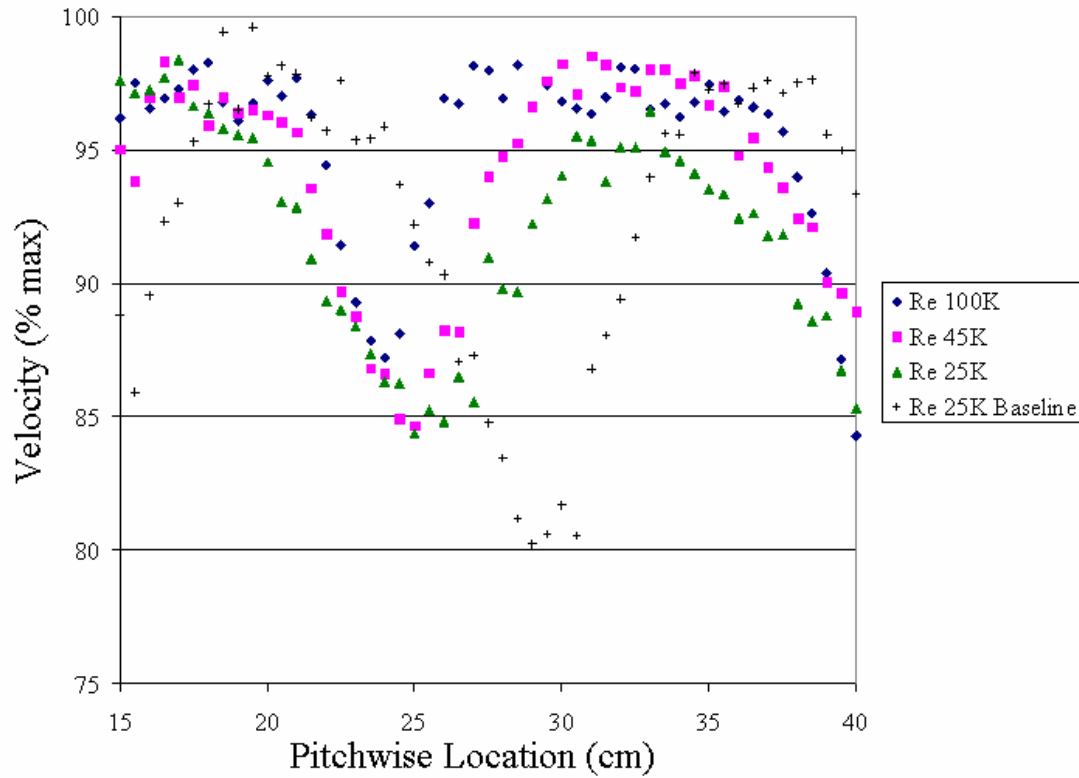


Figure 33. Wake velocity profiles for varying Reynolds numbers behind a Pak-B blade with dimples at 65% of the axial chord with 2.22 cm spacing at 1%  $Tu$

A qualitative result apparent in each of the plots is the fact the profiles are smoother and the blade passage region is more cleanly resolved than for the unmodified case. This is evidence that the vortex shedding due to separation has decreased significantly.

Figure 34 shows comparisons of the current research with Rouser's work. Once again agreement is achieved between the two experiments.

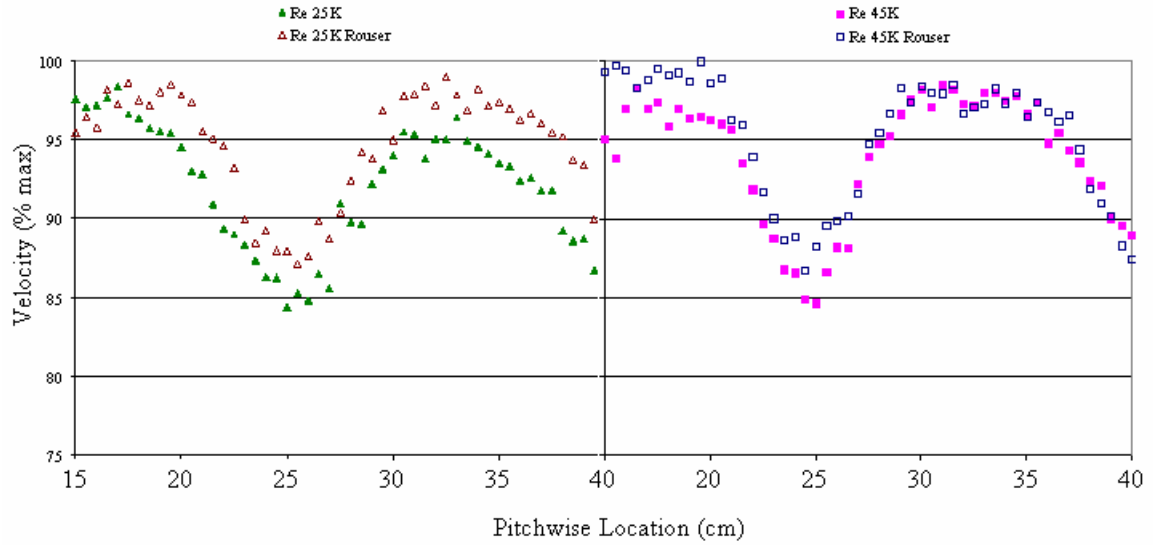


Figure 34. Wake velocity profile comparisons with previous research for a Pak-B blade with dimples at 65% of the axial chord with 2.22 cm spacing and 1% Tu

### 3.6.3 Wake Velocity Profiles for Pak-B with Dimples at 65% of the axial chord with 4.44 cm Spacing at Tu 1%

Multiple spanwise traverses were taken for the 4.44 cm spacing case at Re 45k and 1% freestream turbulence. The reason for this was to confirm there was no spanwise variation in the wake profile due to the wide spacing of the dimples. The 3 traverses yield information in the wake of a dimple, 1 cm lower than a dimple and centered in the space between two dimples. Figure 35 illustrates the profiles for these cases and shows there is no significant spanwise variation.



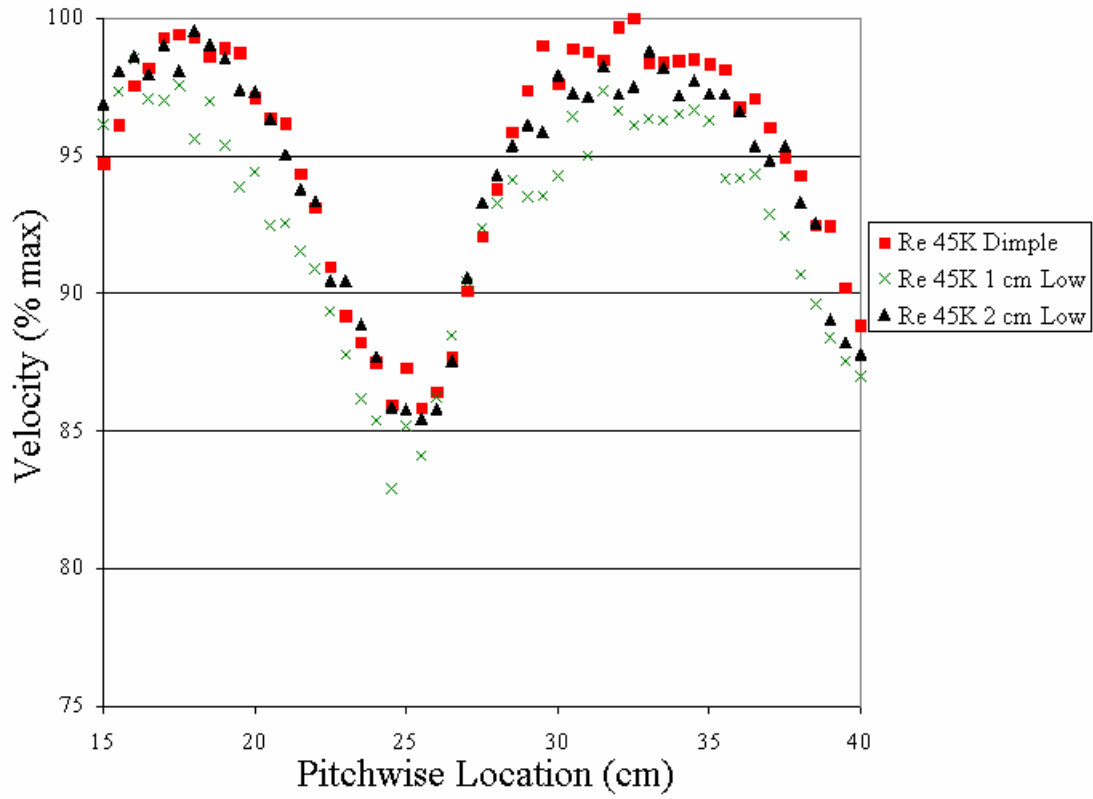


Figure 35. Wake velocity traverses for dimples at 65% of the axial chord with 4.44 cm and 1% Tu at 3 spanwise locations

### 3.7 Total Pressure Loss Coefficient

Measurements of total pressure loss through the cascade is the most direct way to evaluate turbine performance. Total pressure loss measurements evaluate the entropy production in the system. In this research, total pressure is measured both upstream and downstream of the Pak-B blade cascade. From this information a non-dimensional quantity can be calculated, namely the total pressure loss coefficient. The total pressure loss has a direct correlation to engine efficiency as shown in Section 2.1, Eqn. 10. An area-weighted average total pressure loss coefficient using the inlet dynamic pressure based on the differential of inlet total and static pressure was used in this research (Eqn.

17, page 43). Also, for a bulk performance indicator the local total pressure loss coefficient was integrated over and normalized by the pitch (Eqn. 13, page 36)

Similar to the wake velocity profiles, the loss coefficient profiles focused on the wake region behind blade #5. A complete set of profiles is included in Appendix E.

### 3.7.1 Total Pressure Loss Coefficient Profiles for an Unmodified Pak-B Blade

Figure 36 represents the wake loss profiles for an unmodified Pak-B blade at varying Reynolds numbers. The peak local total pressure loss coefficient clearly decreases and moves to a smaller pitchwise value (inward) as Reynolds number increases. At Re 25k the peak loss occurs at about 34 cm at a value of about 0.9. The loss profile at Re 25k spreads over 15 cm.

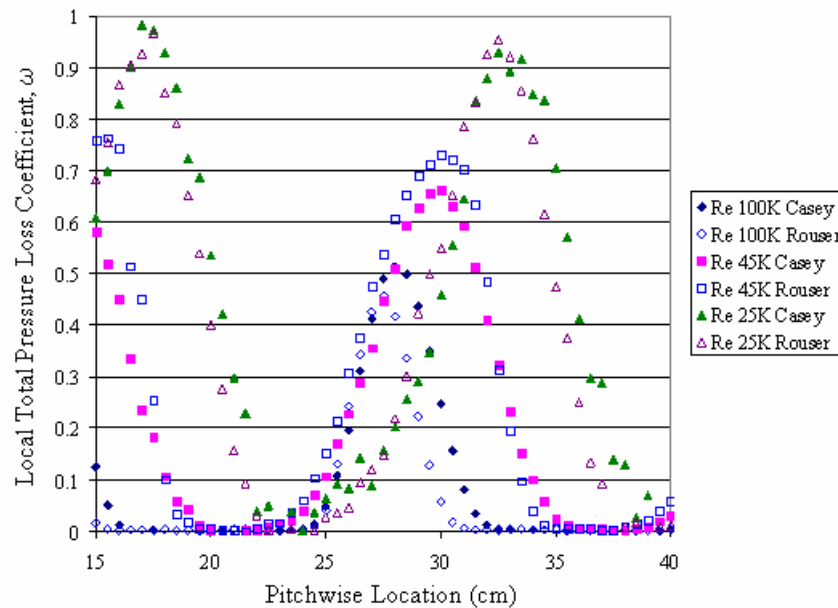


Figure 36. Wake loss profile comparisons with previous research for varying Reynolds numbers behind an unmodified Pak-B blade and 1% Tu

Increasing the Reynolds number to 45k shifts the peak inward 4 cm and decreases the loss coefficient by 25%. The peak loss coefficient at Re 100k is 40% less than that of Re

25k and has shifted inward 8 cm to be centered about 27 cm. Further, the loss profile at Re 100k expands over 8 cm, about half that of Re 25k. The dramatic loss reduction at higher Reynolds numbers speaks to the significant affect separation has on blade efficiency. Also contained in Fig. 36 are comparisons to Rouser's work. The peak amplitude as well as the pitchwise shift match closely.

### **3.7.2 Total Pressure Loss Coefficient Profiles for a Pak-B with Several Dimple Patterns at Tu 1%**

The local total pressure loss coefficient profiles for the unmodified case, dimples at 65% of the axial chord with 2.22 cm and 4.44 cm spacing, and two rows of dimples at 65% and 76% of the axial chord with 4.44 cm spacing in a chevron pattern are shown in Fig. 37 through Fig. 39. It is clear from the Re 25k case, each of the dimple patterns provides about a 33% loss improvement (Fig. 37). There is little quantitative evidence that indicates any of the dimple patterns performs best. Qualitatively, however, it appears that the multiple row case has a much smoother profile than the other two cases. At Re 45k, there was no substantial loss improvement; however, each of the dimpled cases profiles shifted slightly inboard indicating an improvement in turbine loading (Fig. 38). The Re 100k case also returned no loss coefficient improvement, however, a clear narrowing of the loss coefficient profile was realized (Fig. 39).

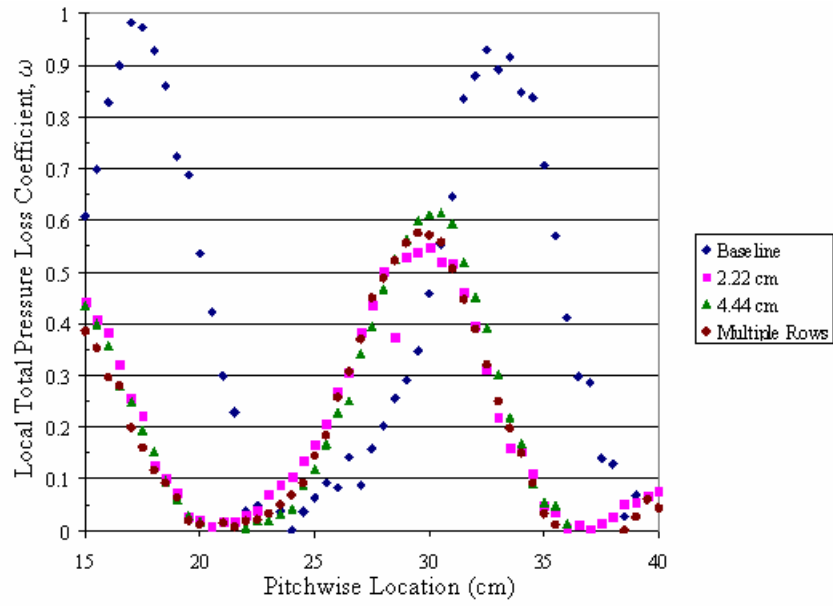


Figure 37. Wake loss profiles for various dimple patterns at Re 25k and 1% Tu

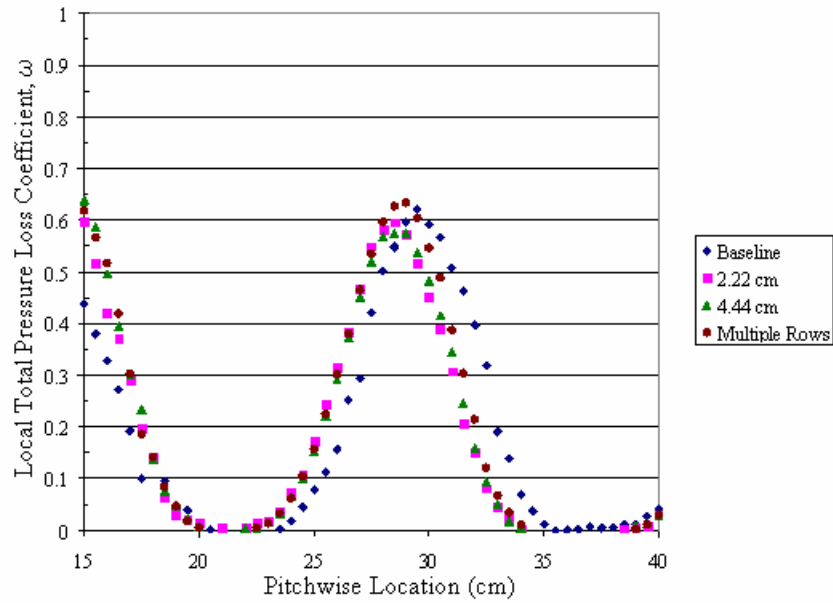


Figure 38. Wake loss profiles for various dimple patterns at Re 45k and 1% Tu

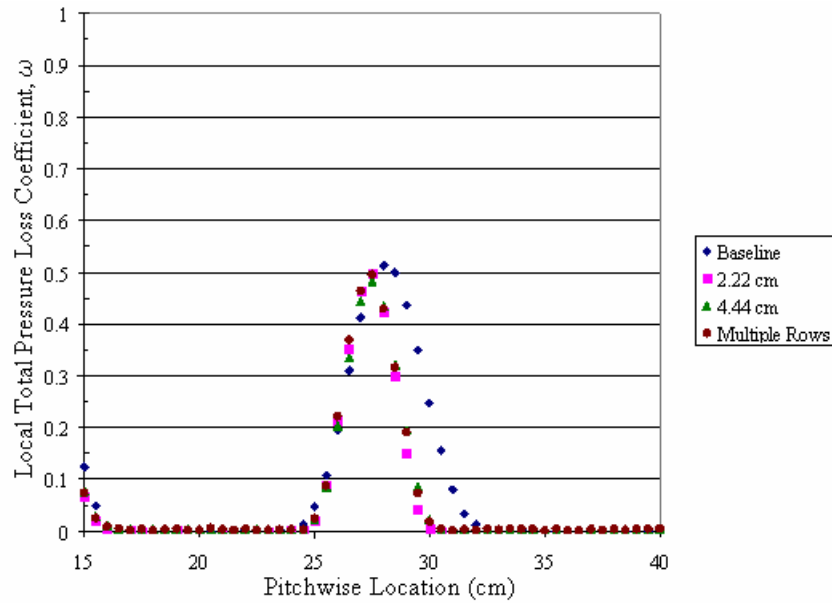


Figure 39. Wake loss profiles for various dimple patterns at Re 100k and 1% Tu

Based on the data returned from the wake velocity and wake loss profiles it can be reasoned that since all of the examined dimple patterns provide similar improvements, the optimal configuration is dimples at 65% of the axial chord with 4.44 cm spacing. This pattern returns the same loss reduction, with minimal machining.

### 3.7.3 Comparison of Average Total Pressure Loss Coefficients

Integrating the local total pressure loss coefficient,  $\omega$ , across the cascade pitch (15.75 cm) and normalizing by the pitch yields an average total pressure loss coefficient,  $\gamma$ . This is a bulk quantity that provides insight into the total effect of the various dimple configurations. As seen in Fig. 40, the average loss coefficient improves over the unmodified case for each of the dimple patterns considered. Each of the dimple patterns returns nearly the same average loss coefficient indicating that additional dimples do not provide any benefit. The average improvement of the average loss coefficient was 35%, 17%, and 32% for Re 25k, 45k, and 100k, respectively.

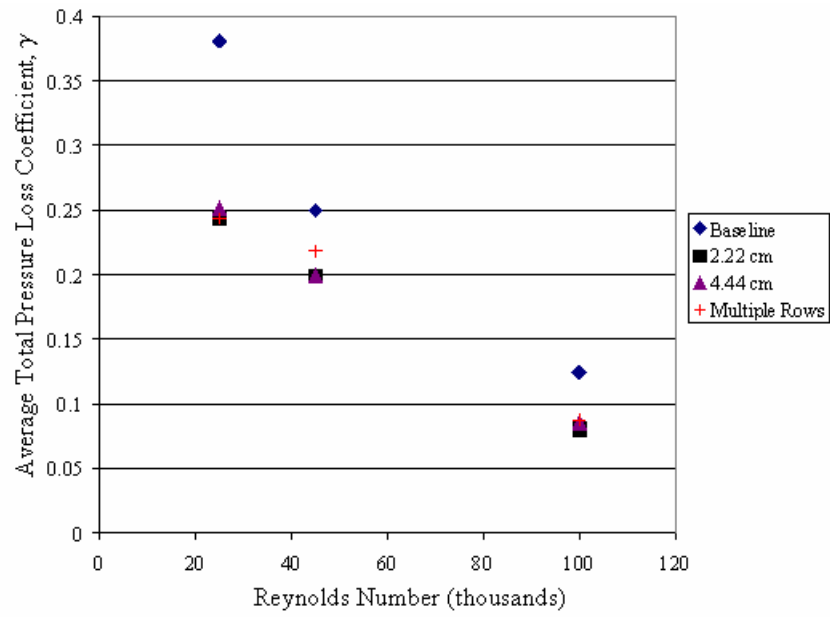


Figure 40. Average Total Pressure Loss Coefficients for various Reynolds numbers and dimple patterns at 1% Tu

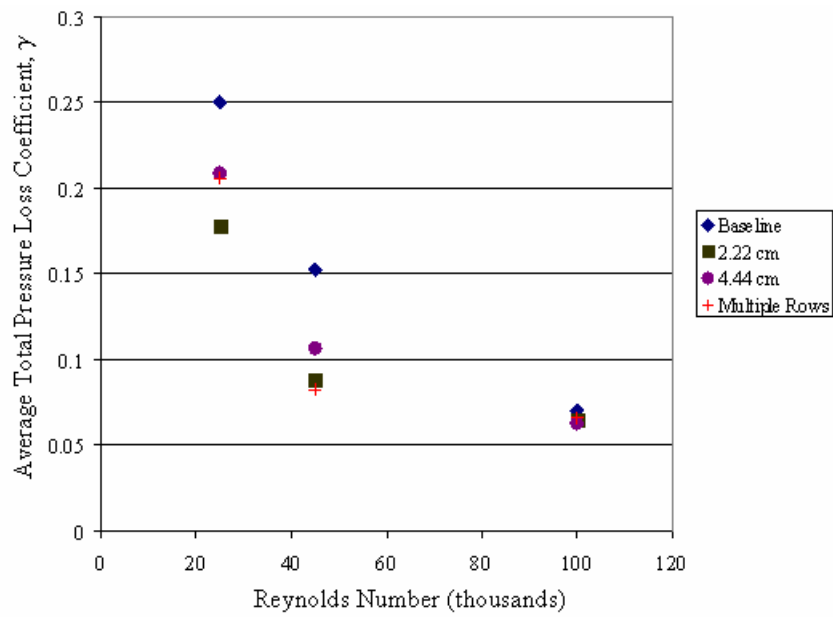


Figure 41. Average Total Pressure Loss Coefficients for various Reynolds numbers and dimple patterns at 4% Tu

Figure 41 shows the average total pressure loss coefficient for the three Reynolds number cases and each of the dimple patterns at 4% Tu. The average loss coefficient improved over the unmodified case for the Re 25k and Re 45k cases. The average loss coefficient remained the same at Re 100k. At Re 25k the closely spaced single row performed the best, but at Re 45k and 100k no clear advantage can be determined from any dimple pattern.

As expected, the average loss coefficient is reduced dramatically by the increased turbulence. Figure 42 is a replot of previously presented data. Figure 42 shows the average total pressure loss coefficients for the unmodified case at both turbulence levels. The loss coefficient improves by 34%, 39%, and 44% for Re 25k, 45k, and 100k, respectively. This further supports the claim that inducing turbulence into the flow will dramatically increase the turbine efficiency.

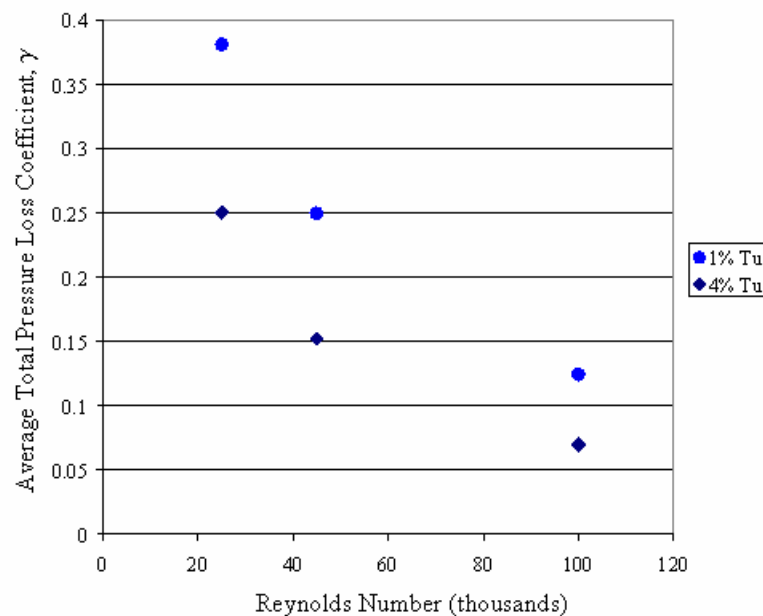


Figure 42. Average Total Pressure Loss Coefficients for unmodified blade at various Reynolds numbers and freestream turbulence levels

### **3.8 Summary and Conclusions of Experimental Research**

This research involved analyzing the effectiveness of various dimple patterns on boundary layer separation control on low-pressure turbine blades. Three experimental measurement techniques were used in this research; surface pressure scans, boundary layer traverses, and wake traverses. The blade configurations tested were an unmodified blade, a blade with a single row of dimples at 65% of the axial chord with 2.22 cm and 4.44 cm spacing, and a blade with two rows of dimples one at 65% and the other at 76% of the axial chord with 4.44 cm spacing on each row.

The surface pressure scans showed that different dimple configurations had very little impact on the pressure side of the adjacent blade. Moreover, consistency was shown as the current research agreed well with previous works. From the surface pressure scans, separation on the unmodified blade was seen at about 67% of the axial chord. It was shown that the separation location is very stable, and does not have a large dependency on freestream turbulence or Reynolds number. The reattachment location; however, is dramatically affected by turbulence and Reynolds number. This leads to the conclusion that within the range of Reynolds numbers tested separation location is primarily an effect of blade geometry and inlet angle, but the reattachment location is a function of flow conditions. Therefore, vortex generators can be used to affect a change in the reattachment location. If the separated region on a blade is minimized, then the blade loading and efficiency will increase.

Boundary layer measurements gave insight into the flow structure on the blade surface. The boundary layer plots clearly show the separation bubble growing as it



moves down the blade. The modified blades tended to begin to separate at about the same location as the unmodified blade. The reattachment location shifted upstream in the surface modified cases. For the Re 25k case and 1% Tu a single row at 65% of the axial chord appears almost fully reattached at 89.8% of the axial chord, while the unmodified blade under the same conditions had a separation bubble at least 6 mm thick. This dramatic improvement in reattachment location should have a profound effect on blade efficiency. The dimple spacing did not affect the boundary layer plots. Dimples at 65% of the axial chord with 2.22 cm and 4.44 cm spacing performed similarly in the boundary layer plots.

Whereas boundary layer plots provided a detailed perspective of flow structure, the wake traverses tend to provide meaningful data in the overall blade efficiency. Two measurement techniques were employed in the wake traverses; wake velocity measurements and total pressure loss measurements. These two sets of data were helpful in determining the outboard shift of the wake profile. An outboard shift is an indication of separated flow. Integrating the local total pressure loss coefficient and normalizing by the blade pitch yields an average total pressure loss coefficient for the respective blade. Each dimpled case dramatically improved the turbine efficiency over the unmodified case at all flow conditions considered in the current research. At Re 25k and 1% Tu each case improved over the unmodified blade by about 35%. Due to the fact, that each of the dimple configurations returned similar efficiency improvements, it is concluded that a single row at 65% of the axial chord with 4 cm spacing is the best solution. This conclusion is based on the fact that the same improvements are returned with a minimum amount of machining.

## **CHAPTER 4. COMPUTATIONAL FLUID DYNAMICS STUDY**

Three dimple patterns of interest were modeled computationally. The computational models accurately represent experimental geometries by centering a dimple on a Pak-B blade at 65% of the axial chord. The first model is 2 cm wide, while the second is 4 cm wide. The third centers a dimple at 65% of the axial chord and places another row of dimples at 76% of the axial chord. The second row of dimples is staggered off the first such that the center of the upstream dimple is at the mid-point between two downstream dimples. This blade is 2 cm wide. Rouser [2] developed an unmodified Pak-B CFD model. This grid was employed in the current research. Each of the 4 models studied was constructed from Pak-B blade profile coordinates. The coordinates were used to map the 2-D shape that was extruded in the spanwise direction. The grid and geometry generation was performed in Gridgen. A more detailed discussion of grid topology is given in Chapter 4.2.

Simulations were performed for an axial chord Reynolds number based on the inlet velocity of 25k. A partially converged steady-state flowfield simulation was used to develop the gross properties of the flowfield. This solution was employed as the initial condition for each of the unsteady runs. The unsteady solutions were run for at least 0.6 seconds of flow time. Differences in actual solution time between the cases are a result of available computer resources. It is maintained that this is a sufficient length of time to wash out initial transients from the flow field. Results from a brief time history investigation are presented in Appendix G.

Rouser [2] discovered that conventional RANS turbulence models exhibited significant damping resulting in a steady attached flowfield. This is a well known limitation of RANS models for the simulation of unsteady separated flows, and is inconsistent with experimental evidence. Therefore, in the current research, each case was run without turbulence modeling. Experimental observations indicate that the flow is unsteady and transitional with the primary separation being laminar in nature; and turbulent downstream of any separation point. Current turbulence models do not capture the transitional nature of the flow. It is believed that the laminar modeling accurately predicts the separation and that the transitional and turbulent flows downstream of separation do not have a significant impact upon the primary separation point. More advance turbulence modeling such as LES or Hybrid RANS are desirable, but beyond the scope of the current work.

Primarily, this CFD research was used as a tool to better understand the flow physics existing in and around dimples on a Pak-B blade. Knowledge of the highly complex flows associated with the transitional nature of this problem will help direct experimental efforts. The end goal is to eliminate separated flow in low-pressure turbines at low Reynolds number conditions. It should be noted, as with the experiment, the CFD research neglects 3-D effects of taper, sweep, and the rotating nature of the blade assembly. The CFD investigation, however, intends to accurately model the flow field locally on the mid-span of an actual blade. In the end, the CFD efforts helped to qualify trends in flow behavior, and visualize flow structure variations due to surface modifications.

## 4.1 Computational Software and Flow Solver Characteristics

Three software packages were used in the CFD research: Gridgen v15, Fluent<sup>®</sup> v6.1, and FIELDVIEW<sup>®</sup> v9.1 [41]. The physical blade and dimple geometries were built in Gridgen. Gridgen is a grid generation package specifically designed to interface with CFD packages such as Fluent<sup>®</sup>. Gridgen can also be used to build meshes for other codes. Grids are built by specifying the number of nodes in a region on a grid boundary. In a structured grid, a single node on one boundary corresponds to a given node on the opposite boundary. As the nodes are connected, cells are formed representing a specific region in space. Structured grids have an implied connectivity. Nodes are also connected to form cells in an unstructured grid; however, there is no correlation between any two nodes in the mesh. The connectivity in unstructured grids must be specified. The current research employed hybrid grids where portions of the flowfield were generated in both a structured and an unstructured manner to adequately and efficiently resolve the flow physics.

The boundary conditions were set in Gridgen. Each of the cases studied employed a *velocity inlet* boundary condition at the inlet face, and a *pressure outlet* boundary condition at the outlet face. Further, each case used *periodic* boundary conditions in the pitchwise direction to simulate an infinite blade cascade. All grids utilized *periodic* boundary conditions on the spanwise faces as well. This simulated a blade of infinite length, and allows for cross-flow. The periodic conditions also simulated an infinite row of dimples with 2 cm or 4 cm dimple spacing, respectively. Once the mesh was developed a case file was written out of Gridgen in a Fluent<sup>®</sup> format.

Fluent<sup>®</sup> interpreted the case file, and predicted the flow field at the node locations developed in Gridgen. Fluent<sup>®</sup> is a commercial CFD code that employs a finite volume method to the Navier-Stokes equations. Finite volume methods are derived from the integral form of the equations of motion. The conservation laws are then applied to a finite volume in space. The finite volumes are the cells of the grid structure, and flow properties are assumed constant throughout each cell. The physical quantities are conserved throughout the finite-volumes. To accomplish this, density is usually integrated throughout the volume to determine the instantaneous mass of the cell. The time rate of change of the mass of the fluid within a cell is equal to the total mass flux through each of the cell faces. Average weighted formulas are used to reconstruct the fluxes through the cell faces based on the flow parameters contained in adjacent cells. In this way, all the flow properties are determined in each cell throughout the domain [Tannehill et al., 40].

Within Fluent<sup>®</sup>, the inlet and outlet conditions were set. Each case operated at an axial chord Reynolds number based on inlet velocity near 25k, with inlet x and y components of velocity equal to 1.77804m/s and 1.221704m/s, respectively. This corresponds to an inlet angle of 34.5°. The inlet absolute pressure was set to 101,325 Pa, and the outlet gauge pressure set to -4.4 Pa. Naturally, the no-slip condition was imposed at the blade surface.

Fluent<sup>®</sup> has both steady and unsteady flow simulation modes. Steady solvers tend to wash out initial transients from non-physical initial conditions in less wall-clock time since they employ a variable time-step across the entire domain. The premise is large cells in the farfield where flow parameters change very little can handle a large time-step.

At the same time, smaller interior cells that experience wide fluctuations in flow parameters are afforded a small time step to maintain stability, as the flow field is resolved. The unsteady calculations, however, set a global time step by which every cell is incremented. This creates a more realistic transient solution, but the most time critical region of the domain limits the incremental time. The unsteady solver advances forward in time as far as the user prescribes, however, there are also a number of local iterations per time step. The maximum number of local iterations is user defined. This number can be lessened internally if certain convergence criteria are met. For the unmodified, 4 cm single row, and multiple row cases the time-step utilized for the unsteady solver was 0.00005 sec with a maximum of 20 local convergence iterations. The 2 cm single dimple case experienced more numeric instability and required a time-step of 0.00001 sec. The residuals of continuity, x, y, and z velocities were monitored at each local iteration. If each of the monitored residuals fell below  $10^{-6}$ , convergence was met and the time incremented. Each of the cases were run in parallel upon 10 to 64 processors upon either the Air Force Institute of Technology's 16 node Beowulf cluster or at the Wright-Patterson Air Force Base Major Shared Resource Center's Compaq ES40/45 system.

Once a solution was achieved the data was post-processed. For the current research, FIELDVIEW<sup>®</sup> was used to display the computed solution in a meaningful manner. Fluent<sup>®</sup> is equipped to write out data files that FIELDVIEW<sup>®</sup> can understand, and so while Fluent<sup>®</sup> solved the flow field it wrote out appropriate data files every 0.00075 or 0.001 seconds of flow time. This corresponds to either 15 or 100 time steps depending on the size of the global time step. In this way, a snapshot of the current state of the flow field was received. FIELDVIEW<sup>®</sup> linked the snapshots together in a flipbook

to allow inspection of flow structure development. Specific points in time could also be analyzed to determine separation and reattachment locations, velocity magnitude contours over the blade, and streak line visualization. The streak lines helped produce intricate pictures of vortex structures within the dimple.

Boundary layer profiles were extracted from the simulations. Within Fieldview a 2-D plot was generated plotting the velocity magnitude at 500 equally spaced positions along a vector 2 cm long and normal to the blade surface. The boundary layer measurement segment was centered spanwise on each blade. The boundary layer plots were generated at 8 equally spaced time steps over the solution range. The time step for averaging was 0.045 sec; approximately half the vortex shedding cycle. Boundary layer calculations were taken at 67.2%, 73.0%, 79.3%, 84.8% and 89.8% of the axial chord.

Wake loss measurements were extracted from the simulations. Two vectors were created at the mid-span of the domain. One of the vectors was upstream of the blade along the inlet face. The second vector was positioned 1.5 axial chord lengths downstream of the blade parallel to the exit face. Total pressure was recorded at 500 locations along both vectors, and dynamic pressure was also recorded along the upstream vector. The difference between the upstream and downstream total pressures normalized by the upstream dynamic pressure yields a local total pressure loss coefficient. The local total pressure loss coefficient was also integrated over the pitch to determine an average total pressure loss coefficient. As with the boundary layer calculations the wake loss measurements were made at eight times 0.045 sec apart. The eight measurements were averaged to determine a time averaged loss coefficient.

The three software packages utilized provided a very powerful mechanism for studying the flow development about a Pak-B blade at Re 25k.

## **4.2 Grid Model Characteristics**

Coordinates accurately describing the pressure and suction surfaces from a 2-D Pak-B profile were imported into Gridgen. The 2-D profile was then extruded in the z-direction to return a blade with a span of 2 cm. Three primary cell structures were used to adequately capture the flow physics. Most of the blade surface was covered with quads that were extruded from the blade surface to make a structured near wall region filled with hexahedral cells. The region away from the surface was an unstructured grid with tetrahedral cells. For the models containing dimples, the surface within and around the dimples was represented by triangles. The triangles were extruded filling the near wall region with prism cells. The interface region from hexahedral to tetrahedral cells yielded the creation of pyramid shaped cells.

### **4.2.1 Grid Topology for an Unmodified Pak-B Blade**

For the unmodified investigation, Rouser's unmodified Pak-B grid was used. This grid was rerun at AFIT to investigate the effect of initial conditions. This solution was resolved on 10-14 processors to a flow time of 0.78675 sec. (Rouser [2] ran the unmodified Pak-B blade with a steady solver only.) In this grid, 41 nodes were arranged across the span, and a square structured grid was projected onto the blade surface [Rouser, 2]. A high density of cells was desired near regions where high flow gradients were expected for better flow resolution. For this reason, Rouser clustered surface grid points near the leading and trailing edges, in addition to the expected separation point (Fig. 43). A total of 421 nodes are placed in the streamwise direction around both the



suction and pressure surfaces. The surface grid is then extruded normal to the blade surface 0.0042 m in 42 equal steps. This is expected to enclose the boundary layer in the hexahedral region of the mesh [Rouser, 2]. The region representing the passage between adjacent blades is then filled with tetrahedral cells. The unstructured grid solver in Gridgen was utilized to generate a mesh with 15 pitchwise nodes at the inlet and outlet faces along with 231 nodes along the streamwise mid-passage faces (Fig. 44). The pitchwise length (or passage width) accurately represents the cascade geometry, delivering an axial chord to spacing ratio (solidity) of 1.129. 830,625 nodes creating 1,319,992 cells (688,800 hexahedral and 631,192 mixed pyramid and tetrahedral) comprise the unmodified model.

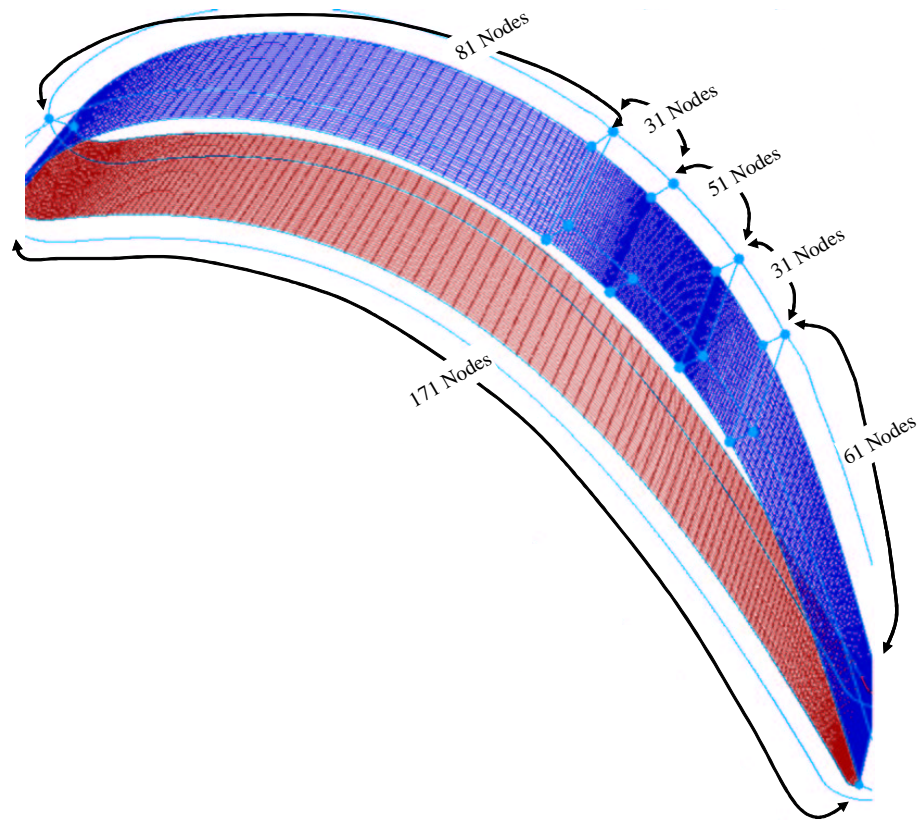


Figure 43. Pak-B blade unmodified surface topology [Rouser, 2]

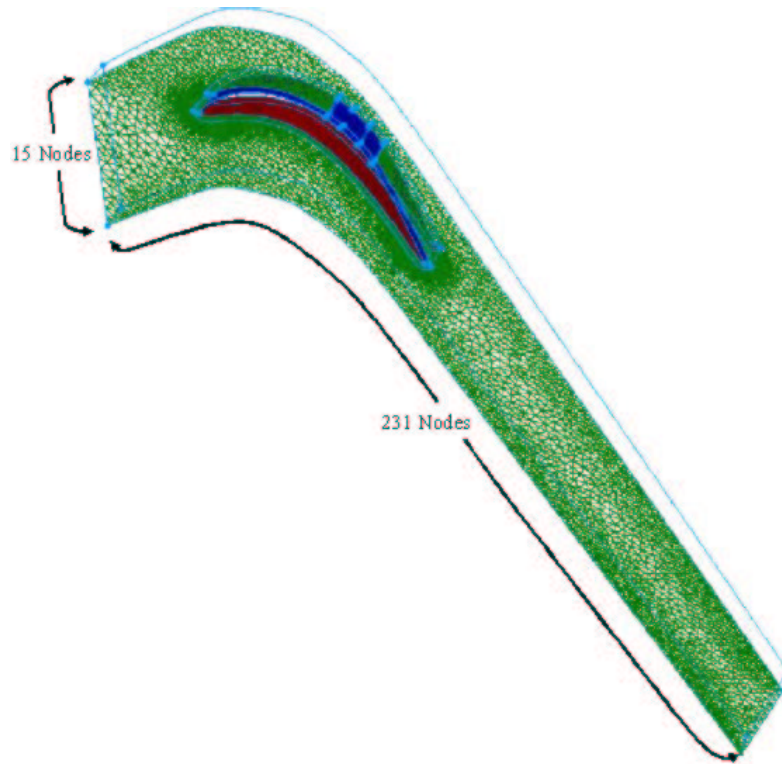


Figure 44. Pak-B blade mid-passage grid topology [Rouser, 2]

#### 4.2.2 Grid Topology for Pak-B Blade with 2 cm Dimple Spacing

The single row of dimples at 65% of the axial chord with 2 cm spacing grid was run at AFIT on 10-20 processors to a flow time of 0.629 sec. A spherical database structure 5.08 cm in diameter was created in Gridgen. This database was merged with the Pak-B blade shape database. A cut was made along the union of the two databases and a domain projected onto the surface of the sphere to insert a dimple into the blade surface. The resulting dimple was centered on the blade at 65% of the axial chord with a depth of 1.588mm.

The spanwise surface nodes of the structured grid remained at 41 (Fig. 45). The surface domain around the dimple was triangulated containing 10,995 nodes. This includes 151 nodes on the boundary faces in the streamwise direction. The nodes were

arranged with a higher density downstream of the dimple where greater resolution was desired (Fig. 46). Around the dimple's edge there are 360 nodes (Fig. 46), with a triangulated surface domain containing 18,834 nodes inside the dimple. The two domains comprising the dimple and its immediate surroundings contain 58,556 triangular elements. These domains were extruded along a path normal to the blade surface, in concert with the adjacent hexahedral grid containing 42 nodes. The hexahedral grid contained 81 streamwise nodes upstream and 61 streamwise nodes downstream of the dimple region. Also, the hexahedral grid contained 171 streamwise nodes on the pressure side of the blade (Fig. 45). The region away from the blade contained 231 streamwise nodes, 15 pitchwise nodes, and 7 spanwise nodes as in the unmodified case (Fig. 44). There are a total of 508,400 hexahedral cells in the near wall region, 2,400,796 prism cells in the dimpled region, and 489,195 mixed pyramid and tetrahedral cells in the region away from the wall.

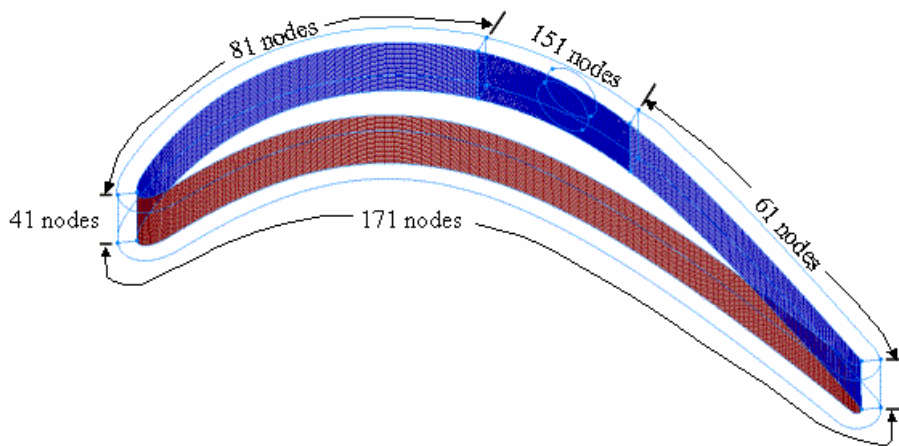


Figure 45. Pak-B blade with dimples at 65% of the axial chord and 2 cm spacing grid topology

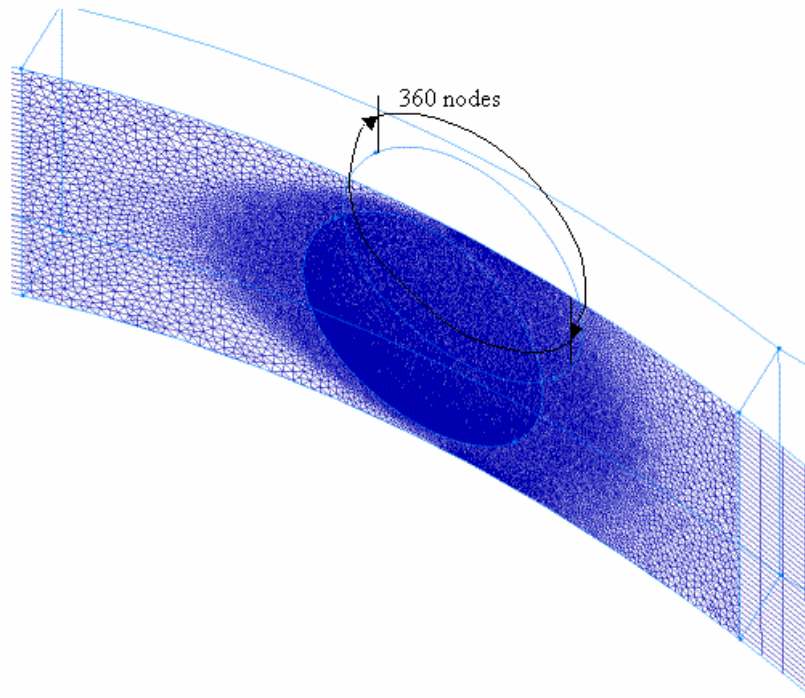


Figure 46. Pak-B blade with 2 cm center-on-center dimple close-up

#### 4.2.3 Grid Topology for Pak-B Blade with 4 cm Dimple Spacing

The single row of dimples at 65% of the axial chord with 4 cm spacing was run to 0.76995 sec at the ASC/MSRC on 32-64 processors. Simply separating the spanwise faces comprising the 2 cm grid 1 cm in each direction created the 4 cm grid. In this case, the hexahedral grid was extended to 82 spanwise nodes (Fig. 47). Therefore, 1,029,510 hexahedral cells define the near wall region. The triangulated domain within and around the dimple contained 47,865 nodes. Again nodes were clustered downstream of the dimple for better resolution. The dimple geometry was left unchanged. The triangulated block around the dimple has 3,876,386 prism cells. The spanwise nodes in the tetrahedral grid were increased to 14 for the wider grid. The other dimensions were left unchanged, and the region away from the wall resulted in 1,453,930 mixed pyramid and tetrahedral cells.

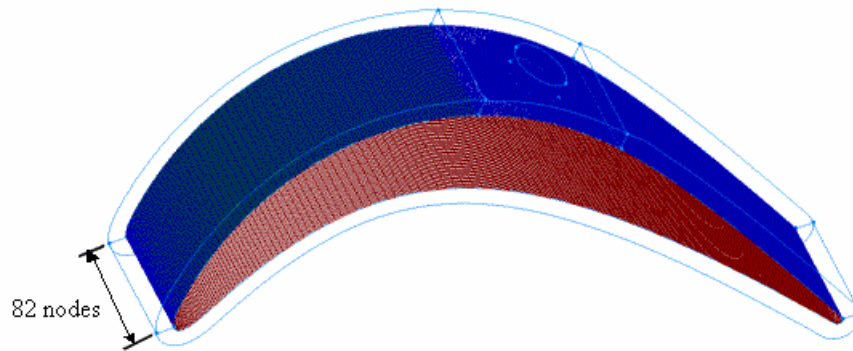


Figure 47. Pak-B blade with dimples at 65% of the axial chord and 4 cm spacing grid topology

#### 4.2.4 Grid Topology for Pak-B Blade with Multiple Rows

The multiple row case was run to 0.80005 sec on 32-64 processors at the ASC/MSRC. Again the foundation for this grid stemmed from 2 cm single dimple grid. Two more half dimples were constructed centered on the spanwise boundary at 76% of the axial chord. The hexahedral grid had 81 streamwise nodes upstream and 71 streamwise nodes downstream of the dimple region, and 171 streamwise nodes on the pressure surface (Fig. 48). These three regions combined for 524,800 hexahedral cells. The region around the dimples was much larger extending over a greater portion of the suction surface. There are 151 streamwise nodes connecting the upstream hexahedral mesh with the front edge of the half dimples, and 61 nodes connecting the back edge of the half dimples and the downstream hexahedral mesh (Fig. 49). The half dimples contained 79 nodes in the streamwise direction on the spanwise boundary, and 181 nodes on the dimple edge. The region between the upstream and downstream dimples had a very high node density. The surface domains including the dimples and unstructured mesh around the dimple contained 49,889 nodes. The triangulated block in the dimple region contains 4,004,552 prism cells. The farfield contains 231 streamwise, 15

pitchwise, and 7 spanwise nodes. The farfield increased in size to 1,139,054 cells. The reason the farfield contained many more cells than the other 2 cm case was a result of the transition required from the high density cells near the dimples.

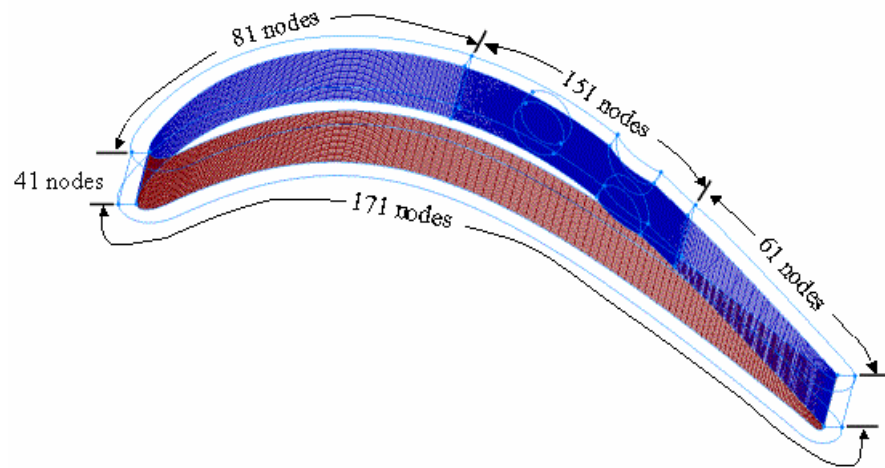


Figure 48. Pak-B blade with multiple rows grid topology

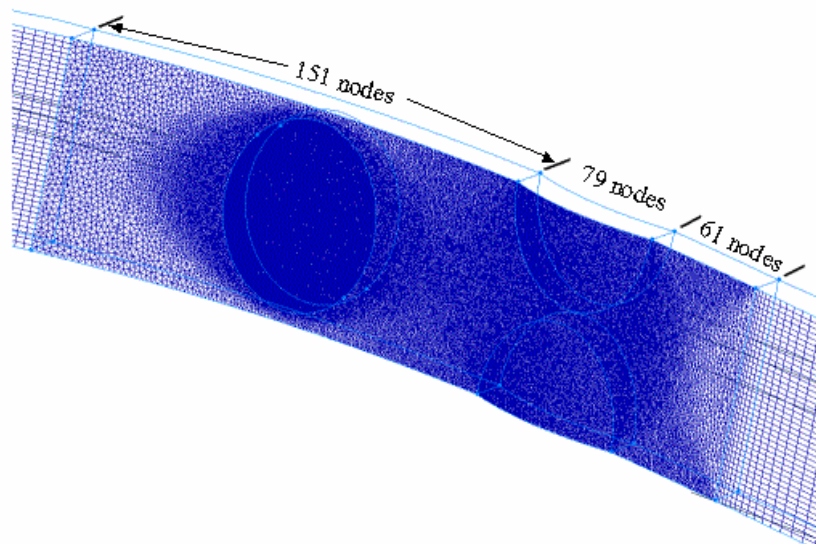


Figure 49. Pak-B blade with multiple rows of dimples close-up

## **4.3 Computational Results**

The computational results demonstrate that the unmodified case separates between 64.5% and 68.5% of the axial chord at  $Re$  25k. For the unmodified blade, this separation location is fairly stable and the start of a large separation region. Large-scale vortices shed off the unmodified blade approximately every 0.09 sec evidenced by the traveling separation line. In addition, the separation location and velocity magnitude fields provide insight to the flow field conditions. Streak lines provide a detailed picture of the flow in the dimples. Boundary layer and wake loss measurements provide a means of assessing the computationally predicted blade efficiencies, and provide a medium to compare directly to experimental results.

### **4.3.1 Separation Location**

The unmodified Pak-B blade was run time-accurate and fully laminar to ascertain the consequences of beginning a steady laminar solution from a fully attached turbulent solution as was done in the previous work [Rouser, 2]. Figure 50 shows the major separation location occurring at about 66% of the axial chord. (Green dots on separation plots depict a ruler measuring percent of the axial chord.) This agrees with both Rouser's [2] computational work, the current experimental work, and experimental work by Bons et al. [20]. The flow attempts to reattach further downstream, but a fully reattached flow is not achieved. The separation location oscillates slightly from about 64.5% to 68.5% of the axial chord. The oscillations appear cyclical at about 11 Hz.



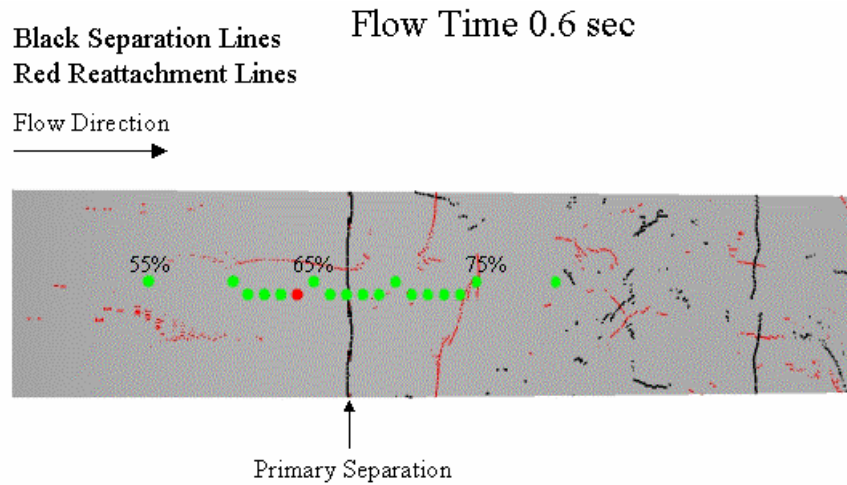


Figure 50. Separation and reattachment lines on an unmodified Pak-B computational model at Re 25k and 0% Tu

For the case of a single row of dimples at 65% of the axial chord with 2 cm spacing, the separation location is at 71% of the axial chord at a flow time of 0.275 sec (Fig. 51a). At this time there is a contained vortex in the dimple. This is evidenced by the separation line on the upstream edge of the dimple and reattachment near the downstream edge of the dimple. The primary reattachment location is at 83% of the axial chord. As time progresses to 0.35 sec the separation line moves upstream into the dimple and holds steady at 67% of the axial chord from about 0.35 to 0.629 sec (Fig. 51b). The phenomenon of large scale vortex shedding appears to be eliminated. At this mature solution, reattachment attempts are made as far upstream as 76% of the axial chord.



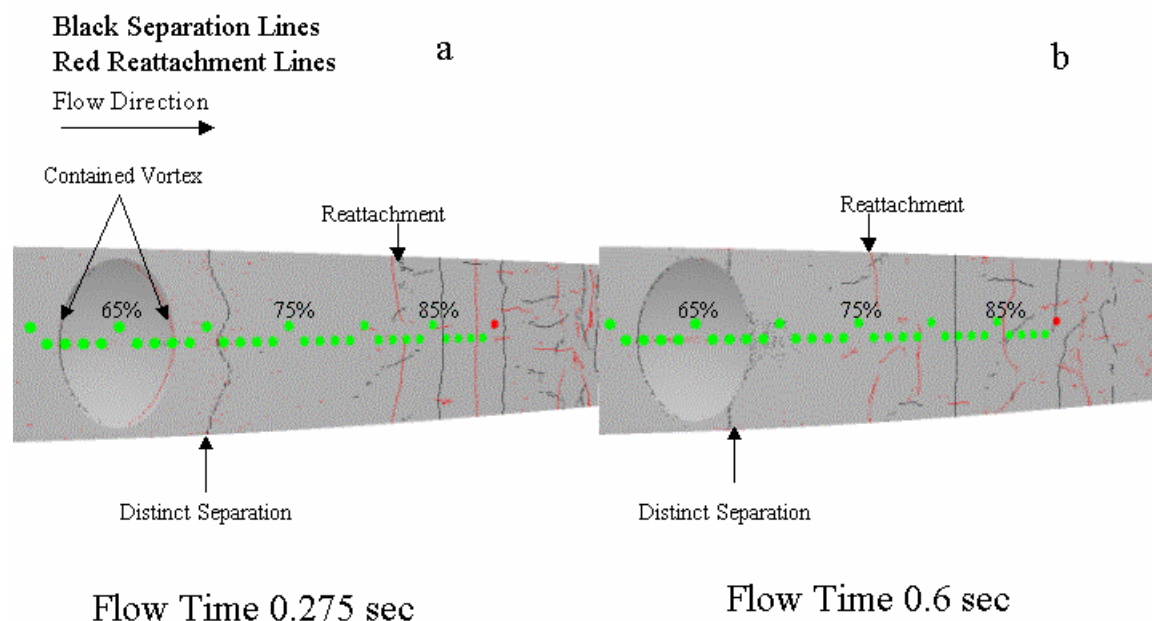


Figure 51. Separation and reattachment lines on a computational Pak-B blade with dimples at 65% of the axial chord with 2 cm spacing at Re 25k and 0% Tu

The solution with dimples spaced 4 cm center-on-center is very similar to the 2 cm case. Early in the solution a separation line is seen just aft the dimple at 70% of the axial chord, and a substantial reattachment region is produced at 79% of the axial chord (Fig. 52a). At this point the vortex in the dimple is contained with a separation line on the upstream edge and a reattachment line on the downstream edge of the dimple. As time progresses, the dimple vortex becomes larger than the dimple itself (as will be shown in Section 4.3.3), drawing flow upstream into the dimple creating a large backflow region. At 0.6 seconds the most significant separation line occurs at 67% of the axial chord and hold steady at this location. This is similar to the 2 cm grid. At 0.6 sec there is a sharp reattachment line at 75% of the axial chord (Fig. 52b).

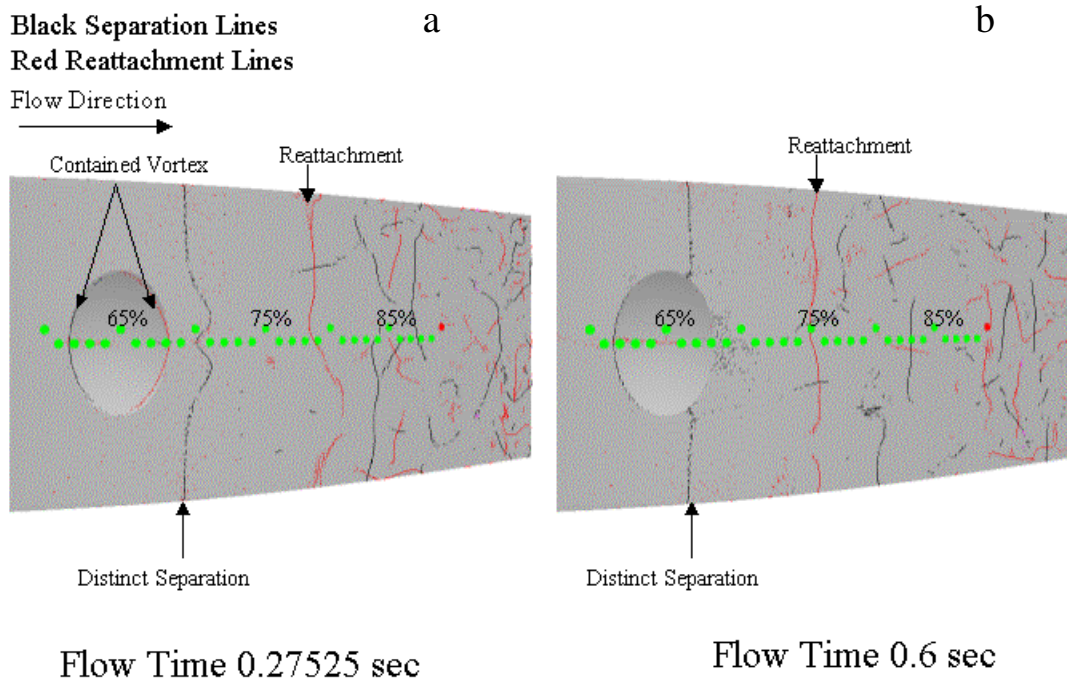


Figure 52. Separation and reattachment lines on a computational Pak-B blade with dimples at 65% of the axial chord with 4 cm spacing at Re 25k and 0% Tu

The multiple row case has a fairly well defined separation line on the upstream edge of the dimple at 65% of the axial chord. This is a localized effect of the dimple with a similar reattachment location contained within the dimple (Fig. 53). The region between the separation and reattachment lines defines the vortex contained within the dimple. The flowfield is attached until 73% of the axial chord where a separation region begins. Again this is a localized effect from the downstream dimple. A sharp reattachment line is seen at 83% of the axial chord (Fig. 53). The separation and reattachment lines upstream of 83% of the axial chord are not time varying. Downstream 83% of the axial chord the field is very chaotic.

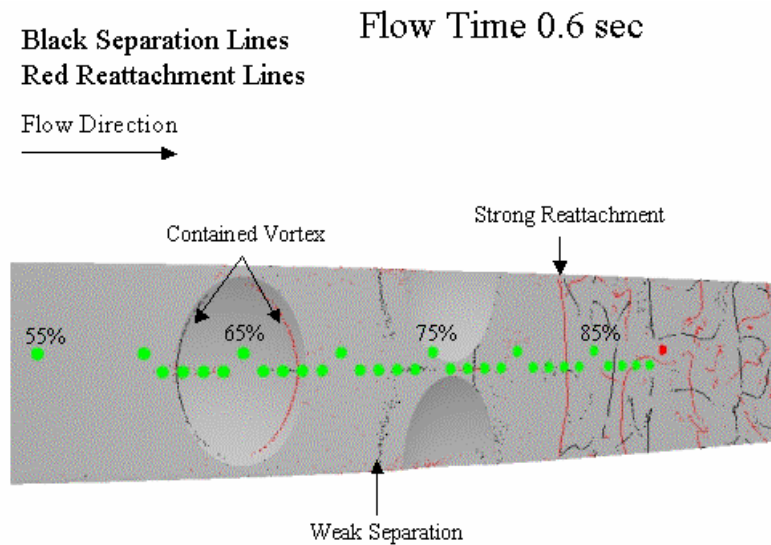


Figure 53. Separation and reattachment lines on a computational Pak-B blade with dimples at 65% and 76% of the axial chord with 2 cm spacing at Re 25k and 0% Tu

#### 4.3.2 Velocity Field Comparisons

Figure 54 shows a velocity magnitude contour plot of the unmodified blade. Represented in Fig. 54 are large vortical structures shedding off the blade. Also the separation location is plainly seen where the boundary layer begins to grow off of the blade. The low velocity region is evidence of separated flow.

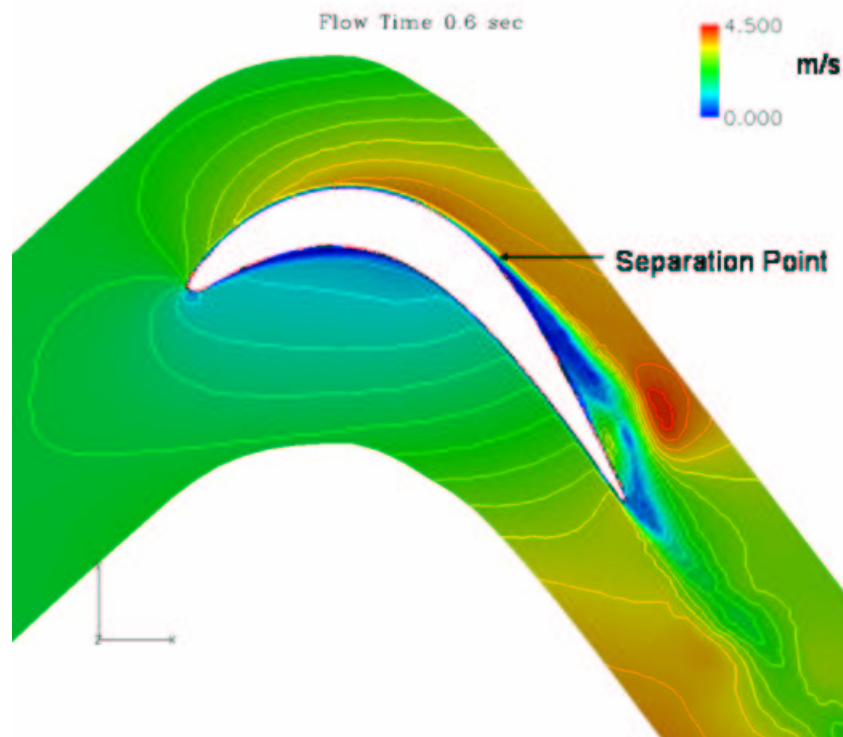
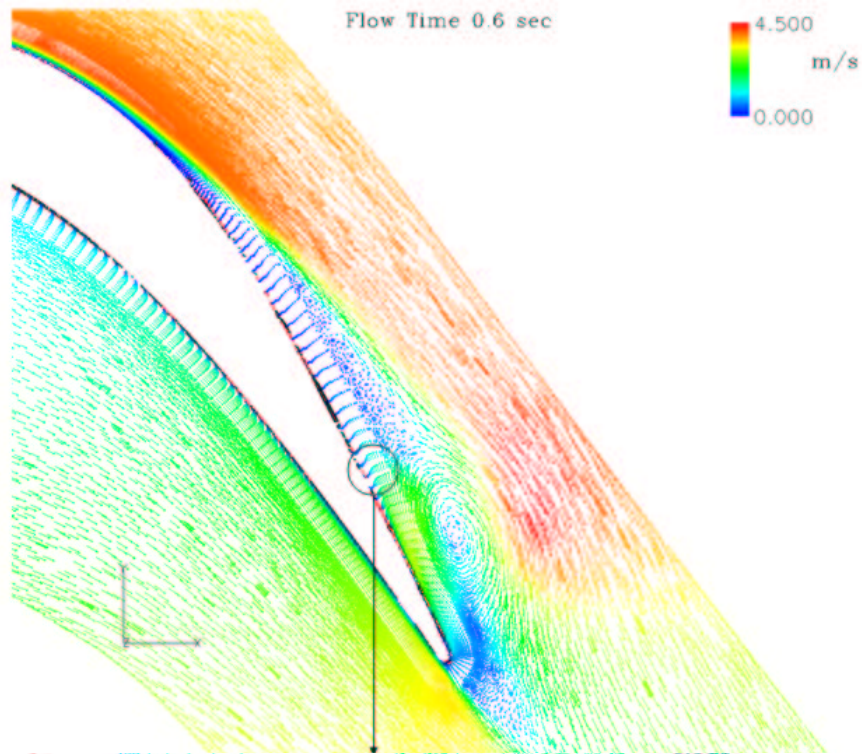
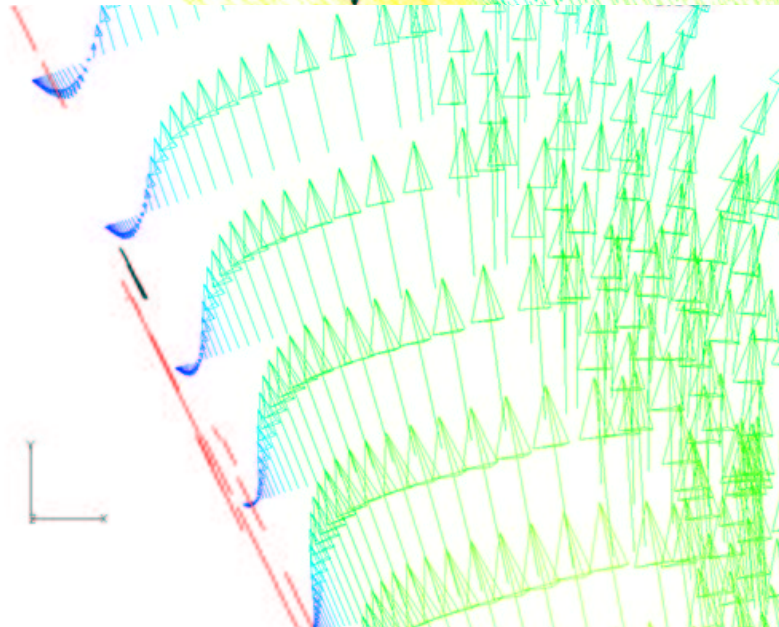


Figure 54. Velocity magnitude contours for an unmodified Pak-B computational model at Re 25k and 0% Tu

The velocity contours yield insight into the overall flow structure. Analyzing the velocity vectors provides a different perspective on how the flow is developing. Figure 55 shows velocity vectors for the unmodified blade. A large vortical structure is seen shedding off of Fig. 55a. Figure 55b shows reattachment attempts, although a strong backflow region denies full reattachment. The attempts at reattachment seem to be associated with the shedding of the vortices. The strongest reattached locations occur just after the vortex passes downstream. This concurs with theoretical and experimental data [Halstead et al., 4].



a



b

Figure 55. Velocity magnitude vectors for an unmodified Pak-B computational model at Re 25k and 0% Tu



The velocity field for the single row case with 2 cm dimple spacing is shown in Fig. 56 at 0.6 sec. There is a large backflow region extending from the downstream edge of the dimple to 79% of the axial chord. The flow appears to flow upstream into the dimple at 65% of the axial chord. At 79% of the axial chord the flow begins to reattach. The regions of reattached flow are small due to a strong shear layer forcing separation (Fig. 56b).

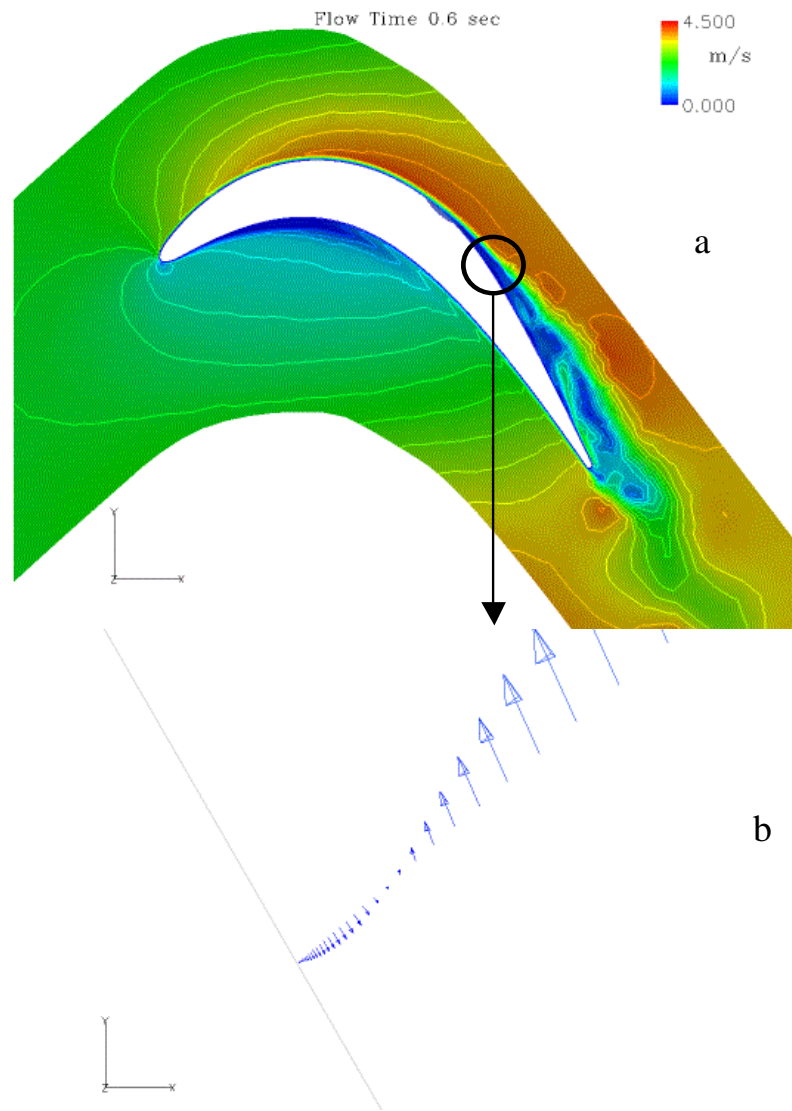


Figure 56. Velocity magnitude contours and vectors for a computational Pak-B model with dimples at 65% of the axial chord and 2 cm spacing at Re 25k and 0% Tu

Once again, the solution for the 4 cm case is very similar to the 2 cm case. The velocity field for the single row at 65% of the axial chord and 4 cm spacing shows a significant backflow region at 0.27525 sec of flow time. The region extends from the trailing edge of the dimple to 81% of the axial chord. At this location the flow shows attempts at reattachment. The large shear layer above the blade prevents the flow from fully reattaching. The surface flow goes through this attachment-separation cycle several times for the remainder of the blade surface. The regions of backflow are always much larger and stronger than the regions of attached flow by at least an order of magnitude. By 0.45 seconds the first instance of attempted reattachment occurs near 76% of the axial chord. Again the reattached flow is short lived, but the point where reattachment attempts begin is no longer time varying. By 0.6 seconds of flow time there is a significant region of backflow extending from the dimple to about the 75% axial chord location. This region appears to be drawn upstream into the dimple (Fig. 57). Figure 58a provides an image of the entire velocity field. A large vortex is clearly seen near the trailing edge of the blade. Figure 58b shows at 75% of the axial chord the flow is reattached. There is a strong shear layer that prevents the flow from remaining attached. By 80% of the axial chord separation begins again and at 83% of the axial chord the flow is fully separated with a large back flow region that extends down the remainder of the blade.

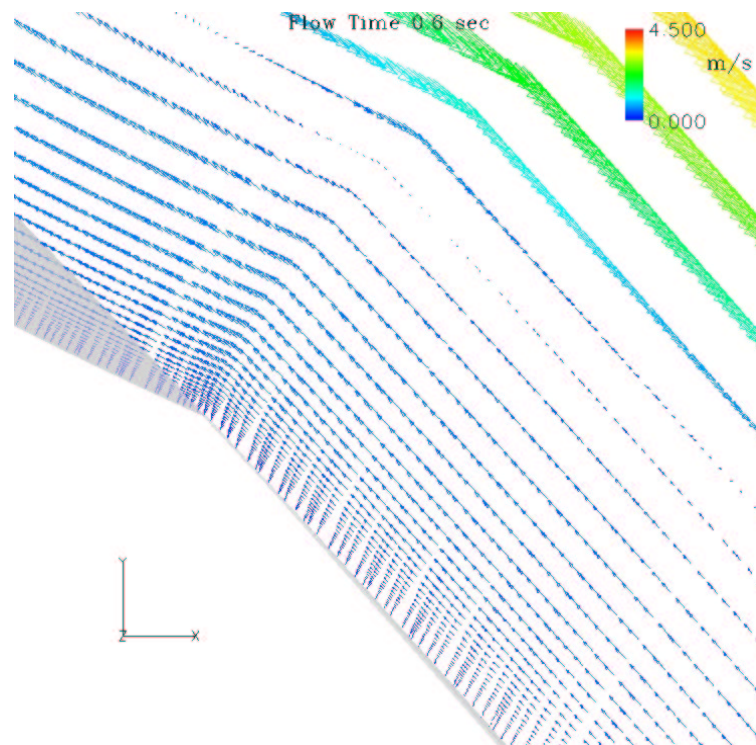


Figure 57. Velocity vectors pointing upstream entering the dimple at 65% of the axial chord with 4 cm spacing



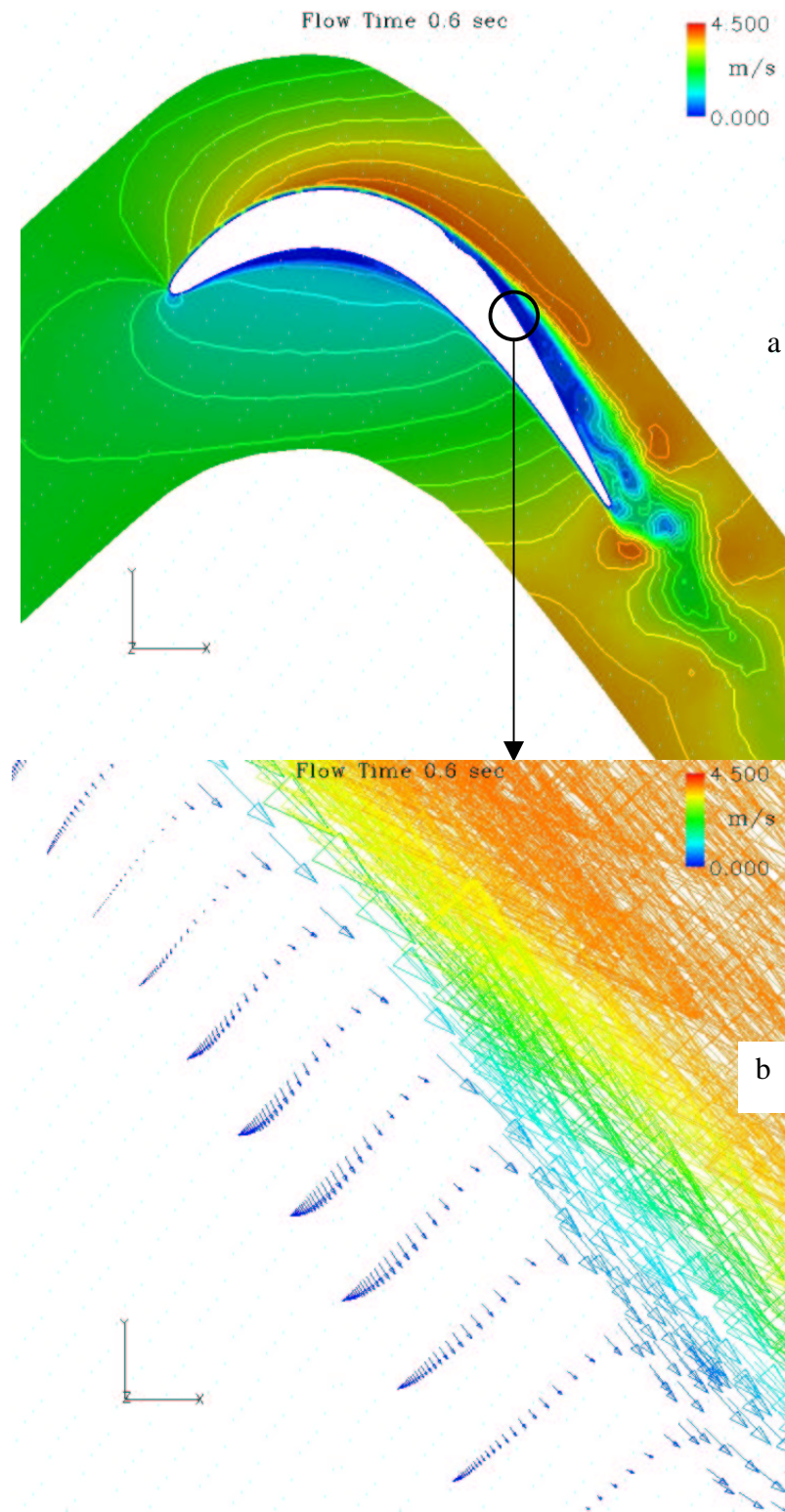


Figure 58. Velocity magnitude contours and vectors for a computational Pak-B model with dimples at 65% of the axial chord and 4 cm spacing at Re 25k and 0% Tu

Figure 59d shows contours of velocity at 0.6 sec for the multiple row case. For convenience, the velocity contours for the other 3 cases are also shown. The unmodified blade displays an extensive separation region (Fig. 59a). The 2 cm and 4 cm cases show a slightly thinner separation bubble, and a thinner, yet, more turbulent downstream wake region (Fig. 59b-c). This is evidence of the intermittent reattachment-separation cycles that characterize the field aft of about 76% of the axial chord. The multiple row case significantly reduces the separation bubble thickness. Further, the wake region nearly follows the ideal exit angle of  $60^\circ$  (Fig. 59d).

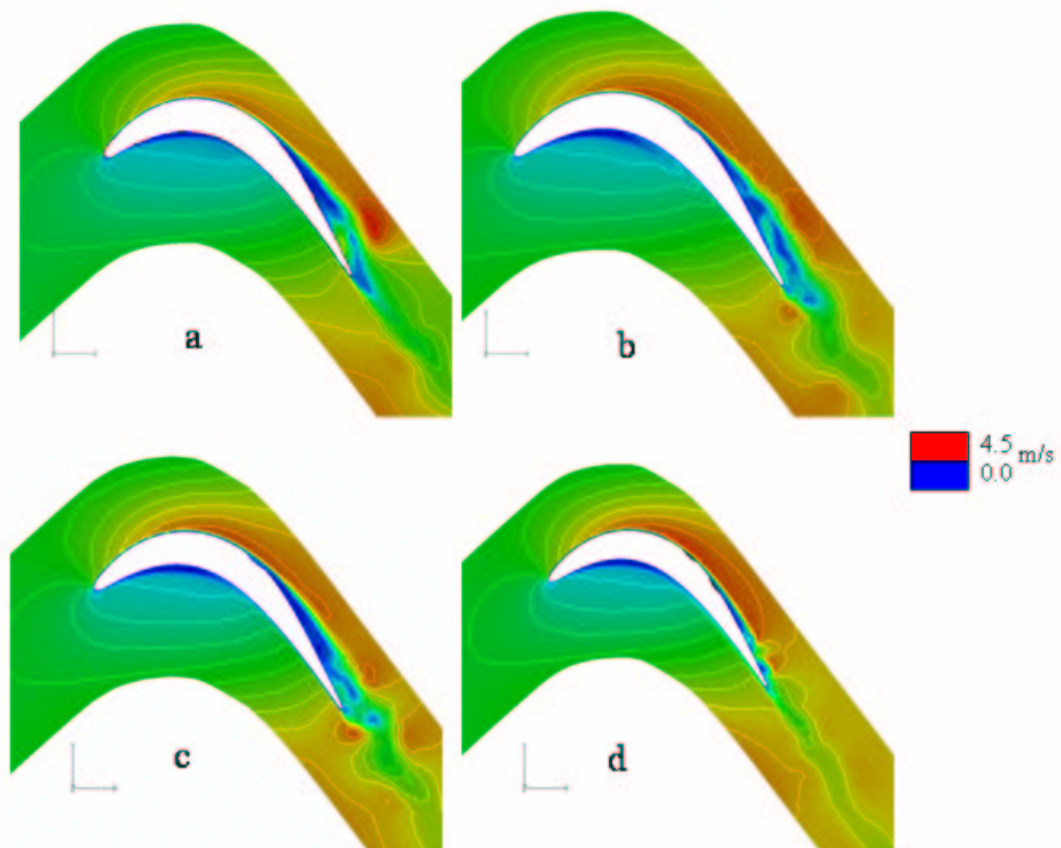


Figure 59. Velocity contours for each of the computational grids examined at 0.6 sec

By 0.2505 sec large scale changes in the multiple row case solution have ceased. The region between the upstream and downstream rows is fully attached. The vortex contained in the dimple at 65% of the axial chord seems to be more confined to the dimple (as will be shown in Section 4.3.3). For the single row cases, a large back flow region traveled upstream into the dimple. Figure 60 is a picture of the downstream edge of a dimple at 65% of the axial chord. Figure 60 shows a tightly wrapped vortex in the upstream dimple and attached flow aft the 65% axial chord dimple. It is believed that the vortex in the downstream dimples draws the flow downstream mitigating the large backflow region aft upstream dimple. Similar to the single row cases, the region aft the downstream row of dimples flows upstream into the dimples. The backflow region extends from the dimple to 83% of the axial chord. At this location, reattachment begins and the boundary layer is fully attached until 87% of the axial chord.

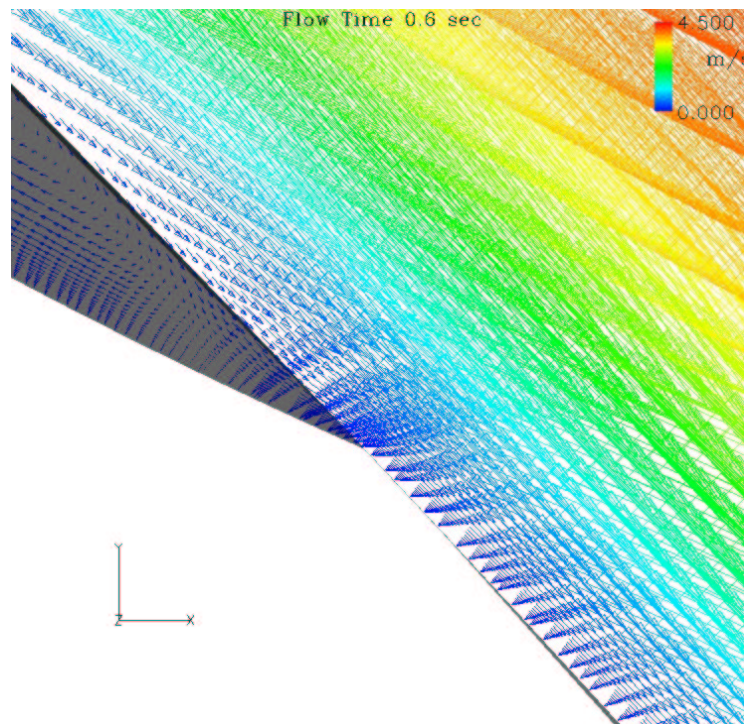


Figure 60. Velocity vectors near the upstream dimple on a computational Pak-B blade with dimples at 65% and 76% of the axial chord at Re 25k and 0% Tu

### 4.3.3 Streak Line Comparisons

Streak lines help draw a detailed picture of the complex flow field around the dimples. The vortex generated within the dimples has its axis aligned in the spanwise direction of the blade (Fig. 61a and b). The flow is drawn towards the center of the dimple before being expelled downstream down the dimple centerline. As discussed in Section 4.3.1, the vortex is contained within the dimple at 0.275 sec (Fig. 61a). As the solution matures, the vortex intensity grows and it becomes slightly larger than the dimple (Fig. 61b).

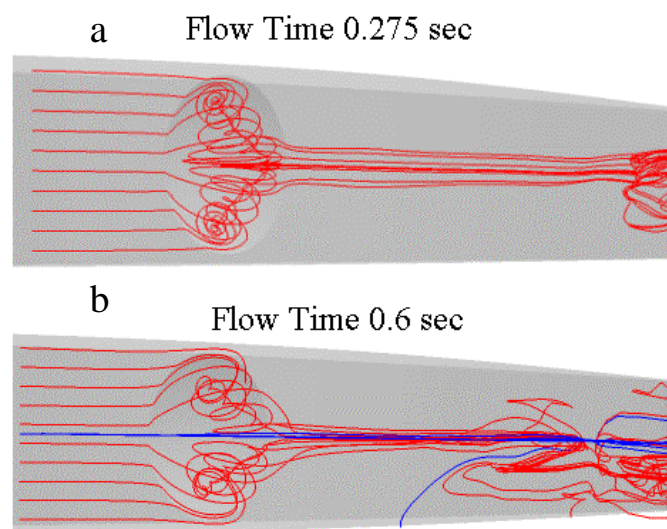


Figure 61. Streak lines through a dimple at 65% of the axial chord with 2 cm spacing at Re 25k and 0% Tu

Another perspective of this phenomenon is provided in Fig. 62. Figure 62 depicts a spanwise view of dimples at 65% of the axial chord. The dimple is represented by the gray region. Figure 62a shows the vortex is slightly above the blade surface acting like a bump in the flow. As the solution matures this vortex grows even larger becoming much larger than the dimple acting as a bump forcing the flow even further from the blade (Fig. 62b).

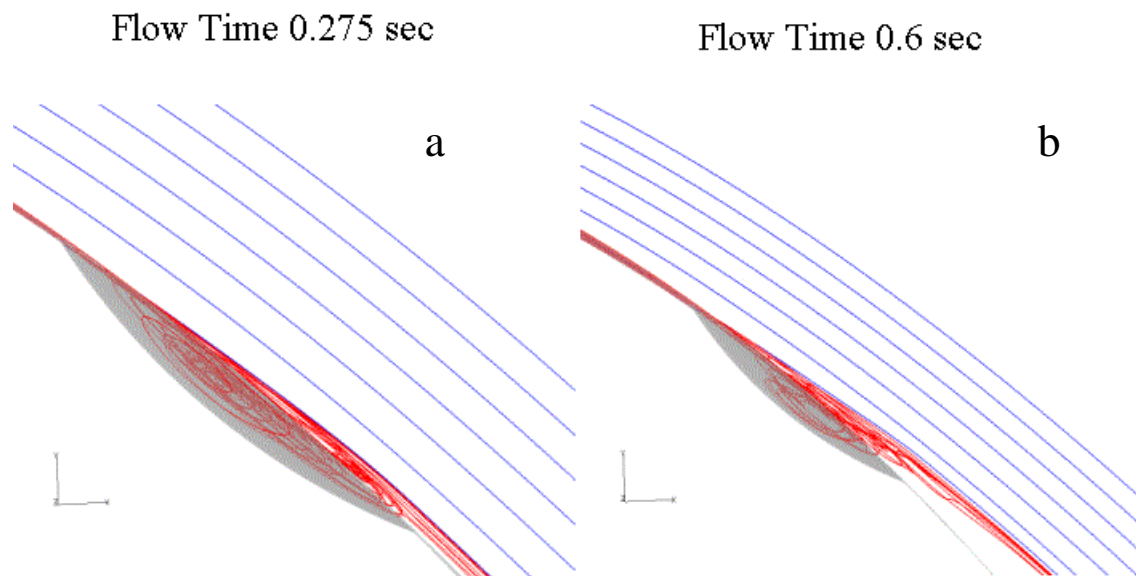


Figure 62. Vortex within dimple at 65% of the axial chord with 2 cm spacing at Re 25k and 0% Tu

The single row at 65% of the axial chord and 4 cm spacing was interesting because it gave insight into the spanwise influence of a single dimple. Figure 63 shows streak lines beginning at 55% of the axial chord. The streak lines show signs of being drawn towards the vortex core from 1 cm on either side of the dimple. As time passes the effect of the dimple vortex intensifies affecting a larger region of the blade span (Fig. 64). Figure 64a represents streak lines that were seeded upstream of the dimple, while Fig. 64b shows streak lines whose seeds are within the dimple.



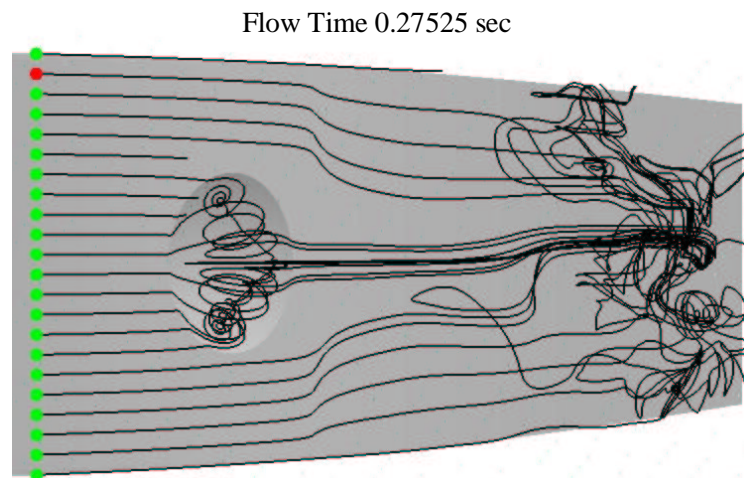


Figure 63. Surface streak lines on a computational Pak-B blade with dimples at 65% of the axial chord and 4 cm spacing at Re 25k and 0% Tu at 0.27525 sec

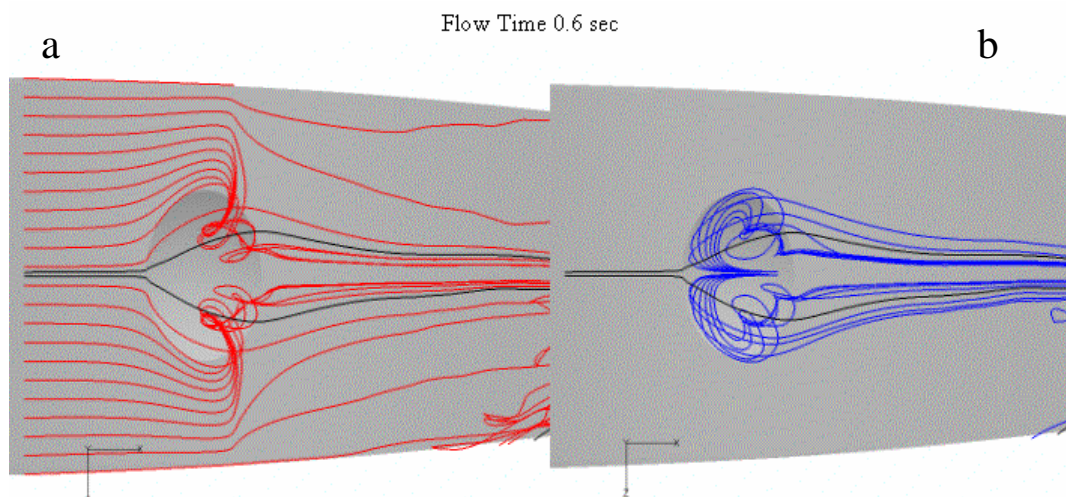


Figure 64. Streak lines on a computational Pak-B blade with dimples at 65% of the axial chord and 4 cm spacing at Re 25k and 0% Tu at 0.6 sec

Only those streak lines very near the blade surface actually enter the dimple. The vortex generated within the dimple ultimately acts like a bump on the surface as the vortex extends above the blade. Figure 65 illustrates the streak lines passing over the dimple bump and the streak lines from within the dimple working backwards upstream until they are expelled downstream.

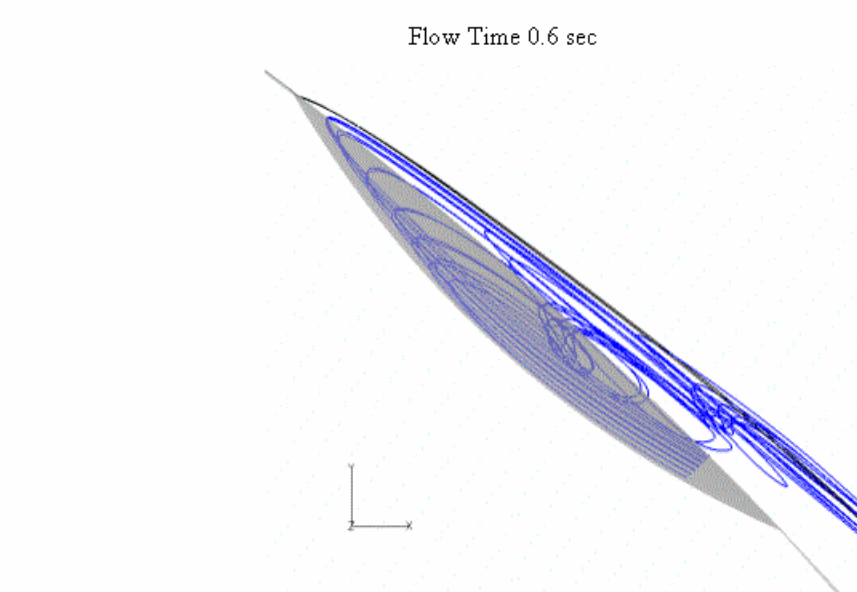


Figure 65. Streak lines above and within a dimple at 65% of the axial chord with 4 cm spacing

The multiple row case resolved a more tightly wrapped vortex in the upstream dimple resulting in fully attached flow until the upstream edge of the downstream dimples. The vortex in the 65% axial chord upstream dimple is fully contained within the dimple and does not act like a bump as in the single row cases (Fig. 66). The flow exiting the upstream dimple tends to wrap up towards the center of the dimple and flow downstream between and over the downstream dimples (Fig. 67b).

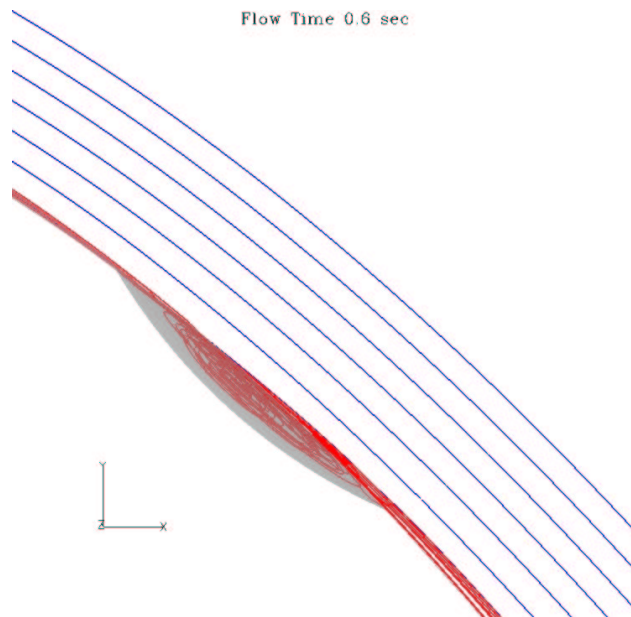


Figure 66. Streak lines at the 65% axial chord dimple on multiple row Pak-B computational blade at Re 25k and 0% Tu

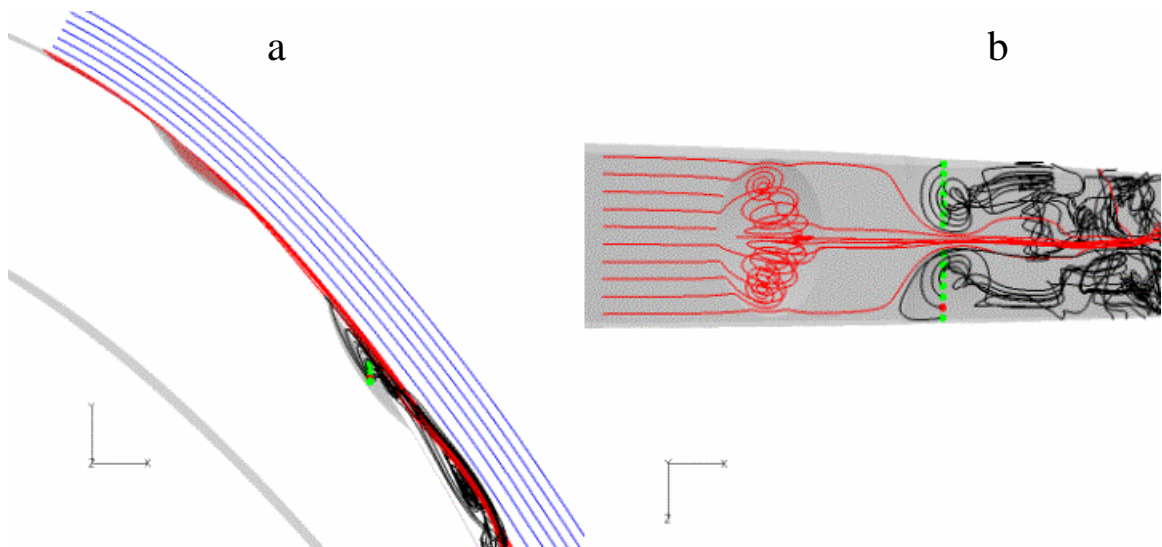


Figure 67. Streak lines on a computational Pak-B blade with dimples at 65% and 76% of the axial chord at Re 25k and 0% Tu at 0.6 sec

The most effective way to view the overall effect of dimples on the streak lines is to compare them side by side. Figure 68 illustrates the streak lines passing over the blade and a qualitative wake expanse of each of the CFD models. Figure 68a shows the streak



lines over an unmodified blade. There is a very large separation region covering much of the blade all the way to the trailing edge. Figure 68b-c depict the streak lines for the single row cases 2 cm and 4 cm, respectively. Again there is a fairly large separation region, but it is thinner than that for the unmodified blade and the flow exits at an angle closer to the design exit angle. Figure 68d shows fairly attached flow and a nearly on-design exit angle. It appears from these pictures that the boundary layer is most greatly affected by the multiple dimple case.

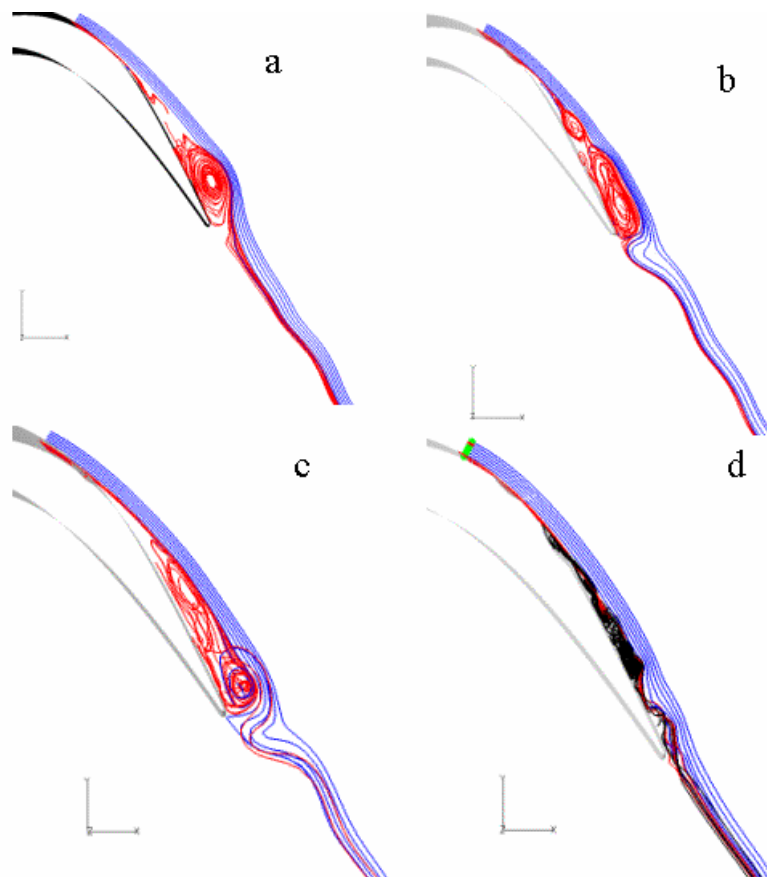


Figure 68. Streak lines showing exit angles over each of the CFD models examined at 0.6 seconds

#### **4.3.4 Computational Boundary Layer Measurements**

The boundary layer measurements for the Pak-B computational models provide a detailed picture of the velocity magnitudes near the blade surface. A full set of the boundary layer plots is contained in Appendix F. Figure 69 compares the boundary layer profiles for the unmodified blade and the 3 dimpled cases.

The clean blade profile shows a slight inflection point at 67.2% of the axial chord indicating that separation has already begun. By 73.0% of the axial chord a large separation bubble has formed. The separation bubble continues to grow down the rest of the blade. At 89.8% of the axial chord the boundary layer is thicker than 20 mm. This is a result of large vortical structures shedding from the suction side of the blade.

The boundary layer profiles for the single row cases were similar to one another. For the single row cases a separation bubble was evident at 73.0%, and was very pronounced at 79.3% of the axial chord. At both of these locations the thickness of the separated region is about 60% of the unmodified blade. By 89.8% of the axial chord the boundary layer thickness is greater than 15 mm for the single row case. This is a 5 mm improvement over the unmodified case.

The multiple row case shows that the boundary layer can be significantly decreased by an additional row. A slight inflection point is seen at 73.0% of the axial chord, but a substantial separation bubble is not clear until 79.3% of the axial chord. The boundary layer is only 10 mm thick at 89.8% of the axial chord; half as thick as the unmodified blade.

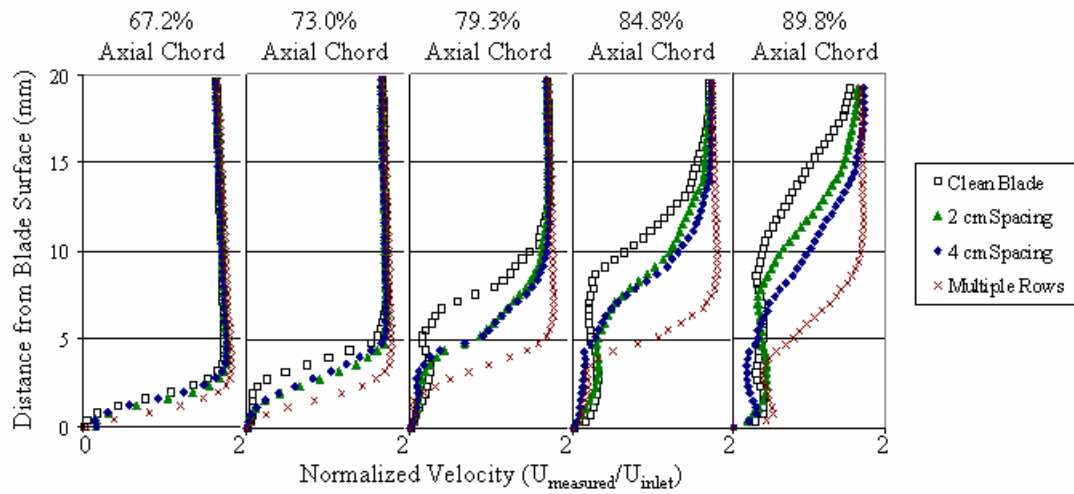


Figure 69. Time averaged boundary layer profiles for computational Pak-B blades at Re 25k and 0% Tu

#### 4.3.5 Computational Wake Loss Measurements

Wake loss measurements yield information regarding the overall blade efficiency. As seen in Fig. 70, the loss profile for the unmodified blade extends slightly beyond the grid domain. The other three cases produce a loss profile that are contained within the grid domain.

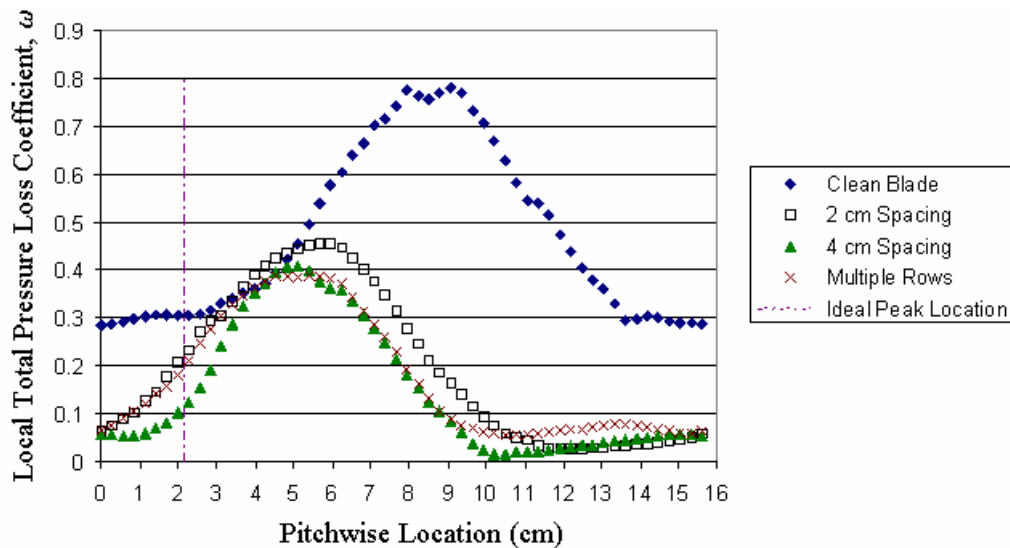


Figure 70. Time averaged wake loss profile for computational Pak-B blades at Re 25k and 0% Tu

Figure 70 clearly depicts the shift toward the pressure side of the adjacent blade (an outward shift) of the loss profile as separation increases. The unmodified blade has a peak loss of 0.77 at 9.08 cm. Extending a vector from the trailing edge of the blade to the downstream total pressure measurement location determines that the ideal peak loss location should occur at a pitchwise location of 2.14 cm. Each loss profile has a degree of outward shift, but clearly the unmodified blade contains the greatest shift at 6.94 cm. Placing dimples at 65% of the axial chord with 2 cm spacing returned a peak loss of 0.46 at 5.68 cm. The multiple row and singled dimple at 65% of the axial chord with 4 cm spacing had similar profiles. The single dimple case had a slightly narrower profile, but both peaks were at about 0.40 and 5.10 cm, an outward shift of just 2.96 cm, less than half the shift associated with the unmodified case.

The expanse of the loss profile is reduced for the modified blades as well. The unmodified blade had a loss profile of 14 cm. The loss profile associated with a blade that has a single row of dimples at 65% of the axial chord with 2 cm spacing was 11 cm. The multiple row case resulted in a loss profile 10 cm wide, and the 4 cm single row case had a 9 cm wide loss profile. The reduction in loss profile expanse directly correlates to the increased loading on the blade.

Integrating the curves in Fig. 70 the total loss over the profile is determined. Normalizing the integrated total pressure loss by the pitch (15.75 cm) yields an average total pressure loss coefficient. Figure 71 shows the average total pressure loss coefficient for each case studied. Each dimpled case improved over the unmodified case by 58%-68%. The average loss coefficients for the dimpled blades are very close to one another with the 4 cm spaced singled dimple blade having a slight advantage.

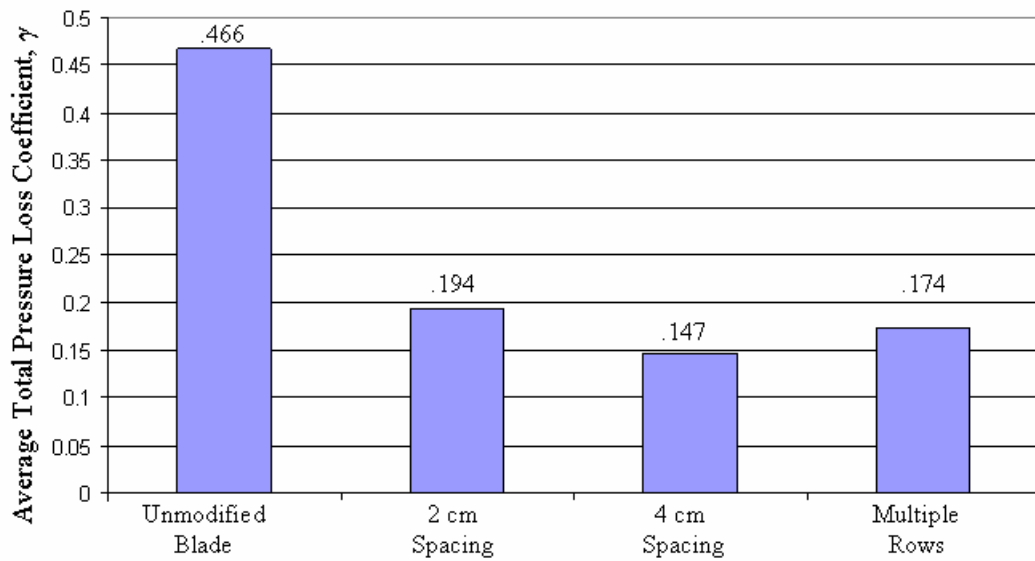


Figure 71. Computational average total pressure loss coefficients at Re 25k and 0% Tu

Figure 72 is provided to prove that a reasonable time average of the flow field has been determined. Plotted are two curves averaged over the entire time solution at different averaging intervals. The fact that the curves are nearly identical indicates that an time independent flow field has been achieved.

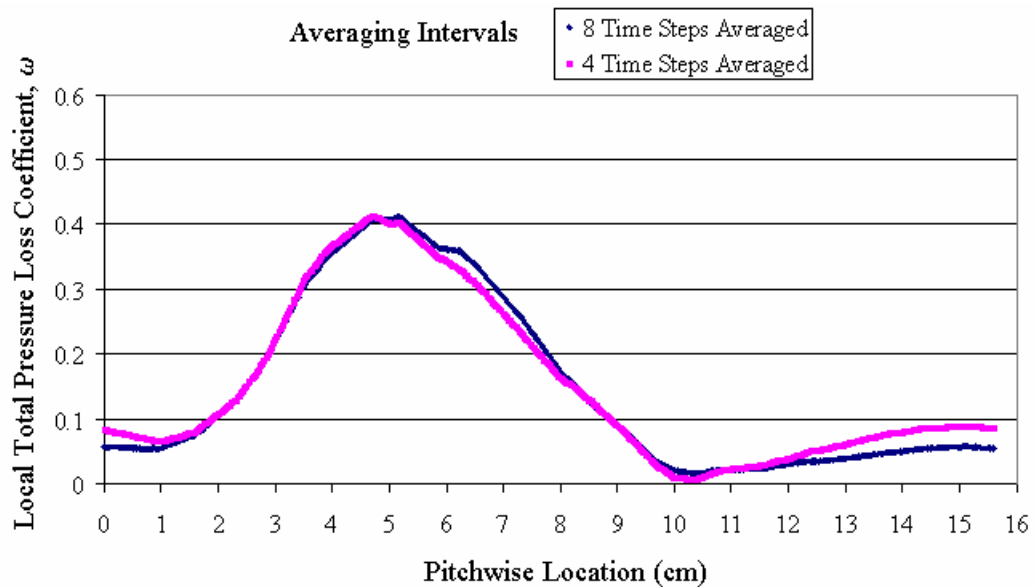


Figure 72. Wake loss calculations over two different averaging intervals

#### **4.4 Summary and Conclusions of Computational Research**

The CFD efforts showed that dimples dramatically reduce the loss coefficient on a Pak-B blade at  $Re = 25k$ . The boundary layer separation was significantly reduced for each of the modified blades examined. As the boundary layer separation is reduced, the blade efficiency was increased.

The separation location plots showed that the unmodified blade separated between 64.5% and 68.5% of the axial chord. This separation location seemed to be periodic with a period of 0.09 sec. The primary separation location was not affected by the single row cases. The reattachment location for these cases was affected, however, resulting in reattachment attempts being made as far upstream as 76% of the axial chord. The multiple row case pushed the onset of separation back to 73% of the axial chord.

The velocity field visualization provided more insight into the separation and reattachment locations. Also it is clear from the velocity contour plots that the wake region is dramatically reduced for the modified cases.

Investigation of the streak lines confirmed that the axis of the vortex contained within the dimples is oriented in the spanwise direction. The single row cases resulted in a vortex larger than the dimple itself. The vortex in this case acted as a bump; forcing the freestream flow around the dimple. The vortex seemed to draw flow upstream creating a strong back flow region directly behind the dimple. The multiple row case resulted in a slightly different vortex geometry. The upstream dimple had a vortex fully contained within the dimple. The region directly behind the dimple at 65% of the axial chord was fully attached. The dimples at 76% of the axial chord seemed to draw the flow downstream thus forcing the upstream vortex to remain contained in the dimple.

Boundary layer measurements mapped the average velocity magnitudes along a normal vector to the blade. These measurements clearly showed the separation bubble thickness. Each of the dimpled cases improved thickness of the separated region over the unmodified blade. The multiple row case returned the greatest reduction in the boundary layer thickness from the unmodified case by 50% at 84.8% and 89.8% of the axial chord.

The wake loss measurements provided a quantitative means of measuring the blade efficiency. Each of the modified cases resulted in a dramatic reduction in the average total pressure loss coefficient. The single row case with 2 cm dimple spacing reduced the loss coefficient by 58%. The single row case with 4 cm dimple spacing reduced the loss coefficient by 68%, and the multiple row case returned a 63% improvement in loss coefficient.

From the boundary layer measurements and streak line comparisons the multiple row case appeared to provide the greatest advantage over the unmodified blade. The wake loss measurements; however, showed that the single row case with 4 cm dimple spacing had a slight advantage in blade performance improvement. Although, each of the dimple patterns improved the blade performance over the unmodified blade, none of the dimple patterns investigated is decidedly better than the others. It is concluded that a single row of dimples at 65% of the axial chord with 4 cm dimple spacing was the best pattern of the patterns considered because the benefits are comparable to the other patterns with minimal machining.

## **CHAPTER 5. COMPARISONS BETWEEN EXPERIMENTAL & COMPUTATIONAL RESULTS**

The usefulness of the computational fluid dynamics study is fully realized when compared to experimental data. In this research boundary layer measurements were made both computationally and experimentally. Likewise, plots of local total pressure loss coefficients were obtained through both mediums. Comparing and contrasting the results will yield information about the effectiveness of the computational schemes and help direct research in the future.

### **5.1 Boundary Layer Measurement Comparisons**

Boundary layer comparisons are seen in Figs. 73 to 75. For all three cases the computational and experimental results agree very well at 67.2% of the axial chord. This is attributed to the fact that this is far upstream where separation is just beginning. The CFD solver is laminar and therefore should resolve any regions of the flow where the flow can be considered laminar. From this information it is clear that forcing laminar behavior upstream of the 67.2% axial chord location is a good assumption as oppose to applying turbulent models throughout the domain. Unfortunately, as the flow separates the physical dynamics become much more complex and a laminar solver cannot accurately resolve the flow field.

Figure 73 represents the data from the unmodified blade. Clearly, the CFD predicts a large separation region as expected. The solver seems to over estimate the thickness of the separation bubble. It is believed that as separation begins the vortical



structures that form help induce a degree of turbulence that leads to the slight suppression of the separation bubble. The CFD simulation cannot resolve this physical phenomenon because the grid lacks the require cells to resolve the smallest turbulent length scales. Turbulent modeling attempts to numerically induce turbulent terms without an extremely large number of cells. The current turbulent models fail to accurately predict the transitional nature of the low Reynolds number flows studied in the current research, and therefore a laminar solver is more accurate, however, still less than perfect.

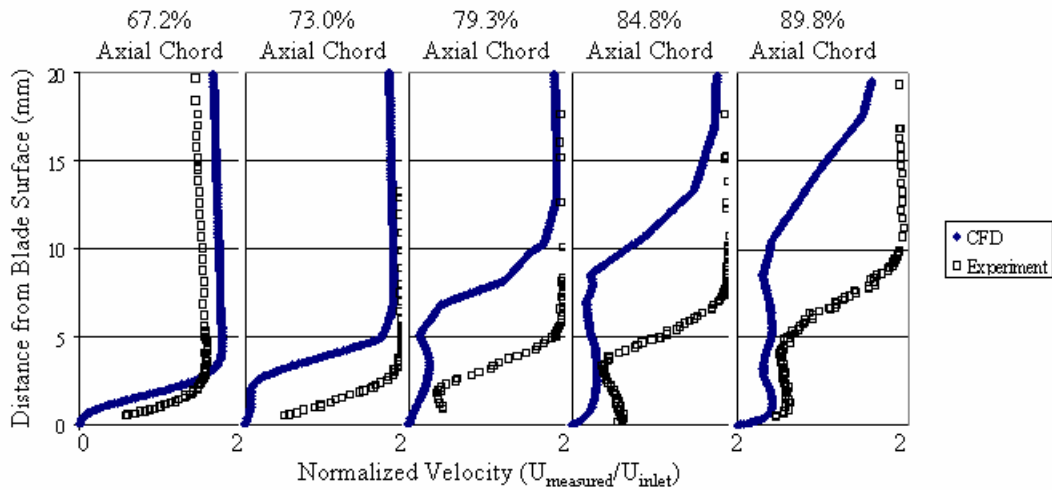


Figure 73. Boundary layer comparisons between CFD and Experiment for an unmodified Pak-B blade at Re 25k and 0% Tu

Figures 74 and 75 depict the boundary layer comparisons for the single row case with 2 cm and 4 cm dimple spacing. Qualitatively, the solutions appear to agree much better than they did for the unmodified case. In both cases, the CFD and experiment agree well for 67.2% to 79.3% of the axial chord. For these three chordwise locations, the extent of the separation bubble and slope of the boundary layer as it approaches the freestream are nearly equivalent.

At 84.8% and 89.8% of the axial chord, however, the correlation fails. The laminar solver cannot adequately handle the separated flow. The dimple geometry helps to delay the onset of separation and vortex shedding, thus making the CFD more accurate over a larger portion of the blade surface.

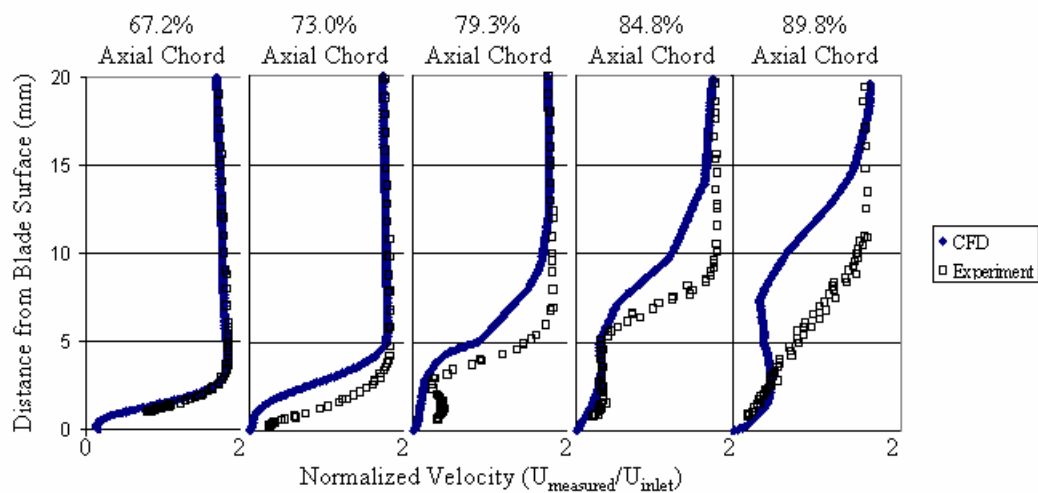


Figure 74. Boundary layer comparisons between CFD and Experiment for a Pak-B blade with a single row of dimples at 65% of the axial chord with 2 cm spacing at Re 25k

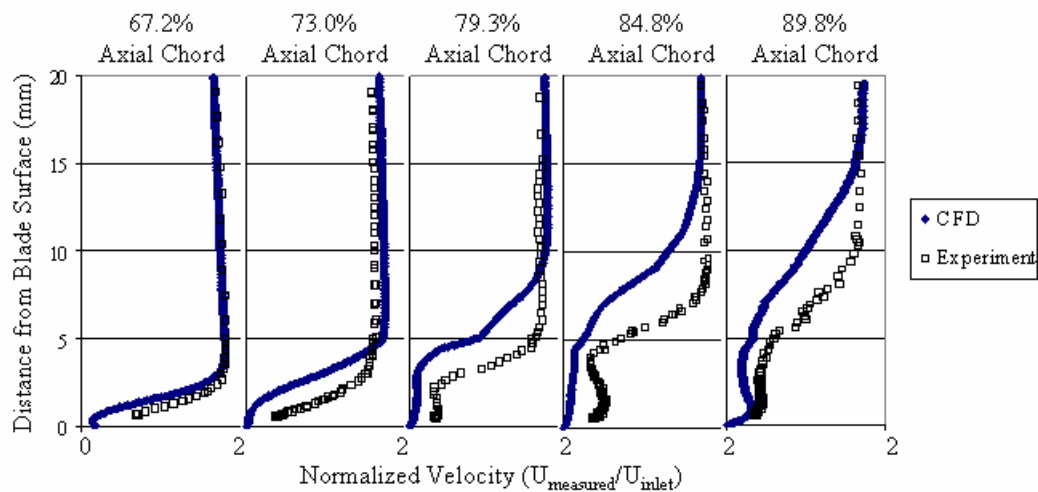


Figure 75. Boundary layer comparisons between CFD and Experiment for a Pak-B blade with a single row of dimples at 65% of the axial chord with 4 cm spacing at Re 25k

## 5.2 Wake Loss Comparisons

A laminar solver is not conditioned to handle the complexity of a large separation region as seen on the Pak-B blade. A loss study was performed to see if it could possibly resolve the bulk performance of the turbine blade. Comparing the average total pressure loss coefficients proved to be a meaningful way to determine the ability of CFD to predict blade efficiency. Figure 76 compares the average total pressure loss coefficients for the cases considered. Certainly, the improvement trends are the same for both the CFD and experimental research. Each dimpled case reduces the loss coefficient when compared to the unmodified case, but no dimpled case was decidedly better than the others. The difference between the average total pressure loss coefficient for the unmodified blade is 22.6%, for the 2 cm spacing it is 20.5%, for the 4 cm spacing it is 41.3%, and for the multiple row case it is 28.3%. The difference between the CFD and experiment is attributed to the fact that the CFD solution was forced to be laminar failing to capture relevant turbulent flow characteristics.

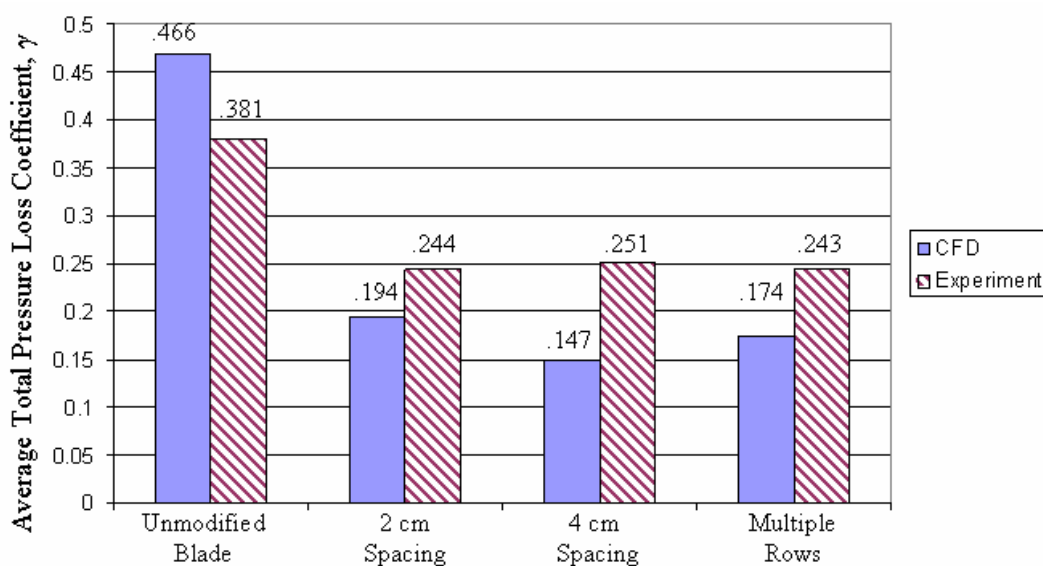


Figure 76. Average total pressure loss coefficients for each of the cases studied

The relative shift in wake loss profile is shown in Fig. 77. The CFD and experimental results are similar. The wake profile shifts 3.5 cm toward the suction side of the adjacent blade with the addition of dimples at 65% of the axial chord with 2 cm spacing.

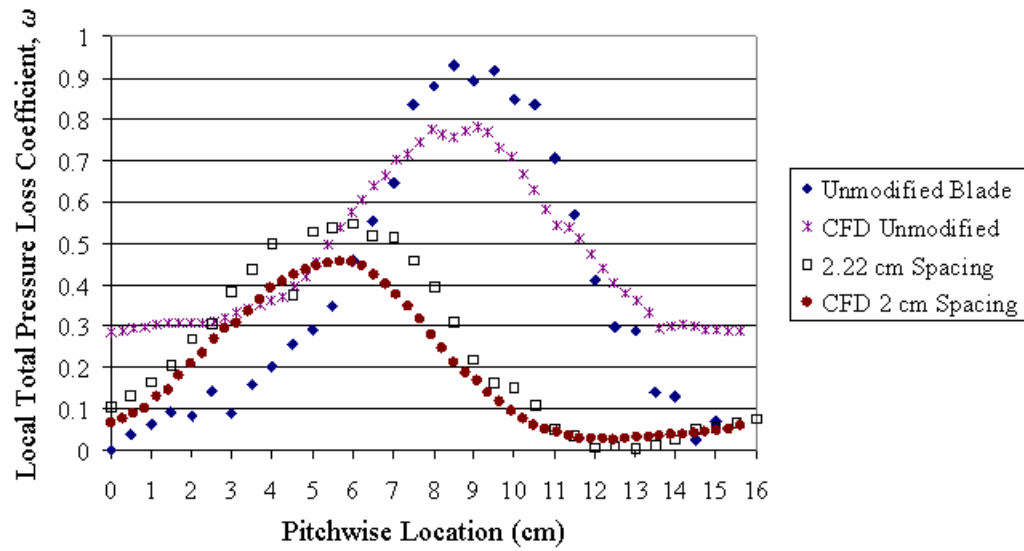


Figure 77. Total pressure loss profile comparisons between CFD and experimental results.

## **CHAPTER 6. SUMMARY AND RECOMMENDATIONS**

The low-pressure turbines in aircraft flying at high altitudes and low velocities experience low Reynolds number conditions. The effect of the large turning angles associated with the low-pressure turbine blades operating at low Reynolds numbers is laminar flow separation. Mission essential systems, such as Global Hawk, are impacted by the problem of boundary layer separation resulting from low Reynolds number flows. Naturally, the decreased loading associated with the separated flow results in a dramatic reduction in the turbine efficiency. Decreasing the turbine efficiency directly results in limiting the aircraft range, operating ceiling and extractable electrical power from the turbine.

Passive boundary layer separation control techniques were investigated using a Pratt and Whitney Pak-B LPT blade. Passive separation control techniques allow for relatively easy application to existing hardware without adding additional weight. Further, passive separation control techniques do not require additional power. Dimples at 65% of the axial chord have been shown to reduce the losses associated with boundary layer separation [Rouser, 2]. Three dimple patterns have been applied to a Pak-B blade to determine their relative effectiveness on the improvement of blade efficiency. The effectiveness of the dimple patterns was investigated both experimentally and computationally.

Experimentally, the three patterns considered were a single row at 65% of the axial chord with 2.22 cm center-on-center dimple spacing, the same row with 4.44 cm center-on-center dimple spacing and a multiple row pattern involving 4.44 cm center-on-

center dimple spacing at both 65% and 76% of the axial chord. The multiple row case was a chevron pattern. That is to say the downstream row was placed such that the dimple at 65% of the axial chord was between two downstream dimples. Each pattern was compared to an unmodified blade.

Computationally, the three patterns considered were a single row at 65% of the axial chord with 2 cm center-on-center dimple spacing, the same row with 4 cm center-on-center dimple spacing, and a multiple row case with a row of dimples at 65% and 76% of the axial chord in a chevron pattern with 2 cm center-on-center dimple spacing. Each pattern was compared to an unmodified blade.

The experimental work was performed in a low-speed, draw down wind tunnel containing an 8 blade linear cascade in the test section. Measurements were made on each of the dimple patterns as well as the unmodified blade at Reynolds numbers of 25k, 45k and 100k at freestream turbulence levels of 1% and 4%. Surface pressure, boundary layer velocity, wake velocity and wake loss measurements were made to document changes in the flow field due to dimple pattern and assess any improvement in turbine efficiency.

The computational fluid dynamics study afforded a detail picture of the flow field. Further, flow structure development could be watched as the solutions were run time-accurate. The CFD models were 3-D and the flow field was resolved with a laminar solver at Re 25k. Analysis of separation location, velocity field development and streak line structure provided a means by which different patterns can be compared qualitatively. Boundary layer and wake loss measurements enabled quantitative

comparisons between dimple patterns, as well as, a direct comparison to the experimental results.

The experimental result showed that each of the modified blades returned a substantial improvement over the unmodified blade. Each dimple pattern improved the loss coefficient by 35% at  $Re$  25k and 1%  $Tu$ . Further evidence is shown that inducing turbulence into the flow field does not radically affect the separation location. On the other hand, the reattachment location is dramatically affected by the turbulent flow associated with the dimples.

The experiment showed that no pattern considered performed substantially better than the others. Realizing that dimples spaced 2.22 cm apart or 4.44 cm apart returned the same loss reduction leads to the conclusion that the spanwise influence of each dimple extends at least 1 cm on either side of each dimple. Since each of the dimple patterns considered performed in the same manner the best solution is the single row at 65% of the axial chord with 4.44 cm spacing. This pattern retains the dimple advantage with minimal machining.

Computational results at  $Re$  25k at 0%  $Tu$  show that the separation location on the unmodified blade oscillates between 64.5% and 68.5% of the axial chord with a frequency of 11 Hz. The modified cases show that the dimples create a spanwise vortex. In the single row cases, this vortex extends above the blade acting like a bump on the surface. In the multiple row case, the vortex is contained within the dimple and the primary separation location is delayed to 73% of the axial chord. CFD boundary layer and wake loss measurements showed that the modified blades improve the loss characteristics of the unmodified blade. The boundary layer measurements showed the

modified cases reduce the separation bubble thickness by as much as 50% for the multiple row case at 84.8% and 89.8% of the axial chord. The wake loss measurements showed that the average total pressure loss coefficient was reduced by 58% to 68%. As with the experimental results, each of the modified cases improves the unmodified blade dramatically, but no pattern significantly out performed the others. Therefore, the single row of dimples at 65% of the axial chord with 4 cm spacing is the best choice for boundary layer separation control.

Comparisons between the experimental and computational boundary layer and wake loss measurements showed that the CFD simulations return the same trends as the experiment. Further, the CFD boundary layer results agreed well with the experiment at 67.2% of the axial chord. The implication here is that the CFD performs well as long as the flow was nearly attached. Once separation occurred, the quality of the correlation between the experimental and the CFD results depreciated, although the trends were still present. Similar results were found during wake loss comparisons. The trends were the same but the numerical values differed between 21% and 41%. Although a fully turbulent solution is not prudent as shown by Rouser [2], some laminar to transition turbulent modeling is required to capture the flow, particularly downstream of the separation point.

There is still a lot of room for investigation of this problem. Correlations between the CFD simulations and the experiment provide support for the idea that CFD can be a design tool to direct the experimental research. Computational experiments should be performed with turbulent modeling to accurately define the flow field in the separated regions. Attempts to turn on turbulent modeling within the separation zone should be



made to try to improve the boundary layer mapping. Also a large eddy simulation (LES) or a detached eddy simulation (DES) solution should be attempted to see if a more physically accurate solution can be achieved. Further, grid independence should be investigated to ensure the results do not possess grid artifacts. Finally, rigorous efforts should be made to prove conclusively the solutions are fully time independent.

Experimentally, the effect of a single dimple should be determined. Placing a single dimple on the blade and measuring the boundary layer at various spanwise and chordwise locations behind the dimple would define the expanse and intensity of a single dimple effect. This would help determine the required spanwise spacing of a row of dimples. Once this spacing is known, further experiments can be performed to locate the optimum chordwise location. Multiple rows should not be ruled out at this point. Further investigation into the relative chordwise spacing between the two rows is necessary.

In conclusion, this research provided information about the spanwise effect of dimples for boundary layer separation. Advances in the parameterization of dimple patterns are required to optimize the dimple effectiveness. Clearly, the dimples provide a passive means of controlling boundary layer separation. Determining the exact dimple pattern to totally reduce the boundary layer separation will dramatically improve turbine efficiency. This will allow for potentially significant improvements in aircraft mission effectiveness and capabilities.

## APPENDIX A. Instrumentation Interface

Figure 78 illustrates the instrumentation system implemented in the current research to collect and process the data. The primary controller is a Dell Pentium 4 personal computer (PC). Installed in the PC is an MXI-3 fiber-optic interface board that is connected to a National Instruments PXI 1010 chassis. Three PCI cards are also contained in the Dell to drive the traverses and collect data from the hot films and the X-film.

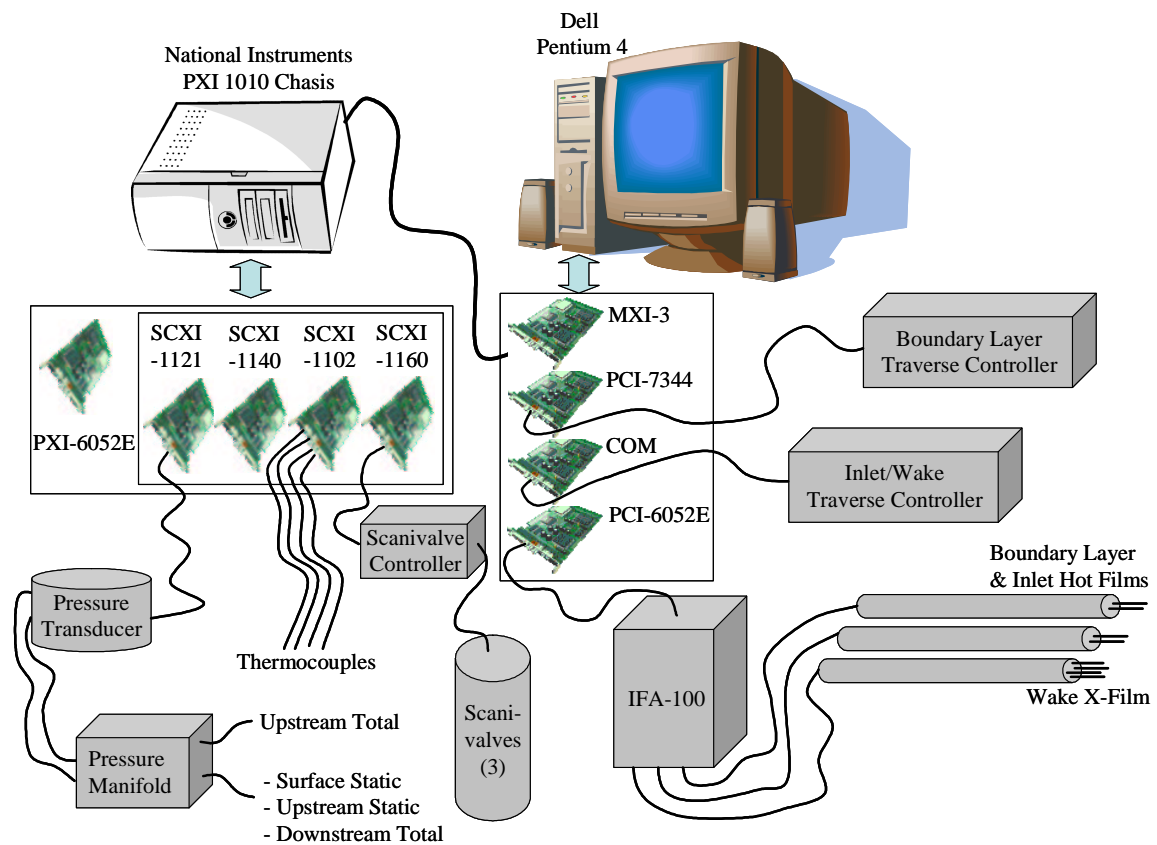


Figure 78. Instrumentation Schematic [Rouser, 2]

An IFA-100 receives a direct signal from the hot-film elements. Initially, the IFA-100 needed to be set-up. Once the IFA-100 is balanced, the hot films can be calibrated. The single element hot films utilize a non-dimensional curve fit between

Nusselt and Reynolds numbers for calibration, as described by Bruun [42]. The heat transfer across the element is determined by balancing a Wheatstone bridge within the IFA-100. The Nusselt number is related to the heat transfer. The heat transfer is a function of velocity. A non-dimensional relationship is as follows:

$$\text{Nu} = C + D (\text{Re}^{0.45}) \quad (19)$$

where Nu is Nusselt number,  $C$  is the curve intercept on the Y-axis and  $D$  is the slope. The exponential value of 0.45 is chosen to provide an acceptable curve fit for measuring low speed flow [Rouser, 2]. Equation 19 yields a correlation between voltage and velocity. The calibration was performed using a TSI Model 1127 calibration stand and the Druck LPM 5481 pressure transducer. Detailed calibration procedures are outlined in Appendix B.

The boundary layer traverse, a National Aperture, Inc. motorized 5.08 cm MM-3M micro traverse, is controlled through the PCI-7344 card inside the PC. It has a movement resolution of 20157.4 steps per cm. The traverse position encoder provides a linear spatial resolution of  $\pm 5.08 \times 10^{-5}$  cm. The traverse position is controlled and powered by a National Aperture, Inc. MC-4SA servo amplifier, which is in-turn connected to the PCI-7344 card.

The main 3 axial Velmex traverse sits on top of the tunnel, and positions the downstream Kiel probe and X-film. This traverse is controlled through the PC via a standard RS 232 Com card. The power and control component for the main traverse is a Velmex V-9000 controller combined with a Sony LH61 digital position display accurate to  $\pm 0.005$ . The TSI, Inc. IFA-100 Flow Analyzer sends the voltages returned from the

hot film and X-film directly to the PC through a National Instruments PCI-6052E A/D card which has a 16 bit resolution and a 333 ks/s sampling rate.

A PXI-6052E A/D board with 16-bit resolution over  $\pm 10$  Volts is contained within the PXI 1010 chassis. The A/D board is connected to an SCXI cluster. A thermocouple board designated SCXI-1102 is connected to the four thermocouples. Further, an SCXI-1160 relay controller included in the SCXI cluster commands three Scanivalve controllers. The pressure transducer is a Druck LPM 5481 connected to an SCXI-1121 signal-conditioning card. The Druck's range is -0.2 to 0.8 in H<sub>2</sub>O. It requires a 10-30 volt power supply and outputs 0-5 volts. One side of the pressure transducer always receives the inlet total pressure from the upstream pitot-static probe. The Scanivalves determine whether the input to the other side of the Druck is inlet static pressure, exit total pressure, or surface static pressure. The two inputs received allow for differential pressure readings.

The four thermocouples connect to the PXI 1010 chassis through the SCXI-1102. The SCXI-1102 is used as a signal conditioner, and connects to an SCXI-1303 thermocouple block. The SCXI-1303 uses a thermistor for a cold junction temperature reference. Differential measurements are made between thermocouples and the thermistor inside the SCXI-1303. Voltages are relayed through the PXI 1010 chassis to the A/D board in the PC. The computer then converts the voltages to temperatures.

## **APPENDIX B. Calibration Procedures**

The pressure transducer and each of the hot-films used in this research require calibration. The pressure transducer needed to be calibrated first since it is used during the calibration of the hot films.

### **B.1 Pressure Transducer Calibration**

#### Hardware Setup

1. Carefully unpack deadweight pressure calibration device
2. Set up pressure calibrator following the instruction manual [43]
3. Connect output from positive pressure reference on calibrator to high side (+) of transducer
4. Unhook or vent low side of transducer

#### Software Setup

1. Open LabView
2. Open 'Pressure Cal' vi
3. Set Xdcr Ch (1) to '1' (first input on MIO)
4. Set device to '2' (MIO board controlling SCXI)
5. Set 'Pxdcr Ch' to 'sc1 ! md1 ! 0' (SCXI device 1, module 1, channel 0)
6. Select sample rate and number (recommend 1000Hz max & 30,000 samples min)

#### Calibration Procedure

1. Place reference weight for max desired pressure on reference
2. Run vi and enter data filename
3. Enter reference pressure setting and hit OK
4. Wait for data acquisition

5. Change out reference weight to reduce pressure
6. Allow approximately 15 seconds for pressure to stabilize
7. Press 'TAKE DATA' button to take next data point
8. Repeat from step 3 until data taken at minimum reference pressure
9. Shut off reference and vent both sides of transducer (zero pressure point)
10. Press 'TAKE DATA' button
11. Enter '0' for pressure setting and hit OK
12. Wait for data acquisition
13. Press 'DONE DO FIT' button
14. Record calibration constants (Slope, Intercept, MSE). Flag with RED ink.

#### Hardware Takedown

1. Disconnect and repack pressure calibrator
2. Reconnect instruments to transducer  
Reset valves on transducer (vents closed, measure open)

### **B.2 IFA-100 Setup Procedure**

Begin by ensuring that you have proper cables; Anemometer channel is set for proper length and sensor type; Anemometer is given sufficient time to stabilize temperature (30 min.).

*First, record identifying information for the probe in the notebook.*

#### Measure Cable Resistance

1. Install the shorting plug(s) in the end of the probe holder to be used during testing.
2. Press RES MEAS to select the NULL DISPL mode.
3. Adjust the OPERATE RES knob to zero the display (balance the bridge)
4. Press RES MEAS to select the DISPL RES mode. The measured cable resistance will be displayed - record this value.

5. Press ENTER to store the value of the cable resistance in the IFA-100 Memory.

#### Measure Probe Resistance And Calculate the Overheat Ratio

1. CAREFULLY install the probe to be calibrated in the probe holder. Tighten the probe holder into the probe holder traverse of the calibration jet so that the probe is: less than one jet diameter (~0.25in.) from the exit of the jet, centered over the jet, and perpendicular to the flow.
2. With the pressure tap disconnected, or both sides of the transducer manifold vented, obtain a zero intercept from the pressure transducer using the 'Continuous Ptrans Scan' vi.
3. Connect the pressure tap from the calibration jet to the pressure transducer.
4. Open the valve on the calibration jet until the 'Continuous Ptrans Scan' vi reads 0.05 in H<sub>2</sub>O.
5. Press RES MEAS to select the NULL DISPL mode and adjust the OPERATE RES to zero the display (balance the bridge).
6. Press RES MEAS to select the DISPL RES to display the measured probe resistance - record this value.
7. Calculate operating resistance:  
$$\text{Operating Resistance} = ((\text{Probe Resistance} - \text{Internal Probe } \Omega (R_{\text{int}})) * \text{OHR}) + R_{\text{int}}$$

where:           OHR = 1.5 for a film probe (- 10/- 20)  
                  OHR = 1.8 for a wire probe (- T1.5)
8. Press OPERATE RES and adjust the OPERATE RES knob until the display value matches your calculated value.
9. Press ENTER to store the value.

#### Adjust The Bridge Frequency Compensation

1. Press BRIDGE COMP and adjust the BRIDGE knob until the displayed value matches the correct value where:  
$$\text{BRIDGE COMP} \cong 115 \text{ for a film probe (- 10/- 20)}$$
$$\text{BRIDGE COMP} \cong 35 \text{ for a wire probe (- T1.5)}$$
2. Press ENTER to store the value.
3. Increase the calibration jet flow to the maximum expected flow while testing.

4. Press RUN/STANDBY to go to “RUN” mode.
5. Turn the CABLE knob fully CCW. If the OSC light is off, then go to step 7.
6. Turn the CABLE knob CW until the OSC light goes out. Go to step 7.
7. Turn the CABLE knob CW until the OSC light turns on. Turn the CABLE knob CCW until the OSC light turns off. Frequency Compensation is roughly adjusted.
8. Connect the signal out to an oscilloscope to monitor the OUTPUT. Set the oscilloscope to 10 mV / div.,  $\cong 200\mu\text{Sec}$  / div. and normal trigger.
9. Press TEST SIGNAL and adjust the CABLE knob until a desirable waveform without oscillations is visible on the oscilloscope.
10. Press TEST SIGNAL to turn the test signal off.

### **B.3 Single-Element Hotwire/Hotfilm Calibration**

#### Hardware setup

1. Verify calibration of pressure transducer if required
2. Connect hotwire/hotfilm calibrator pressure tap to pressure transducer high side
3. Vent both sides of pressure transducer
4. Blow dust out of calibrator by opening valves fully
5. Shut valves
6. Mount hotwire/hotfilm in calibrator with sensor centered over nozzle perpendicular to flow
7. Follow instructions for IFA100 setup

#### Software Setup

1. Open LabView
2. Open ‘Continuous Ptrans Scan’ vi.
3. Set device to ‘2’ (MIO board controlling SCXI)
4. Set ‘Pxdcr Ch’ ‘sc1 ! md 1 ! 0’



5. Input latest calibration constants (slope and intercept) for transducer
6. Open 'Hot wire Cal' vi
7. Set dewpoint and barometric pressure
8. Set number of samples and sample rate
9. Set DAQ channel to correct MIO channel (depends on IFA channel – Check IFA note or wiring)
10. Enter probe parameters from IFA-100 setup procedure

#### Calibration Procedure

1. Verify both sides of the pressure transducer are vented “zero pressure”
2. Run 'Continuous Ptrans Scan' vi
3. Obtain current zero intercept from 'Continuous Ptrans Scan' vi, and enter this value in the 'Hot wire cal' vi
4. Stop 'Continuous Ptrans Scan' vi
5. Open valves on calibrator slightly to begin flow over hotwire/hotfilm
6. Set high side of pressure transducer to measure
7. Set appropriate IFA HW channel to “RUN”
8. Run 'Hot wire cal' vi
9. Enter data filename. First data is taken as soon as file is created.
10. Open valves on calibrator until jet is at the maximum desired calibration velocity  
DO NOT EXCEED TRANSDUCER MAXIMUM PRESSURE
11. Wait for 'Taking Data' light to go out
12. Reduce calibrator flow to next desired calibration point
13. Allow approximately 15 seconds for pressures to stabilize
14. Press 'TAKE DATA' button

15. Wait for 'Taking Data' light to go out
16. Repeat steps 12-15 until full calibration range is covered
17. Press 'DONE DO FIT' button
18. Record calibration constants (C, D, MSE). Flag with RED ink.

#### Hardware Takedown

1. Shut off isolator valve to calibrator
2. Mount hotwire/hotfilm in tunnel
3. Disconnect calibrator pressure tap from transducer
4. Reconnect instrumentation lines to transducer
5. Reset valves on transducer (vents closed, measure open)

### **B.4 Dual-Element Hotwire/Hotfilm Calibration**

#### Hardware setup

The hardware setup is identical to that for a single element hotwire/hotfilm with one exception. The dual-element hotwire/hotfilm should be placed vertically in the calibrator such that both elements are perpendicular to the flow. Also the rotating collar should be set to pin R6.

#### Software Setup

The software setup is identical to that for a single element hotwire/hotfilm with the following exception.

Instead of the 'Hot wire cal' vi, open the 'X wire probe cal' vi, and set 'Type of Cal' switch to '90'

#### Calibration Procedure

1. Verify both sides of the pressure transducer are vented "zero pressure"
2. Run 'Continuous Ptrans Scan' vi

3. Obtain current zero intercept from 'Continuous Ptrans Scan' vi, and enter this value in the 'X wire probe cal' vi
4. Stop 'Continuous Ptrans Scan' vi
5. Open valves on calibrator slightly to begin flow over dual element hotwire/hotfilm
6. Set high side of pressure transducer to measure
7. Set appropriate IFA HW channel to "RUN"
8. Run 'X wire probe cal' vi
9. Enter data filename. First data is taken as soon as file is created.
10. Open valves on calibrator until jet is at the maximum desired calibration velocity  
DO NOT EXCEED TRANSDUCER MAXIMUM PRESSURE
11. Wait for 'Taking Data' light to go out
12. Reduce calibrator flow to next desired calibration point
13. Allow approximately 15 seconds for pressures to stabilize
14. Press 'TAKE DATA' button
15. Wait for 'Taking Data' light to go out
16. Repeat steps 12-15 until full calibration range is covered
17. Press 'DONE DO FIT' button
18. Record initial calibration constants (C, D, MSE). Flag with RED ink.
19. Move probe holder arm on calibrator to horizontal position
20. Set calibrator flow to a medium speed (approximately half the maximum)
21. Rotate the probe in its sheath until the indicated angle is 0 degrees and lock it down
22. Set "Type of Cal" switch to "45" (enables yaw compensation)
23. Wait for 'Taking Data' light to go out

24. Reduce calibrator flow to next desired calibration point
25. Allow approximately 15 seconds for pressures to stabilize
26. Press 'TAKE DATA' button
27. Wait for 'Taking Data' light to go out
28. Repeat steps 23-27 until full calibration range covered
29. Press 'DONE DO FIT' button (At this point the angle compensation window will pop up)
30. Set jet to highest expected velocity
31. Hit "OK" button
32. Move rotating collar to the R1 pin hole
33. Hit 'Take Data' button
34. Wait for 'Taking Data' light to go out
35. Move rotating collar to next pin hole
36. Hit 'Take Data' button
37. Wait for 'Taking Data' light to go out
38. Repeat steps 35-37 until data has been taken at the last pin location (R11). At this point a new window will pop up asking you to change velocity
39. Set jet to a medium velocity
40. Repeat steps 31-38
41. Set jet to a low velocity
42. Repeat steps 31-38
43. Record final calibration data. Flag with RED ink.
44. Backup calibration file

## Hardware Takedown

1. Shut off isolator valve to calibrator
2. Before removing hotwire/hotfilm from calibrator indicate flow direction on shaft (a 90deg rotation changes the calibration constants)
3. Mount hotwire/hotfilm in tunnel making sure you attach the same sensor to the same IFA channel
4. Disconnect calibrator pressure tap from transducer
5. Reconnect instrumentation lines to transducer  
Reset valves on transducer (vents closed, measure open)

## APPENDIX C. Boundary Layer Traverses

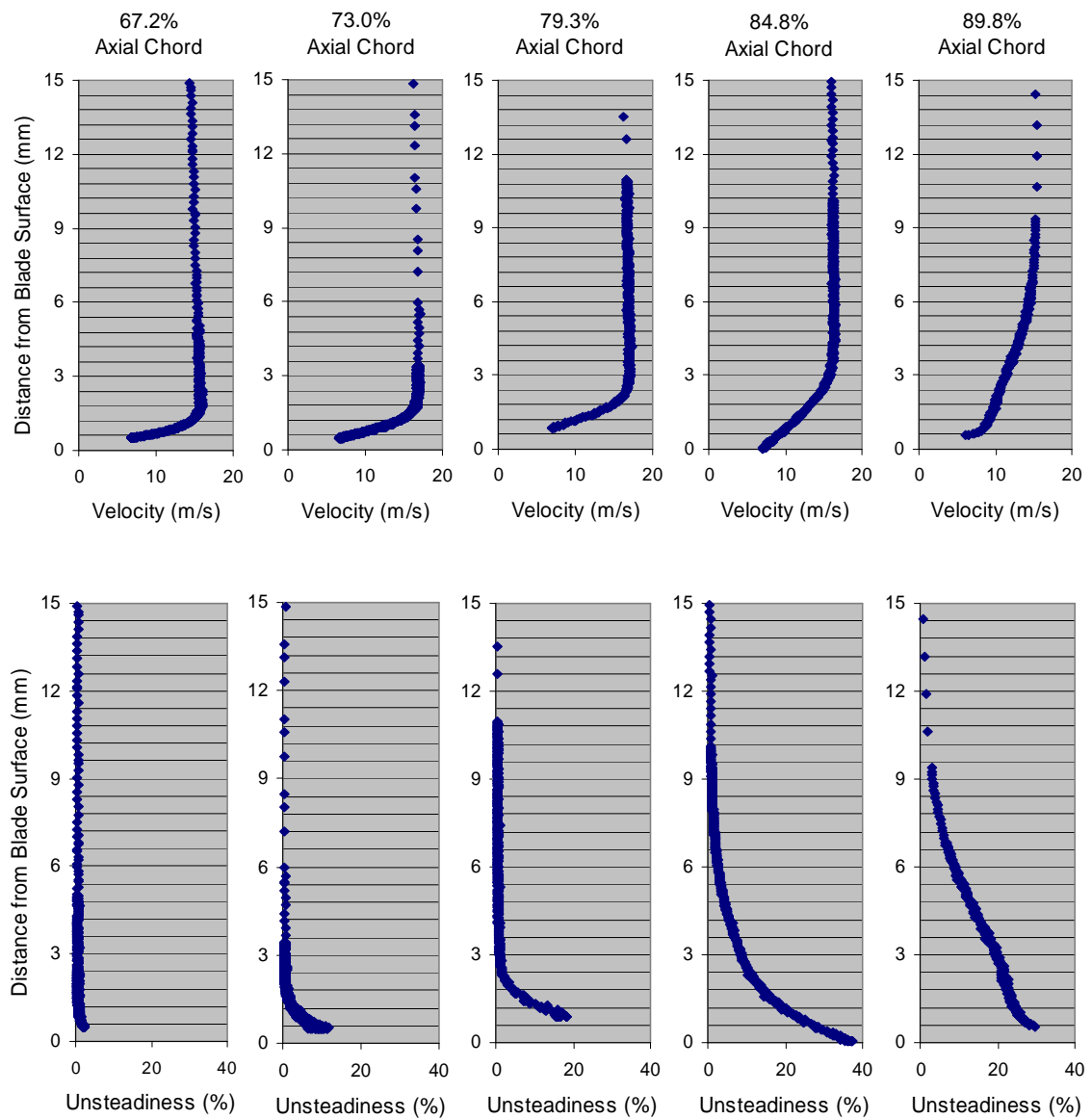


Figure 79. Boundary layer profiles for an unmodified Pak-B blade at  $Re = 100k$  and  $1\% Tu$

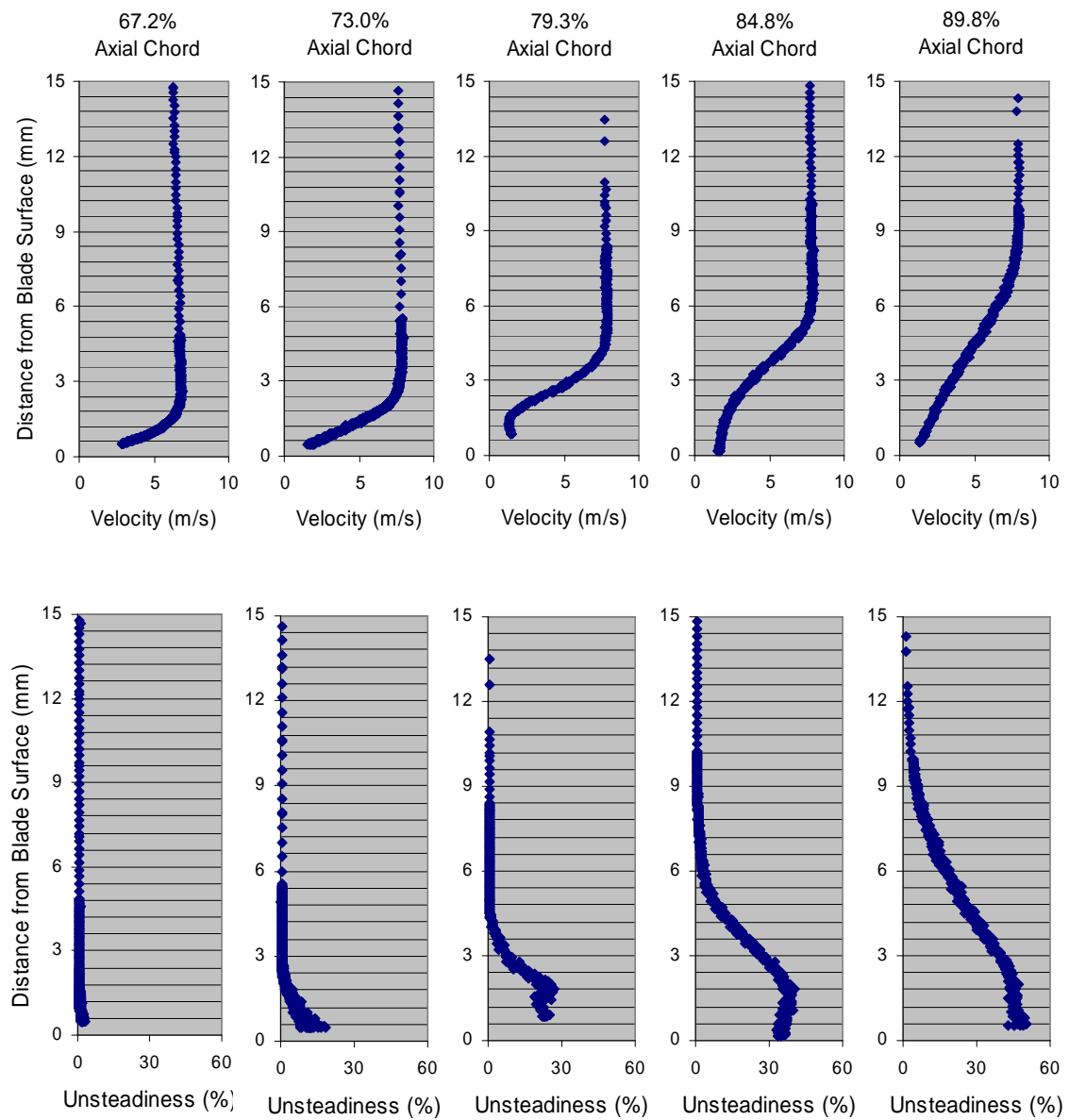


Figure 80. Boundary layer profiles for an unmodified Pak-B blade at  $Re = 45k$  and  $1\% Tu$

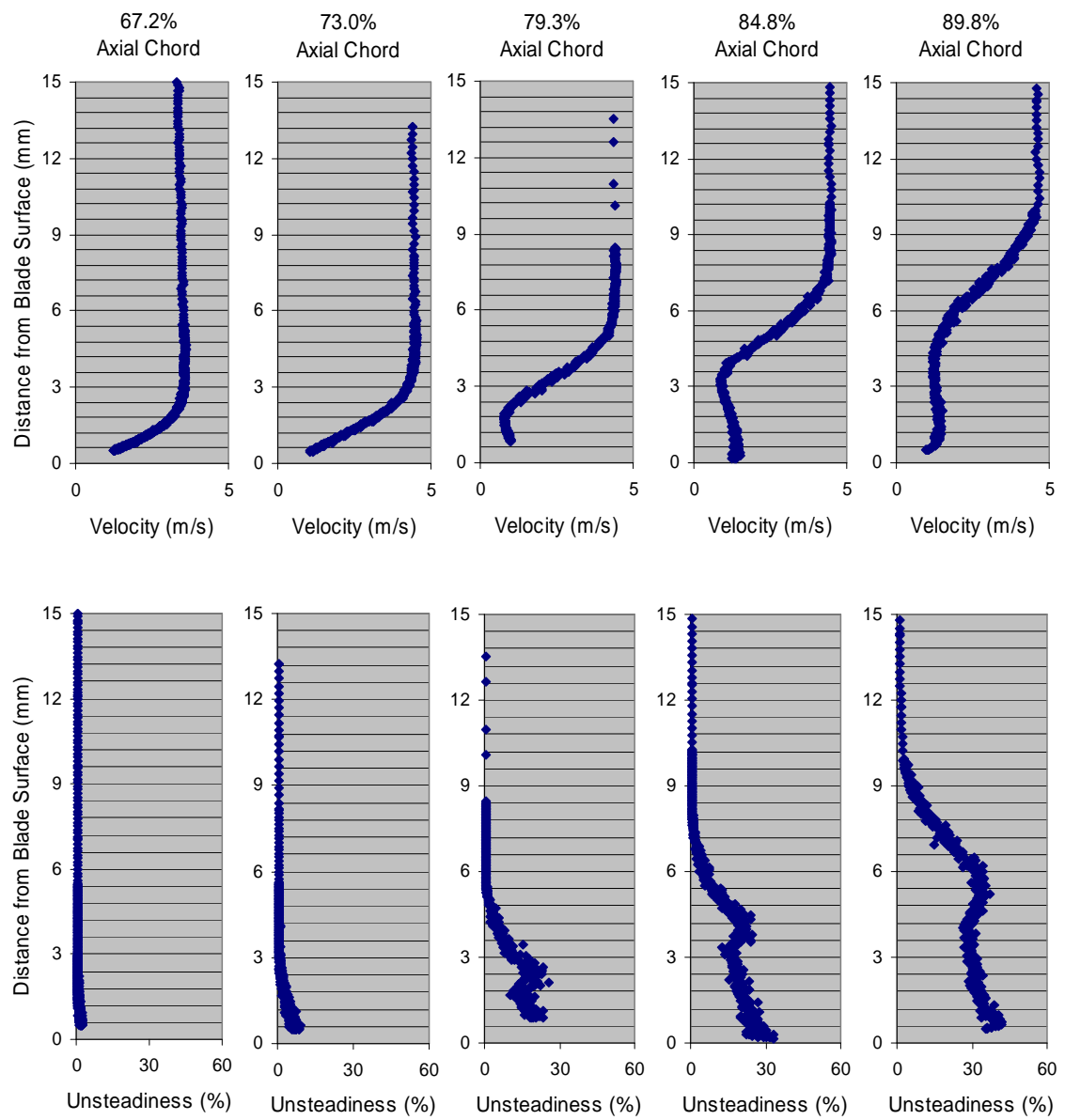


Figure 81. Boundary layer profiles for an unmodified Pak-B blade at  $Re = 25k$  and  $1\% Tu$



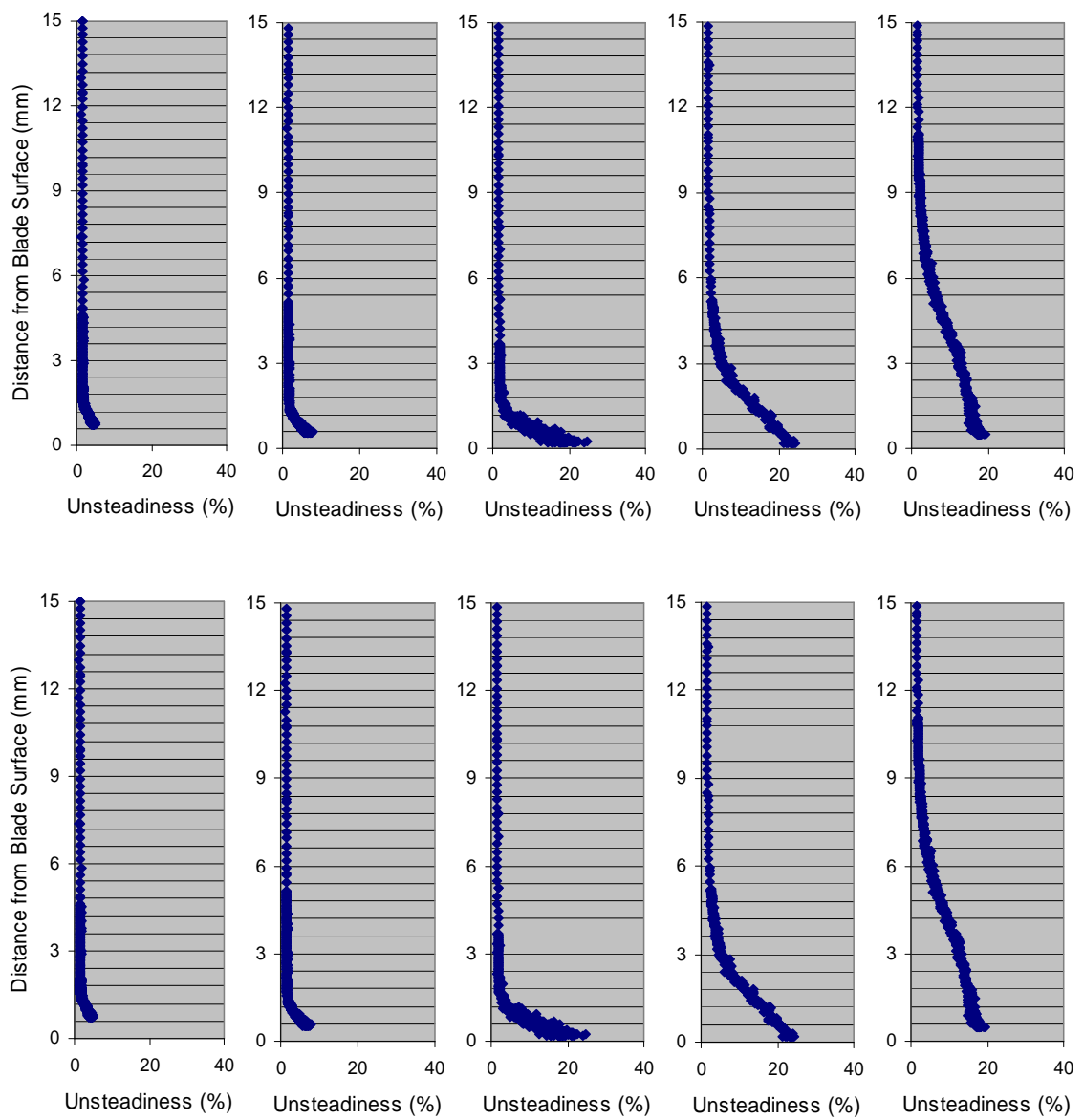


Figure 82. Boundary layer profiles for an unmodified Pak-B blade at  $Re = 100k$  and  $4\% Tu$

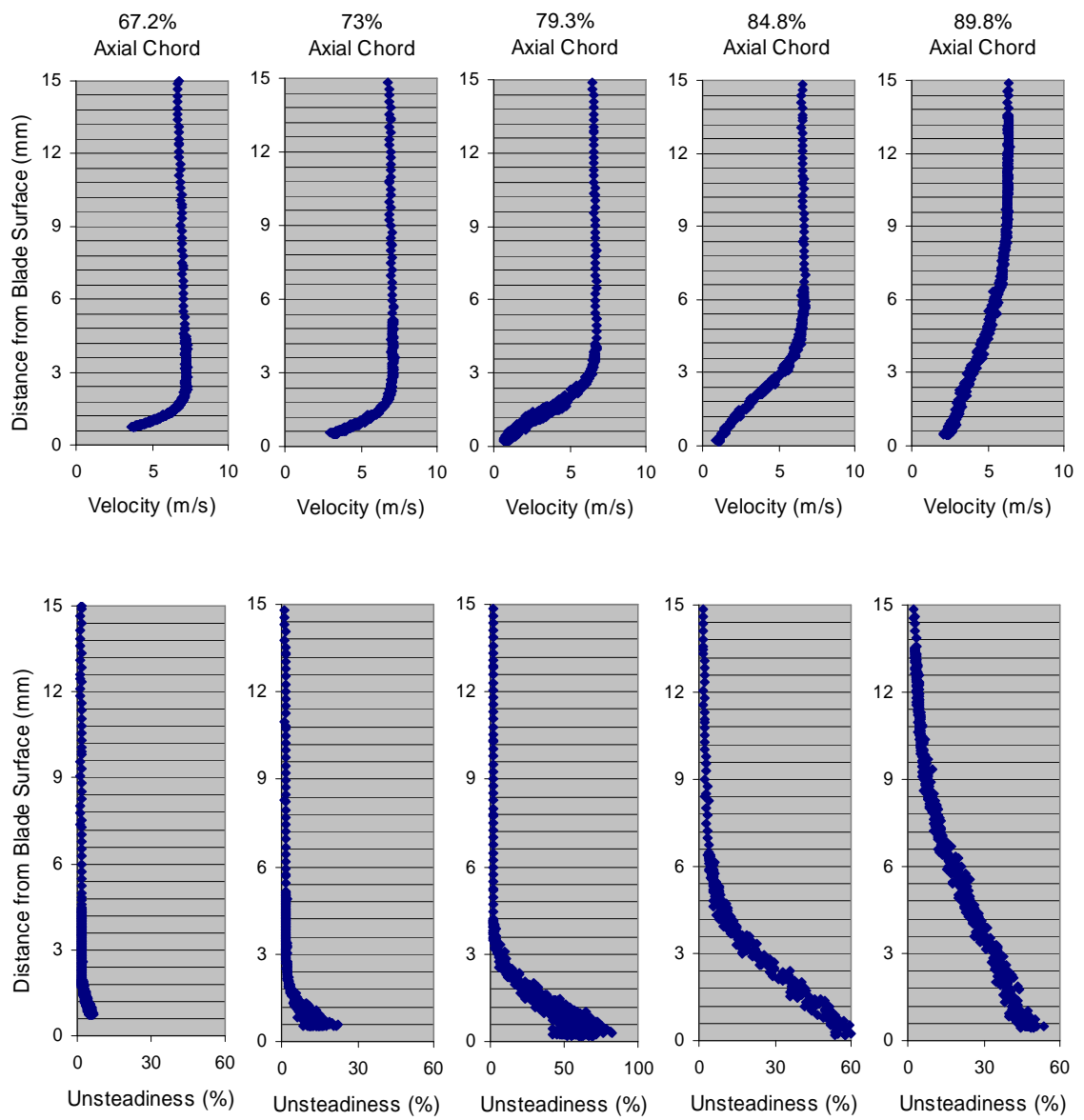


Figure 83. Boundary layer profiles for an unmodified Pak-B blade at  $Re\ 45k$  and  $4\% Tu$

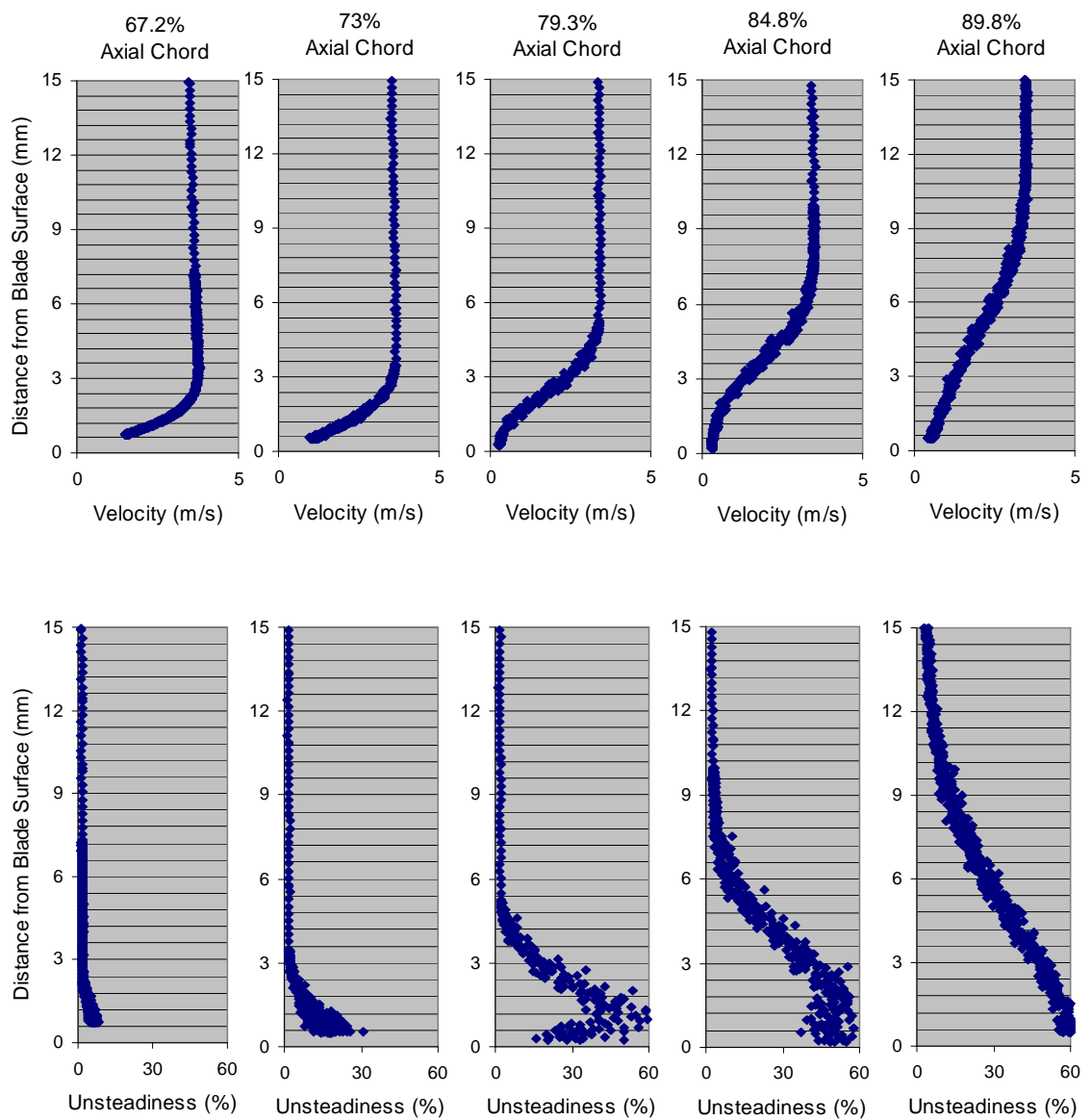


Figure 84. Boundary layer profiles for an unmodified Pak-B blade at  $Re = 25k$  and  $4\% Tu$

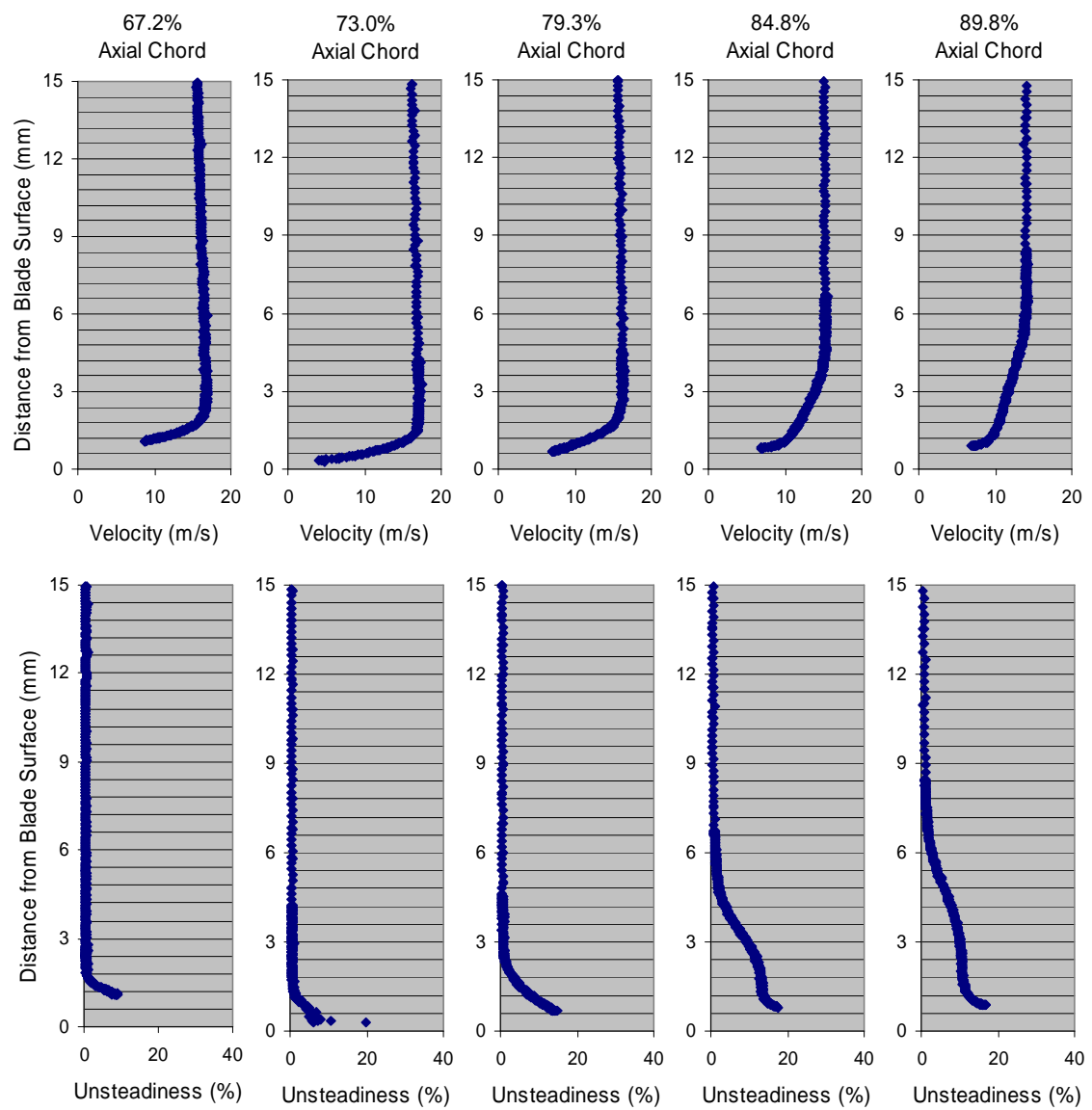


Figure 85. Boundary layer profiles for a Pak-B blade with dimples at 65% of the axial chord with 2.22 cm spacing at  $Re = 100k$  and 1%  $Tu$

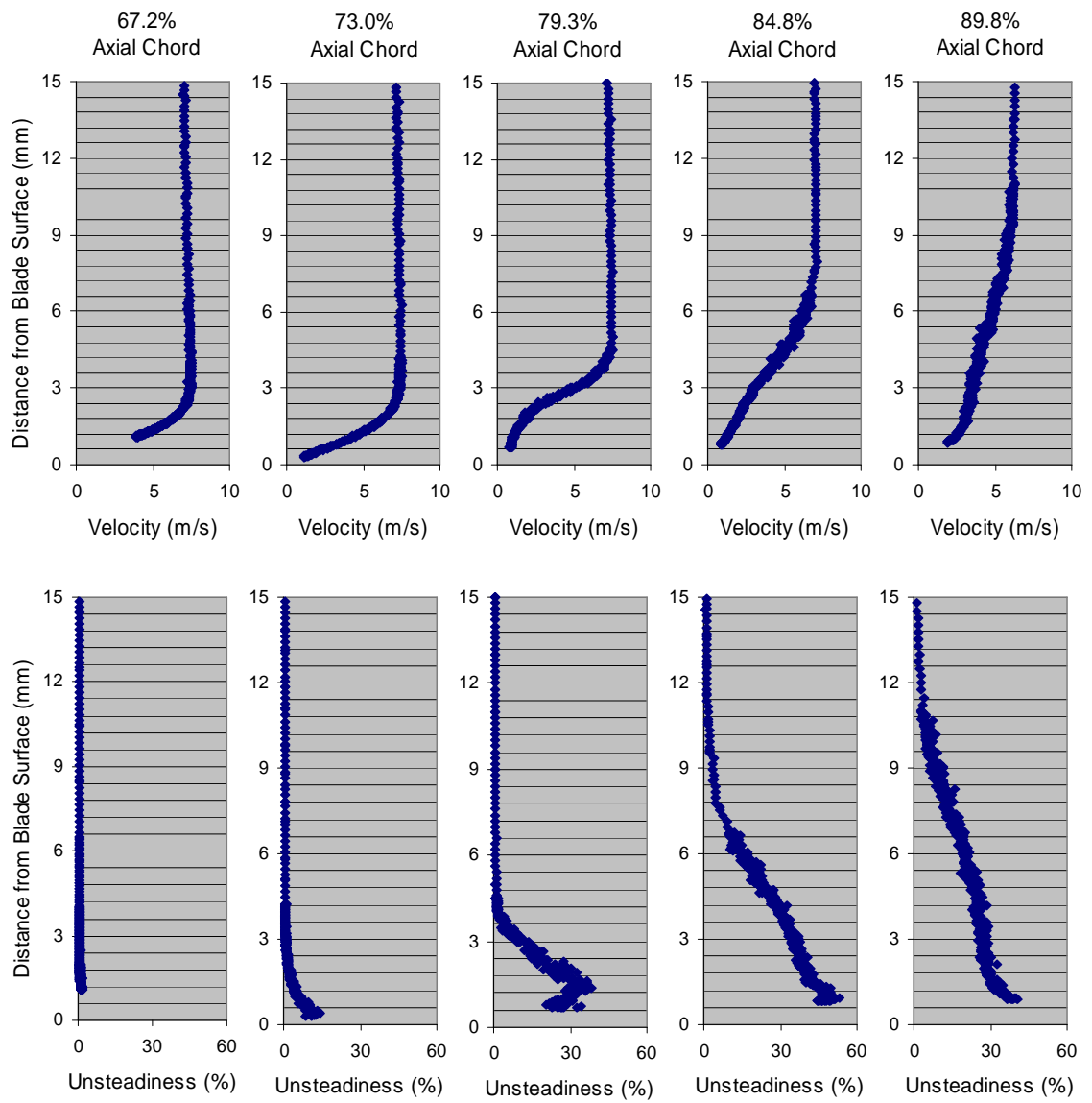


Figure 86. Boundary layer profiles for a Pak-B blade with dimples at 65% of the axial chord with 2.22 cm spacing at  $Re\ 45k$  and 1%  $Tu$

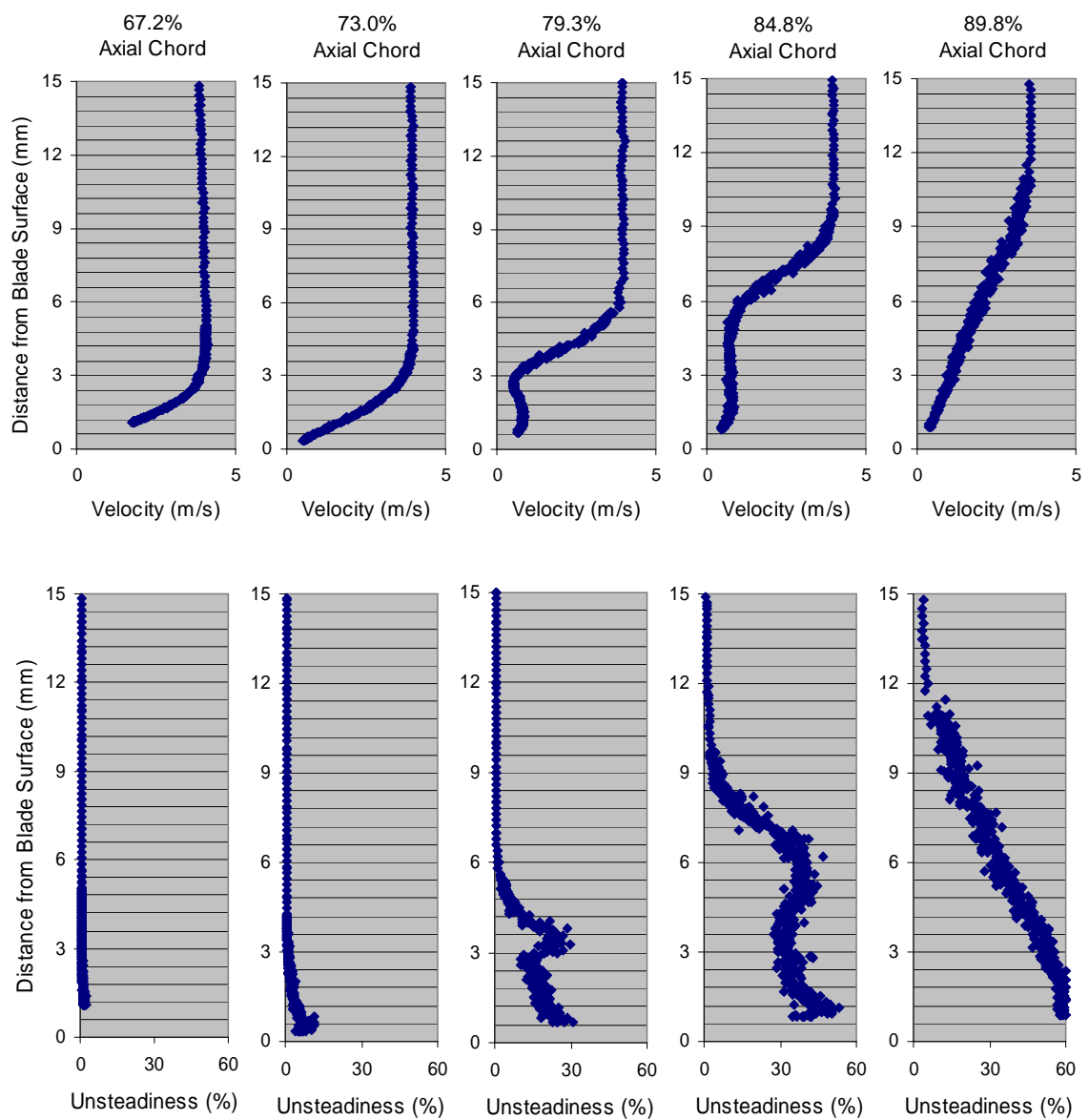


Figure 87. Boundary layer profiles for a Pak-B blade with dimples at 65% of the axial chord with 2.22 cm spacing at  $Re\ 25k$  and  $1\% Tu$

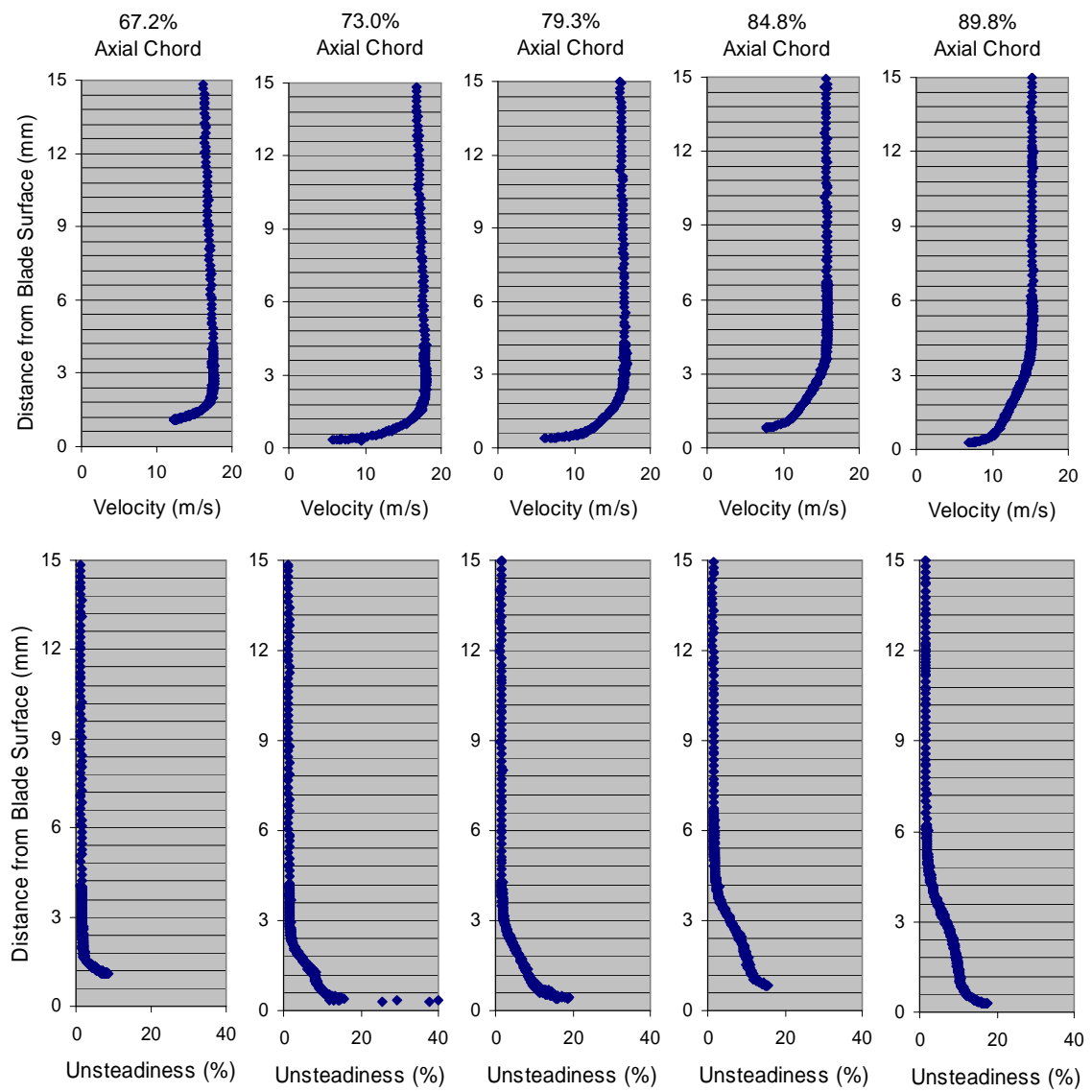


Figure 88. Boundary layer profiles for a Pak-B blade with dimples at 65% of the axial chord with 2.22 cm spacing at  $Re = 100k$  and  $4\% Tu$

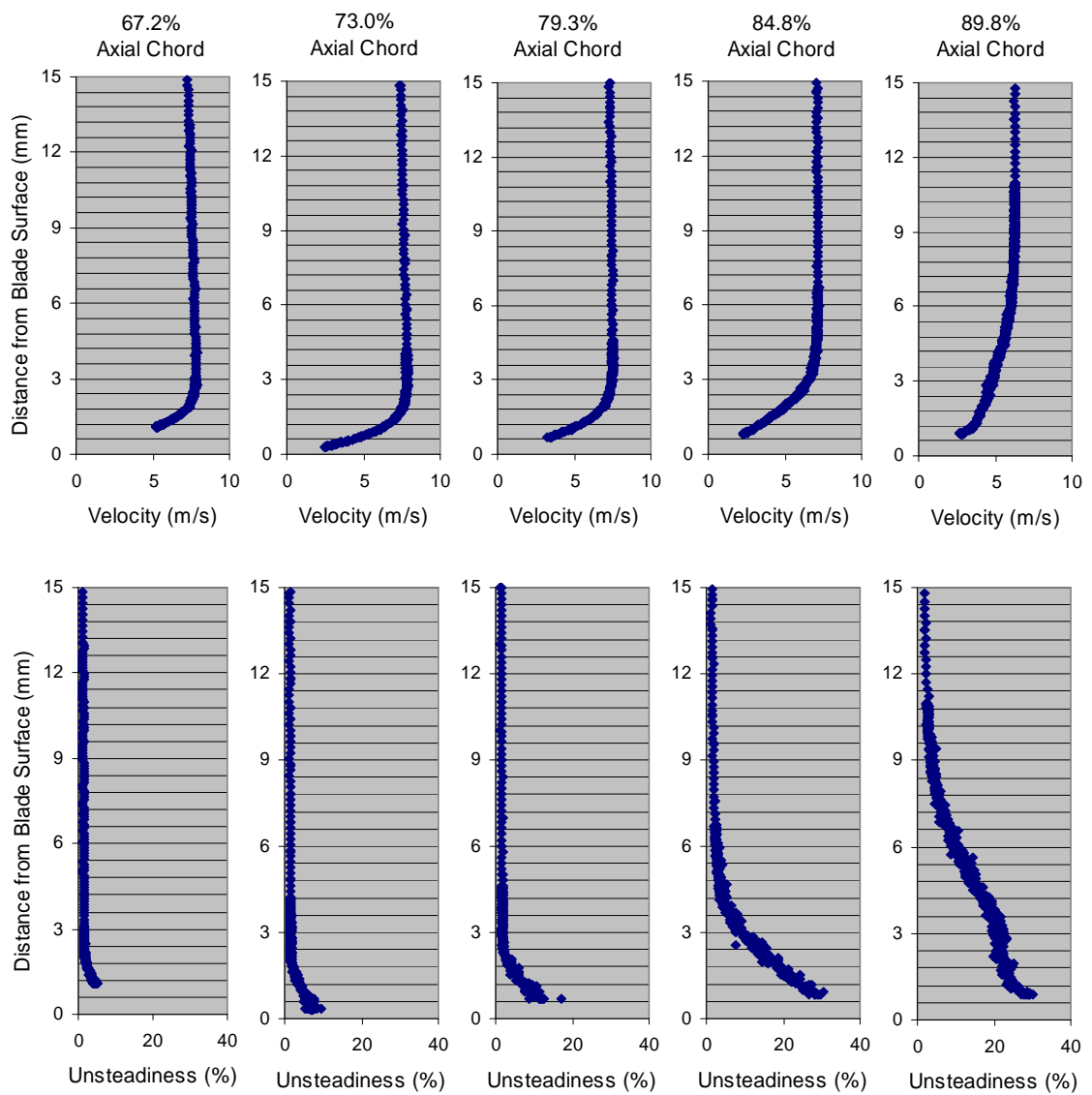


Figure 89. Boundary layer profiles for a Pak-B blade with dimples at 65% of the axial chord with 2.22 cm spacing at  $Re\ 45k$  and 4%  $Tu$



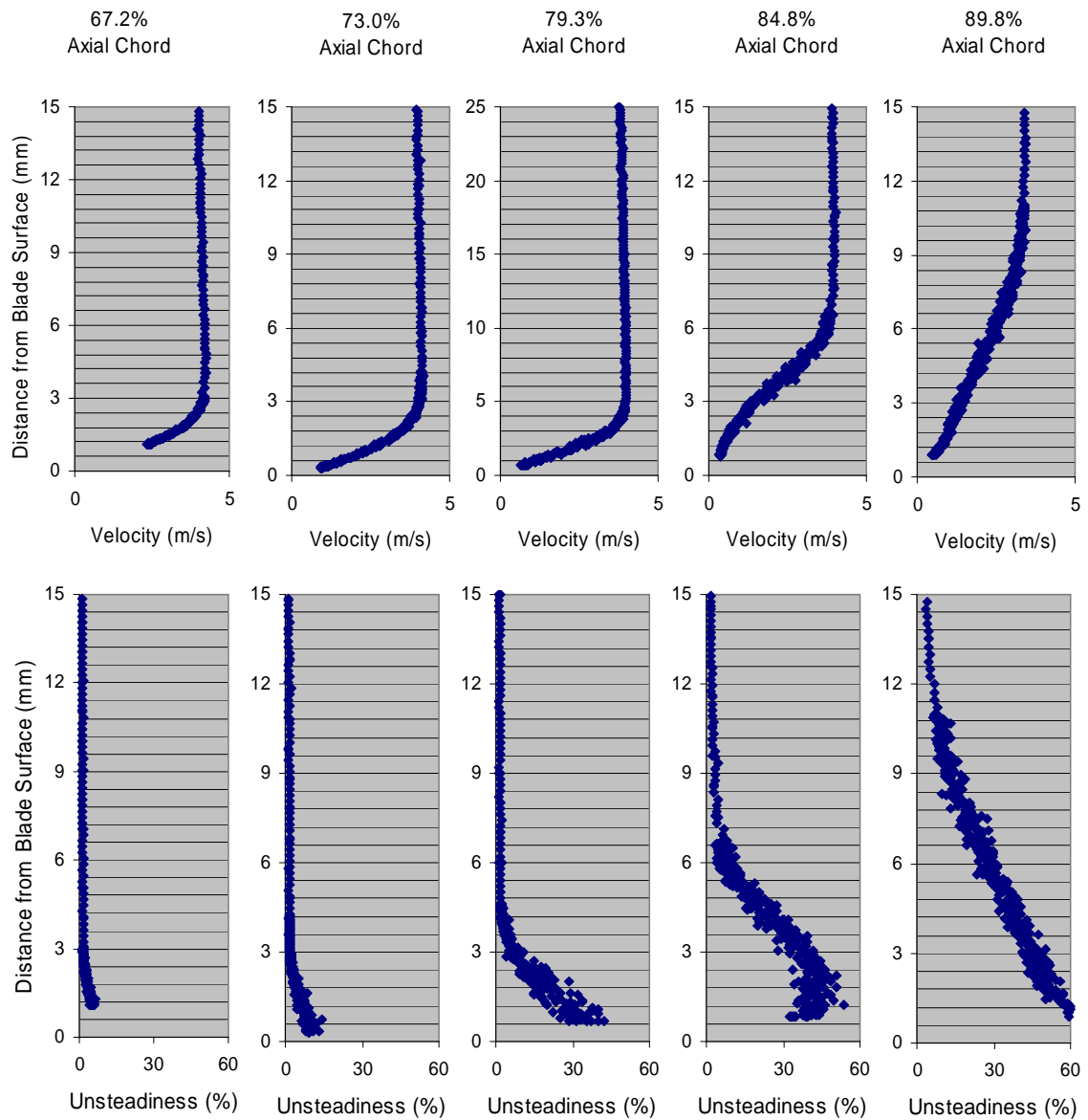


Figure 90. Boundary layer profiles for a Pak-B blade with dimples at 65% of the axial chord with 2.22 cm spacing at  $Re\ 25k$  and 4%  $Tu$

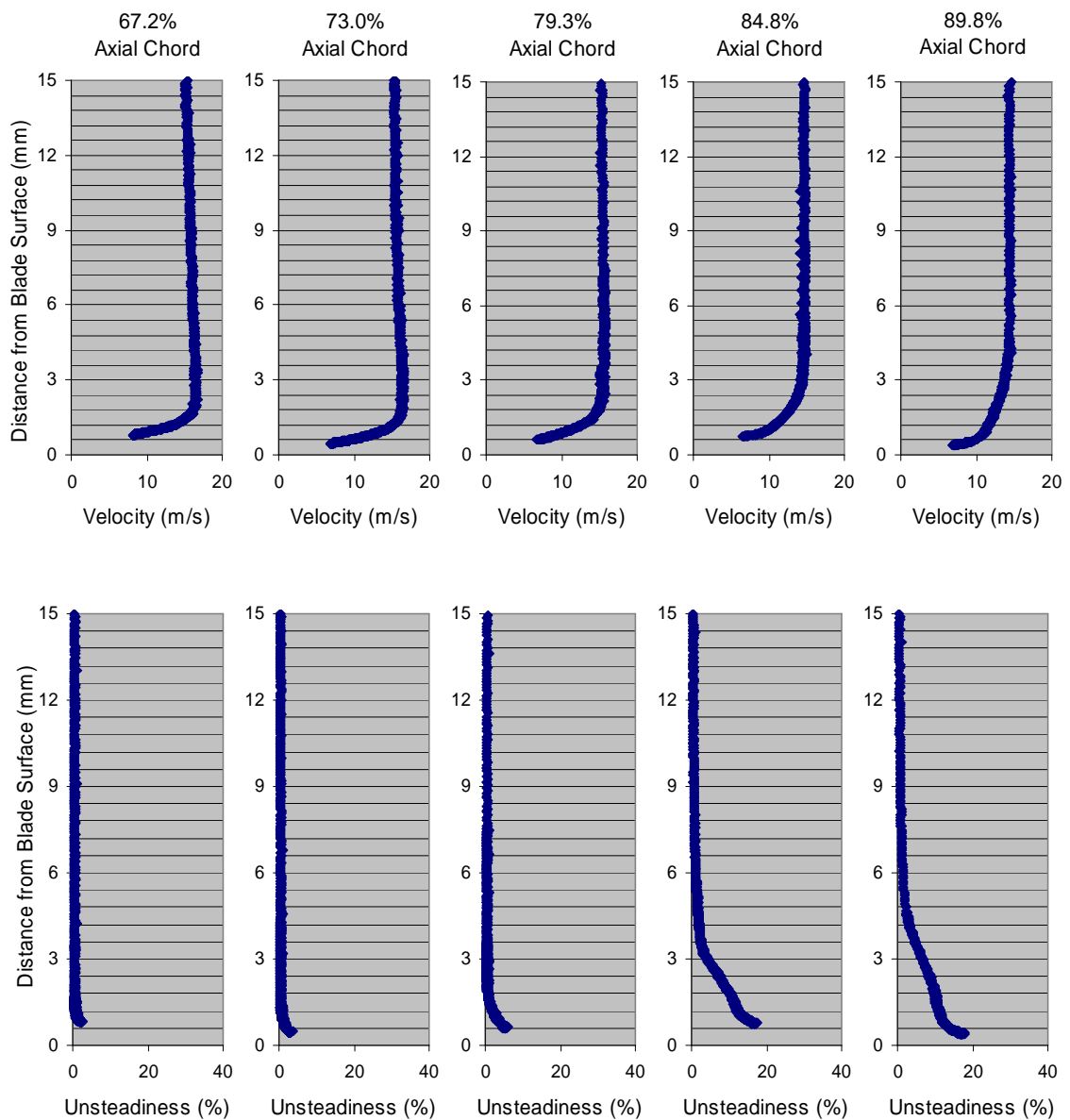


Figure 91. Boundary layer profiles for a Pak-B blade with dimples at 65% of the axial chord with 4.44 cm spacing with probe behind a covered dimple at  $Re = 100k$  and  $1\% Tu$

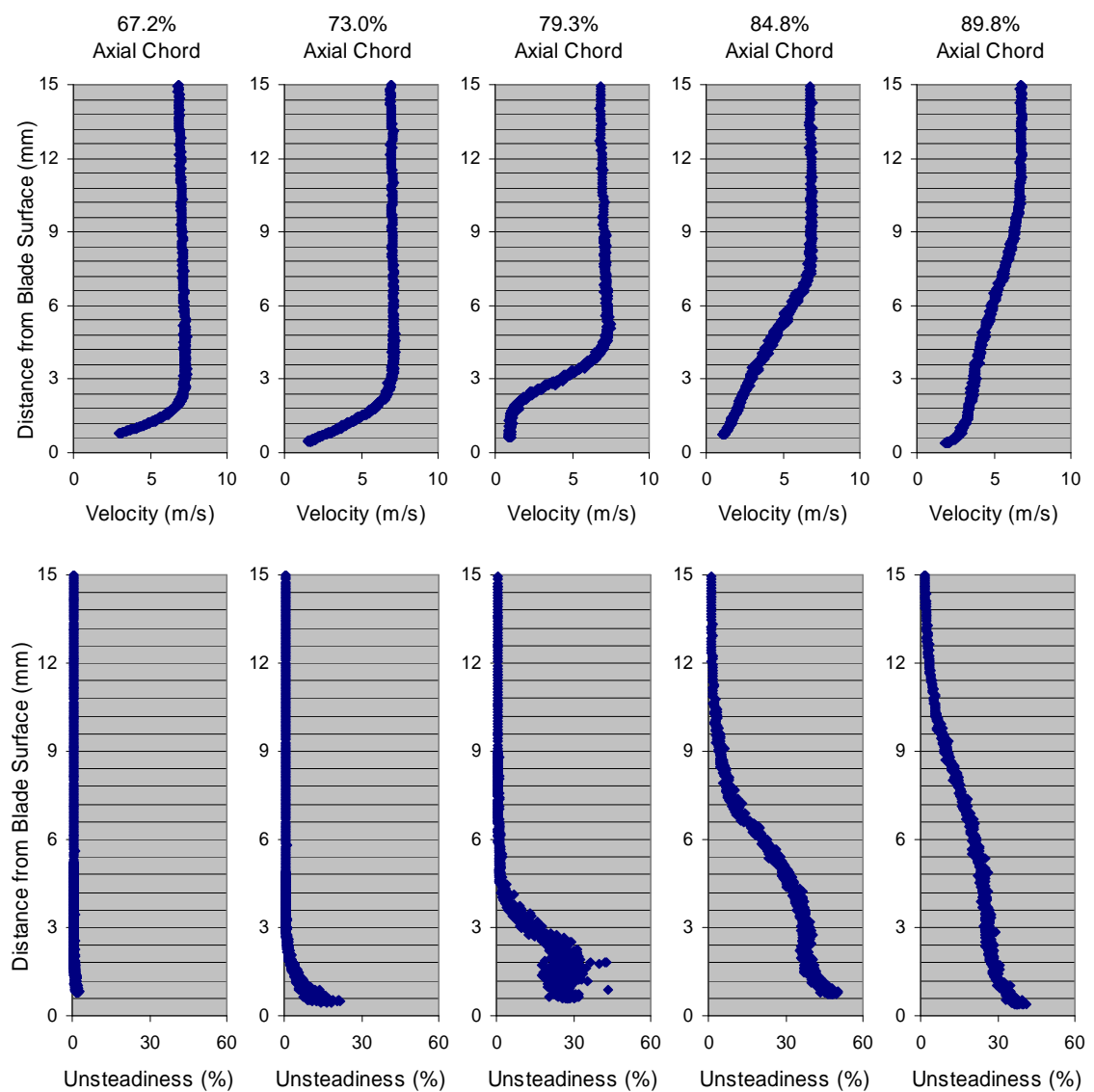


Figure 92. Boundary layer profiles for a Pak-B blade with dimples at 65% of the axial chord with 4.44 cm spacing with probe behind a covered dimple at  $Re = 45k$  and  $1\% Tu$

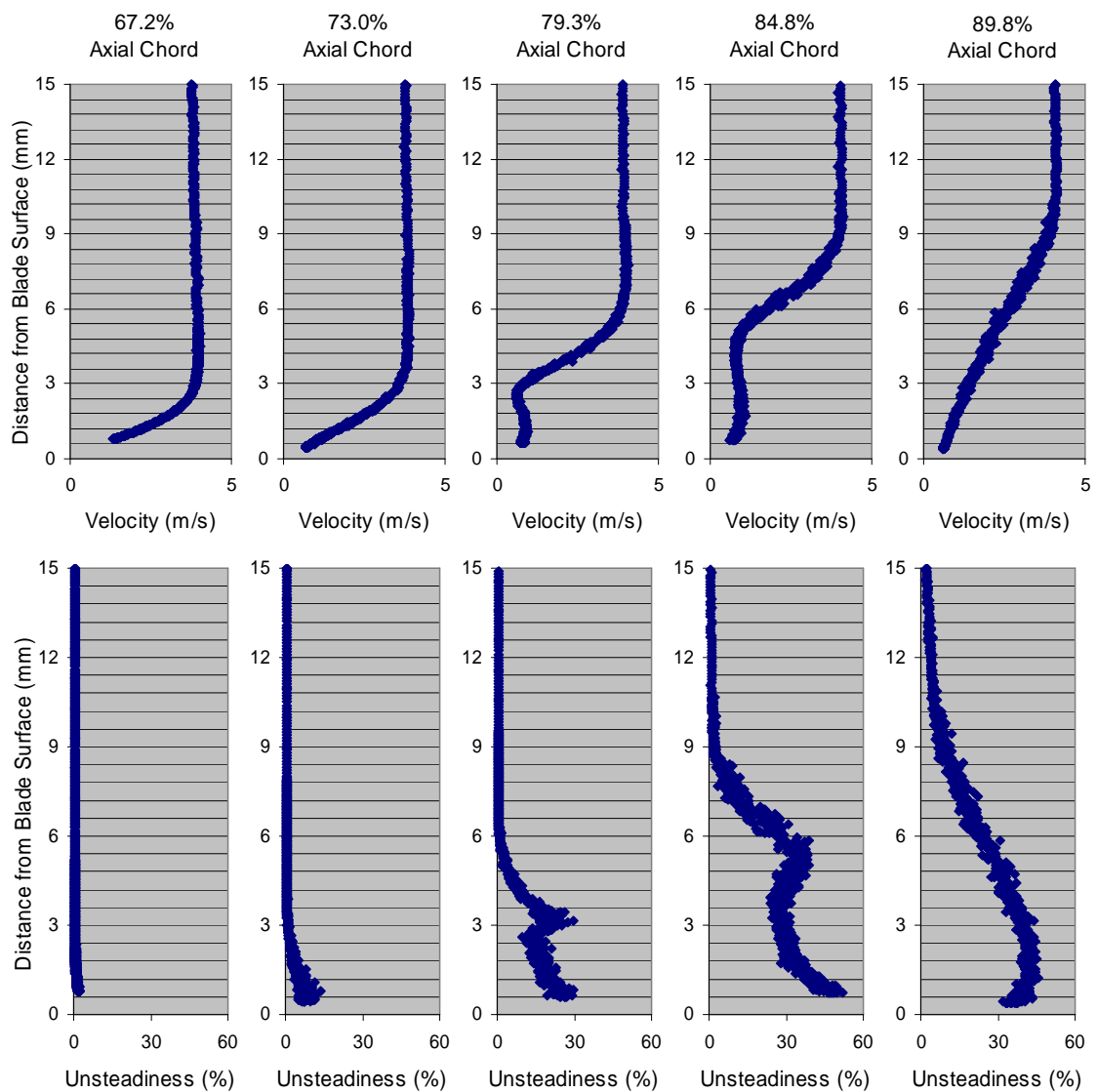


Figure 93. Boundary layer profiles for a Pak-B blade with dimples at 65% of the axial chord with 4.44 cm spacing with probe behind a covered dimple at Re 25k and 1% Tu

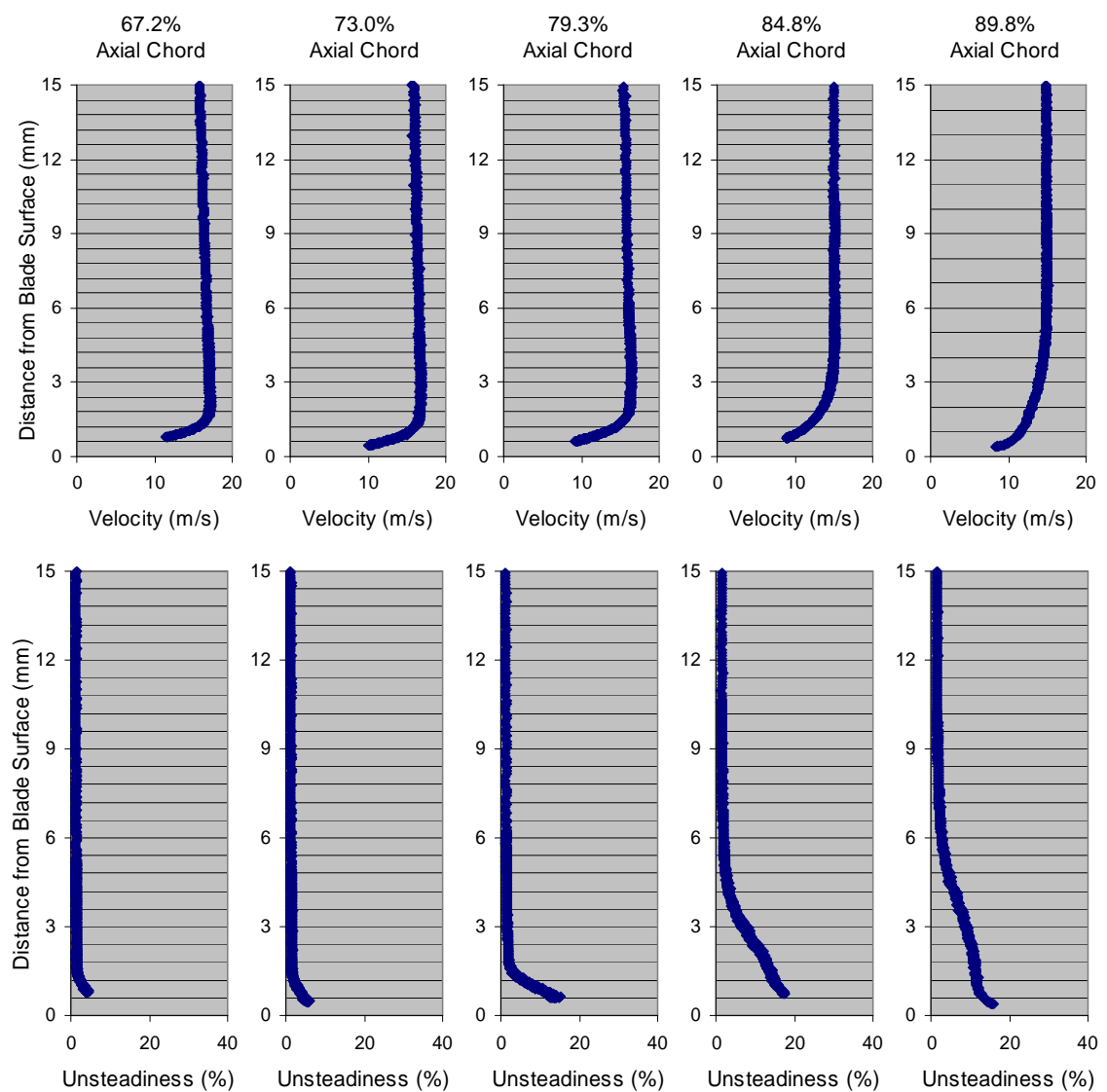


Figure 94. Boundary layer profiles for a Pak-B blade with dimples at 65% of the axial chord with 4.44 cm spacing with probe behind a covered dimple at Re 100k and 4% Tu

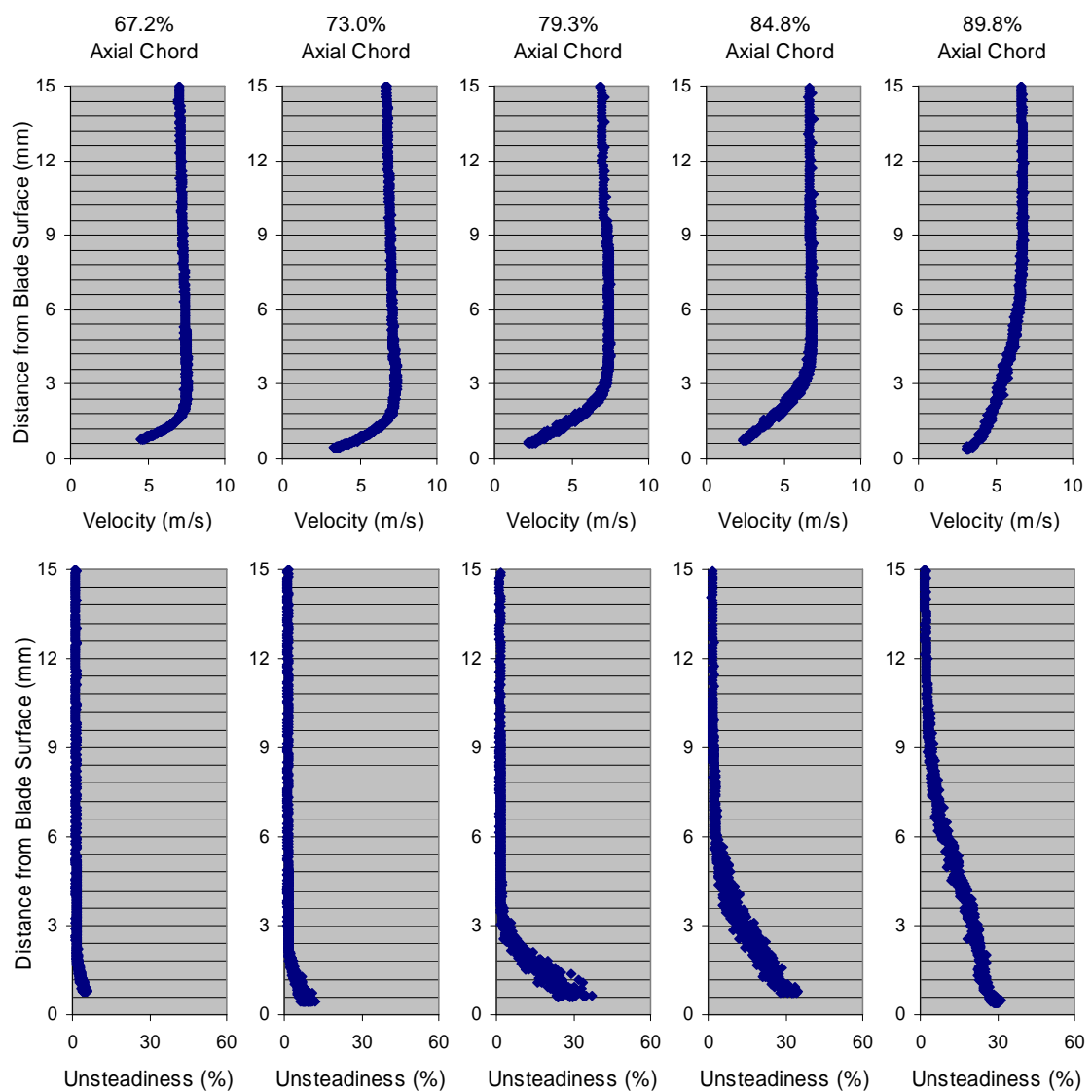


Figure 95. Boundary layer profiles for a Pak-B blade with dimples at 65% of the axial chord with 4.44 cm spacing with probe behind a covered dimple at  $Re = 45k$  and  $4\% Tu$

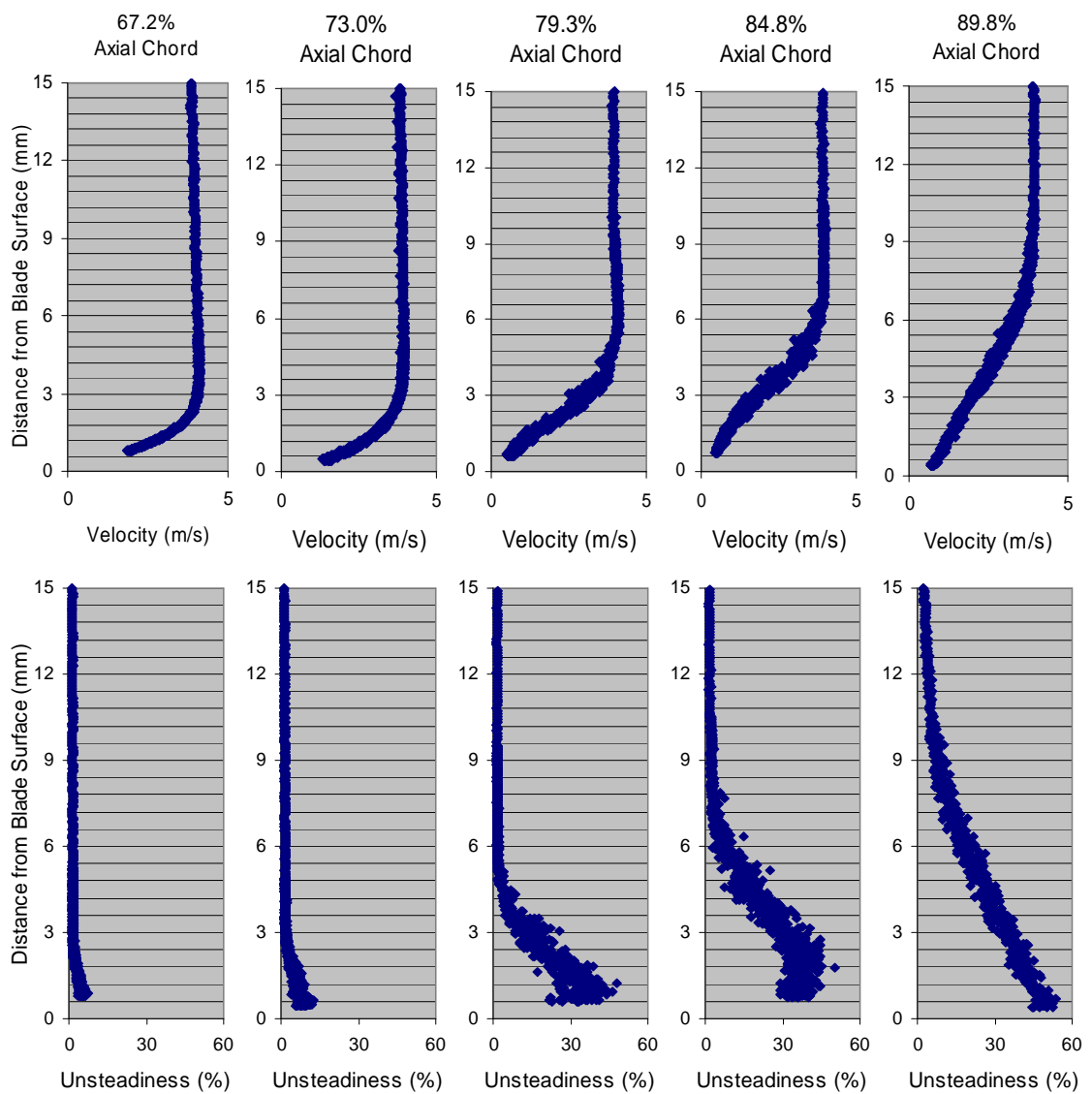


Figure 96. Boundary layer profiles for a Pak-B blade with dimples at 65% of the axial chord with 4.44 cm spacing with probe behind a covered dimple at Re 25k and 4% Tu

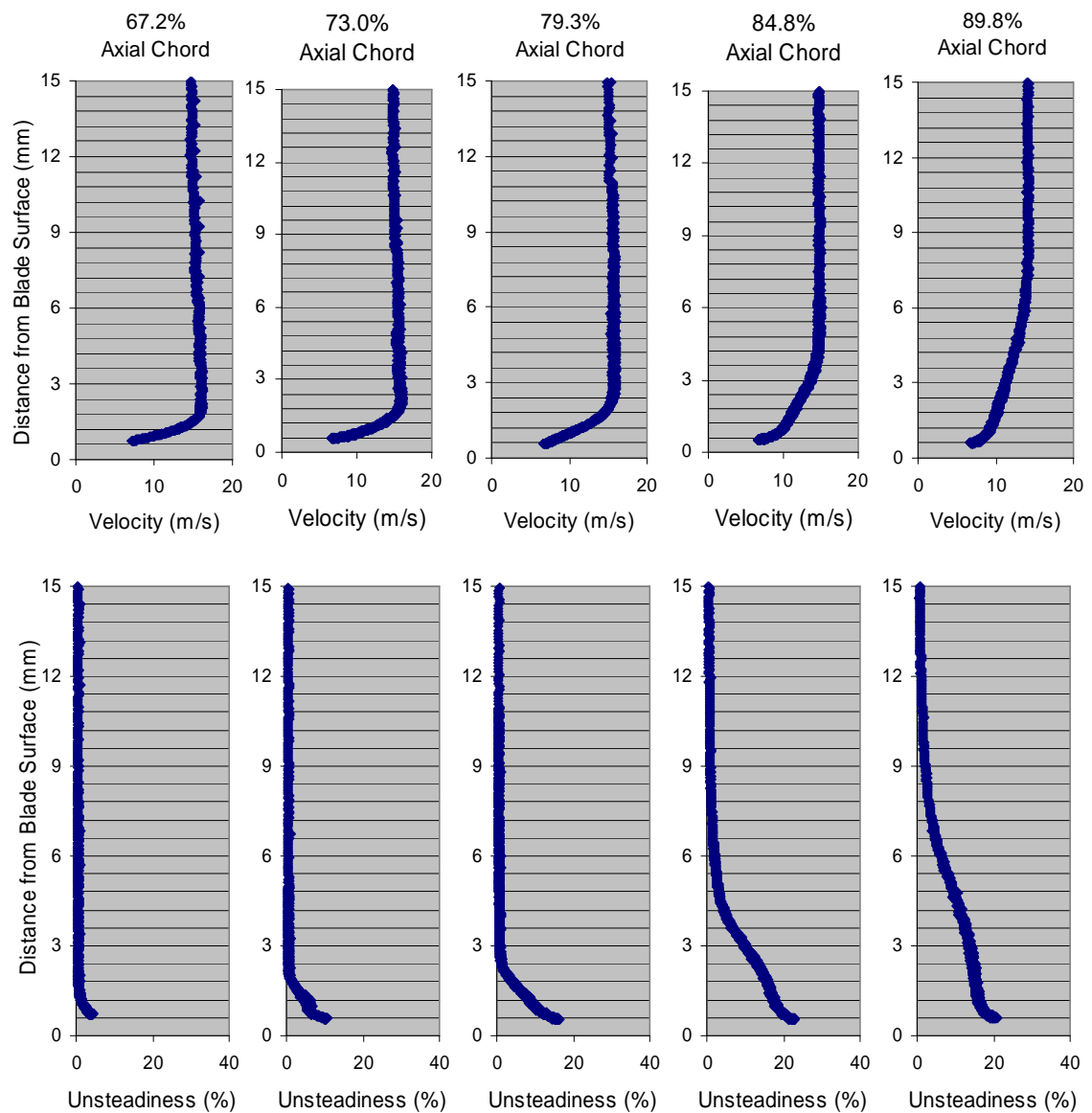


Figure 97. Boundary layer profiles for a Pak-B blade with dimples at 65% of the axial chord with 4.44 cm spacing with probe behind an open dimple at Re 100k and 1% Tu



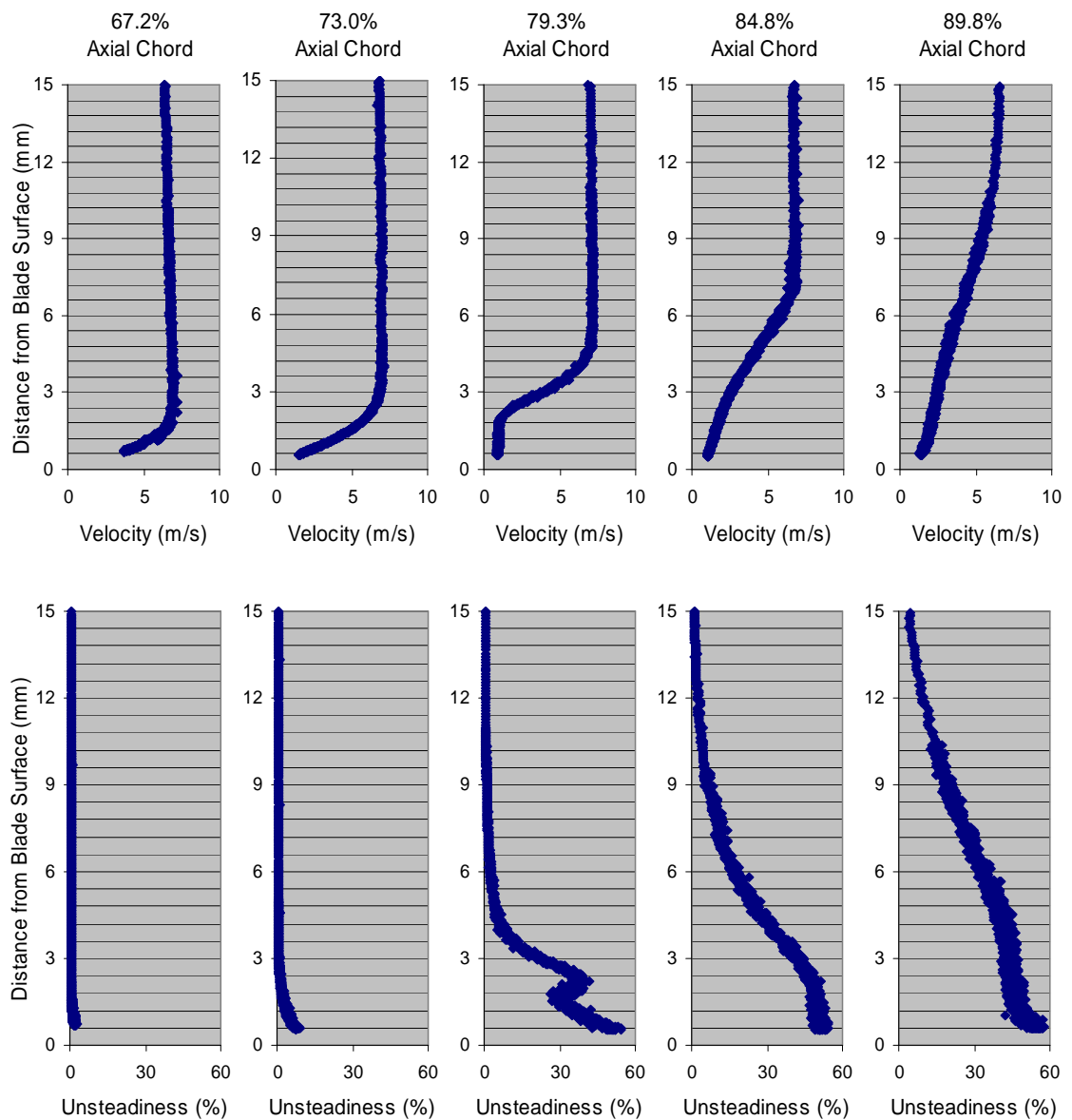


Figure 98. Boundary layer profiles for a Pak-B blade with dimples at 65% of the axial chord with 4.44 cm spacing with probe behind an open dimple at Re 45k and 1% Tu

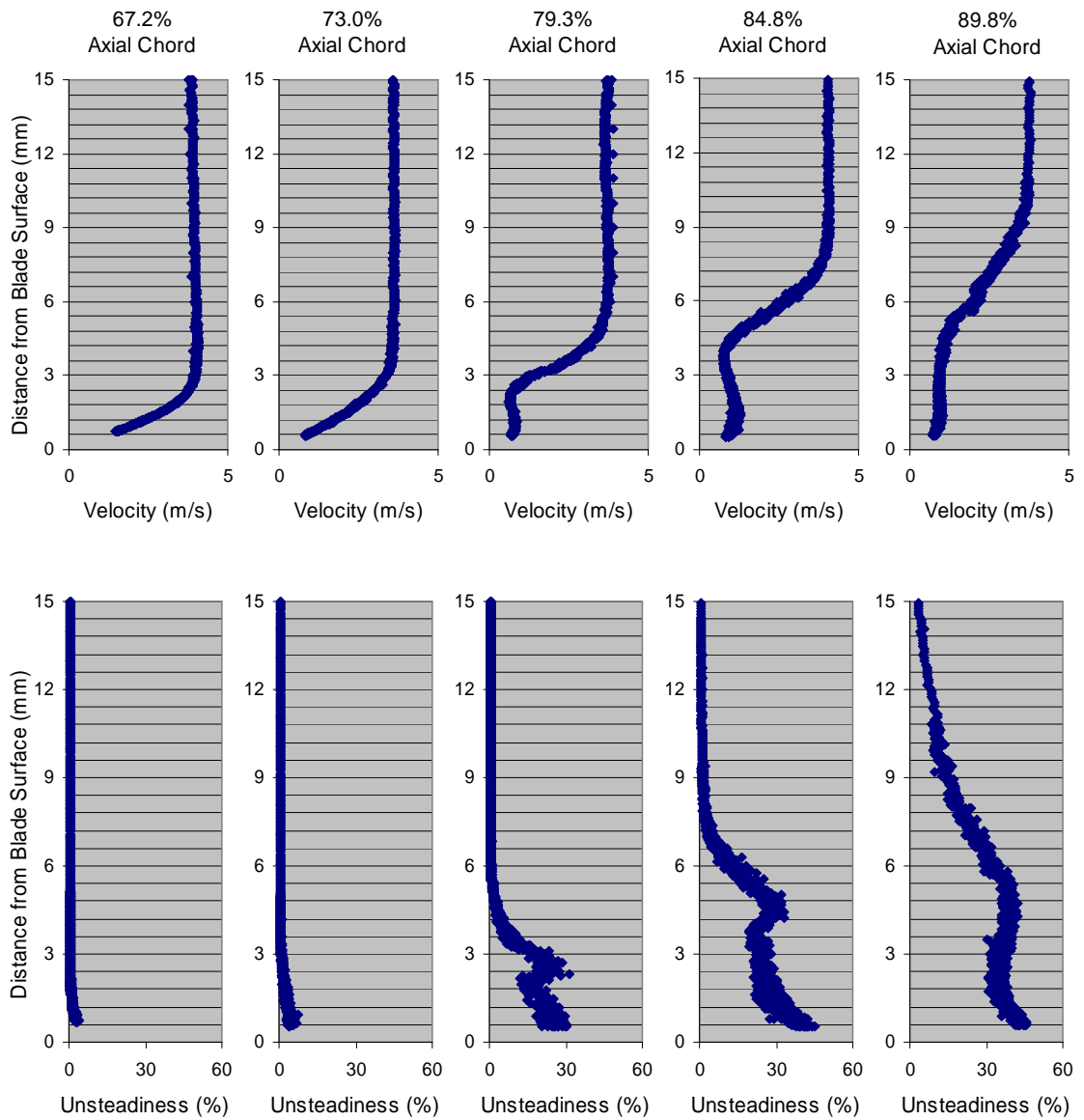


Figure 99. Boundary layer profiles for a Pak-B blade with dimples at 65% of the axial chord with 4.44 cm spacing with probe behind an open dimple at  $Re = 25k$  and  $1\% Tu$

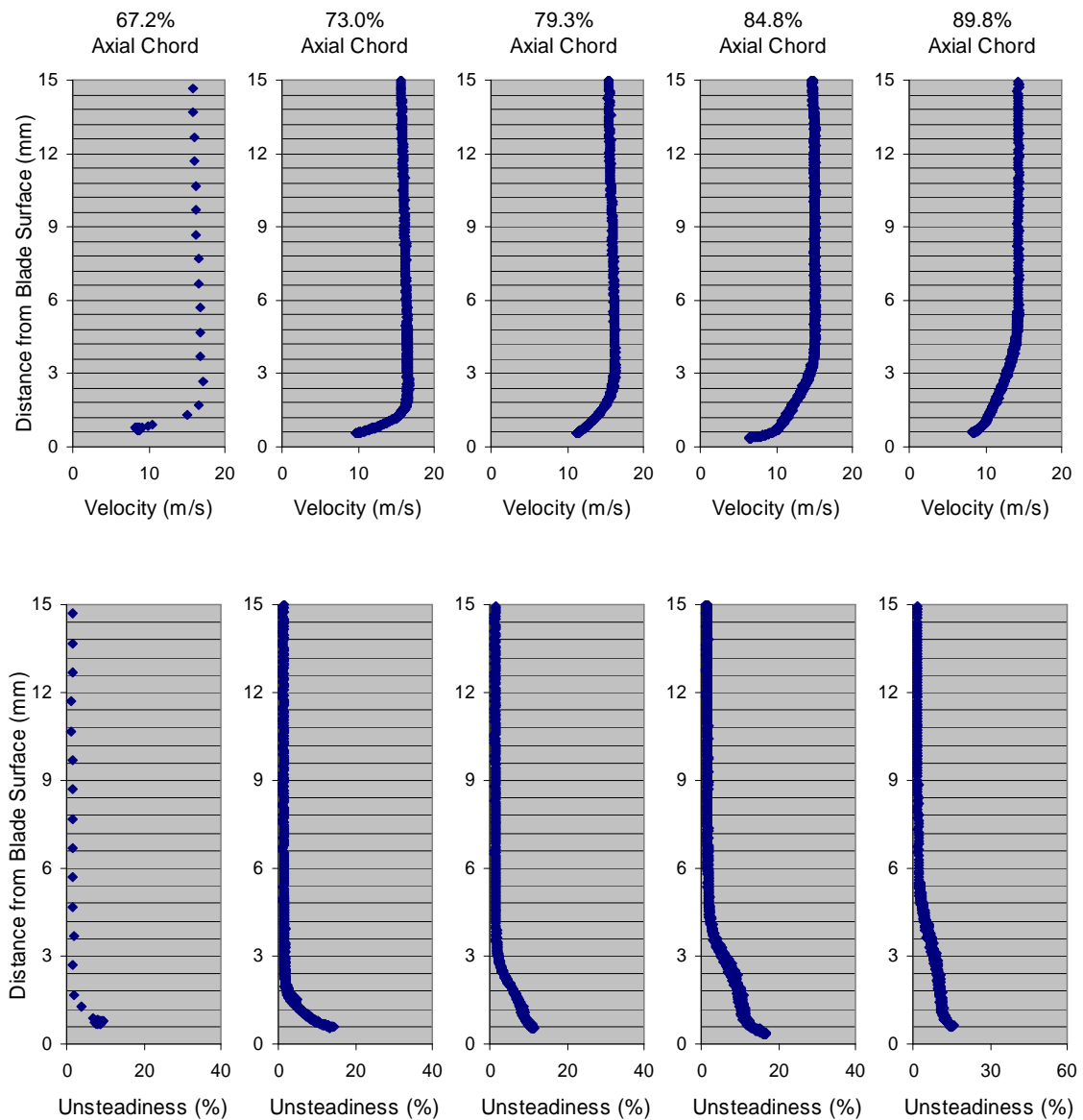


Figure 100. Boundary layer profiles for a Pak-B blade with dimples at 65% of the axial chord with 4.44 cm spacing with probe behind an open dimple at  $Re = 100k$  and  $4\% Tu$

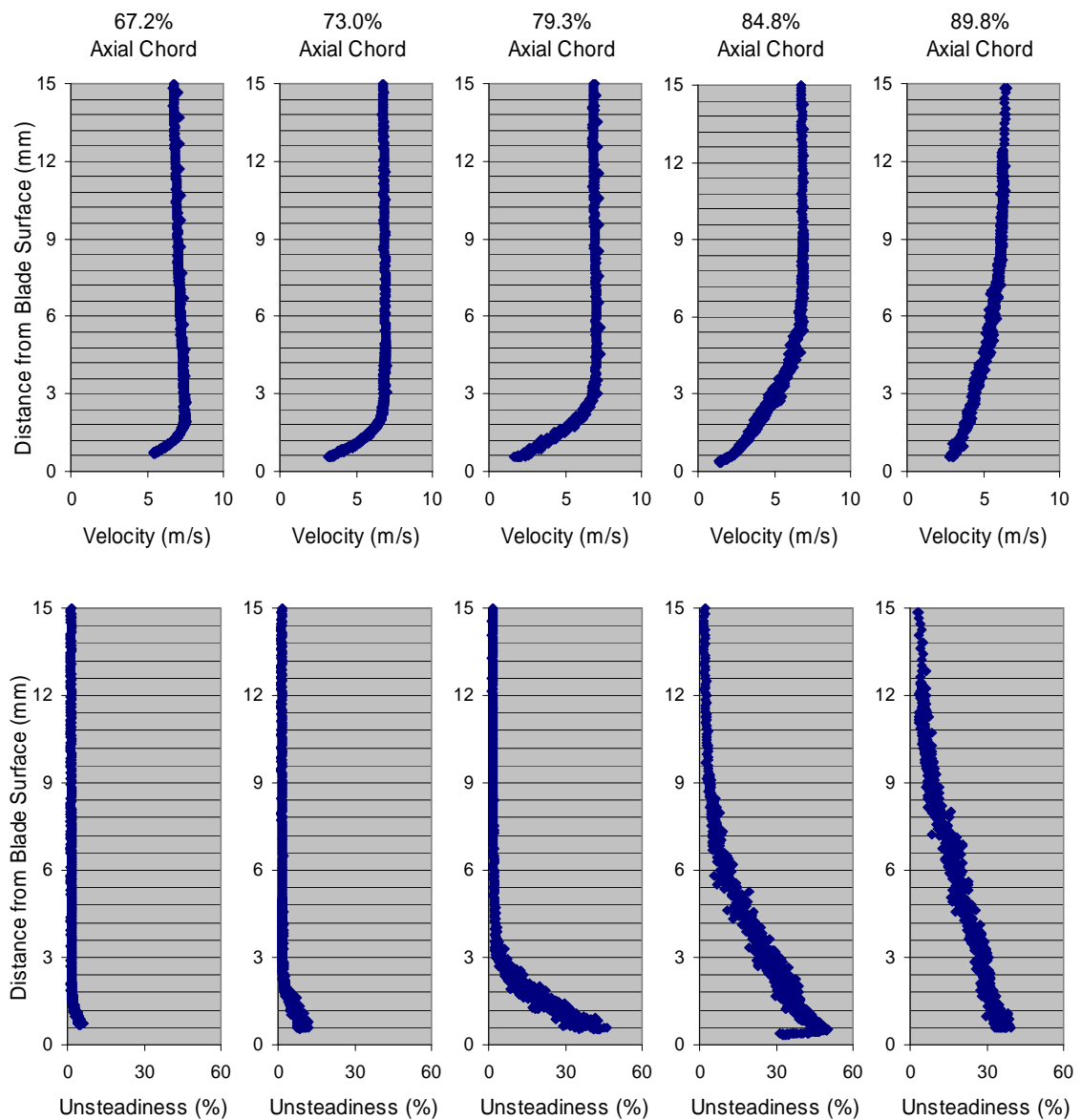


Figure 101. Boundary layer profiles for a Pak-B blade with dimples at 65% of the axial chord with 4.44 cm spacing with probe behind an open dimple at  $Re = 45k$  and  $4\% Tu$

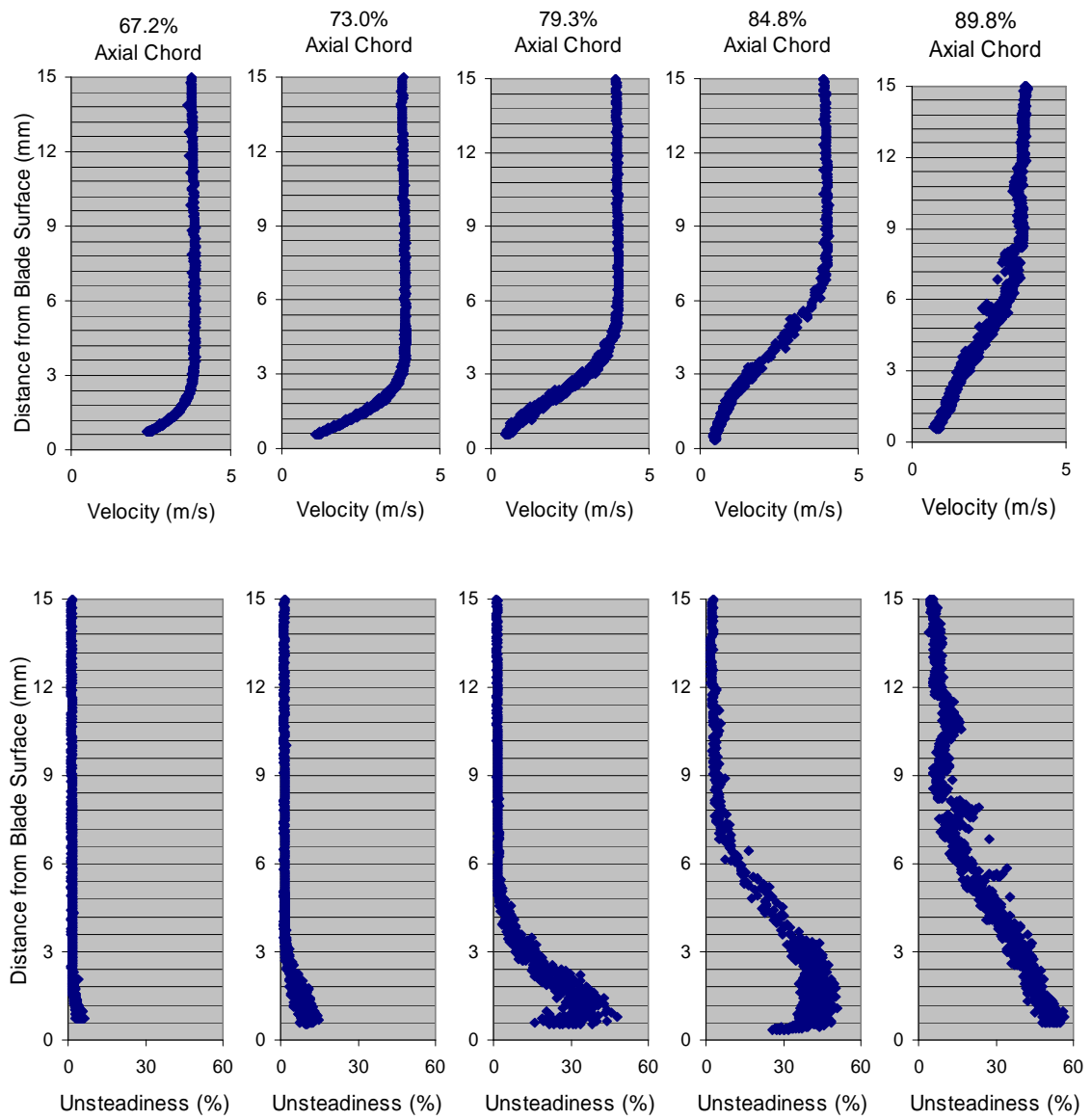


Figure 102. Boundary layer profiles for a Pak-B blade with dimples at 65% of the axial chord with 4.44 cm spacing with probe behind an open dimple at  $Re = 25k$  and  $4\% Tu$

## APPENDIX D. Wake Velocity Profiles

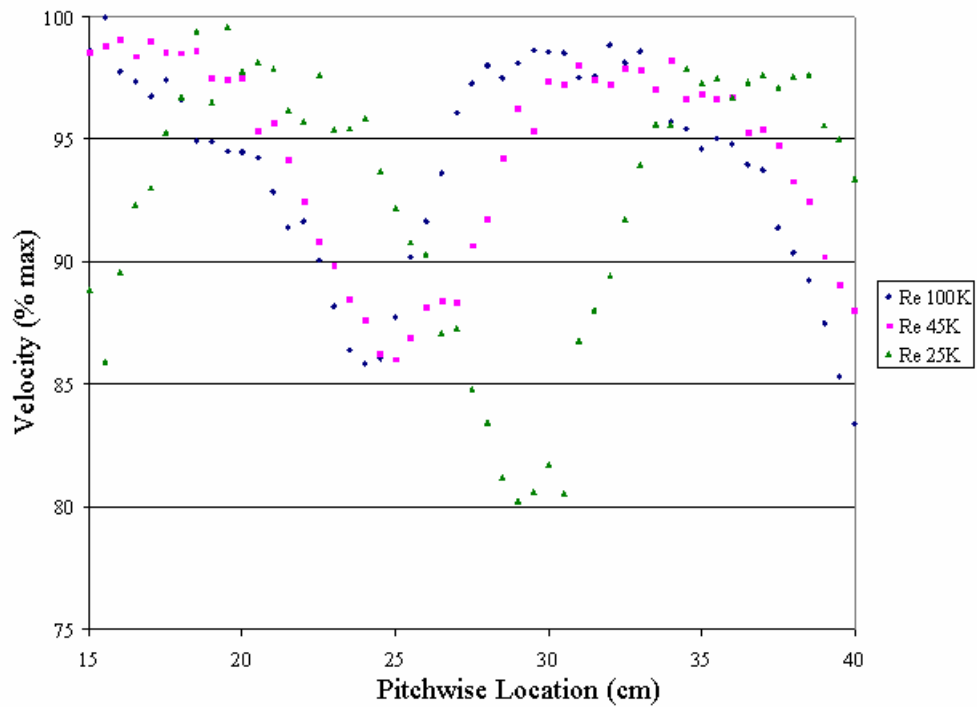


Figure 103. Wake velocity profiles behind an unmodified Pak-B blade and 1% Tu

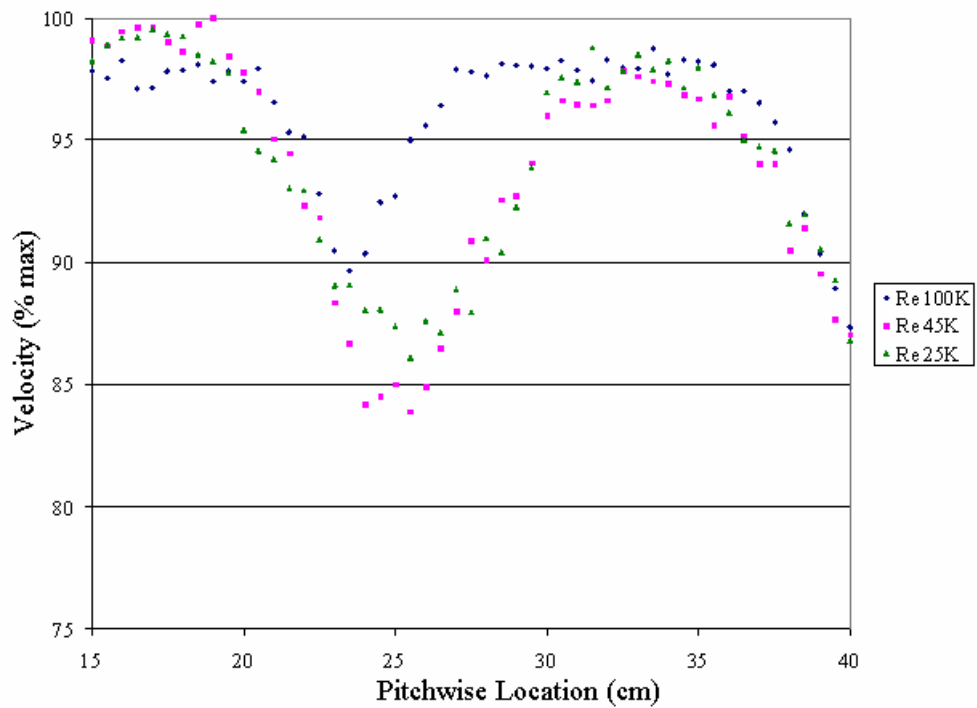


Figure 104. Wake velocity profiles behind an unmodified Pak-B blade and 4% Tu

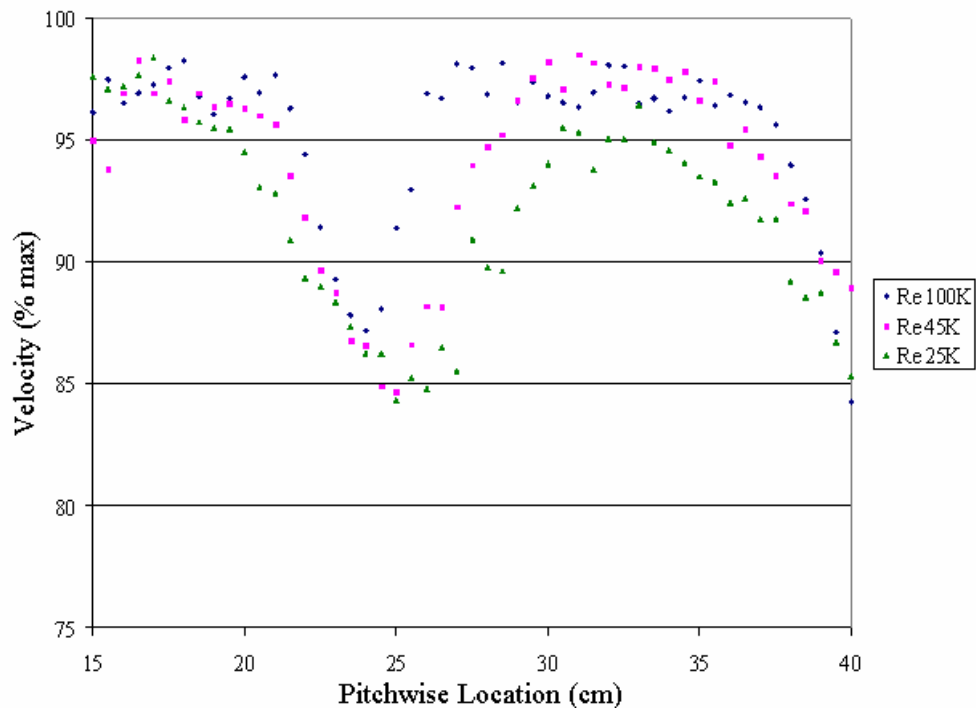


Figure 105. Wake velocity profiles behind a Pak-B blade with dimples at 65% of the axial chord with 2.22 cm spacing and 1% Tu

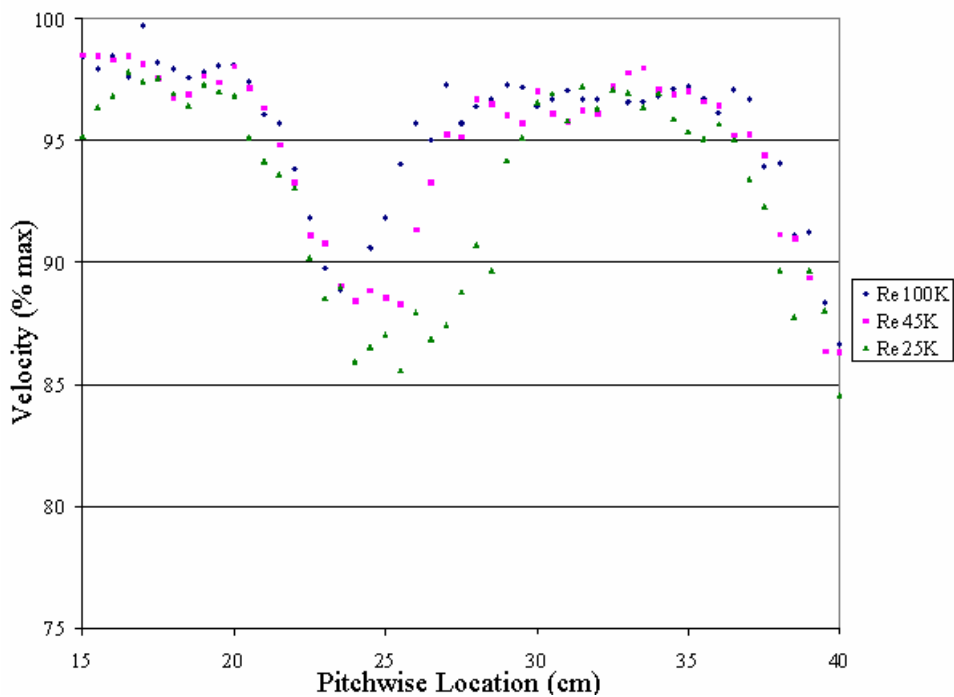


Figure 106. Wake velocity profiles behind a Pak-B blade with dimples at 65% of the axial chord with 2.22 cm spacing and 4% Tu

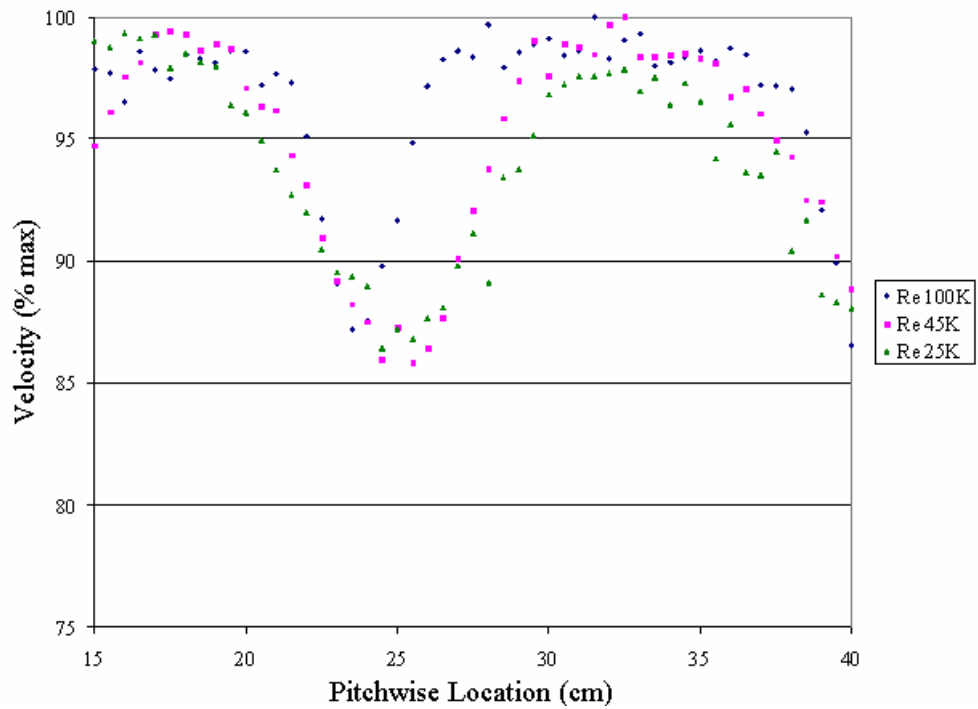


Figure 107. Wake velocity profiles behind a Pak-B blade with dimples at 65% of the axial chord with 4.44 cm spacing and 1% Tu

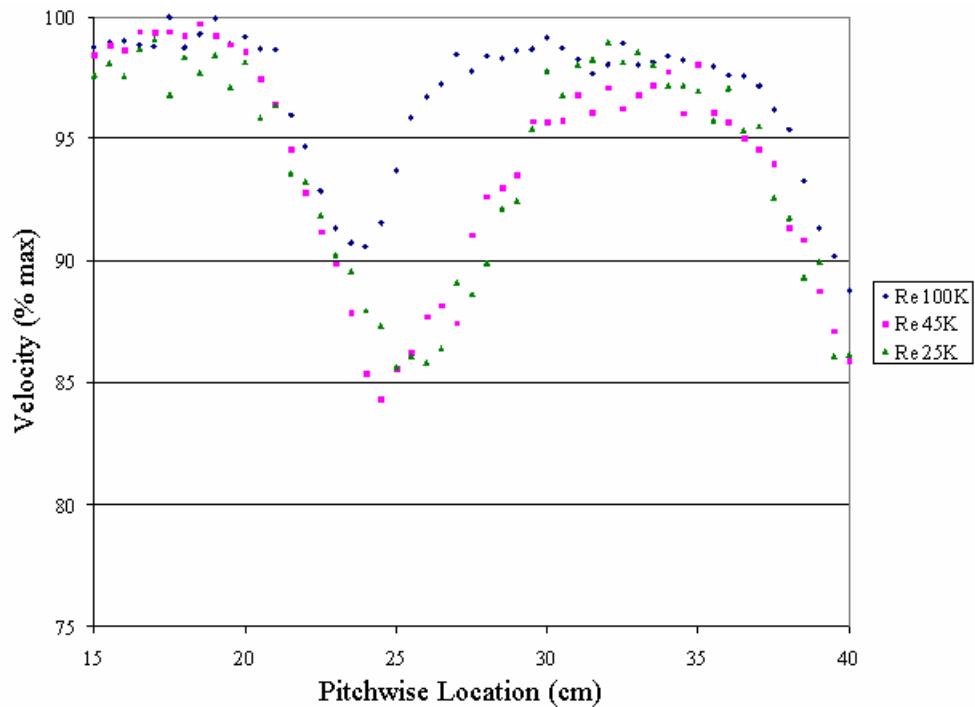


Figure 108. Wake velocity profiles behind a Pak-B blade with dimples at 65% of the axial chord with 4.44 cm spacing and 4% Tu



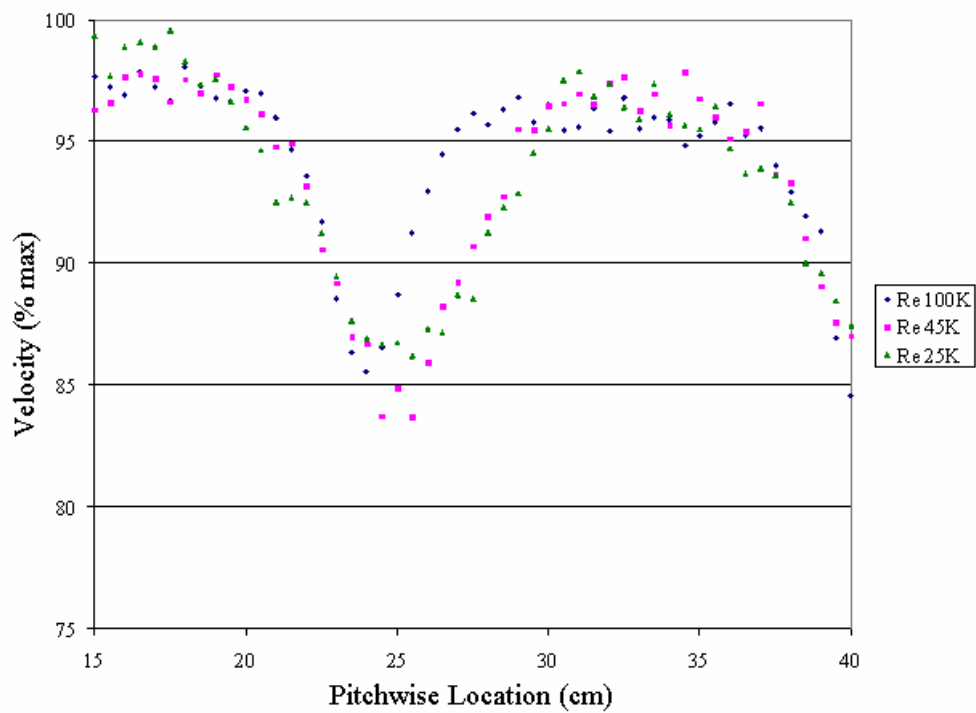


Figure 109. Wake velocity profiles behind a Pak-B blade with dimples at 65% and 76% of the axial chord with 4.44 cm spacing and 1% Tu

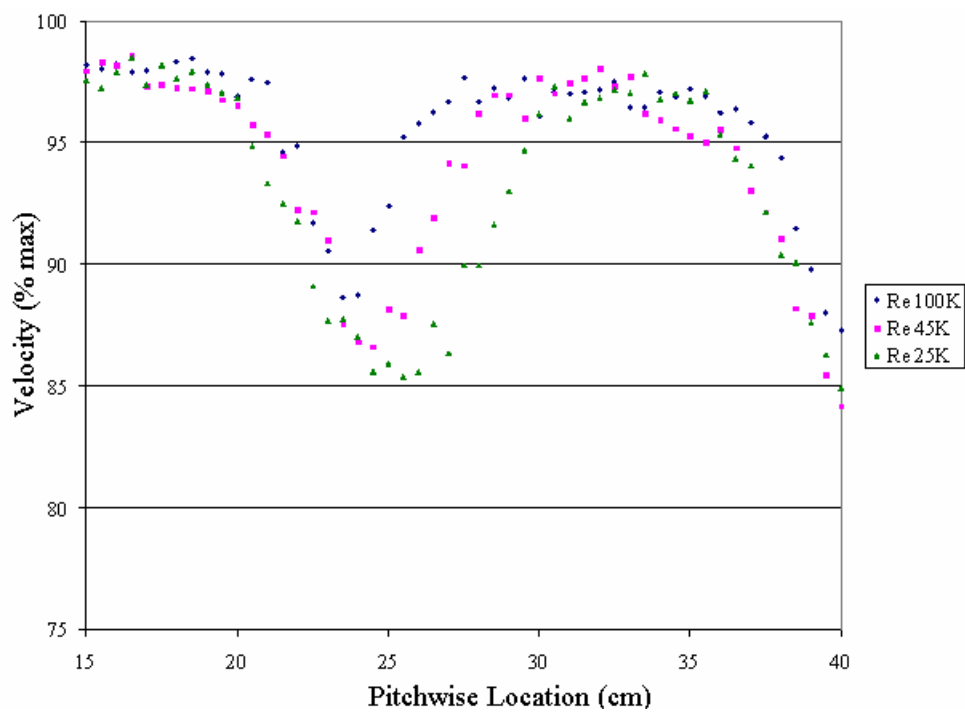


Figure 110. Wake velocity profiles behind a Pak-B blade with dimples at 65% and 76% of the axial chord with 4.44 cm spacing and 4% Tu

## APPENDIX E. Local Total Pressure Loss Coefficient Profiles

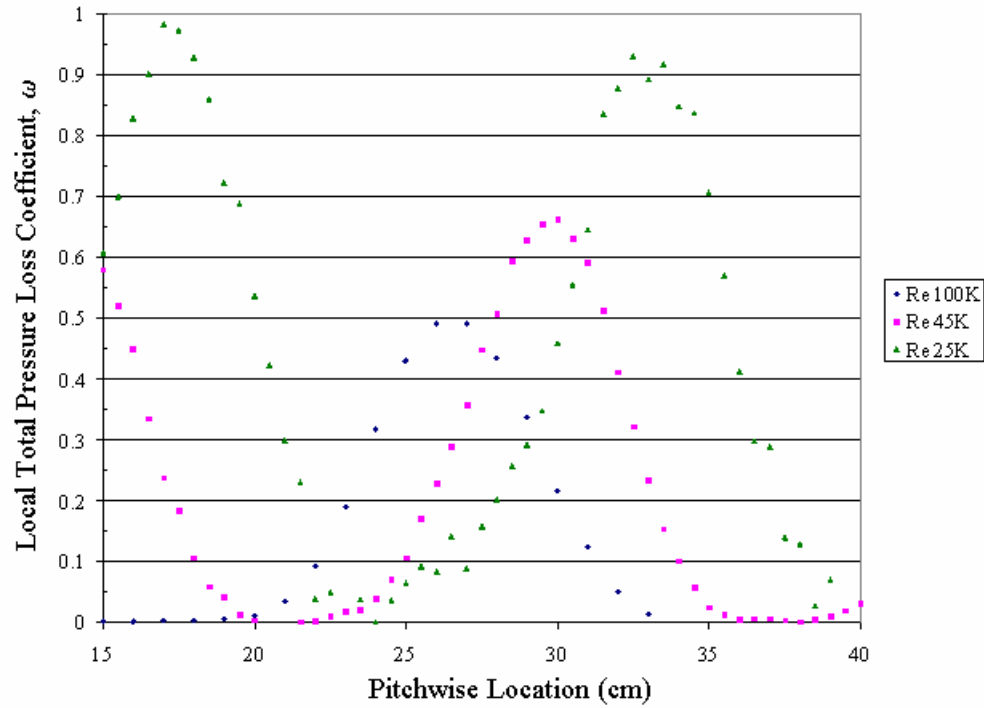


Figure 111. Wake loss profiles behind an unmodified Pak-B blade and 1% Tu

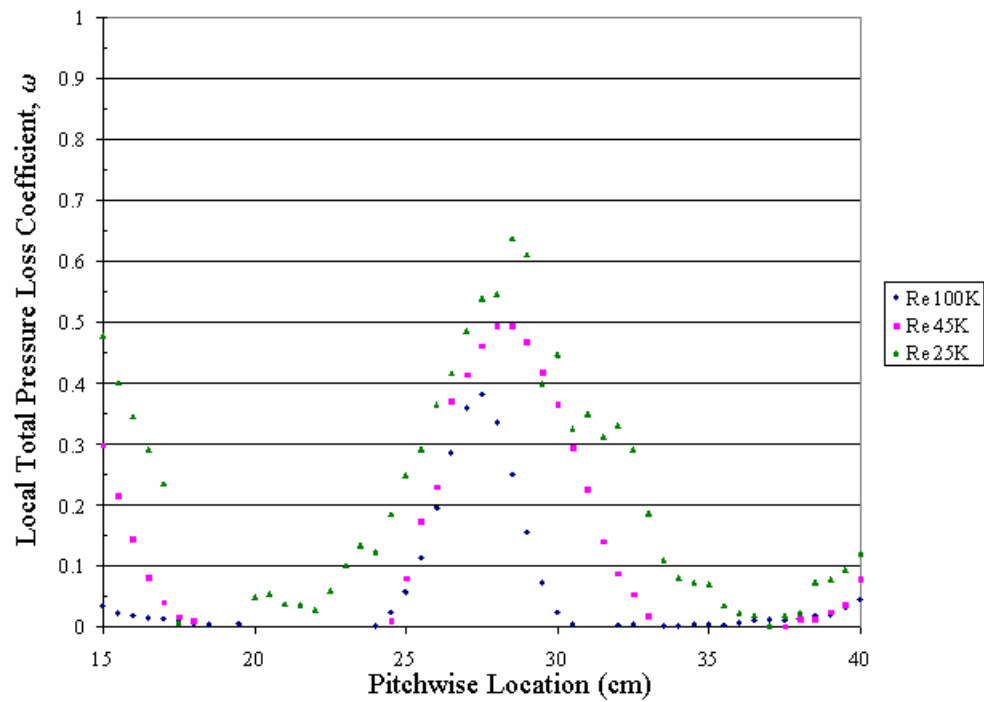


Figure 112. Wake loss profiles behind an unmodified Pak-B blade and 4% Tu

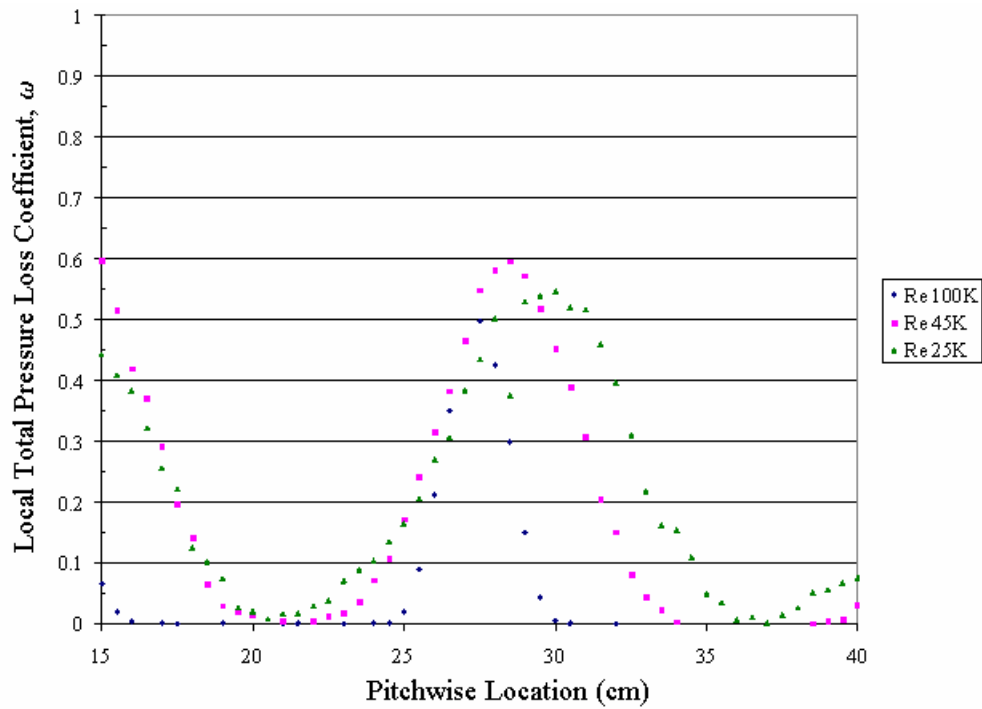


Figure 113. Wake loss profiles behind a Pak-B blade with dimples at 65% of the axial chord with 2.22 cm spacing and 1% Tu

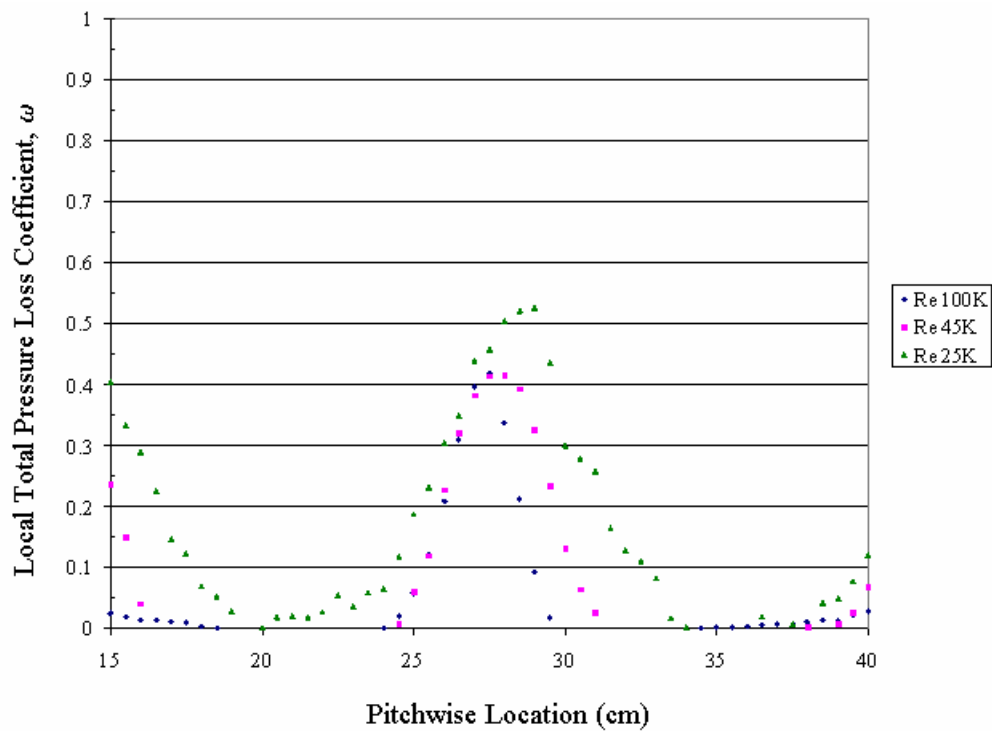


Figure 114. Wake loss profiles behind a Pak-B blade with dimples at 65% of the axial chord with 2.22 cm spacing and 1% Tu

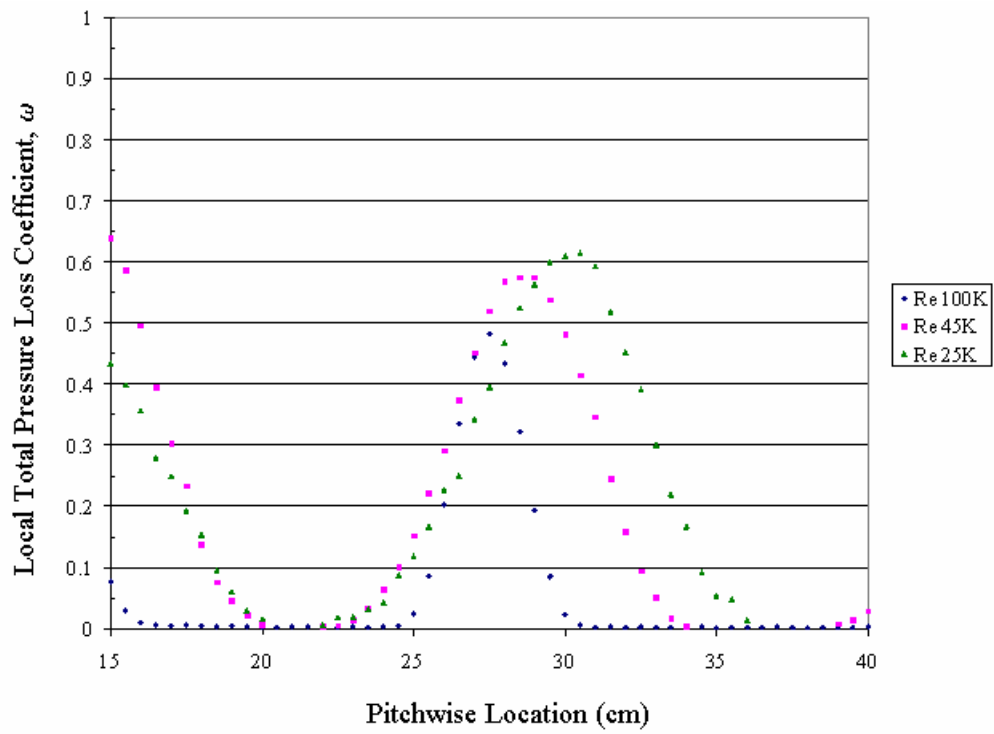


Figure 115. Wake loss profiles behind a Pak-B blade with dimples at 65% of the axial chord with 4.44 cm spacing and 1% Tu

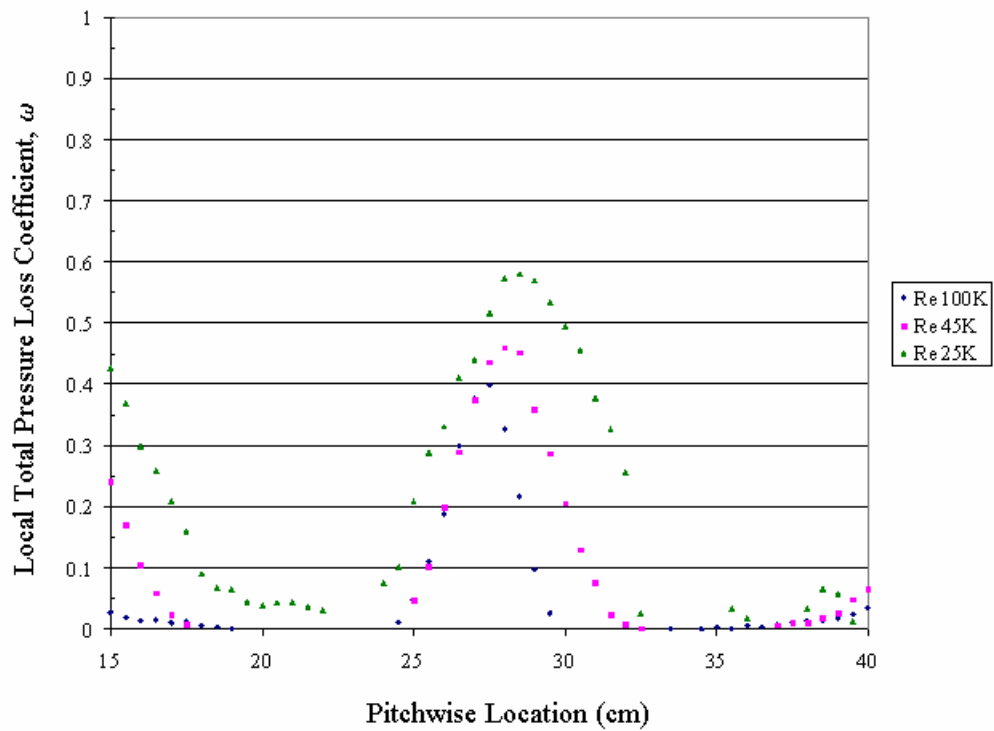


Figure 116. Wake loss profiles behind a Pak-B blade with dimples at 65% of the axial chord with 4.44 cm spacing and 1% Tu

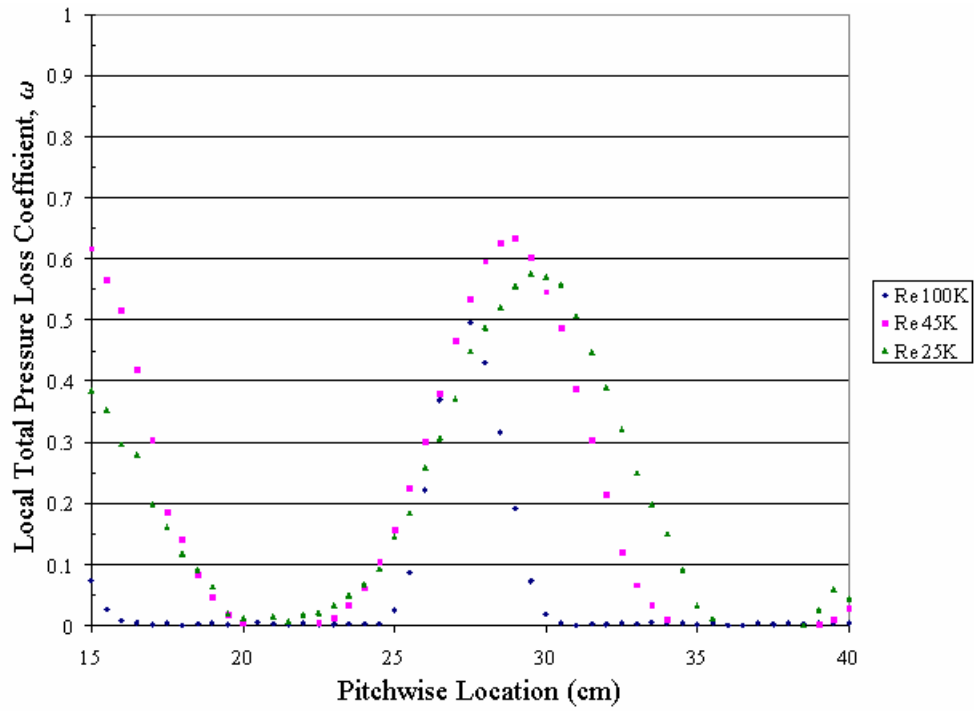


Figure 117. Wake velocity profiles behind a Pak-B blade with dimples at 65% and 76% of the axial chord with 4.44 cm spacing and 1% Tu

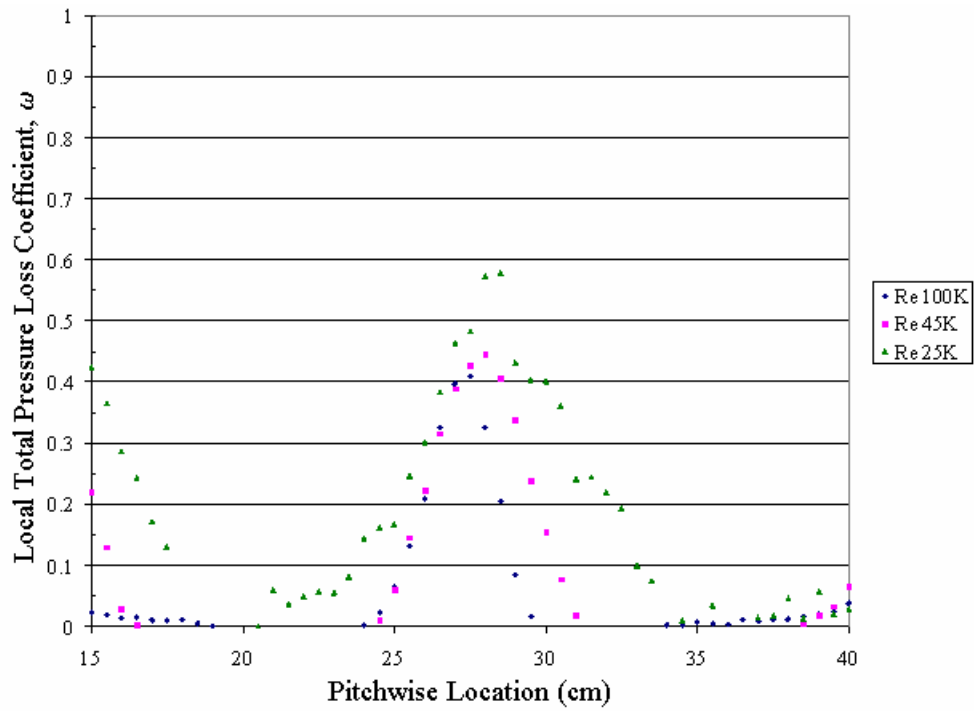


Figure 118. Wake velocity profiles behind a Pak-B blade with dimples at 65% and 76% of the axial chord with 4.44 cm spacing and 4% Tu

**APPENDIX F. Computational Boundary Layer Measurements**

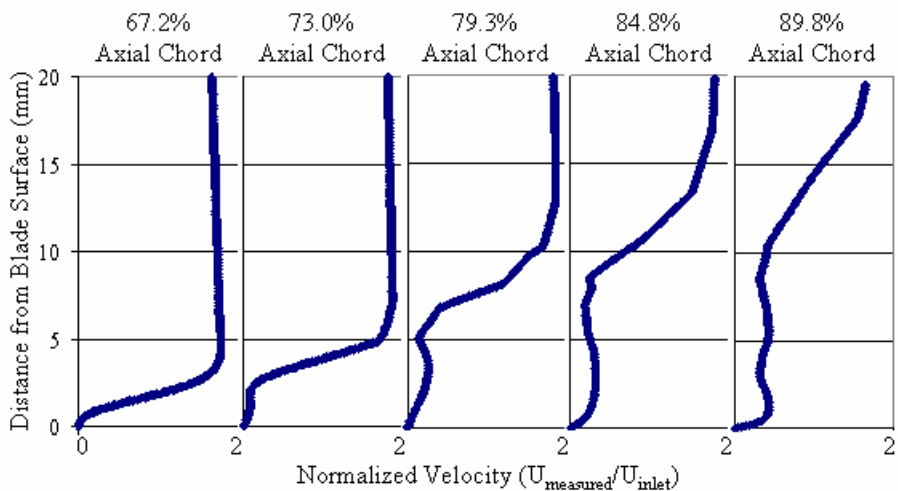


Figure 119. Boundary layer profiles for an unmodified, computational Pak-B blade at  $Re\ 25k$  and  $0\% Tu$

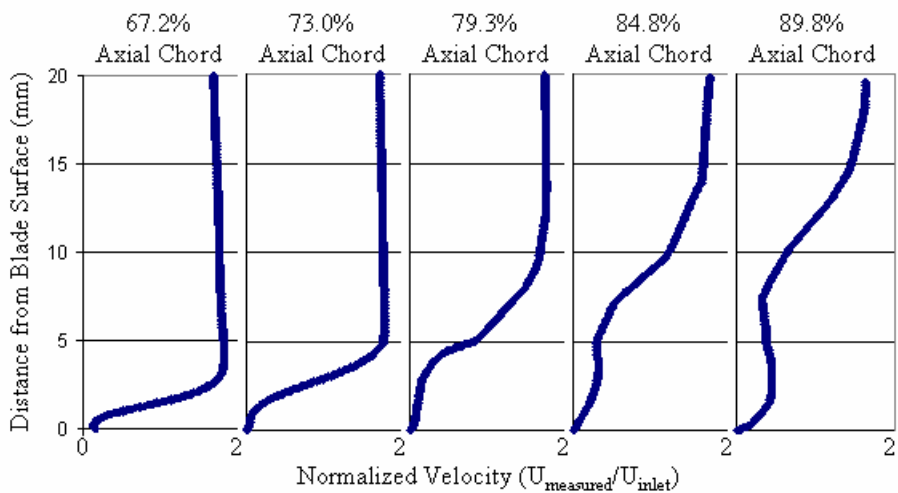


Figure 120. Boundary layer profiles for a computational Pak-B blade with dimples at 65% of the axial chord with 2 cm spacing at  $Re\ 25k$  and  $0\% Tu$

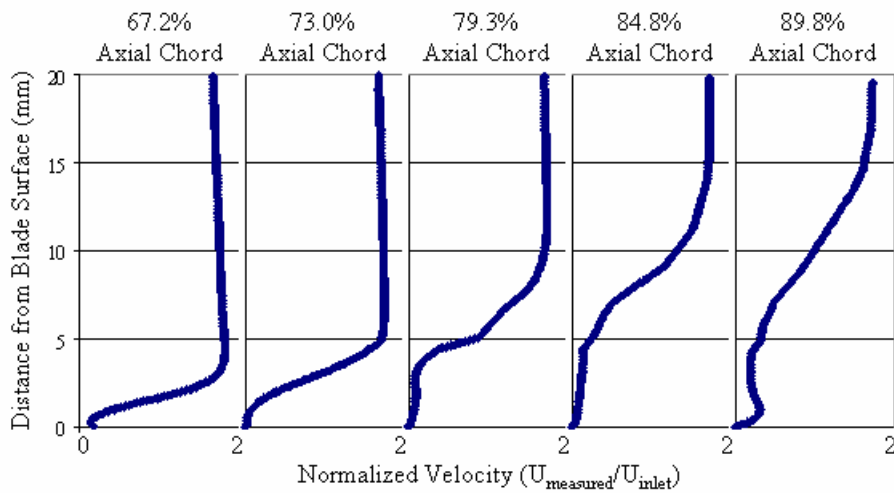


Figure 121. Boundary layer profiles for a computational Pak-B blade with dimples at 65% of the axial chord with 4 cm spacing at Re 25k and 0% Tu

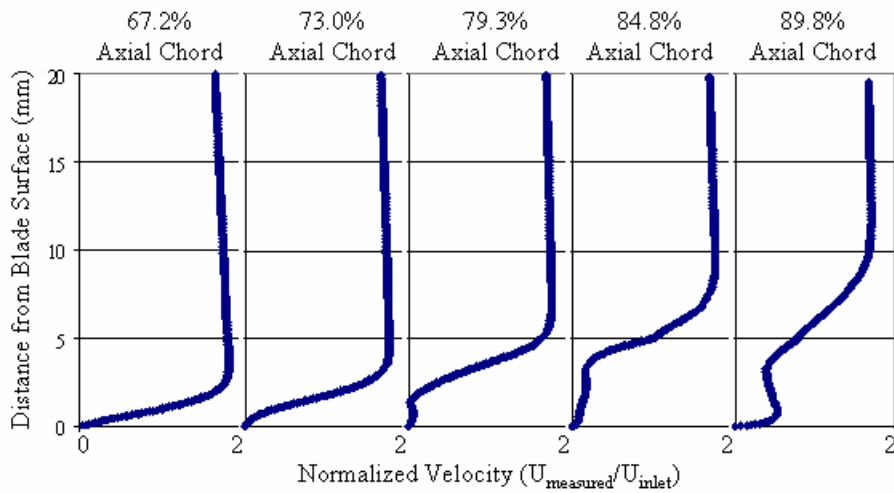


Figure 122. Boundary layer profiles for a computational Pak-B blade with dimples at 65% and 76% of the axial chord with 2 cm spacing at Re 25k and 0% Tu

## **APPENDIX G. CFD Time History Investigation**

A brief study of the transient time history of each of the computational models at a Reynolds number of 25k was performed. The velocity magnitude was measured at a point 3 cm normal to the blade at the 93.75% of the axial chord. This point was selected because it is above the shear layer. A point below the shear layer experiences a large degree of unsteadiness making coherent structures difficult to see. The flow time and corresponding velocity magnitude was recorded at the designated point at each time step throughout the flow solution.

Figure 123 shows a comparison between the time history plots for the four blade configurations studied. The unmodified flow field seems to be dominated by a single shedding frequency. The unmodified blade shows nearly sinusoidal behavior at a frequency of about 11 Hz. It is believed that the unmodified blade has settled into a limit cycle dominated by a large vortex shedding every 0.09 sec by about 0.35 sec of flow time. The unmodified blade also fluctuates by about 30% of the mean from maximum to minimum.

Clearly, the plots for the modified blades illustrate that the flow field has been dramatically altered by the dimple presence. The most obvious change is the elimination of a simple sinusoidal period. It is believed that the low frequency cycle associated with large vortex shedding has been eliminated. The modified blades appear to have very complex flow fields with seemingly random oscillations. One explanation for the high frequency oscillations is that the flow complexity is such that it takes much longer for initial transients to wash out. The implication then would be that the solutions have not been run far enough in time. Another, more likely, possibility is that the flow field has



reached its final state; however, this final state is populated by high frequency oscillations in the shear layer. A more detailed time independence study is required to determine the maturity of the solution.

Another change evident in Fig. 123 is the significant reduction in magnitude of the oscillations. The fluctuation in measured velocity from the maximum to minimum value for both the 2 cm and 4 cm cases is no more than 13% of the mean velocity. The same calculation for the multiple row case shows the maximum to minimum value fluctuations are less than 6% of the mean velocity. Again, the reduction in fluctuation amplitude supports the conclusion that the large scale vortex shedding has been eliminated.

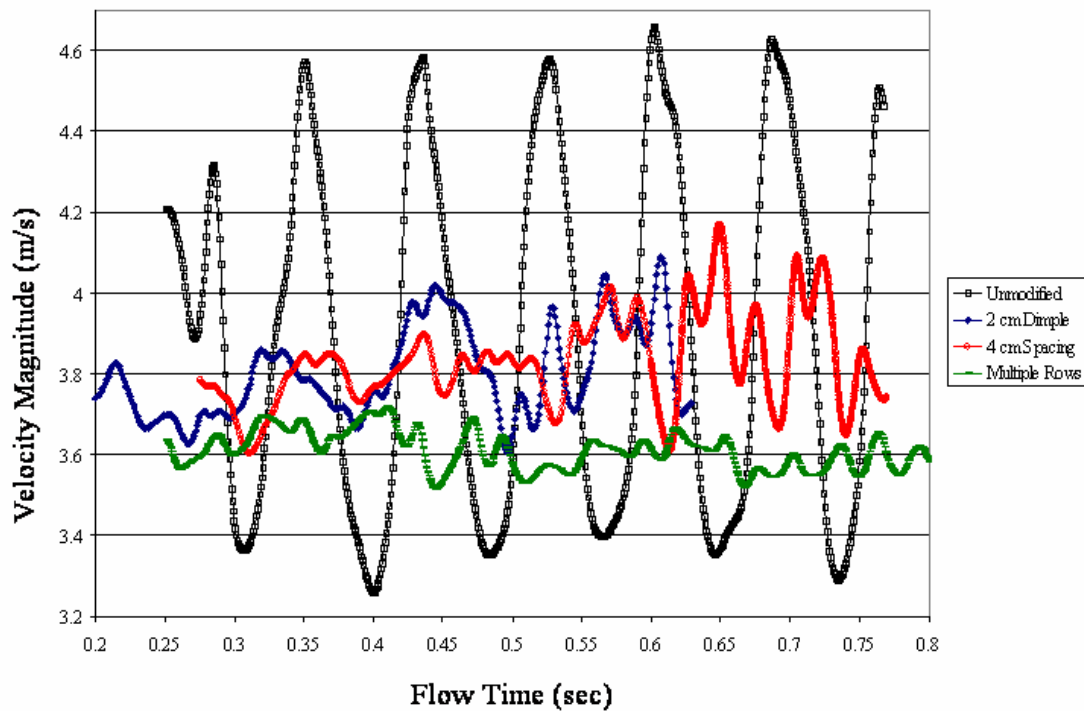


Figure 123. Time History plot of at Re 25k and different dimple patterns

The time step size appears to be adequate in resolving the flow physics as illustrated in Fig. 123. For the unmodified blade, the field was recorded at a frequency of about 1334 Hz. This results in 120 data points per wave form. The 4 cm case with a dimple at 65% of the axial chord and the multiple row case also record values at about 1334 Hz. The 2 cm blade with a single dimple at 65% of the axial chord recorded data at 1000 Hz. For the modified blades there is no clearly defined sinusoidal period, but visual inspection verifies that there is certainly more than 10 points per wave form.

Figure 124 illustrates the differences in average velocity in the blade passage. The larger mean velocity in the blade passage for the unmodified blade is attributed to a blockage effect of the separated flow. The blockage has a tendency to accelerate the flow between the detached shear layer and the adjacent pressure surface. The lower average velocity associated with the modified blades is attributed to less blockage in the blade passage indicating more attached flow.

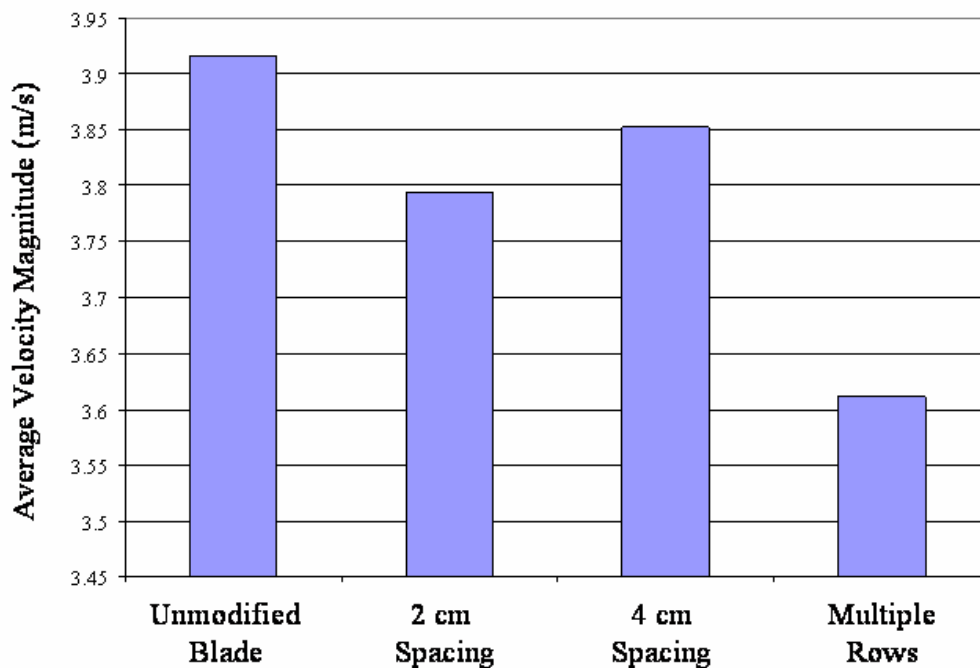


Figure 124. The time averaged velocity magnitude throughout each solution

## APPENDIX H. Tunnel Periodicity Study

Figure 125 depicts a comparison of the measured pressure coefficient over an unmodified Pak-B blade at locations 4 and 6 in the linear turbine cascade. It is important to recognize that there are slight differences due to pitchwise variations in the tunnel. The differences are minimal, however. Also, the inference can be made that the measurements made at blade 5 would be between the two presented curves.

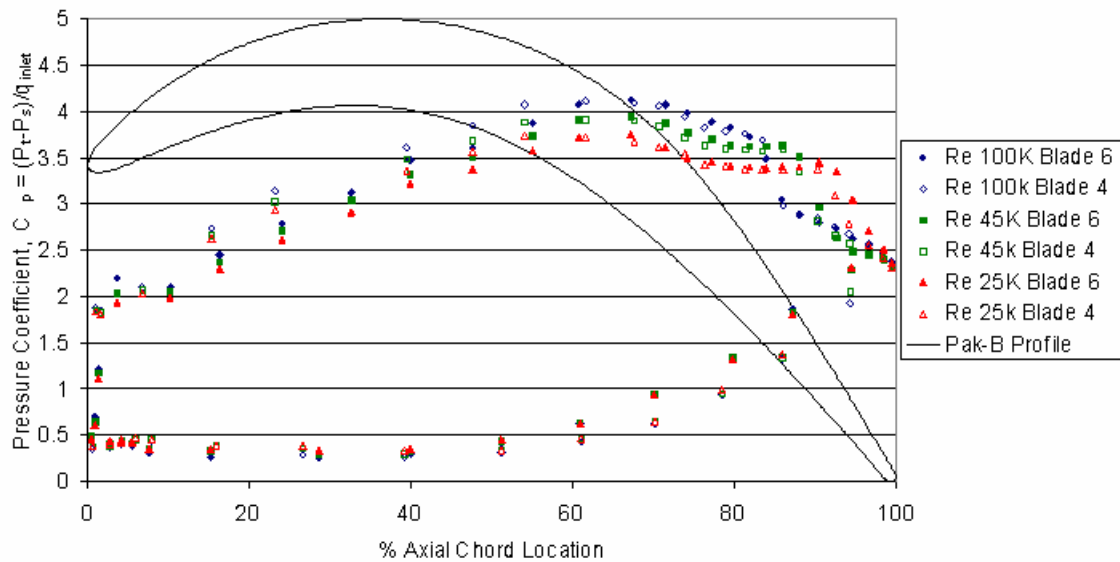


Figure 125. Surface Static Pressure Coefficient Comparison between Blade 4 and Blade 6 at various Reynolds numbers and 4% Tu

## References

1. Lake, James P., "Flow Separation Prevention on a Turbine Blade in Cascade at Low Reynolds Number." *PhD Dissertation*, Air Force Institute of Technology, 1999. AFIT/DS/ENY/99-01.
2. Rouser, Kurt, P., "Use of Dimples to Suppress Boundary Layer Separation on a Low Pressure Turbine Blade." *Masters Thesis*, Air Force Institute of Technology, 2002. AFIT/GAE/ENY/02-13.
3. Halstead, D.E., D.C. Wisler, T.H. Okiishi, G.J. Walker, H.P. Hodson and H.W. Shin, "Boundary Layer Development in Axial Compressors and Turbines Part 1 of 4: Composite Picture." *International Gas Turbine Institute and Aeroengine Congress and Exposition*, Houston, TX, June 1995. ASME Paper No. 95-GT-461.
4. Halstead, D.E., D.C. Wisler, T.H. Okiishi, G.J. Walker, H.P. Hodson and H.W. Shin, "Boundary Layer Development in Axial Compressors and Turbines Part 3 of 4: LP Turbines." *International Gas Turbine Institute and Aeroengine Congress and Exposition*, Houston, TX, June 1995. ASME Paper No. 95-GT-463.
5. Rivir, R.B. "Transition on Turbine Blades and Cascades at Low Reynolds Numbers." *Technical Report WL-TR-96-2084*, Wright Laboratory, 1996.
6. Sharma, O., 1998, "Impact of Reynolds Number on LP Turbine Performance," *Proceedings of the 1997 Minnowbrook II Workshop on Boundary Layer Transition in Turbomachines*, NASA CP-1998-206958, 1998, pp. 65-69.
7. Murawski, C.G., T.W. Simon, R.J. Volino and K. Vafai, "Experimental Study of the Unsteady Aerodynamics in a Linear Cascade with Low Reynolds Number Low Pressure Turbine Blades." *International Gas Turbine Institute and Aeroengine Congress and Exposition*, Orlando, FL, June 1997. ASME Paper No. 97-GT-95.
8. Qui, S. and T.W. Simon, "An Experimental Investigation of Transition as Applied to Low Pressure Turbine Suction Surface Flows." *International Gas Turbine Institute and Aeroengine Congress and Exposition*, Orlando, FL, June 1997.
9. Simon, T.W. and R.J. Volino, "Separating and Separated Boundary Layers." *Technical Report WL-TR-96-2092*, Wright Laboratory, 1996.
10. Hourmouziadis, J. "Aerodynamic Design of Low Pressure Turbines." *AGARD*, pages 1-38. 1989. AGARD-LS-167.

11. Mattingly, J.D. *Elements of Gas Turbine Propulsion*. McGraw-Hill, Inc., New York, 1996.
12. Moran, Michael J. and Howard N. Shapiro. *Fundamentals of Engineering Thermodynamics*. John Wiley and Sons Inc., New York, 1988.
13. Werle, M.J. "Compressor and Turbine Blade Boundary Layer Separation." *AGARD Conference Proceedings*, AGARD-CP-351 (1983).
14. Mayle, R.E. "The Role of Laminar-Turbulent Transition in Gas Turbine Engines." *Journal of Turbomachinery*, 113:509-537 (October 1991). ASME Paper No. 91-GT-282.
15. Addison, J.S. and H.P. Hodson. "Modeling of Unsteady Transition Boundary Layers." *International Gas Turbine and Aeroengine Congress and Exposition*, Orlando, FL, June 1991. ASME Paper No. 91-GT-282.
16. Walker, G.J. "The Role of Laminar-Turbulent Transition in Gas Turbine Engines: A Discussion." *Journal of Turbomachinery*, 115:207-217 (April 1993).
17. Halstead, D.E., D.C. Wisler, T.H. Okiishi, G.J. Walker, H.P. Hodson and H.W. Shin. "Boundary Layer Development in Axial Compressors and Turbines Part 4 of 4: Computational Analysis." *International Gas Turbine and Aeroengine Congress and Exposition*, Houston, TX, June 1995. ASME Paper No. 95-GT-464.
18. Johnston, J.P. and Nishi, M. "Vortex-generator Jets-Means for Flow Separation Control." *AIAA Journal*, Vol. 28, No. 6, June 1990, pp. 989-994.
19. Compton, D.A. and Johnston, J.P. "Streamwise Vortex Production by Pitched and Skewed Jets in a Turbulent Boundary-Layer." *AIAA Journal*, Vol. 30, No. 3, March 1992, pp. 640-647.
20. Bons, Jeffrey P., Sondergaard, Rolf, and Rivir, Richard B. "Turbine Separation Control Using Pulsed Vortex Generator Jets." *ASME Journal*, Vol. 123, April 2001, pp. 198-206.
21. Lin, J.C., Howard, F.G., Bushnell, D.M., and Shelby, G.V. "Investigation of Several Passive and Active Methods of Turbulent Flow Separation Control." *AIAA Paper #90-1598*, 1990.
22. Borgeson, David. "Boundary Layer Control Using Micro-Electromechanical Systems." *MS Thesis*, Air Force Institute of Technology, 2002. AFIT/GSO/ENP/
23. Chang, P.K. *Separation of Flow*. Pergamon Press, 1970.

24. Austin, J.G. "Mach Number, Flow Angle, and Loss Measurements Downstream of a Transonic Fan-Blade Cascade." *MS Thesis*, Naval Postgraduate School, March 1994.
25. Gamerding, P.M. and R.P. Shreeve. "The Effects of Low-Profile Vortex Generators on Flow in a Transonic Fan-Blade Cascade." *34<sup>th</sup> Aerospace Sciences Meeting and Exhibit*, Reno, NV, January 1996. AIAA Paper No. 96-0250.
26. Rao, D.M. and T.T. Kariya. "Boundary-Layer Submerged Vortex Generators for Separation Control – An Exploratory Study." *1<sup>st</sup> National Fluid Dynamic Congress, 1988*. AIAA Paper No. 88-3546-CP.
27. Lin, J.C., F.G. Howard, and G.V. Shelby. "Turbulent Flow Separation Control through Passive Techniques." *AIAA 2<sup>nd</sup> Shear Flow Conference*, Tempe, AZ, March 1989. AIAA Paper No. 89-0976.
28. McCormick, D.C. "Shock-Boundary Layer Interaction Control with Low-Profile Vortex Generators and Passive Cavity." *30<sup>th</sup> Aerospace Sciences Meeting and Exhibit*, January 1992. AIAA Paper no. 92-0064.
29. Wheeler, G. O. "Means for Maintaining Attached Flow of a Flowing Medium." June 1984. United States Patent No. 4,455,045.
30. Walsh, M.J. "Riblets as Viscous Drag Reduction Technique." *AIAA Journal*, 21(4):485-486 (April 1983).
31. Walsh, M.J. "Turbulent Boundary Layer Drag Reduction Using Riblets." *AIAA 20<sup>th</sup> Aerospace Sciences Meeting*, Orlando, FL, January 1982. AIAA Paper No. 82-0169.
32. Bacher, E.V. and C.R. Smith. "Turbulent Boundary-Layer Modification by Small-Scale Riblets." *AIAA Journal*, 24(8):1382-1385. (August 1986).
33. Bacher, E.V. and C.R. Smith. "A Combined Visualization-Anemometry Study of the Turbulent Drag Reducing Mechanisms of Triangular Micro-Groove Surface Modifications." *AIAA Shear Flow Control Conference*, Boulder, CO, March 1985. AIAA Paper No. 85-0548.
34. Maciejewski, P.K. and R.B. Rivir. "Effects of Surface Riblets and Free-Stream Turbulence on Heat Transfer in a Linear Turbine Cascade." *International Gas Turbine and Aeroengine Congress and Exposition*, The Hague, Netherlands, June 1994. ASME Paper No. 94-GT-245.

35. Taylor, H.D. "Summary Report on Vortex Generators." *Technical Report No. R-05280-9*, United Aircraft Corporation Research Department, March 1950.
36. Bloch, D.R. and T.J. Mueller. "Effects of Distributed Grit Roughness on Separation and Transition on an Airfoil at Low Reynolds Numbers." Pages 152-161 (1986). AIAA Paper No. 86-1788.
37. Bearman, P.W. and J.K. Harvey. "Golf Ball Aerodynamics." *The Aeronautical Quarterly*, 27(2):112-122 (May 1976).
38. Bearman, P.W. and J.K. Harvey. "Control of Circular Cylinder Flow by the Use of Dimples," *AIAA Journal*, 31(10):1753-1756 (October 1993).
39. Bons, J.P., R. Sondergaard and R.B. Rivir "Control of Low-Pressure Turbine Separation Using Vortex Generator Jets." *AIAA 37<sup>th</sup> Aerospace Sciences Meeting & Exhibit, Reno, NV, January 1999, AIAA Paper #99-0367*.
40. Tannehill, John C., Dale A. Anderson, Richard H. Pletcher *Computational Fluid Mechanics and Heat Transfer Second Edition*. Taylor and Francis, Levittown, Pa, 1997.
41. *FIELDVIEW: User Manual, Version 9*. Intelligent Light. Lyndhurst, NJ. 2001.
42. Bruun, H.H. *Hot-Wire Anemometry*. Oxford University Press, Oxford, 1995.
43. Pressurements Ltd. "Users Handbook Deadweight Tester Model V1600/3D." Bedfordshire, England.

## **Vita**

2d Lt John Philip Casey graduated from Hunterdon Central Regional High School, Flemington, NJ in June 1998. He entered college at Rensselaer Polytechnic Institute (RPI), Troy, NY, and enrolled in the Air Force Reserve Officer Training Corps in August 1998. While attending school at RPI he was inducted into both Tau Beta Pi and Sigma Gamma Tau. He graduated from RPI in May 2002, earning a Bachelor of Science degree in Aeronautical Engineering and was granted a commission in the USAF in May 2002.

Lt Casey was selected to enter the Air Force Institute of Technology Graduate School of Engineering and Management as a direct accession. He entered active duty in August 2002, and moved to Wright-Patterson AFB, Dayton, OH. There he worked towards a Masters of Science degree in Aeronautical Engineering. Upon graduation he will be assigned to the Air Vehicles Directorate at Wright-Patterson AFB.



REPORT DOCUMENTATION PAGE				Form Approved OMB No. 074-0188	
<p>The public reporting burden for this collection of information is estimated to average 1 hour per response, including the time for reviewing instructions, searching existing data sources, gathering and maintaining the data needed, and completing and reviewing the collection of information. Send comments regarding this burden estimate or any other aspect of the collection of information, including suggestions for reducing this burden to Department of Defense, Washington Headquarters Services, Directorate for Information Operations and Reports (0704-0188), 1215 Jefferson Davis Highway, Suite 1204, Arlington, VA 22202-4302. Respondents should be aware that notwithstanding any other provision of law, no person shall be subject to an penalty for failing to comply with a collection of information if it does not display a currently valid OMB control number.</p> <p><b>PLEASE DO NOT RETURN YOUR FORM TO THE ABOVE ADDRESS.</b></p>					
1. REPORT DATE (DD-MM-YYYY) 23 Mar 04		2. REPORT TYPE Master's Thesis		3. DATES COVERED (From – To) September 2002 – March 2004	
4. TITLE AND SUBTITLE  EFFECT OF DIMPLE PATTERN ON THE SUPPRESSION OF BOUNDARY LAYER SEPARATION ON A LOW PRESSURE TURBINE BLADE				5a. CONTRACT NUMBER	
				5b. GRANT NUMBER	
				5c. PROGRAM ELEMENT NUMBER	
6. AUTHOR(S)  Casey, John, P., 2d Lt, USAF				5d. PROJECT NUMBER	
				5e. TASK NUMBER	
				5f. WORK UNIT NUMBER	
7. PERFORMING ORGANIZATION NAMES(S) AND ADDRESS(S) Air Force Institute of Technology Graduate School of Engineering and Management (AFIT/EN) 2950 Hobson Way WPAFB OH 45433-7765				8. PERFORMING ORGANIZATION REPORT NUMBER  AFIT/GAE/ENY/04-M05	
9. SPONSORING/MONITORING AGENCY NAME(S) AND ADDRESS(ES) AFRL/PRTT Attn: Dr. Rolf Sondergaard 1950 5 <sup>th</sup> Street WPAFB OH 45433-7251 DSN: 785-7190				10. SPONSOR/MONITOR'S ACRONYM(S)	
				11. SPONSOR/MONITOR'S REPORT NUMBER(S)	
12. DISTRIBUTION/AVAILABILITY STATEMENT APPROVED FOR PUBLIC RELEASE; DISTRIBUTION UNLIMITED.					
13. SUPPLEMENTARY NOTES					
14. ABSTRACT <p>Three dimple patterns were investigated to ascertain their relative effectiveness on controlling boundary layer separation from a low-pressure turbine blade. The three cases included a single row of dimples at 65% of the axial chord with 2.22 cm spacing, a single row of dimples at 65% of the axial chord with 4.44 cm spacing, and a two-row staggered pattern with rows at 65% and 76% of the axial chord with 4.44 cm spacing. The multiple row case was such that the center of the upstream dimple set at the midpoint between two downstream dimples. The dimple spacing was measured center-on-center. Each of the dimple patterns was studied and compared to an unmodified blade at axial chord Reynolds numbers based on inlet velocity of 25k, 45k, and 100k. Experimental data was collected in a low-speed, draw down wind tunnel containing a linear turbine cascade of 8 Pak-B blades. Measurements of surface pressure, boundary layer parameters, wake velocity, and total pressure losses were made to examine the flow. No dimple pattern dramatically outperformed the others. Each of the dimple patterns studied improved the average total pressure loss coefficient by 34% for Re 25k and 1% Tu. Complementing the experimental effort was a three-dimensional computational fluid dynamics study. Four models were built and analyzed. The models included an unmodified blade, blades with dimples at 65% of the axial chord with 2 cm or 4 cm spacing, respectively, and a multiple row case consisting of dimples at 65% and 76% of the axial chord with 2 cm spacing. Again the upstream dimple set at the midpoint between two downstream dimples. The computational fluid dynamics study provided detailed flow visualization in and around the dimples as well as a comparison to experimental data for solver verification. It was shown that the computational and experimental results showed similar trends in wake loss and boundary layer traverses.</p>					
15. SUBJECT TERMS Laminar Boundary Layer Separation, Boundary Layer Transition, Turbulent Boundary Layer, Boundary Layer Trips, Passive Boundary Layer Controls, Passive Flow Controls, Low Pressure Turbine Blade, Low Pressure Turbine Blade Performance, Gas Turbine Engine, Low Reynolds Number, Computational Fluid Dynamics, CFD, Boundary Layer Measurements, Wake Loss Measurements, Experimental to Computational Comparisons					
16. SECURITY CLASSIFICATION OF:			17. LIMITATION OF ABSTRACT  UU	18. NUMBER OF PAGES 201	19a. NAME OF RESPONSIBLE PERSON Dr. Paul I. King (ENY)
REPORT U	ABSTRACT U	c. THIS PAGE U			19b. TELEPHONE NUMBER (Include area code) (937) 255-6565, ext 4314; e-mail: Paul.King@afit.edu